Author:
Saunderson, Tom G

Title:
The effect of impurities on the superconducting state

The Effect of Impurities on the Superconducting State

By

TOM G. SAUNDERSON

School of Physics
UNIVERSITY OF BRISTOL

A dissertation submitted to the University of Bristol in accordance with the requirements of the degree of DOCTOR OF PHILOSOPHY in the School of Physics.

OCTOBER 2020

Word count: 30630

Abstract

In this work we have implemented the Bogoliubov-de Gennes (BdG) equation in a screened Korringa-Kohn-Rostoker (KKR) method for solving, self-consistently, the spin-polarised superconducting state for 3d crystals including substitutional impurities. The generalisation to the fully relativistic Dirac-Bogoliubov-de Gennes (DBdG) equations is also implemented for 3d crystals. This method combines the full complexity of the underlying electronic structure and Fermi surface geometry with a simple phenomenological parametrisation for the superconductivity. We apply this theoretical framework to the known s-wave superconductors Nb, Pb, and MgB_2. In these materials multiple distinct peaks at the gap in the density of states were observed, showing significant gap anisotropy which is in good agreement with experiment. For Pb the effects of spin-orbit coupling and the surface gap anisotropy are also addressed. Qualitatively, the results can be explained in terms of the k-dependent Fermi velocities on the Fermi surface sheets exploiting concepts from Bardeen-Cooper-Schrieffer (BCS) theory.

We then investigate how impurities affect the superconducting state by applying the theoretical framework to bulk Nb with non-magnetic impurities. Without non-magnetic impurities, Nb has an anisotropic gap structure with two distinct peaks around the Fermi level. In the presence of non-magnetic impurities those peaks are broadened due to the scattering between the two bulk superconducting gaps, however the peaks remain separated. As a second example of self-consistent real-space solutions of the BdG equations we examine superconducting clusters embedded within a non-superconducting bulk metallic host. This allows us to estimate the coherence length of the superconductor and we show that, within our framework, the coherence length of the superconductor is related to the inverse of the gap size, just as in bulk BCS theory. The resulting local density of states (LDOS) in the superconductor is non-zero at the Fermi level due to the metallic host, giving it a striking resemblance to the pseudogap phase in copper-oxide based superconductors.

Finally we investigate how magnetic impurities affect the superconducting state by embedding 3^{rd} row d-block magnetic impurities into bulk and surface Pb. In the presence of magnetic impurities, there is a pair-breaking effect that results in sub-gap Yu-Shiba-Rusinov (YSR) states which we decompose into contributions from the individual orbital character. In bulk Pb we find that not only are there two distinct YSR resonance pairs coming from the t_{2g} and e_g orbitals, there is a significant but smaller response from the 's' component of the impurity contributing to a third pair of YSR resonances. The intensity of the peaks is governed by the LDOS at the Fermi

level of the impurity in the normal state. This finding is only reinforced when investigating how magnetic impurities, as an adatom and as an embedded impurity, affect the surface electronic structure. In both cases the degeneracy of the t_{2g} and e_g is further split, however in some cases no YSR resonances associated with 'd' orbitals are observed due to the majority and minority peaks being completely below or completely above the Fermi level. This highlights the important fact that multiple YSR states in the presence of 3d magnetic impurities cannot be attributed to the d-moment alone.

Dedication

To my wife, Katherine.

Acknowledgements

There are a lot of people who were instrumental to the completion of my PhD. Of those, I would like to thank the following:

My supervisor, Dr. M. Gradhand, who always had time for my impromptu visits into his office or my flurry of emails, regardless of how much he had on. With his guidance I have been able to take my overenthusiastic nature and turn it into something useful.

I would also like to thank my second supervisor, Professor James F. Annett whose knowledge of superconductivity was fundamental to the success of the project.

Thank you to Dr. G. Csire. You are the reason my PhD project existed in the first place. Not only that, you have put so much effort into testing my version of the implementation that it will be much better for it.

Thank you to Professor B. Újfalussy who invited me over to stay in Budapest multiple times. Whenever I visited, usually something that I was struggling to solve managed to get fixed by the time I got back to England.

I would like to thank Dr. J. Laverock for his tireless work organising the first year of my PhD in the Centre for Doctoral Training in Condensed Matter Physics (CDT-CMP). In addition, thank you to my cohort who would pester me to grab a coffee to get away from the office.

My officemates M.-H. Wu, R. Gupta, O. McHugh and T. Tijssen for our great discussions which sometimes even helped with my PhD. In addition, thank you to J. Crosbie and E. Thill who were always enthusiastic despite the volume of work we gave them.

Thank you to my flatmate, C. Hall, for our fruitful discussions which ranged from discussions on our PhDs to politics and e-sports, inevitably ending up with what we were going to eat for dinner.

I want to thank my parents Jo and Peter, and my sister Emily for always believing in me and inspiring my love of nature and learning.

Last, and my no means least, thank you to my wife Katherine. I could not have done it without you.

AUTHOR'S DECLARATION

I declare that the work in this dissertation was carried out in accordance with the requirements of the University's Regulations and Code of Practice for Research Degree Programmes and that it has not been submitted for any other academic award. Except where indicated by specific reference in the text, the work is the candidate's own work. Work done in collaboration with, or with the assistance of, others, is indicated as such. Any views expressed in the dissertation are those of the author.

SIGNED: ..... DATE: .....

TABLE OF CONTENTS

List of Tables

Table **Page**

List of Figures

Figure **Page**

CHAPTER 1

INTRODUCTION

In 1913, the Nobel prize in physics was given to Heike Kamerlin Onnes "for his investigations on properties of matter at low temperatures which led, inter alia, to the production of liquid helium" [20]. Very little emphasis was put on the fact that in the process of liquefying helium he discovered that Hg was a superconductor with a T_c of 4.15 K [21]. After not very long it was discovered that a whole host of the elemental materials became superconducting at low temperatures such as Pb and Sn [22]. It was initially conjectured by L. Cooper [23] that the electrons in a superconductor bind together and form pairs of electrons. Ever since they have been coined as 'Cooper' pairs after him. From this initial idea the theory of superconductivity was created by J. Bardeen, L. Cooper and J. Schrieffer, known as BCS theory [24]. One of the key features of the theory is the presence of an energy gap Δ in the excitation spectrum. This was a translationally invariant model working purely in k-space, which made the assumption that the material was pure. The year before BCS theory was published it was found that rhodium impurities can enhance the superconductivity of molybdenum [25]. This discovery presented a new concept within the field of superconductivity that could not be described by BCS theory in its current state. Not only that when the superconductor beryllium [26] was prepared as an amorphous crystal it was found to still be superconducting. Finally, with the inclusion of magnetic impurities, superconductivity could also be suppressed [27]. Superconductors had therefore reacted in three different ways to the presence of impurities and interfaces: suppression, enhancement or ignorance. Evidently understanding how each effect originates would give fundamental insight into the superconducting state.

The first attempts at describing impurities in superconductors came only a year after these discoveries. Here, the original transitionally invariant model BCS theory was extended to model the average positions of magnetic and non-magnetic impurities [28, 29]. These models success-

fully described principal effects of impurities, having the drawback that local effects were not considered. Fetter [30] was one of the first to use localised models to describe non-magnetic impurities in the superconducting state and made the conclusion that impurities in real materials will induce both spatial oscillations in the superconducting order paramter $\Delta(r)$ and the charge density $\rho(r)$ and resonant enhancement of the scattering of quasiparticles with momentum near the Fermi momentum. Describing magnetic impurities was then theorised by Yu, [16], Shiba [17] and Rusinov [18]. This provided a local description of how the T_c could be reduced by the presence of magnetic impurities, as bound states would fill the gap with states. Later, Flatté and Byers [31] provide insightful models into how magnetic and non-magnetic impurities behave in a free-electron s-wave (spin singlet) superconducting medium. These models provided qualitative insight of a generic localised perturbation in a superconductor, but lacked any quantitative predictive power for real materials.

Since then, the inclusion of impurities in superconductors has only created more questions than answers. Most notably impurities have been linked to two significant milestones of superconductivity. The first being the discovery of the family of high temperature superconductors known as the cuprates [32–34]. The second was the discovery of iron-based superconductivity [35]. In both cases a parent compound had to be doped with impurities to induce superconductivity. Although there have been attempts to understand the microscopic theory describing the effects [36], this still remains a very active field of research.

One aspect of investigating unconventional superconductors is local scanning tunnelling microscopy around an impurity site. By investigating how the impurities interact with the superconductor it has been possible to use them to define the superconducting order parameters, which has proven a great success for FeSe [37], LiFeAs [38], $CeCoIn_5$ [39], and $Bi_2Sr_2CaCu_2O_{8+\delta}$ [40] along with many others [9].

To model impurity scattering within unconventional materials, delta scatters were considered in realistic tight-binding models for Fe-based [41–44], cuprate [45–47] and heavy fermion [48] superconductors. Since most of the theoretical approaches work in reciprocal space, direct comparison to experiments will typically involve Fourier transformations of the direct real space analysis of the experiments. This is not the natural choice when considering the fact that scanning tunnelling microscopy (STM) probes the local electronic structure, so there is a challenge to find a method that incorporates impurities into localised models.

The STM technique has been used to investigate Yu-Shiba-Rusinov (YSR) states as well [49]. The original theories by Yu, Shiba and Rusinov were simple one band models which would have described how an s-type magnetic impurity would have interacted with the system. In real systems, not only is the underlying electronic structure more complex [2], but multiple YSR peaks were found [7]. Within this paper the assumption is that only the d-states from the impurity contribute to the magnetism, and the d-orbitals are subjected to crystal field splitting, which results in different magnetic moments from each orbital. This, along with the real space dI/dV

maps, enabled them to claim which peaks were associated with each orbital. These assumptions are reasonable, however there could be effects from the interband coupling or diamagnetic responses from other orbitals which contribute to the in-gap states.

This is especially relevant considering that the ultimate goal for these experiments is to introduce chains of magnetic impurities on the surface of superconductors with a high spin-orbit interaction. Such experiments have been shown to induce Majorana Fermions at the edges of the chain [50, 51]. These states are of great interest due to their use in 'fault tolerant quantum computation' [52]. Theoretical work on the subject has already been extensive, but generally has been focused on phenomenological tight binding models [53, 54]. The most advanced work on this subject has been to investigate from first principles the effect that Fe magnetic chains have had on the surface of normal state Rhenium, and then using a tight-binding parameterisation to describe the superconductivity [55].

The logical step from here is to turn to *ab initio* techniques to model these materials. This is currently not feasible for unconventional superconductors, but there is promise with conventional superconductors because modelling of phonon mediated s-wave superconductors has been successful for pure bulk crystals [56]. However, incorporating impurities into these methods poses significant challenges. As for unconventional superconductors discussed above, models including impurities either use a set of various parameters or they are forced to use supercell approaches to incorporate the impurity site [57].

This present work is devoted to exploiting the Korringa-Kohn-Rostoker (KKR) Greens function method, ideally suited to treat the real space impurity problem, in a full quantitative *ab initio* approach [58]. The first principles treatment of the impurity problem is combined with the implementation of the solver for the Bogoliubov-de Gennes (BdG) equations, which has been previously implemented within a layered KKR code for the scalar relativistic [59–61] and fully relativistic [62, 63] formalisms.

The thesis will be organised as follows. Chapter 2 will give a brief overview of the current state of the field of superconductivity, what open questions are yet to be answered and how the effect of impurities on the superconducting state is relevant today. Chapter 3 will discuss the implementation of the BdG equations into the KKR formalism, focusing primarily on how the implementation differs from G. Csire and collaborators [59, 63, 64], then extending the formalism to impurities. Chapter 4 firstly assesses the numerical robustness of the method, investigating the most computationally efficient choice of parameters to successfully perform a superconducting state calculation, how mass corrections in the scalar relativistic limit effect the system, and our choice of exchange correlation functional. Secondly, the chapter will discuss the results of bulk calculations, and assessing the gap anisotropy of various phonon-mediated superconductors. Chapter 5 investigates how impurities affect these superconducting materials, and is divided into three sections. The first section investigates the affect impurities have on the gap anisotropy, the second section applies this method to granular superconductors, solving a

nanoscale superconducting cluster embedded in a normal metallic environment, and the third section assesses how magnetic impurities affect superconductors, in both bulk and surface systems. Finally, Chapter 6 will summarise our findings and focus on future work.

CHAPTER 2

BACKGROUND

Since the discovery of superconductivity [21], the quest to find an industrially practical room temperature superconductor remains one of the key areas of research in condensed matter physics today. On the journey, many exotic phenomena have been found such as quantum criticality [65], topological superconductivity and Majorana fermions [66], Higgs modes [67] along with the psuedogap [68] and strongly correlated superconductivity [69], some of which have far-reaching implications. Fig. 2.1 is a graph from Ref. [8] showing the vast number of families of superconductors that exist, which each have their own history behind them. This chapter aims to give a brief overview of the current state of the field of superconductivity and address the key issues that have stopped us from producing a recipe book for a room temperature superconductor, along with discussing some of the spin-off applications that have created sub-fields in their own right. We start with discussing the progress of conventional BCS superconductors, moving through to the high pressure hydride superconductors. From there we address unconventional superconductors by firstly looking at the high temperature copper oxide (cuprate) superconductors and then moving to the iron pnictides. After this we investigate the more exotic side of superconductivity such as Sr_2RuO_4, twisted bilayer graphene and optically driven materials, along with other candidates for topological superconductivity.

2.1 Conventional Superconductors

After the initial research into superconductivity by HK Onnes [20], discovery of phonon mediated superconductors boomed in the 1940-1950's. One of the key figures in the discovery of many new superconductors is B. T. Matthias [70] who, among many others, discovered NbN [71], Nb_3Al and Nb_3Sn [72] the first superconducting ternary compounds [73] and whole host of others [74]. Beyond this, investigations into the specific heat of superconductors around the transition tem-

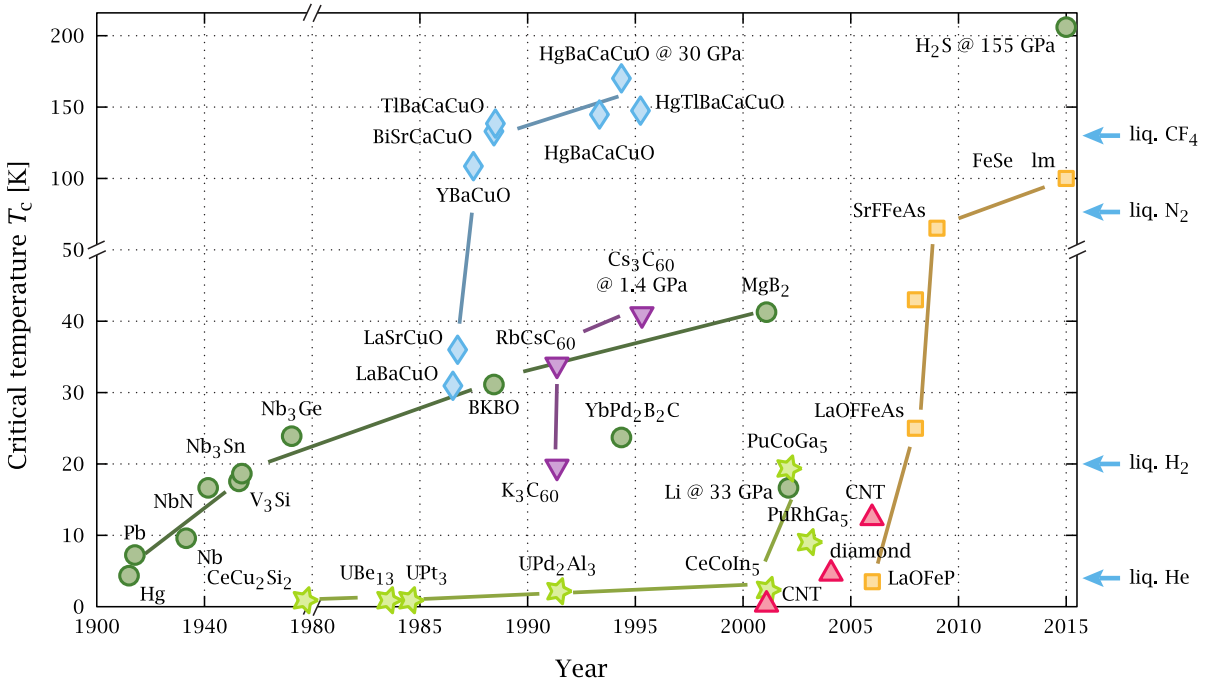

Figure 2.1: The T_c of the superconductor vs the year it was discovered. Different families of superconductors are highlighted: conventional superconductors (green circles), cuprate superconductors (blue diamonds), iron pnictide (orange square), heavy fermion (green stars), carbon (red triangles) and fullerine superconductors (purple). The blue arrows on the right side refer to the melting temperatures of CF_4, N_2, H_2 and He. Figure from [8].

perature [75, 76] were being performed. By the time BCS theory had been published it was clear that Pb had unconventional behaviour where the specific heat did not quite follow the theory's predictions [77]. This was in part due to the strength of the electron-phonon coupling parameter in Pb which was too large for BCS to accurately describe the resulting superconductivity and so the so-called 'strong coupling' theory was developed by Eliashberg [78].

It was only when tunnelling spectra was performed on Pb was it found that the superconducting gap was anisotropic [79], however the results were only cautiously accepted. To reinforce this claim of anisotropy, further specific heat measurements [80] were performed which discovered non-BCS theory like signatures. Here, they were again able to attribute this result to gap anisotropy in Pb, albeit tentatively. The theory for the anisotropy was quickly developed [81], and the anisotropy was further confirmed by more tunnelling conductance measurements [82, 83].

The anisotropy of conventional superconductors was accepted, however very few further materials were investigated. Such examples were specific heat measurements of V [84] or ultrasonic measurements [85] and tunnelling spectra [86] of Nb. However for Nb there were later conflicting reports suggesting that the superconducting energy gap was isotropic from thermal conductivity [87] and specific heat [88] measurements. Detailed research into the gap anisotropy was infrequent from then onwards, with some more concrete evidence for the gap anisotropy in

Nb being presented in Ref. [10]. Not only were the negative results for Nb making it hard to justify further experiments, the requirements for any experiment to observe this anisotropy were technically very challenging as the experimental resolution had to be of the order of a few μeV. Finally, the discovery of the copper-oxide superconductors [33, 89] resulted in low temperature anisotropy of elemental superconductors being all but forgotten.

Despite this, research into the anisotropy present in conventional superconductors gained new ground after the discovery of superconductivity in MgB_2 at 39 K [90]. In the same year experiments using point-contact spectroscopy [91] showed that the energy gap was strongly anisotropic and from multiple gaps yet evidence of the Boron isotope effect [92] clearly implied that the superconductivity was phonon-mediated. This was strong evidence for a need of a more generalised k-dependent theory of phonon-mediated superconductivity which was developed by Ref. [93], explaining the anomalous superconducting properties of MgB_2 [94]. Since then more detailed experiments of Pb surfaces using high resolution scanning tunnelling microscopy (STM) [2] has shown a detailed picture of the gap anisotropy of Pb complete with characterising the Fermi surface information.

Despite these discoveries, only MgB_2, Pb and Nb are considered to be anisotropic phonon-mediated superconductors. In reality many elemental superconductors could display this phenomena due to their complicated Fermi surface structure. A first example would be anisotropy in V due to having a similar Fermi surface structure to Nb, coupled with there already being thermodynamic evidence [84]. The reasoning behind this lack of investigation was partly due to the timing as when these materials were being investigated, from 1911 to the 1960's. Firstly, the discovery of the existence of an energy gap in superconductors was only in 1953 [95, 96] so little attention was being paid to its anisotropy. Secondly, any anisotropy from an elemental superconductor is typically an order of magnitude smaller than the gap, as shown by the experiments on Pb [2] ($150\mu eV$) and Nb [4] ($590\mu eV$), making experimental resolution another key factor. Finally, the discoveries of much higher temperature superconductors made analysis of this anisotropy less of a priority in later years. Despite this, anisotropy has been predicted to change the T_c of Pb by 8% [6] and has created problems for making wires of MgB_2 [97], so a greater understanding of the phenomenon will have to be addressed.

Finally, the red points in Fig. 2.1 refer to conventional superconductivity in systems made from carbon. Such systems include 4 Å single-walled Carbon nanotubes [98] and boron doped diamond [99] of which are the presented data in the figure. In addition superconductivity has also been observed in the Fullerides [100]. This system consists of A_3C_{60} carbon structures where the C_{60} is a Buckminsterfullerine and A refers to K [101] or Rb [102] which get to T_c's of 18K and 28K respectively. The field gained new ground with recent results of the possible optical induction of superconductivity up to 100 K in K_3C_{60} using mid-infrared optical pulses [103]. Despite there being a gap in optical conductivity, a feature present in low temperature ground state superconducting K_3C_{60}, it was not enough to say definitively that the material had gone into

an optically induced superconducting state. However superconductivity was then confirmed in a further experiment [104] for a few femtoseconds at above 150 K with promise that it could extend to room temperature. The drive to achieve a more long lasting optically induced high-temperature superconducting phase continues.

2.2 High Pressure Superconductors

In order to increase the T_c of phonon mediated superconductors, researchers turned to lighter and lighter atoms because phonon modes with higher frequencies have the potential to bind Cooper pairs more strongly. In addition to looking at materials such as MgB_2 and the Fullerides, another principle was considered which concerned trying to turn insulating materials into metals by applying pressure. By putting these materials under high pressure, the atomic orbitals in the crystal overlap more, causing the bandwiths to increase, reducing the energy gap between the valence and the conduction band. At high enough pressures, the valence band crosses the Fermi level and becomes metallic. This has been realised experimentally in materials such as Sulphur [105] and Oxygen [106]. Within these metallic phases, a superconducting transition was then observed [107, 108]. This was an exciting discovery and proved that it is possible to obtain a superconducting transition from these very light elements.

The discovery of superconductivity in high pressure phases of Sulphur [107] and Oxygen [108] is really the middle of the story. The initial idea came from considering the lightest atom in the periodic table, hydrogen. Usually it forms H_2 molecules and crystallises into an H_2 insulating phase at 14.01 K [109], however in 1935 E. Wigner and H. Huntington [110] suggested that, with enough pressure, the molecule would dissociate and the resulting crystal would be metallic. Naively one assumes that the system will be a free electron-like metal [111] at high pressures. Hence the lattice of protons will interact with the bare, unscreened coulomb potential and when minimising the Coulomb potential the body centred cubic lattice (bcc) is the solution [112]. This is the crystal structure that was assumed in Ref. [110] and using this they predicted that the pressure required would be $\sim$ 25GPa. However when looking at Li and Na [113] at high pressure it was not that simple. These materials, which were already free electron-like at room temperature, became a complex set of different phases above 39GPa for Li and 103GPa for Na [113]. This can only be explained by the fact that the electronic screening is enough to destabilise the bcc lattice, hence the result is a multitude of complex phases. The same was therefore predicted for hydrogen meaning that it would be much harder to calculate the insulator-metal transition as the structure is unknown, so structure prediction methods would have to be used.

Generally, density functional theory (DFT) is used as the method of structure prediction. The local density approximation (LDA) and generalised gradient approximation (GGA) exchange correlation functionals were used in Ref. [114] in order to perform these calculations. However, in order to predict the conductor to insulator transition an accurate determination of the bandgap

is required of which these functionals are notorious for struggling to describe [115, 116]. The solution to this is to introduce a self-energy interaction to the Kohn-Sham equations [117], for example, via the GW approximation [118] where the 'G' refers to the Green's function and 'W' the screened Coulomb potential. This method provides a much better estimate of the bandgap and hence the metallisation [119]. Another method to predict the bandgap of solid hydrogen, and hence the metallisation point, is the quantum Monte Carlo (QMC) method [112]. The best estimate of the metallisation of solid hydrogen was 447 GPa which was calculated using a QMC calculation [120]. It is considered the best estimate because it is very similar to the experimental extrapolation from Ref. [121] at 450GPa.

These immense pressures will be incredibly challenging, however it has the potential to have the highest T_c of all phonon-mediated superconductors. Experimental evidence [122] has been met with, initially, limited success as the sample 'disappeared' not long after the publication [123], and other scientists argued whether it was even made at all [124]. Fortunately another group has recently published data [125] that suggests that they could have isolated the phase of metallic hydrogen using synchrotron spectroscopic evidence of the bandgap changing from 0.6eV to less than 0.1eV. A non-invasive reflectivity measurement has now been suggested [126] in order to determine whether the material is superconducting. Finally, there are predictions that at extreme pressures (>20 TPa) there is an fcc phase of metallic hydrogen which could become metastable at room pressures [127]. Experimental realisations of this phase will push the boundaries of current experimental techniques.

It was also found that it is possible to crystallise hydrogen at high pressure with other atoms such as Sulphur [128] and Lanthanum [129]. These materials have been labelled as the highest temperature superconductors known with 203 and 250 K respectively, with more hydride superconductors being predicted to break records [130]. The most recent result has been labelled as the first room temperature superconductor (287.7 ± 1.2 K) and is a 'carbonaceous sulfur hydride' system [131]. Realistically, despite these materials having the highest superconducting transition temperatures, the potential for these materials to be used in industry is remote due to the extreme difficulty in making them, along with their fragility. Despite this, high-pressure hydride research plays a fundamental role in the search for a room temperature superconductor. Finding one has proven that there is a superconducting phase that exists that can survive the thermal fluctuations of room temperature, which implies that others can be found too.

2.3 Copper Oxide (Cuprate) Superconductors

Historically the copper-oxide superconductors, consisting of materials with copper oxide planes such as $YBa_2Cu_3O_{7-x}$ [33], $Bi_2Sr_2CaCu_2O_{8+\delta}$ [132] and $HgBa_2Ca_2Cu_3O_{8+\delta}$ [133], were the first family of high temperature superconductors discovered. These materials do not behave like conventional, phonon mediated superconductors. One of the predominant signatures that they

are unconventional is the presence of a 'pseudogap' [9], which is a gap that appears in the density of states (DOS), yet there is no superconductivity. Experimental evidence of this phenomena has been found in all of the cuprate systems, Fig. 2.2(1) shows that comparison between the gap produced in Nb compared to the gap produced in $Bi_2Sr_2CaCu_2O_{8+\delta}$. Here, as we increase the temperature in both materials the gap spectroscopy begins to get more smeared, and in Nb as the temperature gets to T_c the gap is almost completely obscured. In $Bi_2Sr_2CaCu_2O_{8+\delta}$ the story is slightly different because as T_c, which is 84 K and is defined as the point where the resistance becomes finite again, is reached it appears that a gap is still open and coherence peaks are still visible. This could, in principle, be due to the difference in temperatures associated with the different transitions, so in Fig. 2.2(2) the data from Fig. 2.2(1b) is replotted with two different theoretical methodologies superimposed on top. The first, 2.2(2a), is conventional BCS theory with a temperature dependent gap function along with temperature smearing. The second, 2.2(2b), is where the gap has been kept constant but temperature smearing has still been applied. What we see is that for a BCS-type superconductor the gap will be completely gone by the time T_c is reached, which is the expected result for a conventional superconductor but not at all what the data suggest. The fixed gap calculation fits much better to the data showing that for the cuprate superconductor we see that the gap size is either independent of, or only weakly coupled to, temperature. The gap in the excitation spectrum is not a full gap we can see from Fig. 2.2(2b) as it has a non-zero density at the Fermi level. This implies that there are still Cooper pairs but without the phase coherence that induces zero resistance.

Scanning tunnelling microscopy has been a particularly prominent application to the field of Cuprate superconductors [9]. Not only has it been used to probe the pseudogap regime, as shown in figure 2.2, it has been used to investigate the doping phase diagram [134] and the structure of the vortex cores [135] along with ascertaining k-dependent gap information using quasiparticle interference [136]. It was shown in Ref. [137] investigations into the CuO_2 and BiO planes of $Bi_2Sr_2CaCu_2O_{8+\delta}$ showed that BiO had a V shaped gap and CuO_2 had a U shaped gap. The implications of this are that either they have different pairing symmetry, or that superconductivity in the BiO was being induced. These investigations into the superconducting properties of the cuprates using STM have been numerous [9], and have probed the unconventional superconducting state in great detail.

In order to model these materials theoretically, it was originally suggested by P.W. Anderson [138] that Resonating Valence Bond (RVB) theory could be used to describe these systems. The idea behind this theory involves a quantum spin liquid with charged bosonic 'holons', particles with charge of an electron but a spin of 0, condensing into a superfluid. Although the theory did not describe all aspects of the strongly correlated state, such as the suggestion that the Bose condensate had a charge of 'e', it has influenced condensed matter theory for years [69]. Examples of attempts to model strongly correlated superconductors numerically [139] are ongoing, with *ab initio* modelling of strongly correlated cuprate systems using a combination of GW and DMFT

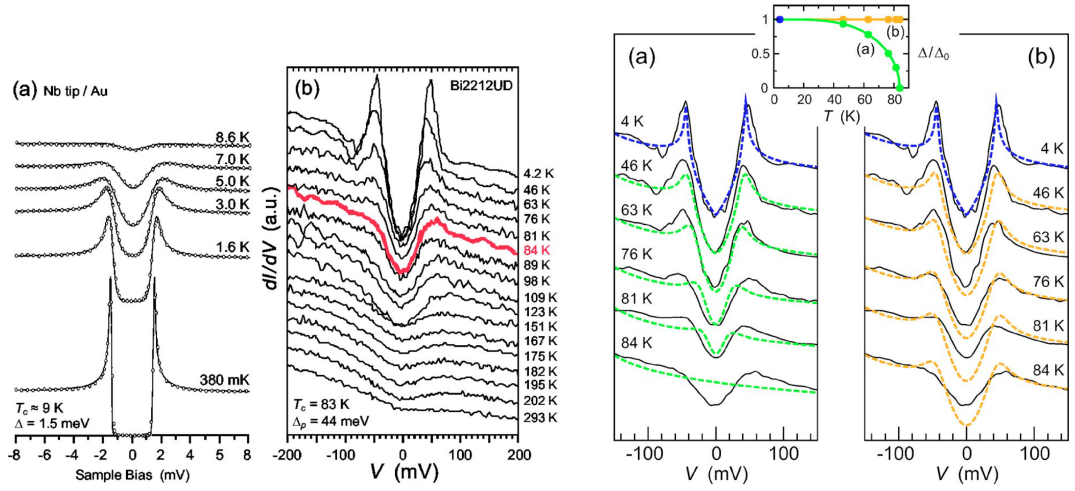

(1) (2)

Figure 2.2: (1a) Differential tunneling conductance of the superconducting gap of Nb at different temperatures. (1b) Differential tunneling conductance of the superconducting gap of $Bi_2Sr_2CaCu_2O_{8+\delta}$ at different temperatures. (2a) Data from (1b) with a temperature-dependent BCS d-wave gap function superimposed on top. (2b) Data from (1b) with a constant gap with temperature smearing superimposed on top. Gap sizes quoted in the figures have been read off directly from x-axes. Images from [9]. Data from (1a) adapted from [10], data from (1b) adapated from [11]. Experimental data from (2a) and (2b) adapted from [11], theoretical data and inset of (2) from [9].

techniques [140] also playing a significant role. Recently a solution to a toy model [141] which includes both Mottness and superconductivity has been developed, potentially opening a new chapter for strongly correlated superconductivity. This model shows a promising similarity to the 'Superconductivity-induced transfer of in-plane spectral weight' for $Bi_2Sr_2CaCu_2O_{8+\delta}$ [142]. Despite these attempts to describe these systems there is still no conclusive theoretical work that ties together all of the observed phenomena of strongly correlated superconductivity, and can predict a T_c of other superconductors that exhibit this behaviour, so this is still a very active field of research.

2.4 Iron-Based Superconductors

Another surprising family of superconductors were the iron-based superconductors [143] as it was believed that magnetism and superconductivity could not coexist. There were classic examples of this like in the Meissner effect [144] and the reduction of T_c for BCS superconductors with the inclusion of magnetic impurities [27]. It was therefore considered that Fe could never be an element that belonged to the make-up of a superconducting material. Despite this, several classes of materials containing Fe were superconducting [143]. These consist of the 122 type consisting of QFe_2Pn_2 where Q is usually B, however has also been be Ca, Sr and Eu and

the Pn refers to an element in the pnictogen family. These superconductors usually require electron doping via partial substitution of Fe by another transition-metal ion, or hole doped by partial substitution of Q by an alkali-metal ion. The 1111 type consists of RFePnO where R refers to a rare earth element. The highest T_c of the superconducting phases is currently in $Sr_{1-x}Sm_xFeAsF$ [65] at 56 K for $x = 0.5$. Their generic phase diagram is similar to that of the cuprate superconductors, however by comparing the two phase diagrams in Fig. 2.3 it is possible to see that, in the case of the cuprate superconducting phase 2.3(a), the antiferromagnetic phase ends and the superconducting phase begins as a function of doping, whereas in the case of the Fe pnictides 2.3(b) the superconducting dome emerges from the antiferromagnetic phase at low temperatures. This implies that the excitations from the antiferromagnetic phase could be key for the iron Pnictide superconductors, whereas in the cuprate superconductors it must, in some way, be different. Despite this, the pseudogap phase also been observed in Iron-based systems such as $BaFe_2(As_{1-x}P_x)_2$ [145] and $La(O_{1-x}F_x)FeAs$ [146], showing that there are still similarities to the underlying electronic structure.

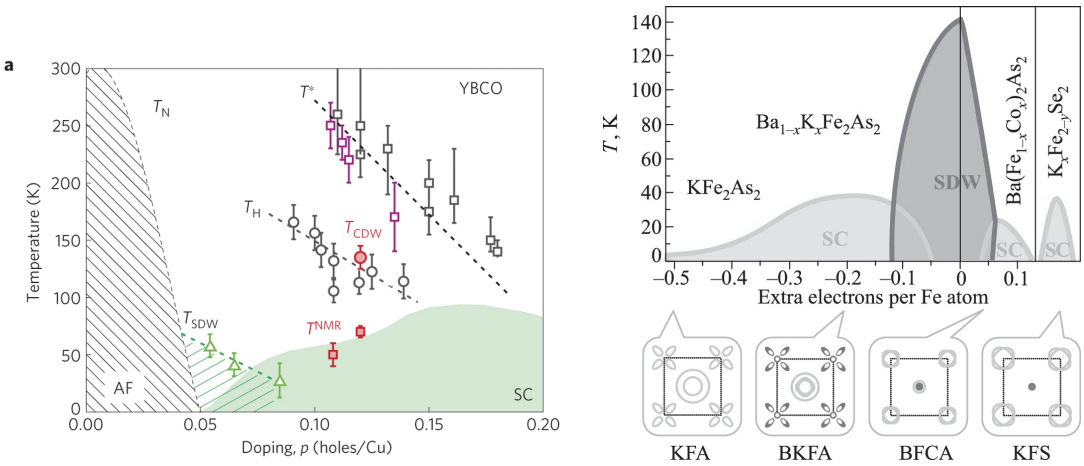

Figure 2.3: (a) Phase diagram of $YBa_2Cu_3O_{7-x}$. T_{SDW} is the spin density wave transition temperature, T_{CDW} of the charge density wave, T_N the Néel temperature, T^* the pseudogap phase and T_{NMR} the temperature scale below which NMR observes field-induced charge order. AF and SC refer to antiferromagnetic and superconducting phases respectively. Image from [12]. (b) Combined phase diagram of the 122 iron pnictide superconductors [13].

FeSe is another notable iron-based material which has exhibited an interesting superconducting phase. It is similar to that of iron pnictides [147] as it is an unconventional superconductor formed with Fe, however it does not contain a pnictogen. As a heterostructure of FeSe and Nb doped $SrTiO_3$ superconductivity above 100 K was realised, bringing iron-based superconductors to a comparable level as the cuprates. This exciting discovery reinforces a previous idea that high temperature superconductivity can be achieved via the electron pairing at interfaces [148, 149]. Investigating the order parameter using scanning tunneling microscopy [37] around an impurity

site it was possible to determine that FeSe is a multiband superconductor with an $s^{\pm}$ order parameter. This is where the phase of the order parameter associated with one of the gaps is opposite to the other, which is similar to other iron based systems [42].

2.5 Exotic Systems

Another material with the same structure as the cuprate superconductors is Sr_2RuO_4 [150] which has always been a superconductor which was considered to be a potential candidate for a spin triplet order parameter [151], where same electron spins pair together, resulting in a Cooper pair with a non-zero orbital angular momentum [152]. However recent research has shown that this original analysis could be incorrect due to an inaccurate knight shift experiment [153] was recently rectified [154]. The new evidence, along with other works [155–157], believe its superconducting order parameter to be more of d-wave order like the cuprate superconducting materials, however the order parameter is still believed by some to have a chiral structure [158].

Heavy-fermion superconductors are another family of superconductors which have strongly correlated ground states. Notable materials include $CeCu_2Si_2$ [159], $PuCoGa_5$ [160] and $CeCoIn_5$ [161]. The cooper pairing mechanism for these materials, just like the cuprates and iron pnictides, is yet to be determined. What is more, the localised f-states present in these materials make it very hard to model [162]. Despite the T_c of these materials being not particularly impressive, they are popular because they have been key materials for the investigation of quantum criticality [163]. This occurs when looking at the near-zero temperature doping-dependence of these unconventional materials. Even at this low temperature, phase transitions between the competing ground states still occurs due to the fluctuations in the many-body quantum wavefunction. By looking at the critical exponents of these transitions, a greater understanding of this exotic phenomena will arise, alongside potential greater understanding of the phases themselves. Iron pnictides are also known for exhibiting quantum criticality [65], whereas similar investigations into cuprate superconductors are in their infancy [164].

Finding exotic order parameters to widen our knowledge of superconductivity goes beyond just using bulk materials. Investigations have also turned to 2d materials and devices to construct these systems. Twisted bilayer graphene [14] is something that has been shown to exhibit strongly correlated superconductivity. The original paper is able to plot the the entire phase diagram around the superconducting dome by sweeping in temperature and carrier density, as shown in Fig. 2.4. The phase diagram looks remarkably like that of a cuprate superconductor, despite the fact that it does not have any of the elemental constituents in common. It was even found in a later study that stripe order and a pseudogap phase was observed using scanning tunnelling microscopy [165]. The advantage of this system is that, using only one material it was possible to dope by applying a voltage to the Pb/Au bottom gate electrode giving it perfect tuneability.

Another method of creating a high temperature superconductor is forcing a material into

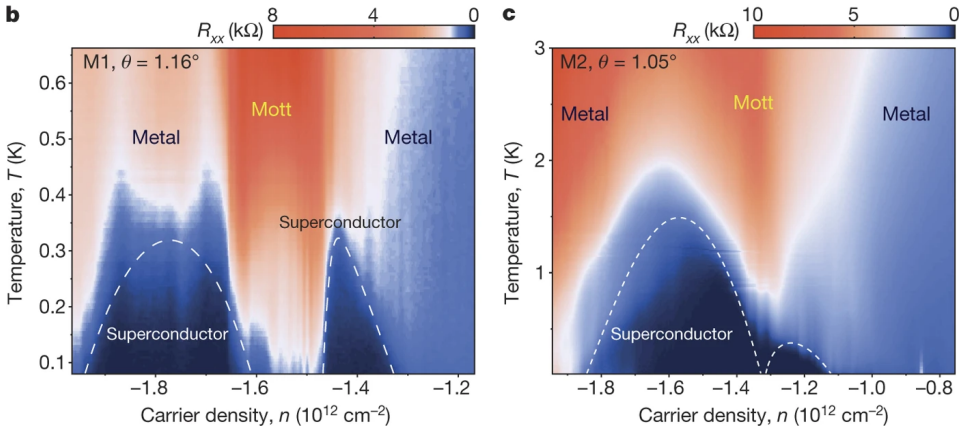

Figure 2.4: Two different phase diagrams of twisted bilayer graphene at different twist angles, (b) $\theta = 1.16$ and (c) $\theta = 1.05$. The carrier density is varied by applying a gate voltage on the Pb/Au substrate, colour represents the R_{xx} resistivity. Image from [14].

a metastable superconducting state with pulsed lasers [103, 166]. Ref. [166] detected this phenomena in $La_{1.675}Eu_{0.2}Sr_{0.125}CuO_4$, and Refs. [103, 104] in the Fullerides as mentioned earlier in section 2.1. There are many technological challenges with this such as holding the system in a metastable state for any length of time, along with measuring it accurately. Theoretically it is also very challenging because modelling out of equilibrium is less well established than conventional mean-field techniques.

2.6 Topological Superconductivity and Majorana Fermions

Ever since the suggestion that Sr_2RuO_4 was a potential candidate of a p-wave superconducting order parameter [151], it has been of great interest within the scientific community to find signatures of p-wave superconductivity. Partially this is to forward the understanding of fundamental physics, however in addition to this, these complex order parameters sometimes generate Majorana fermions which have great potential industrially due to their fault tolerant quantum computation [52]. These particles have two main criterion for generation in a condensed matter system [66]. The first is that the particle must obey the massless Dirac equation, essentially having a linear dispersion with gapless excitations, the second condition is that the particle must be its own antiparticle. Topological superconductivity lends itself naturally to the generation of Majorana Fermions because it supports gapless excitations described by the Dirac equation, and secondly the electron hole symmetry from the superconductivity enables the generation of particles that are their own antiparticles.

There are broadly two categories of topological superconductors, intrinsic ones and artificially generated ones [66]. Intrinsic topological superconductors are materials with topologically non-trivial gap functions brought about by spin orbit interaction coupled with another feature

such as inversion symmetry breaking, whereas artificially generated materials usually consist of topologically nontrivial systems connected to s-wave superconductors with either or both materials having high spin-orbit coupling.

Some examples of intrinsic materials include $Cu_xBi_2Se_3$ [167], which is a superconductor that can be doped into a topological insulator. When $x = 0.3$ the superconducting state is suggested to be topological [168] where the bulk is superconducting and the surface consists of gapless bound states consisting of Majorana fermions which is in good qualitative agreement with theory [169]. Another is $Sn_{1-x}In_xTe$, which is a topological crystalline insulator characterised by a nontrivial mirror Chern number [170, 171] and becomes superconducting with a substitution of 2% Sn of In [172, 173]. UPt_3 is an unconventional heavy fermion superconductor whose order parameter goes through many different phases [174]. It is believed to be spin triplet and there are many papers which have different predictions associated with it, despite this no Majorana modes have been detected, just theoretical and experimental suggestions of topological edge states [175–177].

The first concept of an engineered topological superconducting state that could harbour Majorana bound states was by L. Fu *et al*. [178]. They considered the interaction between an s-wave superconductor and the surface states of a topological insulator. They predicted that a 2-dimensional state resembles a spinless, chiral p-wave state which supports Majorana bound states inside the vortex cores. Experimental evidence on superconductor-topological insulator interfaces is abundant [66], and recent experimental observation of Majorana zero modes has occurred [179, 180].

Further to these systems, other ones have also have been of interest which are semiconductor nanowires with Rasba-split bands in close proximity to an Al or Nb based superconductor [181–183], showing zero-bias conductance peaks in finite magnetic fields. This was promising, however Ref. [184] pointed out that these peaks could be originating from various effects, and hence may not be directly associated with a Majorana fermion. Part of the issue came from the sub-gap excitations being present in these nanowires, making it hard to disentangle all the states. However in Ref. [185], InAs nanowire was epitaxially grown on a Al superconductor add-layer which results in a much cleaner gap structure. This experiment subsequently exhibited more convincing Majorana fermions.

Finally, one of the more recent experiments realising Majorana Fermions involves putting a chain of ferromagnetic impurities on the surface of a superconductor with high spin-orbit coupling. This setup has the potential to generate 1D topological superconductivity, and is has been predicted to produce Majorana zero-modes [186]. Since then, multiple STM experiments have provided evidence for their existence, firstly with Fe chains on a superconducting Pb (110) surface [50, 187], and Fe atom chains on superconducting Re(0001) surfaces [51].

Generating the environment for these particles is quite difficult, and some of the data hard to interpret as was evident with the Fe chain experiment on Pb by Ruby *et al*. [50]. Here, it was discovered that not only was it possible to generate Majorana end-states, but also the Yu-

Shiba-Rusinov states which the topologically nontrivial state originated from can also create their own resonance. In fact in some cases Majorana Fermions did not even form [188]. It is clear that a more involved understanding of how the Yu-Shiba-Rusinov states and the Majorana zero mode interact is required. Further work performed by Ruby *et al*. [7, 189] addresses this very issue. In Ref. [7] an individual magnetic impurity was embedded as an adatom and the ensuing YSR bound states were investigated for their associated orbital character. From this they were able to determine which crystal-field split d-orbital states contributed to each of the resonant peaks formed inside the gap. In Ref. [189] they then took this further and investigated how the resonances hybridise when pairs of magnetic impurities are adsorbed onto a surface. Despite these efforts, theoretical techniques have been limited to just parameterised tight-binding models [190–192] or *ab initio* descriptions of only the normal state electronic structure [55]. In order for a full understanding of the effects occurring from these systems, a full description of the underlying electronic structure coupled directly to the superconductivity is required.

2.7 Scanning Tunneling Microscopy

Throughout the discussions of the various superconductors in the literature, most have had at least one STM experiment performed on them. The general principle of the experiment is to position an atomically sharp tip over the surface of the material in question, allowing only a thin potential barrier between tip and surface such that electronic states quantum tunnel from one to the other. There are multiple modes of operation which will be briefly discussed here. To get an idea of topography, there are two main methods [9]. The first is by keeping the current through the tip constant and the second is by keeping the height constant and varying the current as displayed in Fig. 2.5(1).

The second aspect that can be investigated, is the local tunnelling spectroscopy. By recording the tunnelling current I(V) whilst sweeping the bias voltage at a fixed height it is possible to record the electronic density of states of the surface by investigating dI/dV versus V. The interpretation of the spectra can, however, be quite complex as realistically this quantity is a convolution of the DOS of the tip and surface, along with scattering matrix elements. Usually, the DOS of the tip is considered a trivial constant, and the scattering matrix elements are set to 1.

Despite this approximation, STM has already shown great promise in investigating the electronic structure of complex superconducting systems such as gap anisotropy present in s-wave superconductors [2], the pseudogap regime of cuprates [11] and the full $\mathbf{k}$ and $\mathbf{q}$ dependent gap information from heavy fermion superconductors [162]. Not only that, once impurity scattering is involved it is possible to determine the relative gap phase and anisotropy of unconventional superconductors [37, 155], and also investigate topological superconducting states and Majorana fermions [187] within local magnetic adatom structures [7, 189]. This technique has already proved itself as a powerful tool that has a range of possibilities, and the data it obtains are almost

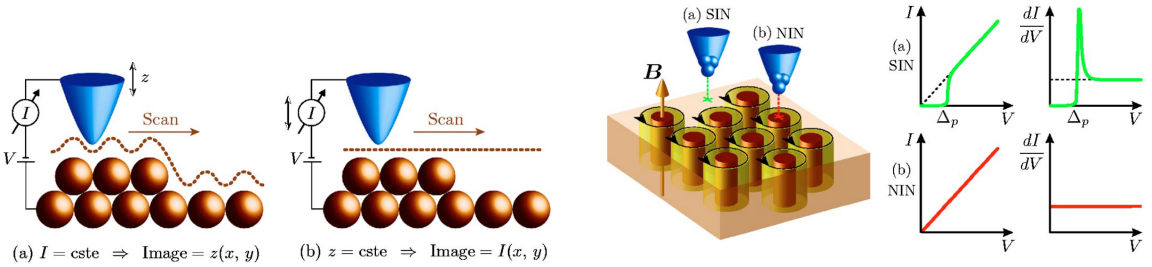

(1) (2)

Figure 2.5: Panel 1: Generic STM operating modes: (a) constant-current and (b) constant-height imaging. Panel 2: Illustration of the vortex-lattice imaging by STM: (a) Local SIN junction with typical BCS s-wave characteristics when the tip is between vortices. (b) Local NIN junction with a constant conductance where the tip is positioned over the vortex core. $\Delta_p = \Delta$. Images from [9].

a direct comparison to the density of states, making it a simple theoretically to obtain data to compare.

CHAPTER 3

THEORY

It is clear from chapter 2 that impurities have a large role to play in the field of superconductivity. They have the potential to make devices for quantum computation [187], they have the ability to probe the underlying electronic structure of superconductors [37] and unconventional superconductivity relies on impurity doping for high transition temperatures, such as $YBa_2Cu_3O_{7-x}$ [12]. This chapter is dedicated to introducing the theoretical framework that we use to investigate the real-space impurity scattering of s-wave superconductors. We start from BCS theory in 3.1 and discuss its principal ideas and shortcomings. Section 3.2 will introduce in more detail the Bogoliubov-de Gennes equations, and 3.3 will establish how the equations are implemented into density functional theory. The Green's function method will then be presented in 3.4, and from there 3.5 will describe the implementation of the BdG equations into the KKR formalism. Finally the KKR formalism will be extended to describe the Dirac-Bogoliubov-de Gennes equations in section 3.6, accounting for relativistic effects such as the spin-orbit interaction.

3.1 BCS Theory

A key breakthrough in understanding the microscopic theory of superconductivity was achieved by Cooper [193], who proved that if two electrons existed above the Fermi sea, it would only take an arbitrarily weak, positive interaction potential for them to form a paired state, assuming that it was a spin singlet pair. This model implied, with the proper many-body treatment, the presence of an energy gap in the excitation spectrum. With this gap, the total energy of the system in the paired state would be lower than that of the normal state allowing the pairs to form.

Initially we define the interaction Hamiltonian for a paired state, and to do this we must

define some operators in the language of second-quantisation. We define the vacuum state $|\phi_0\rangle$ and the creation $\hat{c}^\dagger_{\mathbf{k}\sigma}$ and annihilation $\hat{c}_{\mathbf{k}\sigma}$ operators for an electron with wave vector $\mathbf{k}$ and spin $\sigma = \{\uparrow, \downarrow\}$. These operators obey the anticommutation relations,

$$\hat{c}^\dagger_{\mathbf{k}\alpha}\hat{c}^\dagger_{\mathbf{q}\beta} + \hat{c}^\dagger_{\mathbf{q}\beta}\hat{c}^\dagger_{\mathbf{k}\alpha} = 0, \tag{3.1}$$

$$\hat{c}_{\mathbf{k}\alpha}\hat{c}_{\mathbf{q}\beta} + \hat{c}_{\mathbf{q}\beta}\hat{c}_{\mathbf{k}\alpha} = 0, \tag{3.2}$$

$$\hat{c}^\dagger_{\mathbf{k}\alpha}\hat{c}_{\mathbf{q}\beta} + \hat{c}_{\mathbf{q}\beta}\hat{c}^\dagger_{\mathbf{k}\alpha} = \delta_{\mathbf{kq}}\delta_{\alpha\beta}, \tag{3.3}$$

where α and β refer to spins and $\mathbf{q}$ a wave vector. The Hamiltonian of such a system takes the form [23],

$$\hat{H} = \sum_{\sigma,\mathbf{k}} \xi_{\mathbf{k}} \hat{c}^\dagger_{\mathbf{k}\sigma}\hat{c}_{\mathbf{k}\sigma} + \sum_{\mathbf{k},\mathbf{k}'} V_{\mathbf{k}\mathbf{k}'}\hat{c}^\dagger_{\mathbf{k}'\uparrow}\hat{c}^\dagger_{-\mathbf{k}'\downarrow}\hat{c}_{-\mathbf{k}\downarrow}\hat{c}_{\mathbf{k}\uparrow} \tag{3.4}$$

where we have already restricted ourselves to coupling between $\mathbf{k}$ and $-\mathbf{k}$ wavevectors and spin singlet ($1/\sqrt{2}|\uparrow\downarrow\rangle + 1/\sqrt{2}|\downarrow\uparrow\rangle$) states with potential $V_{\mathbf{k}\mathbf{k}'}$. In addition, we introduce the chemical potential μ as a Langrange multiplier which fixes the average number of electrons,

$$\xi_{\mathbf{k}} = \epsilon_{\mathbf{k}} - \mu, \tag{3.5}$$

where $\epsilon_{\mathbf{k}}$ is the normal state dispersion. Equation (3.4) is referred to in Ref. [194] as the BCS Hamiltonian. This can be misleading as the mean-field approximation is applied in order to obtain the BCS wavefunction (3.9), and the weak coupling approximation is performed to derive equation (3.18).

Solving a Hamiltonian such as (3.4) is very difficult due to the product of four particle operators. Within BCS theory it is simplified using a mean-field approximation. To do this we rely on Wick's theorem [195] which shows that expectation values of products of four particle operators can be replaced by averages over pairs of operators. The theorem states that all interactions are included, however in the case of BCS theory the averages such as $\langle c^\dagger_{\mathbf{k}\uparrow} c_{\mathbf{k}\uparrow}\rangle$ are removed as they can be absorbed into $\epsilon_{\mathbf{k}}$ without much error [194]. The four particle operator is hence approximated as,

$$\hat{c}^\dagger_{\mathbf{k}'\uparrow}\hat{c}^\dagger_{-\mathbf{k}'\downarrow}\hat{c}_{-\mathbf{k}\downarrow}\hat{c}_{\mathbf{k}\uparrow} \approx \langle\hat{c}^\dagger_{\mathbf{k}'\uparrow}\hat{c}^\dagger_{-\mathbf{k}'\downarrow}\rangle\hat{c}_{-\mathbf{k}\downarrow}\hat{c}_{\mathbf{k}\uparrow} + \hat{c}^\dagger_{\mathbf{k}'\uparrow}\hat{c}^\dagger_{-\mathbf{k}'\downarrow}\langle\hat{c}_{-\mathbf{k}\downarrow}\hat{c}_{\mathbf{k}\uparrow}\rangle, \tag{3.6}$$

replacing the Hamiltonian (3.4) with an effective Hamiltonian,

$$\hat{H} = \sum_{\sigma,\mathbf{k}} \xi_{\mathbf{k}} \hat{c}^\dagger_{\mathbf{k}\sigma}\hat{c}_{\mathbf{k}\sigma} + \sum_{\mathbf{k}} \left(\Delta^*_{\mathbf{k}}\hat{c}_{-\mathbf{k}\downarrow}\hat{c}_{\mathbf{k}\uparrow} + \Delta_{\mathbf{k}}\hat{c}^\dagger_{\mathbf{k}\uparrow}\hat{c}^\dagger_{-\mathbf{k}\downarrow}\right). \tag{3.7}$$

Where we define the energy gap $\Delta_{\mathbf{k}}$,

$$\Delta_{\mathbf{k}} = -\sum_{\mathbf{k}'} V_{\mathbf{k}\mathbf{k}'}\langle\hat{c}_{-\mathbf{k}\downarrow}\hat{c}_{\mathbf{k}\uparrow}\rangle. \tag{3.8}$$

Equation 3.7 can be diagonalised via a Bogoliubov-Valatin transformation [194] and the resulting ground state of this Hamiltonian, known as the BCS wavefunction, is [24],

$$|\Psi_{BCS}\rangle = \prod_{\mathbf{k}} \left(u_{\mathbf{k}} + v_{\mathbf{k}} \hat{c}^{\dagger}_{\mathbf{k}\uparrow} \hat{c}^{\dagger}_{-\mathbf{k}\downarrow}\right) |\phi_0\rangle, \tag{3.9}$$

where $u_{\mathbf{k}}$ is the electron amplitude, $v_{\mathbf{k}}$ is the hole amplitude and $\langle \Psi_{BCS} | \Psi_{BCS} \rangle = |u_{\mathbf{k}}|^2 + |v_{\mathbf{k}}|^2 = 1$. One can obtain the conventional expressions for $u^2_{\mathbf{k}}$ and $v^2_{\mathbf{k}}$,

$$u^2_{\mathbf{k}} = \tfrac{1}{2}\left(1 + \tfrac{\xi_{\mathbf{k}}}{E_{\mathbf{k}}}\right), \quad v^2_{\mathbf{k}} = \tfrac{1}{2}\left(1 - \tfrac{\xi_{\mathbf{k}}}{E_{\mathbf{k}}}\right), \tag{3.10}$$

where $E_{\mathbf{k}} = \left(\xi^2_{\mathbf{k}} + \Delta^2_{\mathbf{k}}\right)^{1/2}$. The special case where $\Delta_{\mathbf{k}} = 0$, called the 'Fermi vacuum', defines the normal state conductor where all electronic states with $|\mathbf{k}| < k_F$ are filled and those with $|\mathbf{k}| > k_F$ are empty at 0 K, thus the amplitudes become,

$$\begin{aligned} u_{\mathbf{k}} = 0, \quad v_{\mathbf{k}} = 1, \quad |\mathbf{k}| < k_F, \\ u_{\mathbf{k}} = 1, \quad v_{\mathbf{k}} = 0, \quad |\mathbf{k}| > k_F. \end{aligned} \tag{3.11}$$

Using $|\Psi_{BCS}\rangle$, $\Delta_{\mathbf{k}}$ can be written as,

$$\Delta_{\mathbf{k}} = -\sum_{\mathbf{k}'} V_{\mathbf{k}\mathbf{k}'} u_{\mathbf{k}'} v^*_{\mathbf{k}'}. \tag{3.12}$$

From here, one can re-write equation (3.12) into the self-consistent gap equation,

$$\Delta_{\mathbf{k}} = -\sum_{\mathbf{k}'} V_{\mathbf{k}\mathbf{k}'} \frac{\Delta_{\mathbf{k}'}}{2\epsilon_{\mathbf{k}}}. \tag{3.13}$$

Using the Cooper model potential,

$$V_{\mathbf{k}\mathbf{k}'} = \begin{cases} -V, & |\xi_{\mathbf{k}}| \text{ and } |\xi_{\mathbf{k}'}| \leq \hbar\omega_D, \\ 0, & |\xi_{\mathbf{k}}| \geq \hbar\omega_D \text{ or } |\xi_{\mathbf{k}'}| \geq \hbar\omega_D, \end{cases} \tag{3.14}$$

where ω_D is the Debye frequency, the function $\Delta_{\mathbf{k}}$ will have the form,

$$\Delta_{\mathbf{k}} = \begin{cases} \Delta, & \xi_{\mathbf{k}} < \hbar\omega_D, \\ 0, & \xi_{\mathbf{k}} > \hbar\omega_D. \end{cases} \tag{3.15}$$

Using the approximation (3.14) and (3.15) we can simplify (3.13) to yield,

$$1 = D(0)V \int_{-\hbar\omega_D}^{+\hbar\omega_D} \frac{d\xi}{2\left(\xi^2 + \Delta^2\right)^{1/2}}, \tag{3.16}$$

where $D(0)$ is the density of states (DOS) at Fermi energy in the normal state. The solution to the integral is,

$$\Delta = \hbar\omega_D \left(\sinh\left(\frac{1}{\lambda}\right)\right)^{-1}, \tag{3.17}$$

where $\lambda = VD(0)$. BCS theory uses the weak coupling limit [24] which says $\lambda \ll 1$. Using this, we obtain one of the signature equations in BCS theory,

$$\Delta \approx 2\hbar\omega_D \exp\left(-\frac{1}{\lambda}\right). \tag{3.18}$$

From this we find $\Delta \ll \hbar\omega_D$, which is reasonable because a standard BCS superconductor has a transition temperature T_c of the order $\Delta/k_B \sim T_c \sim 10$ K [23], and the Debye temperatures for these materials are approximately $\Theta_D = \hbar\omega_D/k_B \sim 300K$. This expression can predict the gap size of the superconducting state and can also be used, along with the proportionality $\Delta \approx 1.75kT_c$ [24], to find an approximation of the T_c of the superconductor. In practice, however, BCS theory only gives very rough estimates. In addition, it is difficult to apply BCS theory to inhomogeneous systems where $\mathbf{k}$ is not a good quantum number.

Due to these issues there have been many attempts to generalise the equations, here a short summary will be provided. The McMillan formula [196, 197] improves on equation (3.18) as it is able to account for strong coupling superconductors. The main issue with this method is the Coulomb pseudopotential μ^* which is a renormalisation of λ due to Coulomb repulsion of electron-electron proximity. This quantity has to be fitted from experimental data, making this theory semi-phenomenological. Eliashberg theory [78] is another strong coupling formalism which allows for a more complex determination of λ through a more detailed phonon density of states calculation.

The Bogoliubov-de Gennes (BdG) equations [198, 199] are an extension to BCS theory which can solve inhomogeneous systems, and comes from the diagonalisation of equation (3.7). The equations therefore avoid both the phonon cutoff frequencies of BCS theory and the weak coupling approximation, meaning that the interaction strength can be arbitrarily strong and has been shown to access both the BEC and BCS limits [200]. The most significant improvement on conventional theories of superconductivity was by Oliveira, Gross and Kohn [201] who introduced density functional theory (DFT) for superconductors. This method was able to calculate μ^* from first principles [202, 203], and so can be used to model bulk superconductors in a fully *ab initio* way. However extending these treatments to model impurities from first principles still poses significant challenges.

To that end we choose to treat the superconductivity using the Bogoliubov-de Gennes equations. This method will not be fully from first principles, rather it will treat the superconductivity phenomenologically. However, the underlying normal state electronic structure is from first principles, including the effects from impurities which will be a novel approach to the field.

3.2 The Bogoliubov-de Gennes Equations

The derivation of the Bogoliubov-de Gennes equations [198, 199] is shown in more detail in G. Csire's thesis [64], here I will just state the expressions and discuss approximations associated

with it. The equations are derived from equation 3.7 in section 3.1. Within this formalism the BdG equations are projected into the position basis as we are interested in solving the equations using a localised basis. It is a self-consistent mean-field treatment which is a generalisation of the Hartree-Fock equations to superconductivity. The equations are,

$$\begin{pmatrix} \hat{H}(\mathbf{r}) + U(\mathbf{r}) & \Delta(\mathbf{r}) \\ \Delta^*(\mathbf{r}) & -\left(\hat{H}(\mathbf{r}) + U(\mathbf{r})\right)^* \end{pmatrix} \begin{pmatrix} u_n(\mathbf{r}) \\ v_n(\mathbf{r}) \end{pmatrix} = \epsilon_n \begin{pmatrix} u_n(\mathbf{r}) \\ v_n(\mathbf{r}) \end{pmatrix}. \tag{3.19}$$

where n is the orbital index and the Hamiltonian $\hat{H}(\mathbf{r})$ is defined as

$$\hat{H}(\mathbf{r}) = \frac{1}{2m}(\mathbf{p} - e\mathbf{A})^2 + V(\mathbf{r}) - \mu \tag{3.20}$$

with $\mathbf{A}$ being the vector potential, $V(\mathbf{r})$ an arbitrary external potential and $U(\mathbf{r})$ the Hartree-Fock potential. Superconductivity is included via $\Delta(\mathbf{r})$, the pairing potential, and μ is the chemical potential. Despite $\Delta(\mathbf{r})$ appearing to be a radial 'gap' function, this is a misleading name which shall be discussed in more detail in section 4.1. The $U(\mathbf{r})$ and $\Delta(\mathbf{r})$ potentials are given by self-consistent expressions

$$U(\mathbf{r}) = -\Lambda \sum_n \left(|u_n(\mathbf{r})|^2 f_n + |v_n(\mathbf{r})|^2 (1 - f_n) \right), \tag{3.21}$$

$$\Delta(\mathbf{r}) = \Lambda \sum_n \left(u_n(\mathbf{r}) v_n^*(\mathbf{r}) (1 - f_n) \right), \tag{3.22}$$

where f_n is the Fermi-Dirac distribution and Λ is the electron-electron coupling parameter.

To give a basic idea of the meaning of these equations Fig. 3.1 shows its solution for various scenarios. In all cases the calculation is based on a DFT-LDA calculation for Nb via the KKR method, assuming $\Delta(\mathbf{r}) = 0$ for panel (a) and (b) and $\Delta(\mathbf{r}) = 0.15$eV for panels (c) and (d).

In all cases, shown is the Bloch spectral function, the k resolved density, as introduced later in equation (3.55). For panel (a) and (d) it is the electron Bloch spectral function while for panel (b) and (c) the full quasiparticle spectrum of the BdG equation is shown. With $\Delta(\mathbf{r}) = 0$ and showing the electron spectrum only panel (a) is nothing but the conventional energy dispersion of Nb within the DFT formalism. Showing the full quasiparticle spectrum with $\Delta(\mathbf{r}) = 0$ panel (b) effectively shows the original information of panel 1 combined with the spectrum mirrored at E=0. This is the hole spectrum arising from $-(\hat{H}(\mathbf{r}) + U(\mathbf{r}))^*$. With this representation the system is over described but theoretically either the electron or the hole spectrum could be used to evaluate all properties. For $\Delta(\mathbf{r}) = \Delta_0 = 0.15$ eV (Fig. 3.1(c)) the gap opens around E=0 at all points where the electron and hole spectrum cross. Finally, focusing on the electron spectrum, panel (d), it is just about visible how parts of the original hole spectrum become weakly electron like around the region of the gap. The opening of the gap and the mixture of electron and hole states is reminiscent of the effects of spin-orbit coupling added to a non relativistic DFT calculation. Instead of electron and hole bands it would be spin-up and spin-down bands which would start to interact (hybridise), resulting in the opening of gaps and the mixture of former pure up and down states.

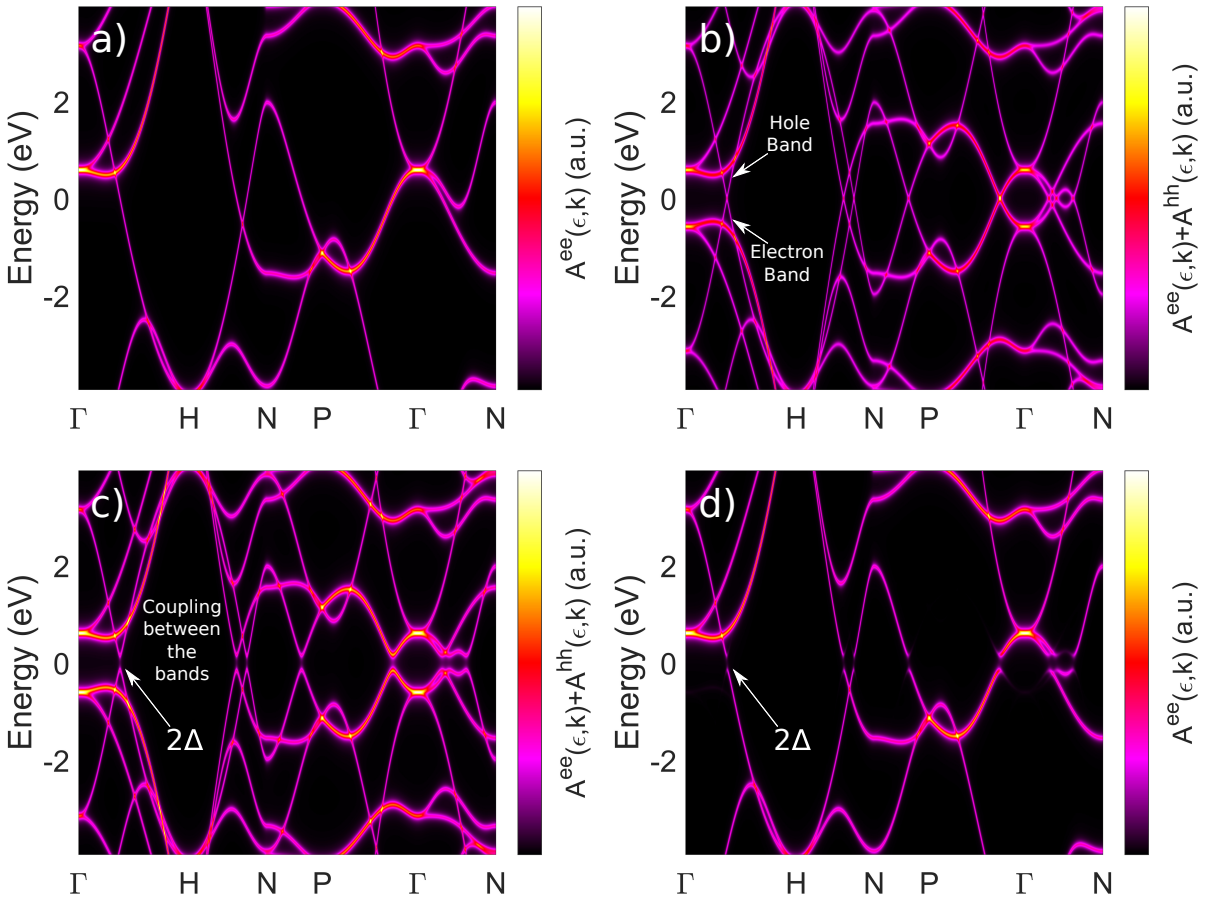

Figure 3.1: Bloch spectral functions, $A^{ab}(\epsilon,\mathbf{k})$ of electron and hole components for Nb of the Bogoliubov-de Gennes equation under different conditions, solved within a DFT calculation. $A^{ab}(\epsilon,\mathbf{k})$ is defined in equation (3.58). Panel a) The electron part of the solutions to the BdG equation with no pairing potential, $\Delta(\mathbf{r}) = 0$. Panel b) quasiparticle spectrum (both electron and hole parts) of Nb with $\Delta(\mathbf{r}) = 0$. Panel c) quasiparticle spectrum of Nb with $\Delta(\mathbf{r}) = \Delta = 0.15$eV. Panel d) electron part of the spectrum of Nb with $\Delta(\mathbf{r}) = \Delta = 0.15$ eV.

3.3 Density Functional Theory for Superconductors

This section will describe how the BdG equations (3.19-3.22) are incorporated into density functional theory. This involves the generalisation of the Kohn-Sham equations to the Kohn-Sham-Bogoliubov-de Gennes (KSBdG) equations [201]. The derivation for the KSBdG equations is present in G. Csire's thesis [64], the principal equations will be highlighted here. Beyond the derivation, there are two separate problems that must be addressed, the first is the choice of exchange-correlation functional and the second is solving the KSBdG equations. The first problem will be addressed here, the second will be discussed in sections 3.4-3.6. Before the exchange correlation functional is addressed, density functional theory will be introduced briefly.

Density functional theory addresses the problem of the intractable many-body Hamilto-

nian. Solving the many-body electron problem directly is too complex as it involves solving the Schrödinger equation for $\sim 10^{23}$ coupled atoms and electrons. The first step is to use the Born-Oppenheimer approximation [204], which decouples the motion of electrons to atoms. The electronic velocity is $\sim 10^6 m/s$ whereas the most atomic velocities are $\sim 10^3 m/s$ [111]. As the electrons move three orders of magnitude faster, they can be assumed to be in instantaneous eigenstates of the Hamiltonian that changes slowly with atomic motion. This significantly reduces the size of the problem, however there are still $N \sim 10^{23}$ coupled electrons to deal with, effectively N^3 degrees of freedom. The idea of DFT starts with the Hohenburg-Kohn theorem [205]. The basic idea is to change the description of the system from being centred around the many-body wavefunction to being centred around an effective density. This avoids the main problem in many-body quantum mechanics of trying to solve the wavefunction directly, instead by solving for the density the degrees of freedom are reduced to just N=3. The first viable method to incorporate this theorem was introduced by Kohn and Sham [206]. They took the many-body Schrödinger equation and rewrote it as a set of single particle equations with an effective potential $V_{eff}(\mathbf{r})$ which contains all the information about the many-body problem within. The density obtained from the effective non-interacting system is equivalent to the many-body density. The Kohn-Sham equations are solved iteratively, and the procedure is given by Fig. 3.2.

The density functional theory for superconductors was initially presented by L. N. Oliveira, E. K. U. Gross and W. Kohn [201], who introduced the effective pairing potential $\Delta_{eff}(\mathbf{r},\mathbf{r}')$, describing the superconducting state in addition to the conventional Kohn-Sham potential. These two potentials are defined as

$$V_{eff}(\mathbf{r}) = V_{ext}(\mathbf{r}) + \int d^3r \frac{\rho(\mathbf{r})}{|\mathbf{r}-\mathbf{r}'|} + \frac{\delta E_{xc}[\rho,\chi]}{\delta\rho(\mathbf{r})}, \tag{3.23}$$

$$\Delta_{eff}(\mathbf{r},\mathbf{r}') = \frac{\delta E_{xc}[\rho,\chi]}{\delta\chi(\mathbf{r},\mathbf{r}')}, \tag{3.24}$$

where $\chi(\mathbf{r},\mathbf{r}')$ is the anomalous density, $\rho(\mathbf{r})$ the charge density, $E_{xc}[\rho,\chi]$ is the exchange correlation functional for a superconductor and $V_{ext}(\mathbf{r})$ is the external potential (e.g. the Coulomb attraction from the protons). In Ref. [201] the full Hamiltonian for a superconductor is diagonalised using a Bogoliubov-Valatin transformation and the coefficients of the transformation $u_n(\mathbf{r})$ and $v_n(\mathbf{r})$ satisfy the BdG equations

$$\left(-\nabla^2 - \mu + V_{eff}(\mathbf{r})\right) u_n(\mathbf{r}) + \int \Delta_{eff}(\mathbf{r},\mathbf{r}') v_n(\mathbf{r}') d\mathbf{r}' = \epsilon_n u_n(\mathbf{r}), \tag{3.25}$$

$$\left(-\nabla^2 - \mu + V_{eff}(\mathbf{r})\right) v_n(\mathbf{r}) - \int \Delta^*_{eff}(\mathbf{r},\mathbf{r}') v_n(\mathbf{r}') d\mathbf{r}' = -\epsilon_n v_n(\mathbf{r}). \tag{3.26}$$

The charge and anomalous densities are given by

$$\rho(\mathbf{r}) = 2\sum_n \left(|u_n(\mathbf{r})|^2 f(\epsilon_n) + |v_n(\mathbf{r})|^2 (1 - f(\epsilon_n)\right), \tag{3.27}$$

$$\chi(\mathbf{r},\mathbf{r}') = \sum_n \left(u_n(\mathbf{r}) v^*(\mathbf{r}')(1 - f(\epsilon_n)) - u_n(\mathbf{r}') v^*(\mathbf{r}) f(\epsilon_n)\right). \tag{3.28}$$

Now that we have introduced the principal equations of superconducting DFT, we proceed to addressing the first of the two problems associated with DFT: the choice of the exchange correlation functional. Suvasini *et al*. [207] approximated $E_{xc}[\rho,\chi]$ by splitting it into two terms, the normal state exchange-correlation functional, $E^0_{xc}[\rho]$, and the pairing kernel $\Lambda[\rho,\chi](\mathbf{r}_1,\mathbf{r}'_1,\mathbf{r}_2,\mathbf{r}'_2)$. The general form of $E_{xc}[\rho,\chi]$ can therefore be written as,

$$E_{xc}[\rho,\chi] = E^0_{xc}[\rho] - \int d^3r_1 d^3r_2 d^3r'_1 d^3r'_2 \chi^*(\mathbf{r}_1,\mathbf{r}'_1)\Lambda[\rho,\chi](\mathbf{r}_1,\mathbf{r}'_1,\mathbf{r}_2,\mathbf{r}'_2)\chi(\mathbf{r}_2,\mathbf{r}'_2). \tag{3.29}$$

Here we take the following assumptions which was described by Ref. [207]. Firstly, that $E^0_{xc}[\rho]$ can be assumed to be described by the local spin density approximation (LSDA) functional [208]. Secondly, further approximations are applied to the kernel where we essentially neglect the dependence on $\rho(\mathbf{r})$ and $\chi(\mathbf{r},\mathbf{r}')$

$$\Lambda[\rho,\chi](\mathbf{r}_1,\mathbf{r}'_1,\mathbf{r}_2,\mathbf{r}'_2) = \Lambda\delta(\mathbf{r}_1-\mathbf{r}'_1)\delta(\mathbf{r}_1-\mathbf{r}_2)\delta(\mathbf{r}_1-\mathbf{r}'_2), \tag{3.30}$$

where Λ is the interaction parameter. This implies that $\Delta_{eff}(\mathbf{r},\mathbf{r}')$ and $\chi(\mathbf{r},\mathbf{r}')$ are local, resulting in

$$\Delta_{eff}(\mathbf{r},\mathbf{r}') = \Delta_{eff}(\mathbf{r})\delta(\mathbf{r}-\mathbf{r}'), \tag{3.31}$$

$$\chi(\mathbf{r},\mathbf{r}') = \chi(\mathbf{r})\delta(\mathbf{r}-\mathbf{r}'). \tag{3.32}$$

Equation (3.24) therefore becomes

$$\Delta_{eff}(\mathbf{r}) = \Lambda\chi(\mathbf{r}). \tag{3.33}$$

The only final problem remaining with the exchange correlation functional is the choice of Λ. The ultimate goal of this work is to compare to experimental data, hence we choose to tune Λ such that the gap in the DOS matches experimental results for the zero temperature gap size $\Delta(T=0)$ of the material in question. During this process we uncover a subtle relationship between the gap in the DOS and $\Delta_{eff}(\mathbf{r})$. Further details of how Λ is tuned and what the relationship between $\Delta_{eff}(\mathbf{r})$ and the gap in the DOS is will be discussed in chapter 4.

Finally we can move onto the second problem of DFT, solving the Kohn-Sham-Bogoliubov-de Gennes equations. From the approximations to the exchange correlation functional that have been discussed earlier we can write down the form of the KSBdG equations which are to be solved. They can now be written conveniently into the 2 by 2 form introduced in section 3.2

$$\begin{pmatrix} \hat{H}(\mathbf{r}) & \Delta_{eff}(\mathbf{r}) \\ \Delta_{eff}(\mathbf{r})^* & -\hat{H}(\mathbf{r})^* \end{pmatrix}\begin{pmatrix} u_n(\mathbf{r}) \\ v_n(\mathbf{r}) \end{pmatrix} = \epsilon_n \begin{pmatrix} u_n(\mathbf{r}) \\ v_n(\mathbf{r}) \end{pmatrix}, \tag{3.34}$$

where the Hamiltonian is

$$\hat{H}_{BdG}(\mathbf{r}) = \begin{pmatrix} \hat{H}(\mathbf{r}) & \Delta_{eff}(\mathbf{r}) \\ \Delta^*_{eff}(\mathbf{r}) & -\hat{H}^*(\mathbf{r}) \end{pmatrix}, \tag{3.35}$$

$$\hat{H}(\mathbf{r}) = \hat{H}_0(\mathbf{r}) + V_{eff}(\mathbf{r}), \tag{3.36}$$

$$\hat{H}_0(\mathbf{r}) = -\nabla^2 - \mu. \tag{3.37}$$

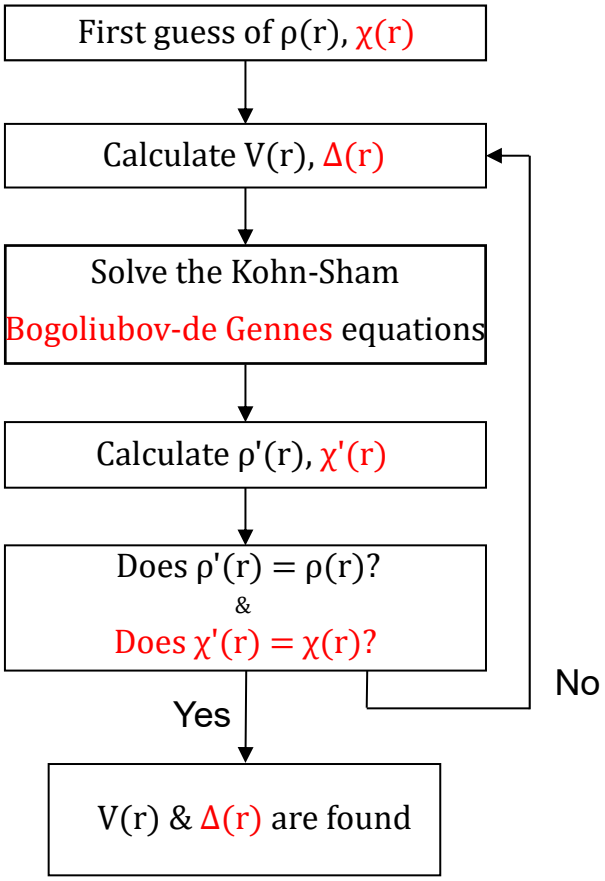

Figure 3.2: A flow chart describing the process for superconducting DFT. The items labelled in red are the additions to the theory that make it superconducting DFT. Removing these return the expressions to conventional DFT.

Here, μ is the chemical potential. The densities reduce from equations (3.28) and (3.27) to

$$\rho(\mathbf{r}) = 2\sum_n \left(|u_n(\mathbf{r})|^2 f(\epsilon_n) + |v_n(\mathbf{r})|^2(1-f(\epsilon_n)\right), \tag{3.38}$$

$$\chi(\mathbf{r}) = \sum_n u_n(\mathbf{r})v^*(\mathbf{r})(1-2f(\epsilon_n)), \tag{3.39}$$

where the sum over n is over all occupied states.

From here the principal method for performing a superconducting DFT calculation is now clear. Assuming it is known how to solve equation (3.34), we use equations (3.38) and (3.39) to find new expressions for $V_{eff}(\mathbf{r})$ and $\Delta_{eff}(\mathbf{r})$ using equations (3.23) and (3.33). From here a new $\hat{H}_{BdG}(\mathbf{r})$ is constructed and thus self-consistency can be achieved. The full self-consistent cycle is presented in Fig. 3.2. There are multiple ways to solve equation (3.34), however we choose to use a Green's function method to do this. Sections 3.4-3.6 detail how this method is performed.

3.4 The Green's Function Method

In order to solve the equations for superconducting density functional theory, namely (3.34), (3.39) and (3.38), the Korringa Kohn Rostoker Green's function method is used. Before we detail the KKR formalism, we will give a brief introduction to Green's functions. For a continuous spectrum the resolution of the identity is given by

$$\hat{I} = \int d\epsilon |\varphi(\epsilon)\rangle \langle \varphi(\epsilon)|, \tag{3.40}$$

where $|\varphi(\epsilon)\rangle$ are the eigenfunctions of the Hamilton operator $\hat{H}$

$$\hat{H}|\varphi(\epsilon)\rangle = \epsilon |\varphi(\epsilon)\rangle. \tag{3.41}$$

Similarly for an unperturbed Hamiltonian with $\hat{H} = \hat{H}_0 + \hat{V}$ the eigenfunctions are

$$\hat{H}_0|\varphi_0(\epsilon)\rangle = \epsilon |\varphi_0(\epsilon)\rangle. \tag{3.42}$$

The Green's functions for these systems are defined as,

$$\hat{G}(z) = (z\hat{I} - \hat{H})^{-1}, \tag{3.43}$$

$$\hat{G}_0(z) = (z\hat{I} - \hat{H}_0)^{-1}, \tag{3.44}$$

where $z = \epsilon + i\delta$. Combining both expressions one can derive the Dyson equation [209] linking $\hat{G}(z)$ and $\hat{G}_0(z)$

$$\hat{G}(z) = \hat{G}_0(z) + \hat{G}_0(z)\hat{V}\hat{G}(z). \tag{3.45}$$

In order to solve this expression, the T-operator $\hat{t}(z)$ is defined

$$\hat{G}(z) = \hat{G}_0(z) + \hat{G}_0(z)\hat{t}(z)\hat{G}_0(z), \tag{3.46}$$

with the $\hat{t}(z)$ operator containing all the information about the potential

$$\hat{t}(z) = \left(\hat{I} - \hat{V}\hat{G}_0(z)\right)^{-1}\hat{V}. \tag{3.47}$$

The imaginary component δ of these functions is a useful tool for the numerical calculation, however in order to calculate real quantities the positive side-limits of $\hat{G}(z)$ and $\hat{t}(z)$ are defined

$$\lim_{|\delta|\to 0^+} \hat{G}(z) = \hat{G}^+(\epsilon) \quad \lim_{|\delta|\to 0^+} \hat{t}(z) = \hat{t}^+(\epsilon), \tag{3.48}$$

where a convenient notation to simplify the expressions is,

$$\hat{G}^+(\epsilon) \to \hat{G}(\epsilon) \quad \hat{t}^+(\epsilon) \to \hat{t}(\epsilon). \tag{3.49}$$

Within this formalism it is possible to connect the perturbed and unperturbed wavefunction via the Lippman-Schwinger equation,

$$|\varphi(\epsilon)\rangle = |\varphi_0(\epsilon)\rangle + \hat{G}_0(\epsilon)\hat{t}(\epsilon)|\varphi_0(\epsilon)\rangle. \tag{3.50}$$

These expressions show that for any Hamiltonian $\hat{H}$ differing from another Hamiltonian $\hat{H}_0$ by a potential $\hat{V}$ the Green's function can be found directly via a Dyson equation. It is important to point out that other methods often make the Born approximation which assumes equation (3.50) can be approximated as

$$|\varphi(\epsilon)\rangle \approx |\varphi_0(\epsilon)\rangle + \hat{G}_0(\epsilon)\hat{V}|\varphi_0(\epsilon)\rangle, \tag{3.51}$$

essentially removing the requirement to compute the $\hat{t}(z)$ operator. This retains the symmetry of the reference system and often excludes important mechanisms. It has been successful in describing impurity effects in superconductors [29], however to fully understand the symmetry breaking effects that impurities have on the local electronic structure the full t-operator must be considered.

In order to link this method to DFT it is useful to introduce the spectral representation of the Green's function

$$\hat{G}(z) = \int dE \sum_{\alpha} \frac{|\varphi_\alpha(E)\rangle\langle\varphi_\alpha(E)|}{(\epsilon + \delta i) - E}. \tag{3.52}$$

This, in turn, can be used to derive the density

$$\rho(\mathbf{r}) = -\frac{1}{\pi}\int_{-\infty}^{0} d\epsilon f(\epsilon)\mathrm{ImTr}(G^+(\epsilon,\mathbf{r},\mathbf{r})), \tag{3.53}$$

where $G(z,\mathbf{r},\mathbf{r}) = \langle\mathbf{r}|\hat{G}(z)|\mathbf{r}\rangle$ is the real-space representation of the Green's function. Similarly, the DOS is defined as

$$D(\epsilon) = -\frac{1}{\pi}\int_{BZ} d^3k \mathrm{ImTr}(G(\epsilon,\mathbf{k})), \tag{3.54}$$

and the Bloch spectral function $A(\epsilon,\mathbf{k})$ is the k-dependent DOS

$$A(\epsilon,\mathbf{k}) = -\frac{1}{\pi}\mathrm{ImTr}(G(\epsilon,\mathbf{k})), \tag{3.55}$$

where $G(\epsilon,\mathbf{k})$ is the Fourier transformation of $G(\epsilon,\mathbf{r},\mathbf{r})$

$$G(\epsilon,\mathbf{k}) = \frac{V}{(2\pi)^3}\int_V d^3r e^{-i\mathbf{kr}} G(\epsilon,\mathbf{r},\mathbf{r}), \tag{3.56}$$

where V is the total volume of the system.

For superconductivity, we aim to incorporate the Bogoliubov-de Gennes equations into the Green's function method. Hence we define a special Green's function, namely the Bogoliubov-de Gennes Green's function, $\hat{G}_{BdG}(z)$. It is defined in full analogy to equation (3.43) but it is

convenient to write it in a 2-dimensional form corresponding to the Hamiltonian in equation (3.35),

$$\hat{G}_{BdG}(z) = \left(z\hat{I}_2 - \hat{H}_{BdG}\right)^{-1} = \begin{pmatrix} \hat{G}^{ee}(z) & \hat{G}^{eh}(z) \\ \hat{G}^{he}(z) & \hat{G}^{hh}(z) \end{pmatrix}, \tag{3.57}$$

where $\hat{H}_{BdG}(\mathbf{r}) = \langle \mathbf{r}|\hat{H}_{BdG}|\mathbf{r}\rangle$ and the indices e and h refer to the electron and hole components respectively. The DOS, $n(\epsilon)$, and the spectral function, $A(\epsilon,\mathbf{k})$, within the Bogoliubov-de Gennes formalism are defined,

$$D^{ab}(\epsilon) = \int_{BZ} d^3k A^{ab}(\epsilon,\mathbf{k}) = -\frac{1}{\pi}\int_{BZ} d^3k \mathrm{ImTr}(G^{ab}(\epsilon,\mathbf{k})), \tag{3.58}$$

where a and b can be either e or h. The extension of the Fourier transformation in equation (3.56) is extended in the same manner.

The relevant densities, $\rho(\mathbf{r})$ and $\chi(\mathbf{r})$, within the Bogoliubov-de Gennes formalism are defined as

$$\begin{aligned} \rho(\mathbf{r}) = &-\frac{1}{\pi}\int_{-\infty}^{0} d\epsilon f(\epsilon)\mathrm{ImTr}_\alpha G^{ee}(\epsilon,\mathbf{r},\mathbf{r}) \\ &-\frac{1}{\pi}\int_{-\infty}^{0} d\epsilon [1-f(\epsilon)]\mathrm{ImTr}_\alpha G^{hh}(\epsilon,\mathbf{r},\mathbf{r}), \end{aligned} \tag{3.59}$$

$$\begin{aligned} \chi(\mathbf{r}) = &-\frac{1}{4\pi}\int_{-\infty}^{0} d\epsilon [1-2f(\epsilon)]\mathrm{ImTr}_\alpha G^{eh}(\epsilon,\mathbf{r},\mathbf{r}) \\ &-\frac{1}{4\pi}\int_{-\infty}^{0} d\epsilon [1-2f(\epsilon)]\mathrm{ImTr}_\alpha G^{he}(\epsilon,\mathbf{r},\mathbf{r}). \end{aligned} \tag{3.60}$$

Unlike the previous expressions, (3.39) and (3.38), that calculate $\rho(\mathbf{r})$ and $\chi(\mathbf{r})$ the above equations show that the densities can be calculated using the single particle Green's function. The self-consistent Kohn Sham equations are now achievable within the Green's function method.

3.5 The Korringa-Kohn-Rostoker Method for Superconductors

The previous sections described how it is possible to implement superconductivity into a density functional theory technique, and how Green's functions can be used to solve for the density. The final ingredient is how the Green's function is constructed. We use the Korringa-Kohn-Rostoker method [210, 211], which is based on multiple scattering theory. Whilst there is vast literature on how these methods are derived and constructed, the important parts to convert the conventional KKR method into the superconducting KKR method will be outlined. Beyond this, we refer to G. Csire's thesis [64] for the in-depth derivation, M. Gradhand's thesis [212] for an overview of the normal state KKR code, and the book by J. Zaboludil *et al*. [213] for in-depth derivations of normal state KKR. G. Csire's work in Ref.[64] details how the BdG equations are implemented into the 2 dimensional layered KKR formalism. This thesis details the implementation into 3 dimensional KKR formalism, along with its extension to impurities. All expressions are in Rydberg atomic units.

3.5.1 The Green's Function

The Green function of the system (3.57) is the starting point, writing it down with more explicit emphasis on the potentials and the 2 by 2 structure we have

$$\begin{pmatrix} \hat{G}^{ee}(z) & \hat{G}^{eh}(z) \\ \hat{G}^{he}(z) & \hat{G}^{hh}(z) \end{pmatrix}^{-1} = \begin{pmatrix} z\hat{I} & 0 \\ 0 & z\hat{I} \end{pmatrix} - \begin{pmatrix} \hat{H}_0 & 0 \\ 0 & -\hat{H}_0^{\dagger} \end{pmatrix} - \begin{pmatrix} \hat{V} & \hat{\Delta} \\ \hat{\Delta}^{\dagger} & -\hat{V}^{\dagger} \end{pmatrix}. \tag{3.61}$$

The potentials are arbitrary and the system can be an infinite crystal, resulting in a very demanding calculation. In order to make this calculation more manageable, further approximations are applied. The main approximation is called the atomic sphere approximation (ASA). The ASA approximation sets a boundary to each atomic site, n, called the ASA radius r_n^{ASA}. This approximation implies that the potentials $V_{eff}(\mathbf{r})$ and $\Delta_{eff}(\mathbf{r})$ can be written in sums

$$V_{eff}(\mathbf{r}) = \sum_n V_n(\mathbf{r}), \tag{3.62}$$

$$\Delta_{eff}(\mathbf{r}) = \sum_n \Delta_n(\mathbf{r}), \tag{3.63}$$

and ensures that $V_n(\mathbf{r}) = 0$ and $\Delta_n(\mathbf{r}) = 0$ if $|\mathbf{r}| \geq r_n^{ASA}$. The analogue of equation (3.33) becomes,

$$\Delta_n(\mathbf{r}) = \Lambda_n \chi_n(\mathbf{r}). \tag{3.64}$$

The volume of the system is correct, but the spheres overlap and the interstitial region is effectively neglected. This approximation therefore works for closely packed systems like metals, but less well for materials with open structures. In addition, the spherical symmetry brought about by the ASA approximation combined with the local approximation for the pairing potential restrict the method to s-wave superconductivity. Any kind of non s-wave superconductivity would need a non-spherical pairing potential, coupling between different orbital channels or coupling between different atomic positions.

The definition for the Green's function can be simplified to

$$\begin{pmatrix} z\hat{I} - \hat{H}_0(\mathbf{r}) - V_n(\mathbf{r}) + \mu & \Delta_n(\mathbf{r}) \\ \Delta_n^*(\mathbf{r}) & z\hat{I} + \hat{H}_0(\mathbf{r}) + V_n(\mathbf{r}) - \mu \end{pmatrix} \mathbf{G}_{BdG}(z, \mathbf{R}^n + \mathbf{r}, \mathbf{R}^{n'} + \mathbf{r}') = \delta_{nn'}\delta(\mathbf{r} - \mathbf{r}'). \tag{3.65}$$

One of the fundamental aspects of the KKR method is that the scattering from the potential and scattering associated with the structure can be solved separately. This aspect arises when inspecting equation (3.65), which is an inhomogeneous differential equation. The inhomogeneous differential equation defines the single-site scattering problem, which only contains information about the potential. The inhomogeneity vanishes when the coordinates are not in the same cell, which defines the multiple scattering solution as it connects different atomic positions, defining the structure. Although the multiple scattering term needs information from the single-site scattering to be solved, they not need to be solved simultaneously. The full solution can be written

as a combination of the single-site and multiple scattering terms

$$\begin{pmatrix} G^{ee,nn'}(z,\mathbf{r},\mathbf{r}') & G^{eh,nn'}(z,\mathbf{r},\mathbf{r}') \\ G^{he,nn'}(z,\mathbf{r},\mathbf{r}') & G^{hh,nn'}(z,\mathbf{r},\mathbf{r}') \end{pmatrix} = \delta_{nn'} \sum_{lm} \begin{pmatrix} G^{ee,n}_{lm}(z,\mathbf{r},\mathbf{r}') & G^{eh,n}_{lm}(z,\mathbf{r},\mathbf{r}') \\ G^{he,n}_{lm}(z,\mathbf{r},\mathbf{r}') & G^{hh,n}_{lm}(z,\mathbf{r},\mathbf{r}') \end{pmatrix} + \sum_{lml'm'} \begin{pmatrix} R^{ee}_{lm}(z,\mathbf{r}) & R^{eh}_{lm}(z,\mathbf{r}) \\ R^{he}_{lm}(z,\mathbf{r}) & R^{hh}_{lm}(z,\mathbf{r}) \end{pmatrix} \begin{pmatrix} G^{ee,nn'}_{lml'm'}(z) & G^{eh,nn'}_{lml'm'}(z) \\ G^{he,nn'}_{lml'm'}(z) & G^{hh,nn'}_{lml'm'}(z)) \end{pmatrix} \begin{pmatrix} R^{ee}_{l'm'}(z,\mathbf{r}') & R^{eh}_{l'm'}(z,\mathbf{r}') \\ R^{he}_{l'm'}(z,\mathbf{r}') & R^{hh}_{l'm'}(z,\mathbf{r}') \end{pmatrix}^{\times} \tag{3.66}$$

where the abbreviation

$$\mathbf{G}_{BdG}(z,\mathbf{R}^n+\mathbf{r},\mathbf{R}^{n'}+\mathbf{r}') = \mathbf{G}^{nn'}_{BdG}(z,\mathbf{r},\mathbf{r}') = \begin{pmatrix} G^{ee,nn'}(z,\mathbf{r},\mathbf{r}') & G^{eh,nn'}(z,\mathbf{r},\mathbf{r}') \\ G^{he,nn'}(z,\mathbf{r},\mathbf{r}') & G^{hh,nn'}(z,\mathbf{r},\mathbf{r}') \end{pmatrix} \tag{3.67}$$

is used. The first of the two terms is the single-site Green's function

$$\mathbf{G}^n(z,\mathbf{r},\mathbf{r}') = \sum_{lm} \begin{pmatrix} G^{ee,n}_{lm}(z,\mathbf{r},\mathbf{r}') & G^{eh,n}_{lm}(z,\mathbf{r},\mathbf{r}') \\ G^{he,n}_{lm}(z,\mathbf{r},\mathbf{r}') & G^{hh,n}_{lm}(z,\mathbf{r},\mathbf{r}') \end{pmatrix}, \tag{3.68}$$

the second term is the multiple scattering term which is expanded into the scattering solutions of the single-site Bogoliubon scatterers

$$\mathbf{R}_{lm}(z,\mathbf{r}) = \begin{pmatrix} R^{ee}_{lm}(z,\mathbf{r}) & R^{eh}_{lm}(z,\mathbf{r}) \\ R^{he}_{lm}(z,\mathbf{r}) & R^{hh}_{lm}(z,\mathbf{r}) \end{pmatrix}, \tag{3.69}$$

defining the structure constants

$$\mathbf{G}^{nn'}_{lml'm'}(z) = \begin{pmatrix} G^{ee,nn'}_{lml'm'}(z) & G^{eh,nn'}_{lml'm'}(z) \\ G^{he,nn'}_{lml'm'}(z) & G^{hh,nn'}_{lml'm'}(z) \end{pmatrix}. \tag{3.70}$$

The single site solutions (3.69) can further be expanded into spherical harmonics $Y_{lm}(\hat{\mathbf{r}})$ where $R^{ab}_{ll'}(z,r)$ being the radial solutions,

$$\mathbf{R}_{lm}(z,\mathbf{r}) = \sum_{l'm'} \begin{pmatrix} R^{ee}_{ll'}(z,r)Y_{l'm'}(\hat{\mathbf{r}}) & R^{he}_{ll'}(z,r)Y_{l'm'}(\hat{\mathbf{r}}) \\ R^{eh}_{ll'}(z,r)Y_{l'm'}(\hat{\mathbf{r}}) & R^{hh}_{ll'}(z,r)Y_{l'm'}(\hat{\mathbf{r}}) \end{pmatrix}, \tag{3.71}$$

In that notation $\times$ implies the conjugate complex of the non-radial part only,

$$\mathbf{R}^{\times}_{lm}(z,\mathbf{r}) = \begin{pmatrix} R^{ee}_{lm}(z,\mathbf{r}) & R^{eh}_{lm}(z,\mathbf{r}) \\ R^{he}_{lm}(z,\mathbf{r}) & R^{hh}_{lm}(z,\mathbf{r}) \end{pmatrix}^{\times} = \sum_{l'm'} \begin{pmatrix} R^{ee}_{ll'}(z,r)Y^*_{l'm'}(\hat{\mathbf{r}}) & R^{he}_{ll'}(z,r)Y^*_{l'm'}(\hat{\mathbf{r}}) \\ R^{eh}_{ll'}(z,r)Y^*_{l'm'}(\hat{\mathbf{r}}) & R^{hh}_{ll'}(z,r)Y^*_{l'm'}(\hat{\mathbf{r}}) \end{pmatrix}^{T}. \tag{3.72}$$

Restricting calculations to s-wave superconductivity and the scalar relativistic approximation makes the radial solutions diagonal in l and m $R^{ab}_{lml'm'}(z,\mathbf{r}) = \delta_{lml'm'} R^{ab}_{lm}(z,\mathbf{r})$,

$$\mathbf{R}_{lm}(z,\mathbf{r}) = \mathbf{R}_l(z,r)Y_{lm}(\hat{\mathbf{r}}) = \begin{pmatrix} R^{ee}_{l}(z,r)Y_{lm}(\hat{\mathbf{r}}) & R^{eh}_{l}(z,r)Y_{lm}(\hat{\mathbf{r}}) \\ R^{he}_{l}(z,r)Y_{lm}(\hat{\mathbf{r}}) & R^{hh}_{l}(z,r)Y_{lm}(\hat{\mathbf{r}}) \end{pmatrix}. \tag{3.73}$$

Using the shorthand expressions defined above a condensed form of the Green's function can be written,

$$\mathbf{G}^{nn'}_{BdG}(z,\mathbf{r},\mathbf{r}') = \delta_{nn'}\mathbf{G}^n(z,\mathbf{r},\mathbf{r}') + \sum_{lml'm'} \mathbf{R}_{lm}(z,\mathbf{r})\mathbf{G}^{nn'}_{lml'm'}(z)\mathbf{R}^{\times}_{l'm'}(z,\mathbf{r}). \tag{3.74}$$

3.5.2 The Structure Constants

The structure constants $\mathbf{G}^{nn'}_{lml'm'}(z)$ can be expressed in terms of the algebraic Dyson equation [209]

$$\begin{pmatrix} G^{ee,nn'}_{lml'm'}(z) & G^{eh,nn'}_{lml'm'}(z) \\ G^{he,nn'}_{lml'm'}(z) & G^{hh,nn'}_{lml'm'}(z) \end{pmatrix} = \begin{pmatrix} G^{ee,nn'}_{0,lml'm'}(z) & 0 \\ 0 & G^{hh,nn'}_{0,lml'm'}(z) \end{pmatrix} + \sum_{l''m'',n''} \begin{pmatrix} G^{e,nn'}_{0,lml'm'}(z) & 0 \\ 0 & G^{h,nn'}_{0,lml'm'}(z) \end{pmatrix} \begin{pmatrix} t^{ee,n''}_{l}(z) & t^{eh,n''}_{l}(z) \\ t^{he,n''}_{l}(z) & t^{hh,n''}_{l}(z) \end{pmatrix} \begin{pmatrix} G^{ee,n''n'}_{l''m''l'm'}(z) & G^{eh,n''n'}_{l''m''l'm'}(z) \\ G^{he,n''n'}_{l''m''l'm'}(z) & G^{hh,n''n'}_{l''m''l'm'}(z) \end{pmatrix}^{T}. \tag{3.75}$$

Inverting this matrix equation and introducing the KKR matrix,

$$\mathbf{M}^{nn'}_{lml'm'}(z) = \sum_{n'} \sum_{l'm'} \begin{pmatrix} t^{ee,n'}_{l}(z) & t^{eh,n'}_{l}(z) \\ t^{he,n'}_{l}(z) & t^{hh,n'}_{l}(z) \end{pmatrix}^{-1} \delta_{lml'm'}\delta_{nn'} - \begin{pmatrix} G^{e,nn'}_{0,lml'm'}(z) & 0 \\ 0 & G^{h,nn'}_{0,lml'm'}(z) \end{pmatrix} \tag{3.76}$$

yields

$$\begin{pmatrix} G^{ee,nn'}_{lml'm'}(z) & G^{eh,nn'}_{lml'm'}(z) \\ G^{he,nn'}_{lml'm'}(z) & G^{hh,nn'}_{lml'm'}(z) \end{pmatrix} = \sum_{nn'} -\delta_{nn'} \begin{pmatrix} t^{ee,n}_{l}(z) & t^{eh,n}_{l}(z) \\ t^{he,n}_{l}(z) & t^{hh,n}_{l}(z) \end{pmatrix}^{-1} - \begin{pmatrix} t^{ee,n}_{l}(z) & t^{eh,n}_{l}(z) \\ t^{he,n}_{l}(z) & t^{hh,n}_{l}(z) \end{pmatrix}^{-1} \begin{pmatrix} M^{ee,nn'}_{lml'm'}(z) & M^{eh,nn'}_{lml'm'}(z) \\ M^{he,nn'}_{lml'm'}(z) & M^{hh,nn'}_{lml'm'}(z) \end{pmatrix}^{-1} \begin{pmatrix} t^{ee,n'}_{l'}(z) & t^{eh,n'}_{l'}(z) \\ t^{he,n'}_{l'}(z) & t^{hh,n'}_{l'}(z) \end{pmatrix}^{-1} \tag{3.77}$$

where $t^{ab,n'}_{l}(z)$ is an element of the t-matrix $\mathbf{t}^{n}_{l}(z)$ and $G^{a,nn'}_{0,lml'm'}(z)$ are the components of the free electron structure constants.

3.5.3 The T-Matrix

In order to compute the t-matrix, the solution comes from projecting the Lippmann-Schwinger equation (3.50) into the scattering solutions of single site Bogoliubon scatterers. This is a standard procedure in the normal state and detailed, for example, in Ref. [213]. Its extension to the superconducting state is derived by G. Csire [64]. The result of this derivation is the structure of the wavefunction outside of the atomic sphere $r > r^{ASA}_{n}$,

$$\mathbf{R}_{l}(z,r) = \mathbf{j}_{l}(z) - i\mathbf{p}\mathbf{h}_{l}(z)\mathbf{t}^{n}_{l}(z) \tag{3.78}$$

where,

$$\mathbf{h}_{l}(z,r) = \begin{pmatrix} h^{+}_{l}(p^{e}r) & 0 \\ 0 & h^{-}_{l}(p^{h}r) \end{pmatrix}, \quad \mathbf{j}_{l}(z,r) = \begin{pmatrix} j_{l}(p^{e}r) & 0 \\ 0 & j_{l}(p^{h}r) \end{pmatrix} \tag{3.79}$$

$j_{l}(p^{a}r)$ and $h^{\pm}_{l}(p^{a}r)$ are Bessel and Hankel functions respectively and

$$\mathbf{p}(z) = \begin{pmatrix} p^{e} & 0 \\ 0 & p^{h} \end{pmatrix} \tag{3.80}$$

where,

$$p^e = \sqrt{\mu + z}, \qquad p^h = \sqrt{\mu - z}. \tag{3.81}$$

Expression (3.78) returns to the free electron solution when $\mathbf{t}_l^n(z) \to 0$. In order to solve for $\mathbf{t}_l^n(z)$, the solutions for $r < r_n^{ASA}$ and $r > r_n^{ASA}$ must be matched at the r_n^{ASA} boundary. When computing the elements inside the atomic sphere one has to solve the Bogoliubov-de Gennes equations for an arbitrary potential, and therefore it must be done numerically. The solution to this is performed in appendix A. For now, the total wavefunction is defined as,

$$\mathbf{R}_l(z,r) = \begin{cases} \tilde{\mathbf{R}}_l(z,r)\boldsymbol{\alpha}_l^n(z); & r < r_n^{ASA} \\ \\ \mathbf{j}_l(z,r) - i\mathbf{p}\mathbf{h}_l(z,r)\mathbf{t}_l^n(z); & r > r_n^{ASA} \end{cases} \tag{3.82}$$

where $\tilde{\mathbf{R}}_l(z,r_n)$ is the unnormalised numerical solution, and

$$\boldsymbol{\alpha}_l^n(z) = \begin{pmatrix} \alpha_l^{ee,n}(z) & \alpha_l^{eh,n}(z) \\ \alpha_l^{he,n}(z) & \alpha_l^{hh,n}(z) \end{pmatrix} \tag{3.83}$$

are the normalisation constants. The wavefunction and its differential must be continuous across the boundary, resulting in two simultaneous matrix equations

$$\tilde{\mathbf{R}}_l(z,r_n^{ASA})\boldsymbol{\alpha}_l^n(z) = \mathbf{j}_l(z,r_n^{ASA}) - i\mathbf{p}\mathbf{h}_l(z,r_n^{ASA})\mathbf{t}_l^n(z) \tag{3.84}$$

$$\tilde{\mathbf{R}}_l'(z,r_n^{ASA})\boldsymbol{\alpha}_l^n(z) = \mathbf{j}_l'(z,r_n^{ASA}) - i\mathbf{p}\mathbf{h}_l'(z,r_n^{ASA})\mathbf{t}_l^n(z) \tag{3.85}$$

where the differential of the wavefunction $\tilde{\mathbf{R}}_l'(z,r_n)$ is defined

$$\tilde{\mathbf{R}}_l'(z,r_n) = \frac{d}{dr_n}\begin{pmatrix} \tilde{R}_l^{ee,n}(z,r_n) & \tilde{R}_l^{eh,n}(z,r_n) \\ \tilde{R}_l^{he,n}(z,r_n) & \tilde{R}_l^{hh,n}(z,r_n) \end{pmatrix}. \tag{3.86}$$

Likewise for $\mathbf{h}_l'(z,r_n)$ and $\mathbf{j}_l'(z,r_n)$. The values $\tilde{\mathbf{R}}_l(z,r_n^{ASA})$, $\mathbf{h}_l(z,r_n^{ASA})$ and $\mathbf{j}_l(z,r_n^{ASA})$ are known quantities, therefore these equations can be solved for $\mathbf{t}_{l,n}(z)$ and $\alpha_{l,n}(z)$. The t-matrix elements obey the symmetry relation [64],

$$t_l^{he}(z) = t_l^{eh}(-z) \tag{3.87}$$

$$t_l^{ee}(z) = -t_l^{hh}(-z). \tag{3.88}$$

3.5.4 The Single-Site Term

By performing the single-site expansion of the Green's function, one can obtain the expression,

$$\mathbf{G}^n(z,\mathbf{r},\mathbf{r}') = \sum_{lm}\begin{pmatrix} H_{lm}^{ee}(z,\mathbf{r}) & H_{lm}^{eh}(z,\mathbf{r}) \\ H_{lm}^{he}(z,\mathbf{r}) & H_{lm}^{hh}(z,\mathbf{r}) \end{pmatrix}\begin{pmatrix} R_{lm}^{ee}(z,\mathbf{r}') & R_{lm}^{eh}(z,\mathbf{r}') \\ R_{lm}^{he}(z,\mathbf{r}') & R_{lm}^{hh}(z,\mathbf{r}') \end{pmatrix}^{\times} \tag{3.89}$$

where,

$$\mathbf{H}_{lm}(z,\mathbf{r}) = \mathbf{H}_l(z,r)Y_{lm}(\hat{\mathbf{r}}), \tag{3.90}$$

are the irregular solutions. They are defined as,

$$\mathbf{H}_l(z,r) = \begin{cases} \tilde{\mathbf{H}}_l(z,r); & r < r_n^{ASA}, \\ \\ -i\mathbf{ph}_l(z,r); & r > r_n^{ASA}. \end{cases} \tag{3.91}$$

Hence, at the ASA boundary,

$$\tilde{\mathbf{H}}_l(z,r^{ASA}) = -i\mathbf{ph}_l(z,r^{ASA}). \tag{3.92}$$

The irregular solutions inside the muffin tin, $\tilde{\mathbf{H}}_l(z,r^{ASA})$, are solved numerically just like the regular solutions $\tilde{\mathbf{R}}_l(z,r)$. Equation (3.92) can be used to define the starting values for $\tilde{\mathbf{H}}_l(z,r)$.

3.5.5 The Free Electron Structure Constants

The structure constants are given by

$$G^{e,nn'}_{0,lml'm'}(z) = -4\pi \sum_{l''m''} i^{l-l'-l''} h^{+}_{l''}(pR_{nn'})Y_{l''m''}(\hat{\mathbf{R}}_{nn'})C^{l'm'}_{lml''m''} \tag{3.93}$$

$$G^{h,nn'}_{0,lml'm'}(z) = -4\pi \sum_{l''m''} i^{l-l'-l''} h^{-}_{l''}(pR_{nn'})Y_{l''m''}(\hat{\mathbf{R}}_{nn'})C^{l'm'}_{lml''m''} \tag{3.94}$$

where the Gaunt coefficients, $C^{l''m''}_{lml'm'}$, are

$$C^{l''m''}_{lml'm'} = \int d\hat{\mathbf{k}} Y_{lm}(\hat{\mathbf{k}})Y_{l'm'}(\hat{\mathbf{k}})Y^{*}_{l''m''}(\hat{\mathbf{k}}). \tag{3.95}$$

The hole part is related to the electron part via the symmetry [64],

$$G^{e,nn}_{0,lml'm'}(z) = -G^{h,nn}_{0,lml'm'}(-z). \tag{3.96}$$

3.5.6 Screened KKR

In section 3.5.2 we specified free electrons as the reference system. It was shown that using this approach was numerically demanding as Fourier sums to determine the structure constants only converged conditionally [214]. It was later found that the reference system could be designed such that only short range interactions are relevant [215]. The reference potential in this instance consists of an array of repulsive spherical wells. Assuming that the height of the potential well is above the valence energy of the system, the structure constants will decay rapidly with distance, allowing for efficient convergence of the Fourier transformation. Useful references include G. Csire [64] for the extension to superconductivity, M. Gradhand [212] for screened normal state

KKR and J. Zabloudil [213]. The main change to the KKR formalism after implementing the screened system is that a new quantity, $\Delta\hat{t}(z)$ is introduced

$$\Delta\hat{t}(z) = \hat{t}(z) - \hat{t}_r(z), \tag{3.97}$$

where $\hat{t}_r(z)$ is the t-matrix associated with the screened reference system and the resulting Dyson equation looks much the same as before

$$\hat{G}(z) = \hat{G}_r(z) + \hat{G}_r(z)\Delta\hat{t}(z)\hat{G}_r(z), \tag{3.98}$$

where $\hat{G}_r(z)$ is the screened Green's function which is generated using a Dyson equation involving the free electron Green's function

$$\hat{G}_r(z) = \hat{G}_0(z) + \hat{G}_0(z)\hat{t}_r(z)\hat{G}_0(z). \tag{3.99}$$

By expanding this expression into the scattering solutions of the single-site scatterer one can obtain a screened analogue to equation (3.75)

$$\begin{aligned}\begin{pmatrix} G^{ee,nn'}_{lml'm'}(z) & G^{eh,nn'}_{lml'm'}(z) \\ G^{he,nn'}_{lml'm'}(z) & G^{hh,nn'}_{lml'm'}(z) \end{pmatrix} &= \begin{pmatrix} G^{ee,nn'}_{r,lml'm'}(z) & 0 \\ 0 & G^{hh,nn'}_{r,lml'm'}(z) \end{pmatrix} + \\ \sum_{l''m'',n''} \begin{pmatrix} G^{e,nn'}_{r,lml'm'}(z) & 0 \\ 0 & G^{h,nn'}_{r,lml'm'}(z) \end{pmatrix} &\begin{pmatrix} \Delta t^{ee,n''}_{l}(z) & \Delta t^{eh,n''}_{l}(z) \\ \Delta t^{he,n''}_{l}(z) & \Delta t^{hh,n''}_{l}(z) \end{pmatrix} \begin{pmatrix} G^{ee,n''n'}_{l''m''l'm'}(z) & G^{eh,n''n'}_{l''m''l'm'}(z) \\ G^{he,n''n'}_{l''m''l'm'}(z) & G^{hh,n''n'}_{l''m''l'm'}(z) \end{pmatrix}^T,\end{aligned} \tag{3.100}$$

where $\Delta t^{ab,n}_l(z)$ is the analogue of $t^{ab,n}_l(z)$ whose elements are defined as

$$\Delta t^{ab,n}_l(z) = t^{ab,n}_l(z) - \delta_{ab} t^{a,n}_{l,r}(z). \tag{3.101}$$

Here the elements a and b cycle through e and h and the screened structure constants $G^{nn'}_{r,lml'm'}(z)$ are determined by an algebraic Dyson equation

$$G^{a,nn'}_{r,lml'm'}(z) = G^{a,nn'}_{0,lml'm'}(z) + \sum_{l''m'',n''} G^{a,nn''}_{0,lml''m''}(z) t^{a,n''}_{l'',r}(z) G^{a,n''n'}_{r,l''m''l'm'}(z). \tag{3.102}$$

3.5.7 Charge Density

This section details how to go from the charge density definition in equation (3.59) and expanding it into the single-site scattering solutions to obtain an expression that can be used for the self-consistency. Starting from equation (3.59), and using (3.74), (3.73) and (3.172) we can rewrite the density as

$$\rho(\mathbf{r}) = -\frac{1}{\pi}\int_{-\infty}^{0} d\epsilon \left(f(\epsilon)\mathrm{Im}G^{ee}_{lml'm'}(\epsilon, r, r') + [1 - f(\epsilon)]\mathrm{Im}G^{hh}_{lml'm'}(\epsilon, r, r') \right) Y_{lm}(\hat{\mathbf{r}}) Y^*_{l'm'}(\hat{\mathbf{r}}') \tag{3.103}$$

where

$$G^{cd,nn'}_{lml'm'}(\epsilon, r, r') = \sum_{ab} \left\{ R^{ca}_l(\epsilon, r) G^{ab,nn'}_{lml'm'}(\epsilon) R^{db}_{l'}(\epsilon, r) + \delta_{nn'}\delta_{lml'm'}\delta_{ab} H^{ca}_l(\epsilon, r) R^{da}_{l'}(\epsilon, r) \right\}. \tag{3.104}$$

Using the shorthand notation

$$\int_{-\infty}^{0} d\epsilon f(\epsilon) G^{ee,nn}_{lml'm'}(\epsilon,r,r) = G^{ee,n}_{lml'm'}(r), \tag{3.105}$$

$$\int_{-\infty}^{0} d\epsilon (1-f(\epsilon)) G^{hh,nn}_{lml'm'}(\epsilon,r,r) = G^{hh,n}_{lml'm'}(r), \tag{3.106}$$

one obtains

$$\rho(\mathbf{r}) = -\frac{1}{\pi} \sum_{lml'm'} \left(\mathrm{Im} G^{ee}_{lml'm'}(r) + \mathrm{Im} G^{hh}_{lml'm'}(r) \right) Y_{lm}(\hat{\mathbf{r}}) Y^{*}_{l'm'}(\hat{\mathbf{r}}'). \tag{3.107}$$

In order to calculate the potential $V_{eff}(\mathbf{r})$, the lm dependent charge density is required. Expanding Eqn. (3.107) into spherical harmonics gives

$$\rho_{lm}(r) = \int d\hat{\mathbf{r}} \rho(\mathbf{r}) Y_{lm}(\hat{\mathbf{r}}) \tag{3.108}$$

resulting in the expression

$$\rho_{lm}(r) = -\frac{1}{\pi} \sum_{l'm'l''m''} \mathrm{Im} \left(G^{ee}_{l'm'l''m''}(r) + G^{hh}_{l'm'l''m''}(r) \right) C^{l''m''}_{l'm'lm} \tag{3.109}$$

where $C^{l''m''}_{l'm'lm}$ are the Gaunt coefficients.

One numerical aspect which has so far been overlooked is performing the energy integrals present in Eqs. (3.105) and (3.106) and some simplifications are needed. In this thesis we are only interested in zero temperature hence equations (3.105) and (3.106) can be simplified to

$$\int_{-\infty}^{0} d\epsilon f(\epsilon) G^{ee,nn}_{lml'm'}(\epsilon,r,r) = \int_{\epsilon_B-\epsilon_F}^{0} d\epsilon G^{ee,nn}_{lml'm'}(\epsilon,r,r), \tag{3.110}$$

$$\int_{-\infty}^{0} d\epsilon (1-f(\epsilon)) G^{hh,nn}_{lml'm'}(\epsilon,r,r) = 0, \tag{3.111}$$

with ϵ_B the band bottom and ϵ_F the Fermi energy. Nevertheless this procedure is numerically demanding especially on the real axis with poles at energies associated with states. A solution is found by replacing the integral with a semi-circular complex contour integral. More details can be find in page 259-261 of Ref. [213].

3.5.8 Anomalous Density

As outlined in section 3.3 any self consistency requires not only the normal density but the anomalous density (Equ. 3.60) as well. This section details how to expand it into the single-site scattering solutions. Taking the matrix elements from equation (3.66) and inserting them into the anomalous density expression one obtains

$$\chi(\mathbf{r}) = -\frac{1}{2\pi} \sum_{lml'm'} \int_{-\infty}^{0} d\epsilon (1-2f(\epsilon)) \mathrm{Im} \left(G^{he,nn}_{lml'm'}(\epsilon,r,r) + G^{eh,nn}_{lml'm'}(\epsilon,r,r) \right) Y_{lm}(\hat{\mathbf{r}}) Y^{*}_{l'm'}(\hat{\mathbf{r}}'). \tag{3.112}$$

Performing the energy integrals

$$\int_{-\infty}^{0} d\epsilon(1-2f(\epsilon))G^{eh,nn}_{lml'm'}(\epsilon,r,r) = G^{eh,n}_{lml'm'}(r), \tag{3.113}$$

$$\int_{-\infty}^{0} d\epsilon(1-2f(\epsilon))G^{he,nn}_{lml'm'}(\epsilon,r,r) = G^{he,n}_{lml'm'}(r), \tag{3.114}$$

we are left with

$$\chi(\mathbf{r}) = -\frac{1}{2\pi}\sum_{lml'm'} \mathrm{Im}\left(G^{he,n}_{lm'm'}(r) + G^{eh,n}_{lml'm'}(r)\right) Y_{lm}(\hat{\mathbf{r}})Y^{*}_{l'm'}(\hat{\mathbf{r}}). \tag{3.115}$$

The superconducting potential $\Delta_{eff}(r)$ is connected to the anomalous density via the interaction parameter Λ. We assume that $\Delta_{eff}(r)$ is spherically symmetric, and therefore only require the spherically symmetric components of $\chi(\mathbf{r})$. Using the expansion as previously

$$\chi_{lm}(r) = \int d\hat{\mathbf{r}}\chi(\mathbf{r})Y_{lm}(\hat{\mathbf{r}}) \tag{3.116}$$

we find the spherically symmetric contribution of $\chi(\mathbf{r})$ for $l = 0$,

$$\chi_0(r) = -\frac{1}{2\pi}\sum_{l'm'} \mathrm{Im}\left(G^{he,n}_{l'm'l'm'}(r) + G^{eh,n}_{l'm'l'm'}(r)\right) C^{l'm'}_{0l'm'}. \tag{3.117}$$

3.5.9 Fourier Transformation

This project deals with periodic crystals. The Bloch condition is imposed, giving the system periodic boundary conditions, a unit cell and three Bravais lattice vectors. Due to this, a new index μ running over the basis atoms is introduced, and the index n refers to different unit cells connected by lattice vectors. This condition naturally leads to quantities such as the Green's function being Fourier transformed into their k-space equivalents. The transformation in our case is,

$$\mathbf{G}^{\mu\mu'}_{BdG}(z,\mathbf{k}) = \sum_{n'} e^{i\mathbf{k}\mathbf{R}^{0n'}}\mathbf{G}^{\mu\mu'0n'}_{BdG}(z,\mathbf{r},\mathbf{r}) \tag{3.118}$$

and the back transformation

$$\mathbf{G}^{\mu\mu'nn'}_{BdG}(z,\mathbf{r},\mathbf{r}) = \frac{V}{(2\pi)^3}\int_{V_{BZ}} d^3k e^{i\mathbf{k}\mathbf{R}^{nn'}}\mathbf{G}^{\mu\mu'}_{BdG}(z,\mathbf{k}). \tag{3.119}$$

Where V is the volume of the unit cell, $V_{BZ} = (2\pi)^3/V$ is the volume of the first Brillouin zone.

3.5.10 Spin Polarised Superconducting KKR

Implementing co-linear spin polarisation into the scalar relativistic BdG formalism is relatively straight forward because it is possible to deal with each spin channel separately. I will give a brief

overview of how the formalism is extended, starting with the superconducting DFT formalism which introduces, the spin density $m(\mathbf{r})$

$$\rho(\mathbf{r}) = \rho_{\uparrow}(\mathbf{r}) + \rho_{\downarrow}(\mathbf{r}), \tag{3.120}$$

$$m(\mathbf{r}) = \rho_{\uparrow}(\mathbf{r}) - \rho_{\downarrow}(\mathbf{r}), \tag{3.121}$$

$$\chi(\mathbf{r}) = \chi_{\uparrow\downarrow}(\mathbf{r}) + \chi_{\downarrow\uparrow}(\mathbf{r}). \tag{3.122}$$

$B_{eff}(\mathbf{r})$ is the effective magnetic field which is calculated from $m(\mathbf{r})$ by using the spin polarised exchange correlation functional $E^0_{xc}[\rho, m]$

$$V_{eff}(\mathbf{r}) = V_{ext}(\mathbf{r}) + \int d^3r \frac{\rho(\mathbf{r})}{|\mathbf{r}-\mathbf{r}'|} + \frac{\delta E^0_{xc}[\rho,m]}{\delta\rho(\mathbf{r})}, \tag{3.123}$$

$$B_{eff}(\mathbf{r}) = B_{ext}(\mathbf{r}) + \frac{\delta E^0_{xc}[\rho,m]}{\delta m(\mathbf{r})}, \tag{3.124}$$

$$\Delta^{\downarrow\uparrow}_{eff}(\mathbf{r}) = \Lambda\chi_{\downarrow\uparrow}(\mathbf{r}), \tag{3.125}$$

$$\Delta^{\downarrow\uparrow}_{eff}(\mathbf{r}) = \Lambda\chi_{\uparrow\downarrow}(\mathbf{r}). \tag{3.126}$$

The BdG equation (3.34) becomes

$$\begin{pmatrix} \hat{H}^{\uparrow\uparrow}(\mathbf{r}) & 0 & 0 & \Delta^{\uparrow\downarrow}_{eff}(\mathbf{r}) \\ 0 & \hat{H}^{\downarrow\downarrow}(\mathbf{r}) & \Delta^{\downarrow\uparrow}_{eff}(\mathbf{r}) & 0 \\ 0 & \Delta^{\uparrow\downarrow}_{eff}(\mathbf{r})^* & -\hat{H}^{\uparrow\uparrow}(\mathbf{r})^* & 0 \\ \Delta^{\downarrow\uparrow}_{eff}(\mathbf{r})^* & 0 & 0 & -\hat{H}^{\downarrow\downarrow}(\mathbf{r})^* \end{pmatrix} \begin{pmatrix} u^{\uparrow}_n(\mathbf{r}) \\ u^{\downarrow}_n(\mathbf{r}) \\ v^{\uparrow}_n(\mathbf{r}) \\ v^{\downarrow}_n(\mathbf{r}) \end{pmatrix} = \epsilon_n \begin{pmatrix} u^{\uparrow}_n(\mathbf{r}) \\ u^{\downarrow}_n(\mathbf{r}) \\ v^{\uparrow}_n(\mathbf{r}) \\ v^{\downarrow}_n(\mathbf{r}) \end{pmatrix}. \tag{3.127}$$

where

$$\hat{H}^{\sigma\sigma}(\mathbf{r}) = \hat{H}_0(\mathbf{r}) + V^{\sigma\sigma}_{eff}(\mathbf{r}), \tag{3.128}$$

$$V^{\uparrow\uparrow}_{eff}(\mathbf{r}) = V_{eff}(\mathbf{r}) + B_{eff}(\mathbf{r}), \tag{3.129}$$

$$V^{\downarrow\downarrow}_{eff}(\mathbf{r}) = V_{eff}(\mathbf{r}) - B_{eff}(\mathbf{r}). \tag{3.130}$$

Equation (3.127) can be block diagonalised

$$\begin{pmatrix} \hat{H}^{\sigma\sigma}(\mathbf{r}) & \Delta^{\sigma\sigma^*}_{eff}(\mathbf{r}) \\ \Delta^{\sigma^*\sigma}_{eff}(\mathbf{r})^* & -\hat{H}^{\sigma^*\sigma^*}(\mathbf{r})^* \end{pmatrix} \begin{pmatrix} u^{\sigma}_n(\mathbf{r}) \\ v^{\sigma^*}_n(\mathbf{r}) \end{pmatrix} = \epsilon^{\sigma}_n \begin{pmatrix} u^{\sigma}_n(\mathbf{r}) \\ v^{\sigma^*}_n(\mathbf{r}) \end{pmatrix}, \tag{3.131}$$

where σ^* represents the opposing spin to σ. Therefore the corresponding quantities within the KKR formalism can equally be written in block diagonal form e.g.,

$$\mathbf{G}^{nn'}_{\sigma}(z,\mathbf{r},\mathbf{r}') = \begin{pmatrix} G^{ee,nn'}_{\sigma\sigma}(z,\mathbf{r},\mathbf{r}') & G^{eh,nn'}_{\sigma\sigma^*}(z,\mathbf{r},\mathbf{r}') \\ G^{he,nn'}_{\sigma^*\sigma}(z,\mathbf{r},\mathbf{r}') & G^{hh,nn'}_{\sigma^*\sigma^*}(z,\mathbf{r},\mathbf{r}') \end{pmatrix}, \tag{3.132}$$

and the equations can be solved using the exact same procedures as described in the previous sections.

3.5.11 Impurities

In order to consider the impurity systems we solve the Dyson equation,

$$\hat{G}^{imp}_{BdG}(z) = \hat{G}_{BdG}(z) + \hat{G}_{BdG}(z)\begin{pmatrix} \delta\hat{V} & \delta\hat{\Delta} \\ \delta\hat{\Delta}^* & -\delta\hat{V}^* \end{pmatrix}\hat{G}^{imp}_{BdG}(z), \tag{3.133}$$

where

$$\delta\hat{V} = \hat{V}_{imp} - \hat{V}, \tag{3.134}$$

$$\delta\hat{\Delta} = \hat{\Delta}_{imp} - \hat{\Delta}, \tag{3.135}$$

in real space. $\hat{V}_{imp}$ and $\hat{\Delta}_{imp}$ are the impurity potentials, $\hat{G}_{BdG}(z)$ is the Green's function of the unperturbed superconducting crystal and $\hat{G}^{imp}_{BdG}(z)$ is the impurity Green's function. Projecting this expression into the position basis, we have

$$\begin{pmatrix} G^{ee,nn'}_{\text{imp},lml'm'}(z,\mathbf{r},\mathbf{r}') & G^{eh,nn'}_{\text{imp},lml'm'}(z,\mathbf{r},\mathbf{r}') \\ G^{he,nn'}_{\text{imp},lml'm'}(z,\mathbf{r},\mathbf{r}') & G^{hh,nn'}_{\text{imp},lml'm'}(z,\mathbf{r},\mathbf{r}') \end{pmatrix} = \begin{pmatrix} G^{ee,nn'}_{lml'm'}(z,\mathbf{r},\mathbf{r}') & G^{eh,nn'}_{lml'm'}(z,\mathbf{r},\mathbf{r}') \\ G^{he,nn'}_{lml'm'}(z,\mathbf{r},\mathbf{r}') & G^{hh,nn'}_{lml'm'}(z,\mathbf{r},\mathbf{r}') \end{pmatrix} + \tag{3.136}$$

$$\sum_{l''m''n''} \begin{pmatrix} G^{ee,nn'}_{lml'm'}(z,\mathbf{r},\mathbf{r}') & G^{eh,nn'}_{lml'm'}(z,\mathbf{r},\mathbf{r}') \\ G^{he,nn'}_{lml'm'}(z,\mathbf{r},\mathbf{r}') & G^{hh,nn'}_{lml'm'}(z,\mathbf{r},\mathbf{r}') \end{pmatrix} \begin{pmatrix} \Delta t^{ee,n''}_{l}(z) & \Delta t^{eh,n''}_{l}(z) \\ \Delta t^{he,n''}_{l}(z) & \Delta t^{hh,n''}_{l}(z) \end{pmatrix} \begin{pmatrix} G^{ee,n''n'}_{l''m''l'm'}(z,\mathbf{r},\mathbf{r}') & G^{eh,n''n'}_{l''m''l'm'}(z,\mathbf{r},\mathbf{r}') \\ G^{he,n''n'}_{l''m''l'm'}(z,\mathbf{r},\mathbf{r}') & G^{hh,n''n'}_{l''m''l'm'}(z,\mathbf{r},\mathbf{r}') \end{pmatrix}^T,$$

where

$$\Delta t^{ab,n}_{l}(z) = t^{ab,n}_{\text{imp},l}(z) - t^{ab,n}_{l,r}(z). \tag{3.137}$$

To solve the impurity problem, a real-space cluster of $\hat{G}_{BdG}(z,\mathbf{r},\mathbf{r}')$ can be created from the bulk solution, with the boundary condition being defined through the Green's function of the pure superconducting crystal. An impurity will be embedded within the cluster and equation (3.136) is solved self-consistently within the DFT framework described above with both the charge and anomalous densities relaxed within the finite impurity cluster.

To perform a full superconducting impurity calculation, the procedure goes as follows,

1. Bulk self-consistency (as outlined in Fig. 3.2).

2. Once converged, check gap in the DOS matches the experimental resolution. If not, change Λ and go to step 1. More detail on this step is provided in section 4.1 of chapter 4.

3. Impurity self-consistency.

    a) Write the structural Green's function of the periodic system in a real space cluster corresponding to the impurity cluster.

    b) Calculation of the radial wave functions and t-matrices of the perturbed cluster using section 3.5.3.

c) Calculation of the perturbed Green's function via equation (3.136).

d) Calculation of new potentials using equations (3.23) and (3.24).

e) Check for convergence ($\rho(\mathbf{r})$, $\chi(\mathbf{r})$, $m(\mathbf{r})$), noting that μ is fixed for impurity calculations. If unconverged mix old and new potentials and go to step 3b.

3.6 Spin Polarised Relativistic KKR Method for Superconductors

In section 3.5.10 the scalar relativistic BdG equations are generalised to involve spin, showing that adding magnetism does not fundamentally change the structure of the equations. Here, in addition to magnetism, we add spin-orbit coupling by solving the Dirac equation. This will couple both spins in the normal state introducing terms like $\hat{H}^{\uparrow\downarrow}(\mathbf{r})$ in the Hamiltonian, ultimately leading the the Dirac-Bogoliubov-de Gennes (DBdG) equations. Useful references include G.Csire and collaborators [62] who have implemented it for the layered 2 dimensional KKR formalism, along with K. Capelle and E.K.U. Gross [216, 217] and J. Zabloudil *et al*. [213]. The work here extends the implementation of the DBdG equations into the 3 dimensional KKR formalism. All expressions are in Rydberg atomic units.

3.6.1 The Dirac-Bogoliubov-de Gennes Equations

The relativistic generalisation of the Hamiltonian leads to

$$H_{DBdG}(\mathbf{r}) = \begin{pmatrix} H_D(\mathbf{r}) & \Delta_{eff}(\mathbf{r})\boldsymbol{\eta} \\ \Delta^*_{eff}(\mathbf{r})\boldsymbol{\eta}^T & -H^*_D(\mathbf{r}) \end{pmatrix}, \tag{3.138}$$

where

$$H_D = c\hat{\boldsymbol{\alpha}}.\hat{\mathbf{p}} + \left(\hat{\boldsymbol{\beta}} - \hat{I}_4\right)c^2/2 + \left(V_{eff}(\mathbf{r}) - \epsilon_F\right)\hat{I}_4 + \hat{\boldsymbol{\Sigma}}B_{eff}(\mathbf{r}), \tag{3.139}$$

$$\hat{\boldsymbol{\alpha}} = \begin{pmatrix} 0 & \boldsymbol{\sigma} \\ \boldsymbol{\sigma} & 0 \end{pmatrix}, \quad \hat{\boldsymbol{\beta}} = \begin{pmatrix} \hat{I}_2 & 0 \\ 0 & -\hat{I}_2 \end{pmatrix}, \quad \hat{\boldsymbol{\Sigma}} = \begin{pmatrix} \boldsymbol{\sigma} & 0 \\ 0 & \boldsymbol{\sigma} \end{pmatrix}, \quad \hat{I}_4 = \begin{pmatrix} \hat{I}_2 & 0 \\ 0 & \hat{I}_2 \end{pmatrix}, \tag{3.140}$$

and, in this instance, $B_{eff}(\mathbf{r}) = (0,0,1)$, $\boldsymbol{\sigma}$ denote the vector of Pauli matrices and $\boldsymbol{\eta}$ is,

$$\boldsymbol{\eta} = \begin{pmatrix} 0 & 1 & 0 & 0 \\ -1 & 0 & 0 & 0 \\ 0 & 0 & 0 & 1 \\ 0 & 0 & -1 & 0 \end{pmatrix} = \begin{pmatrix} i\sigma_y & 0 \\ 0 & i\sigma_y \end{pmatrix} = i\boldsymbol{\Sigma}_y. \tag{3.141}$$

Thus the DBdG equation is

$$\begin{pmatrix} H_D(\mathbf{r}) & \Delta_{eff}(\mathbf{r})\boldsymbol{\eta} \\ \Delta^*_{eff}(\mathbf{r})\boldsymbol{\eta}^T & -H^*_D(\mathbf{r}) \end{pmatrix} \begin{pmatrix} \mathbf{u}_n(\mathbf{r}) \\ \mathbf{v}_n(\mathbf{r}) \end{pmatrix} = \epsilon_n \begin{pmatrix} \mathbf{u}_n(\mathbf{r}) \\ \mathbf{v}_n(\mathbf{r}) \end{pmatrix}, \tag{3.142}$$

where

$$\mathbf{u}_n(\mathbf{r}) = \begin{pmatrix} u_{1n}(\mathbf{r}) \\ u_{2n}(\mathbf{r}) \\ u_{3n}(\mathbf{r}) \\ u_{4n}(\mathbf{r}) \end{pmatrix} \quad \mathbf{v}_n(\mathbf{r}) = \begin{pmatrix} v_{1n}(\mathbf{r}) \\ v_{2n}(\mathbf{r}) \\ v_{3n}(\mathbf{r}) \\ v_{4n}(\mathbf{r}) \end{pmatrix}. \tag{3.143}$$

At this stage it is evident that the spin polarised BdG Hamiltonian (3.127) is a 4 by 4 matrix and the DBdG Hamiltonian (3.138) is an 8 by 8 matrix. This is because the inclusion of relativistic effects naturally leads to the coupling between electron and positron components, in addition to the coupled electron and hole components from the superconducting state. Despite that the systems considered are electron like, the electronic wavefunctions obtain positron components, named the 'small' part. These couplings in turn generate observable effects such as spin-orbit coupling, which manifests itself as a coupling between spin-up and spin-down electronic states.

3.6.2 The Green's Function

The Green's function for this system is defined as

$$\left(z\hat{I}_8 - H_{DBdG}(\mathbf{r})\right) G(z, \mathbf{R}^n + \mathbf{r}, \mathbf{R}^{n'} + \mathbf{r}') = \delta_{nn'}\delta(\mathbf{r} - \mathbf{r}'). \tag{3.144}$$

Using the same steps described in section (3.5.1), the equation becomes

$$\begin{pmatrix} G^{ee,nn'}(z,\mathbf{r},\mathbf{r}') & G^{eh,nn'}(z,\mathbf{r},\mathbf{r}') \\ G^{he,nn'}(z,\mathbf{r},\mathbf{r}') & G^{hh,nn'}(z,\mathbf{r},\mathbf{r}') \end{pmatrix} = \delta_{nn'} \sum_{Q} \begin{pmatrix} G_Q^{ee,n}(z,\mathbf{r},\mathbf{r}') & G_Q^{eh,n}(z,\mathbf{r},\mathbf{r}') \\ G_Q^{he,n}(z,\mathbf{r},\mathbf{r}') & G_Q^{hh,n}(z,\mathbf{r},\mathbf{r}') \end{pmatrix} + \sum_{QQ'} \begin{pmatrix} R_Q^{ee}(z,\mathbf{r}) & R_Q^{eh}(z,\mathbf{r}) \\ R_Q^{he}(z,\mathbf{r}) & R_Q^{hh}(z,\mathbf{r}) \end{pmatrix} \begin{pmatrix} G_{QQ'}^{ee,nn'}(z) & G_{QQ'}^{eh,nn'}(z) \\ G_{QQ'}^{he,nn'}(z) & G_{QQ'}^{hh,nn'}(z)) \end{pmatrix} \begin{pmatrix} R_{Q'}^{ee}(z,\mathbf{r}') & R_{Q'}^{eh}(z,\mathbf{r}') \\ R_{Q'}^{he}(z,\mathbf{r}') & R_{Q'}^{hh}(z,\mathbf{r}') \end{pmatrix}^{\times}, \tag{3.145}$$

where $Q = \{\kappa, \mu\}$ and $\bar{Q} = \{-\kappa, \mu\}$ is the superindex for the $\kappa\mu$ basis set, and $\chi_{Q'}(\hat{\mathbf{r}})$ are the spin spherical harmonics. Expanding the wavefunctions into this basis set yields

$$\mathbf{R}_Q(z,\mathbf{r}) = \begin{pmatrix} R_Q^{ee}(z,\mathbf{r}) & R_Q^{eh}(z,\mathbf{r}) \\ R_Q^{he}(z,\mathbf{r}) & R_Q^{hh}(z,\mathbf{r}) \end{pmatrix} = \sum_{Q'} \begin{pmatrix} g_{QQ'}^{ee,R}(z,r)\chi_{Q'}(\hat{\mathbf{r}}) & g_{QQ'}^{eh,R}(z,r)\chi_{Q'}(\hat{\mathbf{r}}) \\ if_{QQ'}^{ee,R}(z,r)\chi_{\bar{Q}'}(\hat{\mathbf{r}}) & if_{QQ'}^{eh,R}(z,r)\chi_{\bar{Q}'}(\hat{\mathbf{r}}) \\ g_{QQ'}^{he,R}(z,r)\chi_{Q'}^{*}(\hat{\mathbf{r}}) & g_{QQ'}^{hh,R}(z,r)\chi_{Q'}^{*}(\hat{\mathbf{r}}) \\ if_{QQ'}^{he,R}(z,r)\chi_{\bar{Q}'}^{*}(\hat{\mathbf{r}}) & if_{QQ'}^{hh,R}(z,r)\chi_{\bar{Q}'}^{*}(\hat{\mathbf{r}}) \end{pmatrix}, \tag{3.146}$$

$$\mathbf{R}_Q^{\times}(z,\mathbf{r}) = \begin{pmatrix} R_{Q'}^{ee}(z,\mathbf{r}) & R_{Q'}^{eh}(z,\mathbf{r}) \\ R_{Q'}^{he}(z,\mathbf{r}) & R_{Q'}^{hh}(z,\mathbf{r}) \end{pmatrix}^{\times} = \sum_{Q'} \begin{pmatrix} g_{QQ'}^{ee,R}(z,r)\chi_{Q'}^{\dagger}(\hat{\mathbf{r}}) & g_{QQ'}^{eh,R}(z,r)\chi_{Q'}^{\dagger}(\hat{\mathbf{r}}) \\ -if_{QQ'}^{ee,R}(z,r)\chi_{\bar{Q}'}^{\dagger}(\hat{\mathbf{r}}) & -if_{QQ'}^{eh,R}(z,r)\chi_{\bar{Q}'}^{\dagger}(\hat{\mathbf{r}}) \\ g_{QQ'}^{he,R}(z,r)\chi_{Q'}^{T}(\hat{\mathbf{r}}) & g_{QQ'}^{hh,R}(z,r)\chi_{Q'}^{T}(\hat{\mathbf{r}}) \\ -if_{QQ'}^{he,R}(z,r)\chi_{\bar{Q}'}^{T}(\hat{\mathbf{r}}) & -if_{QQ'}^{hh,R}(z,r)\chi_{\bar{Q}'}^{T}(\hat{\mathbf{r}}) \end{pmatrix}^{T}. \tag{3.147}$$

Here, $g^{ab,X}_{QQ'}(z,r)$ and $f^{ab,X}_{QQ'}(z,r)$ are the radial functions in the fully relativistic formalism. The spin spherical harmonics, $\chi_Q(\hat{\mathbf{r}})$, are the eigenfunctions of the square of the total angular momentum $\mathbf{J}^2$, its z component J_z, and the spin-orbit operator $\hat{K} = \boldsymbol{\sigma}\cdot\mathbf{L} + \hat{I}$,

$$\mathbf{J}^2\chi_Q(\hat{\mathbf{r}}) = j(j+1)\chi_Q(\hat{\mathbf{r}}), \tag{3.148}$$

$$J_z\chi_Q(\hat{\mathbf{r}}) = \mu\chi_Q(\hat{\mathbf{r}}), \tag{3.149}$$

$$\hat{K}\chi_Q(\hat{\mathbf{r}}) = -\kappa\chi_Q(\hat{\mathbf{r}}). \tag{3.150}$$

The spin spherical harmonics can be defined in terms of complex spherical harmonics $Y_{lm}(\hat{\mathbf{r}})$

$$\chi_Q(\hat{\mathbf{r}}) = \chi_{\kappa\mu}(\hat{\mathbf{r}}) = \sum_{s=\pm 1/2} C(l,\kappa,1/2|\mu-s,s)Y_{l,\mu-s}(\hat{\mathbf{r}})\phi_s, \tag{3.151}$$

where

$$\phi_{1/2} = \begin{pmatrix}1\\0\end{pmatrix}, \qquad \phi_{-1/2} = \begin{pmatrix}0\\1\end{pmatrix} \tag{3.152}$$

and $C(l,\kappa,1/2|\mu-s,s)$ are the Clebsh-Gordon coefficients. The relationship between these new quantum numbers $\{j,\kappa,\mu\}$ and the old $\{l,m,s\}$ is

$$\kappa = \begin{cases} l & , \quad j = l-1/2 \\ -l-1 & , \quad j = l+1/2 \end{cases} ; j = l \pm \frac{1}{2}, \tag{3.153}$$

$$\mu \in \{-j, -j+1, ..., j-1, j\} \tag{3.154}$$

$$\mu = m + s. \tag{3.155}$$

To describe the hole part, a convenient expansion is chosen transforming from $\chi_Q(\hat{\mathbf{r}}) \rightarrow \chi^*_Q(\hat{\mathbf{r}})$ [62]. The expansion coefficients are,

$$-i\sigma_y\chi^*_{\kappa\mu}(\hat{\mathbf{r}}) = (-1)^{\mu+1/2}S_\kappa\chi_{\kappa-\mu}(\hat{\mathbf{r}}), \tag{3.156}$$

$$i\chi^T_{\kappa\mu}(\hat{\mathbf{r}})\sigma_y = (-1)^{\mu+1/2}S_\kappa\chi^\dagger_{\kappa-\mu}(\hat{\mathbf{r}}). \tag{3.157}$$

where $S_\kappa = \kappa/|\kappa|$ the sign of κ.

3.6.3 The Structure Constants

The free electron structure constants from the scalar relativistic formalism (3.93) can be extended to the fully relativistic formalism. This is done in detail for the electron part in Ref. [213], with the main expression

$$G^{e,nn',D}_{0,QQ'}(z) = \frac{\epsilon_F + z + c^2}{c^2}\sum_s C(l,\kappa,1/2|\mu-s,s)G^{e,nn',S}_{0,l(\mu-s)l'(\mu'-s')}(z)C(l',\kappa',1/2|\mu'-s,s), \tag{3.158}$$

where D represents Dirac and S represents Schrödinger. The hole part, written in the $|\kappa\mu\rangle$ basis set is therefore

$$G^{h,nn',D}_{0,QQ'}(z) = \frac{\epsilon_F - z + c^2}{c^2} \sum_s C(l,\kappa,1/2|\mu-s,s) G^{h,nn',S}_{0,l(\mu-s)l'(\mu'-s')}(z) C(l',\kappa',1/2|\mu'-s,s). \tag{3.159}$$

The hole part is, however, expanded into $\chi^*_Q(\hat{\mathbf{r}})$ and $\chi^T_Q(\hat{\mathbf{r}})$ spin spherical harmonics and so a further transformation is applied to obtain the structure constants for the hole part. Writing the two-centre expansion of the free hole Dirac Green's function expanded with $\chi_Q(\hat{\mathbf{r}})$ and $\chi^*_Q(\hat{\mathbf{r}})$ respectively,

$$G^{h,D}_0(z,\mathbf{R}^n+\mathbf{r},\mathbf{R}^{n'}+\mathbf{r}) = \sum_{QQ'} j_l(p^h r)\chi_Q(\hat{\mathbf{r}}) G^{h,nn',D}_{0,QQ'}(z) j_l(p^h r')\chi^\dagger_{Q'}(\hat{\mathbf{r}}') \tag{3.160}$$

$$= \sum_{QQ'} j_l(p^h r)\chi^*_Q(\hat{\mathbf{r}}) G^{h,nn',D^*}_{0,QQ'}(z) j_l(p^h r')\chi^T_{Q'}(\hat{\mathbf{r}}'), \tag{3.161}$$

where D^* refers to the $\chi^*_Q(\hat{\mathbf{r}})$ structure constants. This problem can be solved by using the relationship between the $\{\kappa,\mu\}$ and $\{l,m,s\}$ basis set, namely that conjugation only affects the spherical harmonic

$$\chi^*_{\kappa\mu}(\hat{\mathbf{r}}) = \sum_{s=\pm 1/2} C(l,\kappa,1/2|\mu-s,s) Y^*_{l,\mu-s}(\hat{\mathbf{r}})\phi_s. \tag{3.162}$$

Using this we can transform the scalar relativistic structure constants $G^{h,nn',S}_{0,lml'm'}(z)$ from $Y_{lm}(\hat{\mathbf{r}}) \rightarrow Y^*_{lm}(\hat{\mathbf{r}})$ with the following the complex conjugation relationship,

$$Y^*_{lm}(\hat{\mathbf{r}}) = (-1)^m Y_{l-m}(\hat{\mathbf{r}}) \tag{3.163}$$

giving the expansion coefficients for this transformation

$$G^{h,nn',S^*}_{0,lml'm'}(z) = (-1)^{(m+m')} G^{h,nn',S}_{0,l-ml'-m'}(z). \tag{3.164}$$

From here, using Eqn. (3.159) but replacing $G^{h,nn',S}_{0,lml'm'}(z)$ for $G^{h,nn',S^*}_{0,lml'm'}(z)$ will directly obtain $G^{h,nn',D^*}_{0,QQ'}(z)$. The screened structure constants can then be constructed using the same procedure as before, discussed in sections 3.5.2 and 3.5.6.

3.6.4 Computing the T-Matrix

Similarly to section 3.5.3 we can calculate the elements of the t-matrix by projecting the Lippman-Schwinger equation into the scattering solutions of the single site Dirac-Bogoliubon scatterers

$$\mathbf{R}_Q(z,\mathbf{r}) = \mathbf{j}_Q(z,\mathbf{r}) - i\mathbf{p}\sum_{Q'} \mathbf{h}_{Q'}(z,\mathbf{r})\mathbf{t}^n_{Q'Q}(z) \tag{3.165}$$

where

$$\mathbf{h}_Q(z,\mathbf{r}) = \begin{pmatrix} h^e_Q(z,\mathbf{r}) & 0 \\ 0 & h^h_Q(z,\mathbf{r}) \end{pmatrix}, \quad \mathbf{j}_Q(z,\mathbf{r}) = \begin{pmatrix} j^e_Q(z,\mathbf{r}) & 0 \\ 0 & j^h_Q(z,\mathbf{r}) \end{pmatrix}, \tag{3.166}$$

$$
\begin{aligned}
h^e_Q(z,\mathbf{r}) &= \begin{pmatrix} h^+_l(p^e r)\chi_Q(\hat{\mathbf{r}}) \\ \frac{iS_\kappa p^e c}{\epsilon_F+z+c^2} h^+_l(p^e r)\chi_{\bar{Q}}(\hat{\mathbf{r}}) \end{pmatrix}, \quad j^e_Q(z,\mathbf{r}) = \begin{pmatrix} j_l(p^e r)\chi_Q(\hat{\mathbf{r}}) \\ \frac{iS_\kappa p^e c}{\epsilon_F+z+c^2} j(p^e r)\chi_{\bar{Q}}(\hat{\mathbf{r}}) \end{pmatrix}, \\
h^h_Q(z,\mathbf{r}) &= \begin{pmatrix} h^-_l(p^h r)\chi^*_Q(\hat{\mathbf{r}}) \\ \frac{iS_\kappa p^h c}{\epsilon_F-z+c^2} h^-_l(p^h r)\chi^*_{\bar{Q}}(\hat{\mathbf{r}}) \end{pmatrix}, \quad j^h_Q(z,\mathbf{r}) = \begin{pmatrix} j_l(p^h r)\chi^*_Q(\hat{\mathbf{r}}) \\ \frac{iS_\kappa p^h c}{\epsilon_F-z+c^2} j_l(p^h r)\chi^*_{\bar{Q}}(\hat{\mathbf{r}}) \end{pmatrix},
\end{aligned} \tag{3.167}
$$

and

$$
\mathbf{p} = \begin{pmatrix} p^e & 0 \\ 0 & p^h \end{pmatrix}, \tag{3.168}
$$

where

$$
p^e = \sqrt{\epsilon_F + z + \tfrac{(\epsilon_F+z)^2}{c^2}}, \quad p^h = \sqrt{\epsilon_F - z + \tfrac{(\epsilon_F-z)^2}{c^2}}. \tag{3.169}
$$

The total wavefunction can therefore be written in the same way as equation (3.82)

$$
\mathbf{R}_Q(z,\mathbf{r}) = \begin{cases} \sum_{Q'} \tilde{\mathbf{R}}_{Q'}(z,\mathbf{r})\boldsymbol{\alpha}^n_{Q'Q}(z); & r < r^{ASA}_n \\ \\ \mathbf{j}_Q(z,\mathbf{r}) - i\mathbf{p}\sum_{Q'} \mathbf{h}_{Q'}(z,\mathbf{r})\mathbf{t}^n_{Q'Q}(z); & r > r^{ASA}_n \end{cases}, \tag{3.170}
$$

with the main difference that the t-matrix is no longer diagonal in Q for the fully relativistic case as it was in l. In order to calculate the t-matrix, the differential is no longer required as there are already enough equations with the large and small parts of the wavefunction. With a co-linear DBdG equation the only existing couplings are between,

$$
Q = \{\kappa,\mu\}, \quad \bar{Q} = \{-\kappa,\mu\}, \quad \widetilde{Q} = \{\kappa,-\mu\}, \quad Q^* = \{-\kappa,-\mu\}. \tag{3.171}
$$

Using this, one can eliminate the angular functions and derive a matching condition with 8 coupled equations, solving for the t-matrix and $\boldsymbol{\alpha}_{QQ}(z)$. The irregular solutions can equally be constructed using the same procedure as defined in section 3.5.4. To obtain the regular $\tilde{\mathbf{R}}_Q(z,\mathbf{r})$ solutions, the DBdG is solved numerically, detail of which is given in appendix B.

3.6.5 The Single-Site Term

By performing the single-site expansion of the Green's function, one can obtain the expression,

$$
\begin{pmatrix} G^{ee,n}_Q(z,\mathbf{r},\mathbf{r}') & G^{eh,n}_Q(z,\mathbf{r},\mathbf{r}') \\ G^{he,n}_Q(z,\mathbf{r},\mathbf{r}') & G^{hh,n}_Q(z,\mathbf{r},\mathbf{r}') \end{pmatrix} = \begin{pmatrix} H^{ee}_Q(z,\mathbf{r}) & H^{eh}_Q(z,\mathbf{r}) \\ H^{he}_Q(z,\mathbf{r}) & H^{hh}_Q(z,\mathbf{r}) \end{pmatrix} \begin{pmatrix} R^{ee}_Q(z,\mathbf{r}') & R^{eh}_Q(z,\mathbf{r}') \\ R^{he}_Q(z,\mathbf{r}') & R^{hh}_Q(z,\mathbf{r}') \end{pmatrix}^\times \tag{3.172}
$$

where,

$$
\mathbf{H}_Q(z,\mathbf{r}) = \begin{pmatrix} H^{ee}_Q(z,\mathbf{r}) & H^{eh}_Q(z,\mathbf{r}) \\ H^{he}_Q(z,\mathbf{r}) & H^{hh}_Q(z,\mathbf{r}) \end{pmatrix} = \sum_{Q'} \begin{pmatrix} g^{ee,H}_{QQ'}(z,r)\chi_{Q'}(\hat{\mathbf{r}}) & g^{eh,H}_{QQ'}(z,r)\chi_{Q'}(\hat{\mathbf{r}}) \\ if^{ee,H}_{QQ'}(z,r)\chi_{\bar{Q}'}(\hat{\mathbf{r}}) & if^{eh,H}_{QQ'}(z,r)\chi_{\bar{Q}'}(\hat{\mathbf{r}}) \\ g^{he,H}_{QQ'}(z,r)\chi^*_{Q'}(\hat{\mathbf{r}}) & g^{hh,H}_{QQ'}(z,r)\chi^*_{Q'}(\hat{\mathbf{r}}) \\ if^{he,H}_{QQ'}(z,r)\chi^*_{\bar{Q}'}(\hat{\mathbf{r}}) & if^{hh,H}_{QQ'}(z,r)\chi^*_{\bar{Q}'}(\hat{\mathbf{r}}) \end{pmatrix}, \tag{3.173}
$$

are the irregular solutions. They are defined as,

$$\mathbf{H}_Q(z,\mathbf{r}) = \begin{cases} \tilde{\mathbf{H}}_Q(z,\mathbf{r}); & |\mathbf{r}| < r_n^{ASA}, \\ \\ -i\mathbf{ph}_Q(z,\mathbf{r}); & |\mathbf{r}| > r_n^{ASA}. \end{cases} \tag{3.174}$$

Hence, at the ASA boundary,

$$\tilde{\mathbf{H}}_Q(z,\mathbf{r}^{ASA}) = -i\mathbf{ph}_l(z,\mathbf{r}^{ASA}). \tag{3.175}$$

The irregular solutions inside the muffin tin, $\tilde{\mathbf{H}}_Q(z,\mathbf{r})$, are solved numerically just like the regular solutions $\tilde{\mathbf{R}}_Q(z,\mathbf{r})$. Equation (3.175) can be used to define the starting values for $\tilde{\mathbf{H}}_Q(z,r)$.

3.6.6 Charge Density

The definition of the charge density $\rho(\mathbf{r})$ in the fully relativistic case is

$$\rho(\mathbf{r}) = -\frac{1}{\pi}\int_{-\infty}^{\infty} d\epsilon f(\epsilon)\mathrm{ImTr}_Q G^{ee}(\epsilon,\mathbf{r},\mathbf{r}') - \frac{1}{\pi}\int_{-\infty}^{\infty} d\epsilon(1-f(\epsilon))\mathrm{ImTr}_Q G^{hh}(\epsilon,\mathbf{r},\mathbf{r}'), \tag{3.176}$$

where

$$G^{ee,nn'}(z,\mathbf{r},\mathbf{r}') = \sum_{Q''\bar{Q}'''} \begin{pmatrix} G^{11,ee,nn'}_{Q''Q'''}(z,r,r')\chi_{Q''}(\hat{\mathbf{r}})\chi^{\dagger}_{Q'''}(\hat{\mathbf{r}}') & G^{12,ee,nn'}_{Q''Q'''}(z,r,r')\chi_{Q''}(\hat{\mathbf{r}})\chi^{\dagger}_{\bar{Q}'''}(\hat{\mathbf{r}}') \\ G^{21,ee,nn'}_{Q''Q'''}(z,r,r')\chi_{\bar{Q}''}(\hat{\mathbf{r}})\chi^{\dagger}_{Q'''}(\hat{\mathbf{r}}') & G^{22,ee,nn'}_{Q''Q'''}(z,r,r')\chi_{\bar{Q}''}(\hat{\mathbf{r}})\chi^{\dagger}_{\bar{Q}'''}(\hat{\mathbf{r}}') \end{pmatrix}, \tag{3.177}$$

$$G^{eh,nn'}(z,\mathbf{r},\mathbf{r}') = \sum_{Q''\bar{Q}'''} \begin{pmatrix} G^{11,eh,nn'}_{Q''Q'''}(z,r,r')\chi_{Q''}(\hat{\mathbf{r}})\chi^{T}_{Q'''}(\hat{\mathbf{r}}') & G^{21,eh,nn'}_{Q''Q'''}(z,r,r')\chi_{\bar{Q}''}(\hat{\mathbf{r}})\chi^{T}_{Q'''}(\hat{\mathbf{r}}') \\ G^{21,eh,nn'}_{Q''Q'''}(z,r,r')\chi_{\bar{Q}''}(\hat{\mathbf{r}})\chi^{T}_{Q'''}(\hat{\mathbf{r}}') & G^{22,eh,nn'}_{Q''Q'''}(z,r,r')\chi_{\bar{Q}''}(\hat{\mathbf{r}})\chi^{T}_{\bar{Q}'''}(\hat{\mathbf{r}}') \end{pmatrix}, \tag{3.178}$$

$$G^{he,nn'}(z,\mathbf{r},\mathbf{r}') = \sum_{Q''\bar{Q}'''} \begin{pmatrix} G^{11,he,nn'}_{Q''Q'''}(z,r,r')\chi^{*}_{Q''}(\hat{\mathbf{r}})\chi^{\dagger}_{Q'''}(\hat{\mathbf{r}}') & G^{12,he,nn'}_{Q''Q'''}(z,r,r')\chi^{*}_{Q''}(\hat{\mathbf{r}})\chi^{\dagger}_{\bar{Q}'''}(\hat{\mathbf{r}}') \\ G^{21,he,nn'}_{Q''Q'''}(z,r,r')\chi^{*}_{\bar{Q}''}(\hat{\mathbf{r}})\chi^{\dagger}_{Q'''}(\hat{\mathbf{r}}') & G^{22,he,nn'}_{Q''Q'''}(z,r,r')\chi^{*}_{\bar{Q}''}(\hat{\mathbf{r}})\chi^{\dagger}_{\bar{Q}'''}(\hat{\mathbf{r}}') \end{pmatrix}, \tag{3.179}$$

$$G^{hh,nn'}(z,\mathbf{r},\mathbf{r}') = \sum_{Q''\bar{Q}'''} \begin{pmatrix} G^{11,hh,nn'}_{Q''Q'''}(z,r,r')\chi^{*}_{Q''}(\hat{\mathbf{r}})\chi^{T}_{Q'''}(\hat{\mathbf{r}}') & G^{12,hh,nn'}_{Q''Q'''}(z,r,r')\chi^{*}_{Q''}(\hat{\mathbf{r}})\chi^{T}_{\bar{Q}'''}(\hat{\mathbf{r}}') \\ G^{21,hh,nn'}_{Q''Q'''}(z,r,r')\chi^{*}_{\bar{Q}''}(\hat{\mathbf{r}})\chi^{T}_{Q'''}(\hat{\mathbf{r}}') & G^{22,hh,nn'}_{Q''Q'''}(z,r,r')\chi^{*}_{\bar{Q}''}(\hat{\mathbf{r}})\chi^{T}_{\bar{Q}'''}(\hat{\mathbf{r}}') \end{pmatrix}. \tag{3.180}$$

and

$$\begin{aligned}
G^{11,cd,nn'}_{Q''Q'''}(z,r,r') &= \sum_{QQ'ab}\left\{g^{ca,n,R}_{QQ''}(z,r)G^{ab,nn'}_{QQ'}(z)g^{db,n',R}_{Q'Q'''}(z,r') - \delta_{nn'}\delta_{QQ'}\delta_{ab}g^{ca,n,H}_{QQ''}(z,r)g^{db,n',R}_{Q'Q'''}(z,r')\right\}, \\
G^{12,cd,nn'}_{\bar{Q}''Q'''}(z,r,r') &= -i\sum_{QQ'ab}\left\{g^{ca,n,R}_{QQ''}(z,r)G^{ab,nn'}_{QQ'}(z)f^{db,n',R}_{Q'Q'''}(z,r') - \delta_{nn'}\delta_{QQ'}\delta_{ab}g^{ca,n,H}_{QQ''}(z,r)f^{db,n',R}_{Q'Q'''}(z,r')\right\}, \\
G^{21,cd,nn'}_{Q''\bar{Q}'''}(z,r,r') &= i\sum_{QQ'ab}\left\{f^{ca,n,R}_{QQ''}(z,r)G^{ab,nn'}_{QQ'}(z)g^{db,n',R}_{Q'Q'''}(z,r') - \delta_{nn'}\delta_{QQ'}\delta_{ab}f^{ca,n,H}_{QQ''}(z,r)g^{db,n',R}_{Q'Q'''}(z,r')\right\}, \\
G^{22,cd,nn'}_{\bar{Q}''\bar{Q}'''}(z,r,r') &= \sum_{QQ'ab}\left\{f^{ca,n,R}_{QQ''}(z,r)G^{ab,n,nn'}_{QQ'}(z)f^{db,n',R}_{Q'Q'''}(z,r') - \delta_{nn'}\delta_{QQ'}\delta_{ab}f^{ca,n,H}_{QQ''}(z,r)f^{db,n',R}_{Q'Q'''}(z,r')\right\}.
\end{aligned} \tag{3.181}$$

Using these definitions and Eqn. 3.176 the charge density can be rewritten as

$$\rho(\mathbf{r}) = -\frac{1}{\pi}\mathrm{Im}\sum_{QQ'}\left\{G^{11,ee}_{QQ'}(r)\chi^{\dagger}_{Q'}(\hat{\mathbf{r}})\chi_{Q}(\hat{\mathbf{r}}) + G^{22,ee}_{QQ'}(r)\chi^{\dagger}_{\bar{Q}'}(\hat{\mathbf{r}})\chi_{\bar{Q}}(\hat{\mathbf{r}})\right\} - \frac{1}{\pi}\mathrm{Im}\sum_{QQ'}\left\{G^{11,hh}_{QQ'}(r)\chi^{T}_{Q'}(\hat{\mathbf{r}})\chi^{*}_{Q}(\hat{\mathbf{r}}) + G^{22,hh}_{QQ'}(r)\chi^{T}_{\bar{Q}'}(\hat{\mathbf{r}})\chi^{*}_{\bar{Q}}(\hat{\mathbf{r}})\right\} \tag{3.182}$$

where,

$$G^{ij,ee}_{QQ'}(r) = \int d\epsilon f(\epsilon) G^{ij,ee}_{QQ'}(\epsilon,\mathbf{r},\mathbf{r}'), \tag{3.183}$$

$$G^{ij,hh}_{QQ'}(r) = \int d\epsilon (1-f(\epsilon)) G^{ij,hh}_{QQ'}(\epsilon,\mathbf{r},\mathbf{r}'). \tag{3.184}$$

Just like in the scalar relativistic case we need to obtain the L component of the density to construct the potential

$$\rho_L(r) = \int d\hat{\mathbf{r}}\rho(\mathbf{r})Y_L(\hat{\mathbf{r}}), \tag{3.185}$$

giving

$$\rho_L(r) = -\frac{1}{\pi}\mathrm{Im}\sum_{QQ'}\left\{G^{11,ee}_{QQ'}(r)\int d\hat{\mathbf{r}}\chi^{\dagger}_{Q'}(\hat{\mathbf{r}})Y_L(\hat{\mathbf{r}})\chi_{Q}(\hat{\mathbf{r}}) + G^{22,ee}_{QQ'}(r)\int d\hat{\mathbf{r}}\chi^{\dagger}_{\bar{Q}'}(\hat{\mathbf{r}})Y_L(\hat{\mathbf{r}})\chi_{\bar{Q}}(\hat{\mathbf{r}})\right\} - \frac{1}{\pi}\mathrm{Im}\sum_{QQ'}\left\{G^{11,hh}_{QQ'}(r)\int d\hat{\mathbf{r}}\chi^{T}_{Q'}(\hat{\mathbf{r}})Y_L(\hat{\mathbf{r}})\chi^{*}_{Q}(\hat{\mathbf{r}}) + G^{22,hh}_{QQ'}(r)\int d\hat{\mathbf{r}}\chi^{T}_{\bar{Q}'}(\hat{\mathbf{r}})Y_L(\hat{\mathbf{r}})\chi^{*}_{\bar{Q}}(\hat{\mathbf{r}})\right\}. \tag{3.186}$$

Using the definitions in equations (3.156) and (3.157), along with

$$\chi^{\dagger}_{Q'}(\hat{\mathbf{r}})\chi_{Q}(\hat{\mathbf{r}}) = \chi^{\dagger}_{\bar{Q}'}(\hat{\mathbf{r}})\chi_{\bar{Q}}(\hat{\mathbf{r}}), \tag{3.187}$$

we find

$$\rho_L(r) = -\frac{1}{\pi}\mathrm{Im}\sum_{QQ'}\left\{\left(G^{11,ee}_{QQ'}(r) + G^{22,ee}_{QQ'}(r)\right)\langle\chi_{Q'}|Y_L|\chi_{Q}\rangle + \left(G^{11,hh}_{QQ'}(r)S_{\kappa'}S_{\kappa} + G^{22,hh}_{QQ'}(r)S_{\bar{\kappa}'}S_{\bar{\kappa}}\right)(-1)^{\mu'+\mu+1}\langle\chi_{\kappa'-\mu'}|Y_L|\chi_{\kappa-\mu}\rangle\right\}, \tag{3.188}$$

where

$$\langle\chi_{\kappa'\mu'}|Y_L|\chi_{\kappa\mu}\rangle = \int d\hat{\mathbf{r}}\chi^{\dagger}_{\kappa'\mu'}(\hat{\mathbf{r}})Y_L(\hat{\mathbf{r}})\chi_{\kappa\mu}(\hat{\mathbf{r}}). \tag{3.189}$$

3.6.7 Anomalous Density

The definition for the anomalous density [62] is

$$\mathrm{Re}\chi(\mathbf{r}) = -\frac{1}{2\pi}\int_{-\infty}^{\infty} d\epsilon(1-2f(\epsilon))\mathrm{ImTr}_Q\eta G^{eh}(\epsilon,\mathbf{r},\mathbf{r}') - \frac{1}{2\pi}\int_{-\infty}^{\infty} d\epsilon(1-2f(\epsilon))\mathrm{ImTr}_Q\eta G^{he}(\epsilon,\mathbf{r},\mathbf{r}'), \tag{3.190}$$

$$\mathrm{Im}\chi(\mathbf{r}) = \frac{1}{2\pi}\int_{-\infty}^{\infty} d\epsilon(1-2f(\epsilon))\mathrm{ReTr}_Q\eta G^{eh}(\epsilon,\mathbf{r},\mathbf{r}') - \frac{1}{2\pi}\int_{-\infty}^{\infty} d\epsilon(1-2f(\epsilon))\mathrm{ReTr}_Q\eta G^{he}(\epsilon,\mathbf{r},\mathbf{r}'). \tag{3.191}$$

Looking at only the real part of $\chi(\mathbf{r})$, we use the definition of η from equation (3.141) to obtain,

$$\begin{aligned}\text{(3.192)}\quad \mathrm{Re}\chi(\mathbf{r}) = -\frac{1}{2\pi}\mathrm{Im}\sum_{QQ'}\Big\{G^{11,eh}_{QQ'}(r)\chi^T_{Q'}(\hat{\mathbf{r}})i\sigma_y\chi_Q(\hat{\mathbf{r}}) + G^{22,eh}_{QQ'}(r)\chi^T_{\bar{Q}'}(\hat{\mathbf{r}})i\sigma_y\chi_{\bar{Q}}(\hat{\mathbf{r}})\Big\} \\ -\frac{1}{2\pi}\mathrm{Im}\sum_{QQ'}\Big\{G^{11,he}_{QQ'}(r)\chi^\dagger_{Q'}(\hat{\mathbf{r}})i\sigma_y\chi^*_Q(\hat{\mathbf{r}}) + G^{22,he}_{QQ'}(r)\chi^\dagger_{\bar{Q}'}(\hat{\mathbf{r}})i\sigma_y\chi^*_{\bar{Q}}(\hat{\mathbf{r}})\Big\},\end{aligned}$$

where

$$\text{(3.193)}\qquad G^{ij,ab}_{QQ'}(r) = \int_{-\infty}^{\infty} d\epsilon(1-2f(\epsilon))G^{ij,ab}_{QQ'}(\epsilon,r),$$

and

$$\text{(3.194)}\qquad \mathrm{Tr}\Big\{\sigma_y\chi_Q(\hat{\mathbf{r}})\chi^T_{Q'}(\hat{\mathbf{r}})\Big\} = \chi^T_{Q'}(\hat{\mathbf{r}})\sigma_y\chi_Q(\hat{\mathbf{r}}).$$

As discussed for the scalar relativistic anomalous density in section 3.5.8 we require only the spherical part to the density

$$\text{(3.195)}\qquad \mathrm{Re}\chi_L(r) = \int d\hat{\mathbf{r}}\mathrm{Re}\chi(\mathbf{r})Y_L(\hat{\mathbf{r}}).$$

which results in

$$\begin{aligned}\text{(3.196)}\quad \mathrm{Re}\chi_L(r) = -\frac{1}{2\pi}\sum_{QQ'}\Big\{I^{11,eh}_{QQ'}(r)\int d\hat{\mathbf{r}}i\chi^T_{Q'}(\hat{\mathbf{r}})\sigma_y Y_L(\hat{\mathbf{r}})\chi_Q(\hat{\mathbf{r}}) + I^{22,eh}_{QQ'}(r)\int d\hat{\mathbf{r}}i\chi^T_{\bar{Q}'}(\hat{\mathbf{r}})\sigma_y Y_L(\hat{\mathbf{r}})\chi_{\bar{Q}}(\hat{\mathbf{r}}) + \\ I^{11,he}_{QQ'}(r)\int d\hat{\mathbf{r}}i\chi^\dagger_{Q'}(\hat{\mathbf{r}})\sigma_y Y_L(\hat{\mathbf{r}})\chi^*_Q(\hat{\mathbf{r}}) + I^{22,he}_{QQ'}(r)\int d\hat{\mathbf{r}}i\chi^\dagger_{\bar{Q}'}(\hat{\mathbf{r}})\sigma_y Y_L(\hat{\mathbf{r}})\chi^*_{\bar{Q}}(\hat{\mathbf{r}})\Big\},\end{aligned}$$

where,

$$\text{(3.197)}\qquad I^{11,eh}_{QQ'}(r) = \mathrm{Im}G^{11,eh}_{QQ'}(r).$$

Using the definitions in equations (3.156) and (3.157), along with (3.187) one can obtain an expression for the anomalous density

$$\begin{aligned}\text{(3.198)}\quad \mathrm{Re}\chi_L(r) = -\frac{1}{2\pi}\sum_{QQ'}\Big\{\Big(S_{\kappa'}I^{11,eh}_{QQ'}(r) + S_{\bar{\kappa}'}I^{22,eh}_{QQ'}(r)\Big)(-1)^{\mu'+1/2}\langle\chi_{\kappa'-\mu'}|Y_L|\chi_{\kappa\mu}\rangle - \\ \Big(S_{\kappa}I^{11,he}_{QQ'}(r) + S_{\bar{\kappa}}I^{22,he}_{QQ'}(r)\Big)(-1)^{\mu+1/2}\langle\chi_{\kappa'\mu'}|Y_L|\chi_{\kappa-\mu}\rangle\Big\},\end{aligned}$$

The imaginary part can equally be constructed using the same method, however, it is only necessary when considering the implementation of a non-colinear solver.

CHAPTER 4

BULK RESULTS

This chapter is dedicated to investigating the results of calculating the pure, periodic crystal. Firstly, in section 4.1, various numerical tests are performed to investigate the robustness of the theoretical framework detailed in chapter 3. This involves careful definition of the superconducting gap and how it can be related to experiments, along with determining the key numerical parameters that need to be tuned to create a fully converged, numerically stable description of the superconducting state within the DFT framework.

Once the requirements of numerical stability are met, we then model known s-wave superconductors Nb, Pb and MgB_2. In these materials multiple distinct peaks at the gap in the DOS are observed, showing significant gap anisotropy. This is briefly touched upon in section 4.1 as it will be used to define the superconducting state, however the main analysis of the anisotropy will be performed in section 4.2. This section will use techniques to map out the Fermi surface to understand the full k-dependence of the superconducting gap. From here, qualitative connections between the k-dependent Fermi velocities and the superconductivity will be performed, exploiting concepts from BCS theory. Investigations into the gap anisotropy similar to this has been done for Pb [6] and MgB_2 [5]. Experiments have also confirmed the anisotropy [2, 3]. These theoretical methods have focused on models with sophisticated electron-phonon coupling, whereas here we ask different question, namely 'what is the minimum model required to generate anisotropy'. From this we are able to argue that any elemental superconductor has the potential for gap anisotropy, and that the results from our calculations for Nb, Pb and MgB_2 are in good agreement with experiments.

4.1 Convergence Tests

Within this code, as with any DFT code, there are many numerical parameters that need to be understood and tuned. With these parameters, there is always a trade off between accuracy and computational expense. Within the KKR formalism the key parameters are the k-mesh, energy mesh, cluster size and l_{max}, the cutoff for the angular momentum basis set. Within the superconducting KKR code we also need to define how to model the superconductivity. This will all be addressed in this section. To start, we define more explicitly the quantities mentioned above. The k-mesh will have already been briefly touched upon within chapter 3, it is the number of k-points chosen within the Brillouin zone to calculate quantities such as $\rho(\mathbf{r})$ the DOS (3.54). The energy mesh deals with the energy integration of quantities such as the charge density (3.54). The cluster size refers to the number of atomic sites n in the screened reference system (equation (3.102)), which acts as a cut-off for long-range interactions, giving the screened KKR method strong similarities to other tight-binding methods [218]. For all systems we chose a minimum of 259 sites. Specifically for each material Nb has 259 sites, Pb had 459 sites and MgB_2 341 sites. For all calculations we took $l_{max} = 3$ as we are working within the ASA scheme. For full-potential a higher l_{max} is required as the potential is expanded into the interstitial region and becomes non-spherical and chapter 21 of Ref. [213] elaborates in more detail here. The remaining quantities, energy mesh, k-mesh and the choice of Λ will be the subject of the rest of this section.

First, we test the numerical parameters and the resulting gaps within our framework. We define the average gap [207]

$$\bar{\Delta}_r^{\mu} = \frac{1}{V_{WS}} \int_{WS} \Delta_{eff}^{\mu}(\mathbf{r}) d^3 r \,, \tag{4.1}$$

where V_{WS} represents the volume of the Wigner-Seitz cell. This is a practical expression, however, in a real band structure this average gap is not the same as the gap in the DOS. This will be addressed in more detail in this section.

The energy mesh refers to the number of energy points required to calculate the energy integrals (equations (3.110-3.111) and (3.115)) for the charge (3.109) and anomalous (3.117) densities. The integral range goes from the band bottom to the Fermi level, with an exponential weighting so that there are more points at the Fermi level so that superconducting energy gap can be resolved. More details can be found in pages 259-261 of Ref.[213]. In Fig. 4.1(a) the results of the convergence tests are summarised for non-relativistic (NR) Nb. For low interaction parameter Λ, all calculations with 30 energy points show a reduced or vanishing average gap indicating the failing to converge. This is natural since a small interaction parameter with subsequently small gap requires a high energy resolution in order to resolve the gap structure. For a large Λ, on the other hand, the energy convergence is reached earlier and the requirements on the number of k points become the relevant constraint. It was decided that 50 energy points and 2×10^5 k-points is the best trade off between accuracy and computational cost.

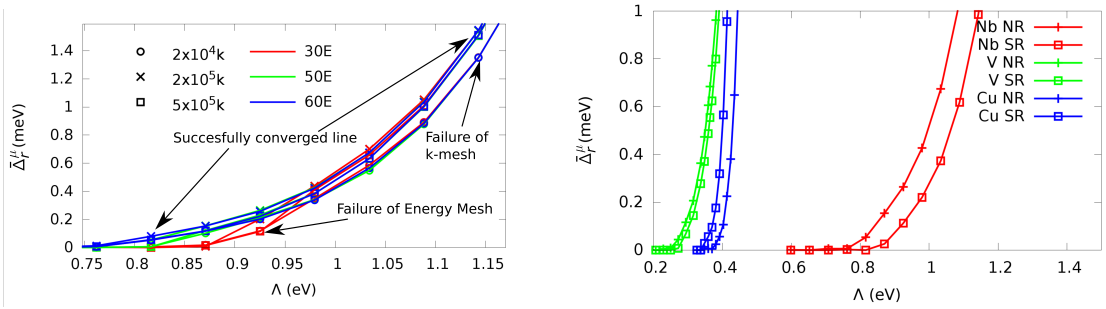

(a) (b)

Figure 4.1: (a) Convergence test for non-relativistic Nb, where the number of energy points and k-points for the calculation is changed to test the robustness of the superconducting state formed. The number of k-points refers to the energy point with the imaginary part closest to the real energy axis. Plot symbols denote 2×10^4 (circle), 2×10^5 (cross) and 5×10^5 (square) k-points, colours denote 30 (red), 50 (green) and 60 (blue) energy points. (b) Comparison of the average gap size of Nb, V and Cu for non relativistic and scalar relativistic calculations as a function of Λ.

A comparison between non relativistic (NR) and scalar relativistic (SR) results is shown in Fig. 4.1(b) for Nb, V and Cu. There is no clear trend in terms of the gap size going from NR to SR. For V and Nb the gap is reduced, for Cu it is increased. The influence becomes more dominant with larger atomic number as expected when including scalar relativistic corrections. For the remainder of this work, unless specified, we perform calculations using the SR BdG equations.

The next test is to assess how to choose Λ, the only free parameter within this framework for our theoretical model. The first attempt will be to try and calculate it from first principles and check if it produces an energy gap comparable to experimental values. This is essentially testing our choice of superconducting exchange-correlation functional. To do this, a well established quantity in the literature is required. In this instance, the electron phonon coupling parameter $\lambda_{eff} = \Lambda D(\epsilon_F)$ was chosen. This quantity is established in BCS theory as the previously defined equation (4.4). Within the KKR formalism it is possible to define this quantity in the Gaspari-Győrffy theory [219] using just the normal state

$$D(\epsilon_F)\Lambda_{GG} = \frac{2m\epsilon_F}{\hbar^2\pi^2}\frac{1}{D(\epsilon_F)}\sum_l \frac{2(l+1)\sin^2(\delta_{l+1}-\delta_l)D_l(\epsilon_F)D_{l+1}(\epsilon_F)}{D_l^{(1)}(\epsilon_F)D_{l+1}^{(1)}(\epsilon_F)}, \tag{4.2}$$

where $D(\epsilon_F)$ is the DOS in the normal state at the Fermi level and $D_l^{(1)}(\epsilon_F)$ is the l-dependent DOS of a free scatterer. Thus $\lambda_{GG} = \Lambda_{GG}D(\epsilon_F)$ is the electron-phonon coupling parameter for Gaspari-Győrffy theory. A similar quantity, $\lambda_{BdG} = \Lambda_{BdG}D(\epsilon_F)$ is the input to the self-consistency. In principle, if the method is successfully consistent within the KKR formalism it should be possible to calculate λ_{GG} and use it in the superconducting KKR, and this should enable the prediction of a superconductor. In Fig. 4.2, the results of this are shown.

The vertical dashed lines indicate the calculated λ_{GG}, and the dot dashed lines indicate experimentally determined λ values. For now, we shall focus on λ_{GG}. Investigating each material

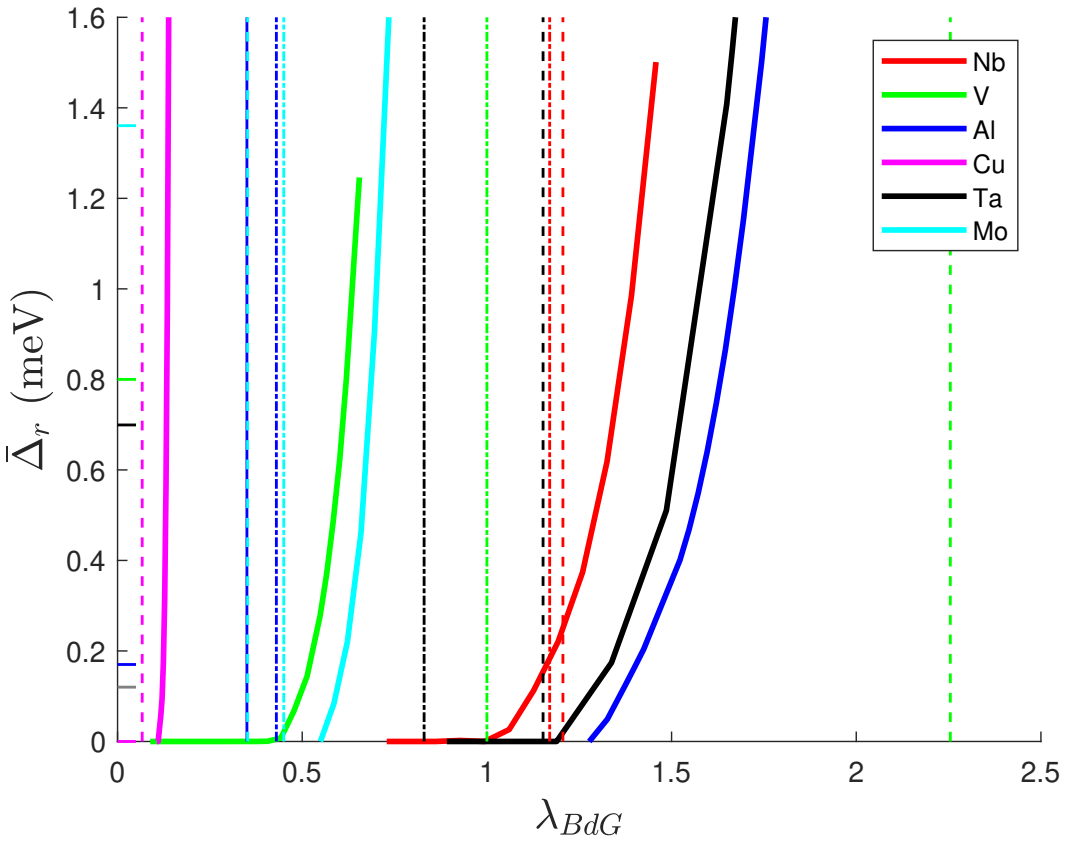

Figure 4.2: Values of $\bar{\Delta^{\mu}}_r$ as a function of λ_{BdG} from the BdG KKR code. Each point making up the lines represents a self-consistent calculation converged to an rms value 10^{-7} Ry for both $V_{eff}(r)$ and $\Delta_{eff}(r)$. For every given interaction parameter chosen for each material, the corresponding average gap is plotted on the y-axis. The dashed lines represent the value of the interaction calculated from Gaspari-Győrffy theory using equation (4.2). The vertical dot-dash lines represent λ values obtained from fits of specific heat data from experiments from Ref. [1], and the horizontal lines at left of the graph represent experimental gap sizes for each of the materials obtained from page 376 of Ref. [15]. The experimental gap of Nb from Ref.[4] is 1.79 meV and is therefore beyond the scale of this figure.

in turn we can make an assessment on how effective our model is at predicting superconductors. Firstly, it is able to predict that Cu is not superconducting as the λ_{GG} is calculated to be too low to induce a gap in Cu. An interesting additional factor is that the solid Cu line has the largest gradient, implying that small changes to Λ have the largest effect of all materials tested. The other materials for which reasonable λ_{GG} values are predicted are Nb, Ta and Mo as they fall in the correct order of magnitude. They are not perfect as Ta and Mo are still predicted to not have a superconducting gap, and for Nb the gap is significantly smaller than it should be from experimental data. Unfortunately, for V and Al the theory fails significantly as for both the value

Quantity	Description
$\Delta(\mathbf{k})$	The gap function produced from k-dependent gap models, such as Eliashberg theory [78]. More sophisticated methods develop the theory for first principles calculations [6].
$\Delta_{eff}(\mathbf{r})$	The gap function produced in this method. The main details are in chapter 3.
$\bar{\Delta}_{\mathbf{k}}$	The average gap produced from other theoretical models. $\bar{\Delta}_{\mathbf{k}} = \frac{1}{V_{BZ}} \int d\mathbf{k} \Delta(\mathbf{k})$
$\bar{\Delta}_{\mathbf{r}}$	The average gap produced from the integral of the gap function $\Delta_{eff}(\mathbf{r})$. $\bar{\Delta}_r = \frac{1}{V_{WS}} \int_{WS} \Delta_{eff}(\mathbf{r}) d^3r$
Δ^{exp}	Measurement of the physical energy gap in the excitation spectrum in experiments.
Δ^{DOS}	Reading off the physical energy gap in the DOS

Table 4.1: A table which collates the various definitions in this chapter used to describe the different quantities used in theoretical descriptions and experiments to describe the superconducting gap size. This table links to table 4.3.

for λ_{GG} is incorrect by an order of magnitude. The overall theory is therefore not good enough to predict the zero temperature gap size of a superconductor consistently. This comes down to a combination of things. Firstly, Gaspari-Győrffy theory is even defined in Ref.[219] as 'simple' of which corrections to the rigid sphere approximation since then have been suggested [220]. In addition, comparing the experimentally obtained Λ values (dot-dashed lines) in Fig. 4.2 to the Λ_{GG} (dashed lines) it is clear that there is a reasonable agreement between most materials, except for V where the comparison completely fails. A more sophisticated method of obtaining Λ is therefore available, as exemplified by Ref. [220]. Secondly, however, the simplification of the pairing kernel $\Lambda[\rho,\chi](\mathbf{r}_1,\mathbf{r}_1',\mathbf{r}_2,\mathbf{r}_2')$ to the interaction parameter Λ in equation (3.30) is drastic, and a more sophisticated theory which provides a better description is required for true first principles calculations of superconductivity, which has been done by Refs. [202, 203] for bulk systems. In this work we are, however, aiming to describe impurity scattering, and incorporating impurities or nanoscale structured materials into these *ab initio* methods would be possible in principle, but would become technically very challenging and computationally demanding. Even in bulk systems the full theory requires six-dimensional integrals both over the electron and phonon Brillouin zones, $\mathbf{k}$ and $\mathbf{Q}$. In systems without translational symmetry the corresponding real-space coupled electron-phonon equations would become significantly more difficult to solve. Due to this we must find another method to determine Λ.

The method chosen is to treat Λ as a tunable parameter, such that the resulting gap matches the experimental zero temperature gap size. The complication, especially for anisotropic gaps or multigap systems, is what definitions are used experimentally and theoretically to establish the gap size. In the following, the method with which the free parameter Λ is constrained in practice

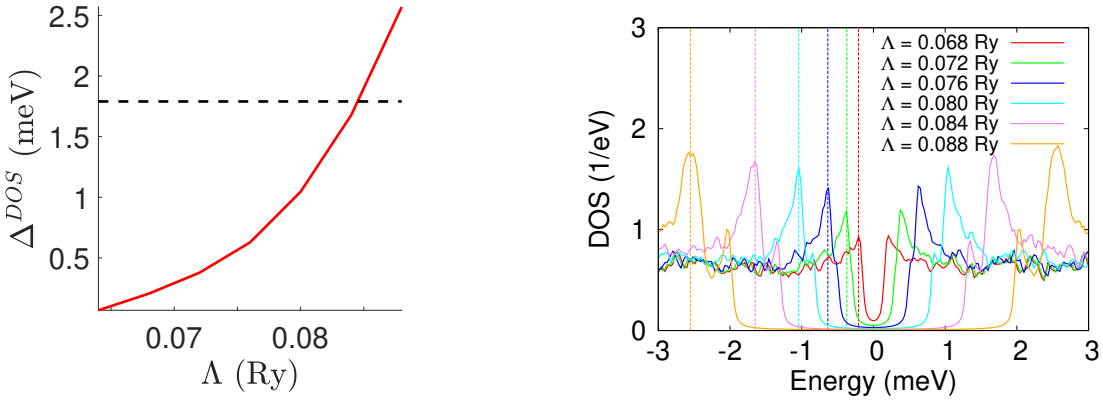

(a) (b)

Figure 4.3: a) The red line is the value of Δ^{DOS} of the outer coherence peak of Nb for the given interaction Λ on the x-axis. The black dashed line represents the value of Δ^{exp} from the (111) surface of Nb in Hahn *et al*. [4]. b) DOS for each interaction parameter Λ. The dashed line represents the value of Δ^{DOS} in (a) which has been read off from the graph.

is discussed. Table 4.1 defines all of the separate quantities used in each method to describe the superconducting gap. We choose Δ^{DOS} as the parameter. More details on how this is obtained is illustrated in Fig. 4.3. In order to match to the experiment the value for each calculation was taken and matched to the zero temperature gap size. Fig. 4.3(a) is an example set of calculations used in the process of finding the value of Λ that matches experimental data, where Fig. 4.3(b) displays how each point in (a) was obtained. The final result for Nb is presented in table 4.2.

The same calculations were also performed for Pb and MgB_2, and the results of each are shown in table 4.2. For both the level of anisotropy is comparable to the anisotropy present in the experimental data. The level of error present in our calculation is a combination of the errors present with the choice of exchange correlation functional along with the accuracy of the gap as a function of k-mesh and energy mesh, described in Fig. 4.1(a). We choose the LSDA functional, as described in section 3.3. There are well established errors within this functional, and for more details we refer to Refs. [221, 222]. In general the propagation of this error into the calculation of observables becomes about 10% [223]. More detail on the anisotropy will be discussed in section 4.2.

It is worth comparing the other quantities presented in table 4.1 because understanding how these quantities relate to each other will give important insight into the method and how each of the quantities are treated. Firstly, the average gap from equation (4.1) will be analysed. This quantity is just the integrated anomalous DOS $\chi(\mathbf{r})$ multiplied by a constant, and does not necessarily relate to the gap seen in the DOS. It can be easily proven comparing Δ^{DOS} and $\bar{\Delta}_{\mathbf{r}}$ for Nb in table 4.3. Clearly these numbers are different from each other. In fact, by comparing the values for $\bar{\Delta}_{\mathbf{r}}$ for Pb and Nb it is possible to see that Nb has a similar $\bar{\Delta}_{\mathbf{r}}$ than Pb. As Nb has

Element	$D(\epsilon_F)$ (Ry^{-1})	Λ (Ry)	Δ^{DOS} (meV)	Δ^{exp} (meV)
Nb	16.53	0.0861	1.79, 1.69, 1.43	(1.79, 1.64, 1.20)[4]
Pb	5.89	0.351	1.46, 1.39, 1.32	1.40, 1.27[2]
MgB_2	3.25	0.291	7.00, 4.77, 3.27	7.0, 3.0[3]

Table 4.2: $D(\epsilon_F)$ is the DOS at the Fermi level in the normal state obtained from our calculations. Λ is the interaction parameter used in this investigation to match our calculations to the experimental zero temperature gap. Δ^{exp} are average gaps from experiments [1–4], Δ^{DOS} are the values read off from the DOS.

a significantly larger T_c than Pb it is obvious that the real gap size must be larger as signified by $\bar{\Delta}_{\mathbf{k}}$. We believe that the fundamental reason for this discrepancy lies in the fact that the relationship between the effective pairing potential $\Delta_{eff}(\mathbf{r})$ and the k-dependent gap $\Delta(\mathbf{k})$ is not trivial. Similarly the average gap found in the literature, $\bar{\Delta}_{\mathbf{k}}$, shown in table 4.3 column 4 is conventionally obtained from a k-space integration of $\Delta(\mathbf{k})$. This quantity is distinct to the average $\bar{\Delta}_{\mathbf{r}}$ calculated from the real space integral over $\Delta_{eff}(\mathbf{r})$ (see Table 4.3, column 2). For Nb and Pb, $\bar{\Delta}_{\mathbf{r}}$ is smaller than $\bar{\Delta}_{\mathbf{k}}$ but for MgB_2 it is larger.

Finally, we would like to summarize the numerical parameters used throughout the thesis. After convergence of the potentials is reached, the imaginary part of the energy, $\delta = 2\mu$Ry, 0.2μRy, 10μRy is used for Nb, Pb and MgB_2 respectively. These are the parameters for the DOS and Bloch spectral function calculations when focusing on the gap structure as well as for $\Delta(\mathbf{k})$. The number of k-points in the irreducible Brillouin zone for DOS calculations are 1×10^7 for Nb and Pb and 2.7×10^6 for MgB_2.

Element	$\bar{\Delta}_{\mathbf{r}}$ (meV)	Δ^{DOS} (meV)	$\bar{\Delta}_{\mathbf{k}}$ (meV)
Nb	1.07	1.79, 1.69, 1.43	1.53[1]
Pb	1.04	1.46, 1.39, 1.32	1.35[1],(1.0, 0.8)[6]
MgB_2	8.03	7.00, 4.77, 3.27	(6.8, 2.45)[5]

Table 4.3: The average gap, $\bar{\Delta}_{\mathbf{r}}$, is calculated using (4.1). Δ^{DOS} are the values read off from the DOS, $\bar{\Delta}_{\mathbf{k}}$ are average gaps from theoretical $\Delta(\mathbf{k})$ integrations [1, 5, 6].

4.2 Gap Anisotropy

We now have successfully calculated the superconducting state for Nb, Pb and MgB_2 that is numerically stable. It was already briefly mentioned that gap anisotropy was observed in these materials, and table 4.2 defines the coherence peaks observed in each of the materials. Looking purely at the theoretical method used, this anisotropy can come as a surprise considering the fact that the interaction parameter Λ is an isotropic constant parameter, and the superconduct-

ing order parameter is, by definition, spherically symmetric. This implies that the underlying electronic structure is the main driver for the anisotropy.

Experimentally, Pb [2, 224–226], MgB_2 [3, 91, 94] and Nb [4, 85, 86, 227, 228] all have documented gap anisotropy. It is understood that in these systems the anisotropy arises from multiple Fermi surface sheets. As many of the elemental phonon-mediated s-wave superconductors exhibit multiple Fermi surface sheets, it is natural to assume that many would exhibit gap anisotropy. Despite this, not many have been identified, in fact in the case of Nb it has even been disputed [87, 88].

This, in part, was because gap anisotropies were not originally the main focus of the theories describing superconductivity. In the original BCS theory [24] only a single spherical band was considered and so it was impossible to obtain any gap anisotropy. In addition, it was limited to the weak coupling regime, which later was rectified by the Eliashberg theory [78, 229] and more recently by full DFT approaches to electron phonon coupling driven superconductivity [202, 203]. Although gap anisotropy analysis is present in such codes, much of the DFT based *ab initio* work focused on other aspects. These aspects being; expanding the description of s-wave superconductivity with emphasis on the correct description of the driving mechanism [230–234], or on the extension to unconventional pairing pushing the boundaries in our treatment of iron based [235], spin [236] and magnetic effects [237, 238].

Beyond the *ab initio* work on superconductivity, there is also extensive work on using parametrised models to describe superconductivity [44, 239–247]. These models are a powerful tool for describing unconventional superconductors and some of the basic principles of standard s-wave superconductors. These methods allow for gap anisotropy in the superconducting order parameter, however they have the drawback that they require the normal state to be parametrised from either experimental data or a DFT calculation. This often results in over-simplification of the normal state band structure in order to construct an efficient model to describe the superconducting state. While this usually leads to deep understanding of aspects of the superconductivity, it might obscure the importance of the complexity and orbital hybridisation of the underlying electronic structure. The result is that although anisotropy is described using complex order parameters, the anisotropy associated with the underlying electronic structure will often be missed.

In this section we show that our method leads to a full electronic structure within the superconducting state giving access to the full gap anisotropy in multi sheet s-wave superconductors. We show quantitatively the complexity of the superconducting gap including its full anisotropy even in simple elemental crystals. We present the resulting gap anisotropy in Nb, Pb and MgB_2 on the various Fermi surface sheets, and some simple arguments on how the normal-state properties drive the observed anisotropies. In all cases we will relate our work to experimental observations.

4.2.1 Nb

The lattice constant of $a = 3.30$Å was used for the bcc structure of Nb. We tuned Λ such that the gap in the DOS around the Fermi level was matched to the experimental gap size via tunnelling experiments [4], as detailed in Fig. 4.3(a). The authors of Ref. [4] found different sizes for the superconducting gap depending on the exposed surface of the single crystalline Nb. The different crystal planes investigated were (001), (110) and (111). The values for the superconducting gap are given by $\Delta_{001} = 1.20$ meV, $\Delta_{110} = 1.64$ meV and $\Delta_{111} = 1.79$ meV. We chose to tune Λ such that the outer peak of our superconducting gap matched Δ_{111}. In the inset of Fig. 4.4 we can identify two clear peaks and one weak shoulder corresponding to three distinct gaps at $\Delta_1 = 1.43$meV, $\Delta_2 = 1.69$meV and $\Delta_3 = 1.79$meV, in reasonable quantitative agreement to the experiment [4]. In comparison to other literature [85, 86, 227, 228] the gap anisotropy is also well matched.

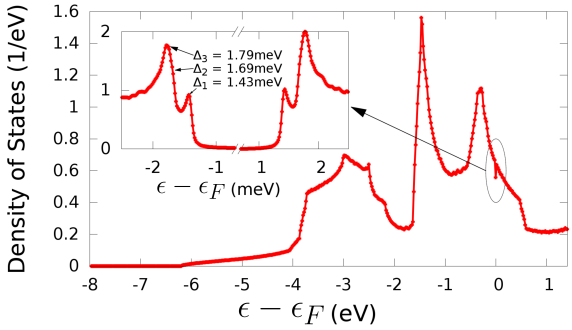

Figure 4.4: A scalar relativistic calculation of the electronic DOS of Nb in the superconducting state, with the inset showing the gap at the Fermi level ϵ_F.

Using a completely isotropic model for the superconductivity with one free parameter, we have found gap anisotropy comparable to experimental data. Its origin must be the underlying electronic structure, and this is what must be investigated next. Hence $\Delta(\mathbf{k})$ is analysed to highlight areas on the Fermi surface with high anisotropy. Once these are found, we analyse the underlying electronic structure by investigating the the k-dependence of the Fermi velocity $v_f(\mathbf{k})$ to ascertain whether a relationship between the two quantities can be reached.

The lower panel of Fig. 4.5(a) shows the Bloch spectral function for a large energy window but in the top panel we focus on the region around the Fermi level along the Γ to N direction with a smaller energy window (-50meV to 50meV). On that scale the opening of the superconducting gap is just about resolved. In order to investigate the gap and the associated anisotropy as highlighted in Fig. 4.4 the relevant energy resolution is -4.5meV to 0meV and for the band structure we focus on the high symmetry line Γ to N in Fig. 4.5(b). A double peaked superconducting gap is clearly resolved, with band gaps 1 and 2 contributing to the outermost gaps Δ_3 and Δ_2 respectively, and the 3rd band gap relating to the inner peak. In order to understand this anisotropy we consider the orbital character associated with each band. While the inner peak is 'p-d' hybridised, the outer peak is almost entirely of a d-electron character. Typically, 'p' character bands will show a

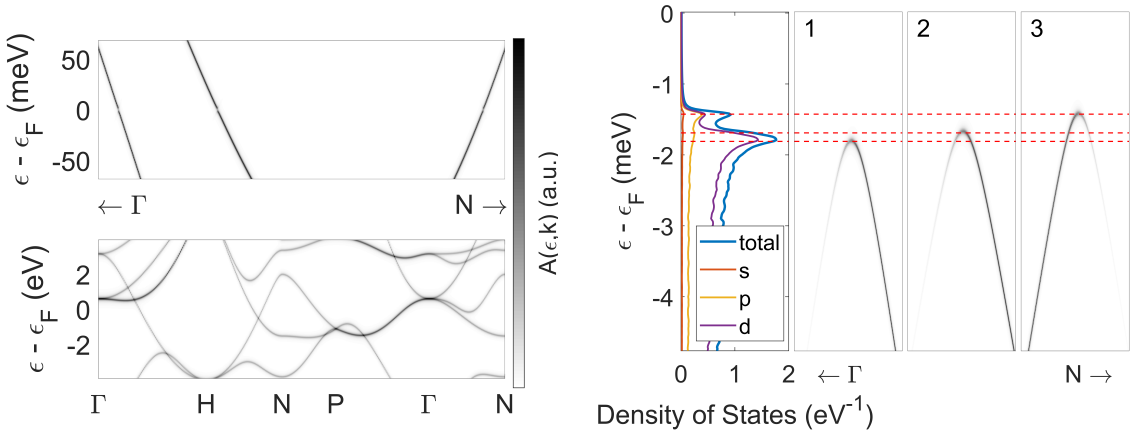

Figure 4.5: (a) A Bloch spectral function of Nb in the superconducting state, showing the band structure in directions of high symmetry. The units of the spectral function are arbitrary. In the top panel with a higher energy resolution the superconducting gap is just about visible. (b) Left Panel: The total and orbital resolved DOS of Nb near the Fermi level. Panel 1-3: Band gaps in the Γ to N direction. Panel 1 is associated with Δ_3, panel 2 with Δ_2 and panel 3 with Δ_1 of Fig. 4.4. The units of the spectral function are arbitrary.

larger Fermi velocity at the Fermi level compared to the 'd' character bands. This is confirmed by calculating the Fermi velocities shown as a colour map on the distinct Fermi surface sheets in Fig. 4.6(a), where points of the Fermi surface associated with panels 1-3 from Fig. 4.5(b) are labelled. Evidently panels 1 and 2 have similar velocities at the point of crossing, whereas panel 3 has a velocity which is noticeably larger. Since the DOS is inversely proportional to the Fermi velocity,

$$D(\epsilon_F) \propto \frac{1}{v_F}, \tag{4.3}$$

and within the BCS theory [23, 24] the gap scales with the DOS

$$\Delta \approx 2k_B\Theta_D \exp\left(-\frac{1}{VD(\epsilon_F)}\right), \tag{4.4}$$

we expect the gap anisotropy to be following the distribution of Fermi velocities on the Fermi surface sheets. In Fig. 4.6(b) we extend this analysis to the full Fermi surface and in compare it to Fig. 4.6(a) a strong correlation between $\mathrm{v}_F(\mathbf{k})$ and $\Delta(\mathbf{k})$ is observed.

4.2.2 Pb

The reason Pb was one of the principal materials of interest in this work, was that it is famously one of the conventional phonon-mediated superconductors that have exhibited signatures of gap anisotropy [80, 224–226]. The trouble with Pb is that the material is often amorphous or disordered. In order to overcome this issue we tuned our system specifically to the experiment

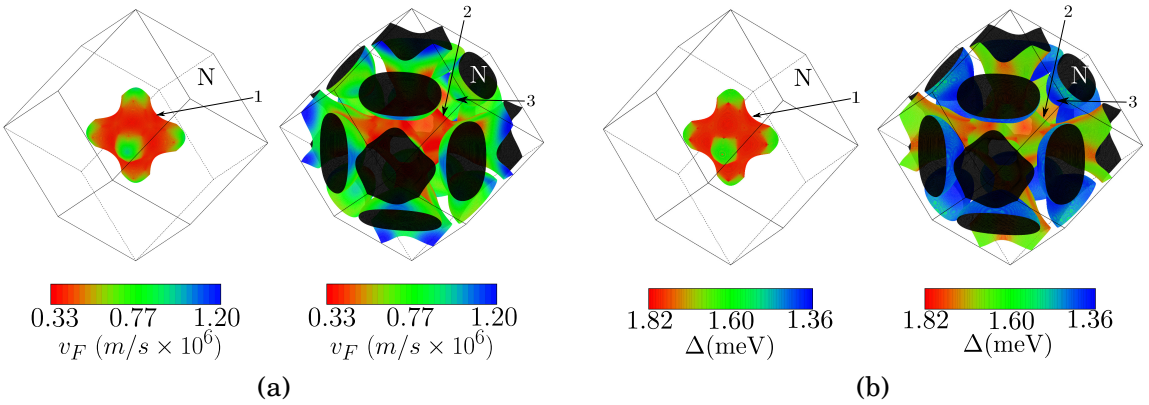

Figure 4.6: (a) The Fermi surface sheets with the colour scale showing the Fermi velocity of Nb. The labels refer to the gaps identified in Fig. 4.5(b). (b) The Fermi surface sheets of Nb in the normal state with the gap size of Nb in the superconducting state superimposed as a colour scale on top. The labels refer to the panels in Fig. 4.5(b) and identify the points on the Fermi surface where the gaps in Fig. 4.5(b) appear.

performed by M. Ruby and collaborators [2]. In this experiment they took single crystalline fcc Pb (001), (110) and (111) surfaces and performed scanning tunnelling microscopy experiments on them using a superconducting tip of W [248]. Using a superconducting tip is preferred because the energy resolution is much higher, resulting in accurate measurements of the level of anisotropy present in superconducting Pb. This increase in resolution is due to the energy width of a superconducting coherence peak being much finer than the energy width of a conventional tip, and is a key factor in the successful determination of the fine levels of anisotropy.

Their further experiments investigated the effects that magnetic impurities had on Pb surfaces [7, 189, 248–250], with the ultimate goal of trying to describe the effects that a chain of magnetic impurities had on the surface of a superconductor [50]. As these methods look at localised effects of individual impurity sites surrounded by a periodic lattice, they are perfectly suited to our method. As such, they will be the subject of sections 5.3 and 5.4. For now we will investigate the pure Pb crystal that is the subject of their initial publication [2]. Firstly we will calculate the fcc bulk crystal of Pb in section 4.2.2.1 and assess its gap anisotropy. Secondly we will assess the gap anisotopy present on the surface in section 4.2.2.2.

4.2.2.1 Pb Bulk

In the experiment performed Ruby *et al.* [2] the authors identified two distinct peaks of the superconducting gap at an energy separation of 150μeV. Within our calculations the fcc crystal structure with a lattice constant of 4.95Å is used. Here we restrict the computation to three dimensional periodic crystals but section 4.2.2.2 will focus on describing the surface explicitly as measured in the experiment. For the bulk material we assume that the gap anisotropy in Pb should at least be of similar order as found in the STM experiments.

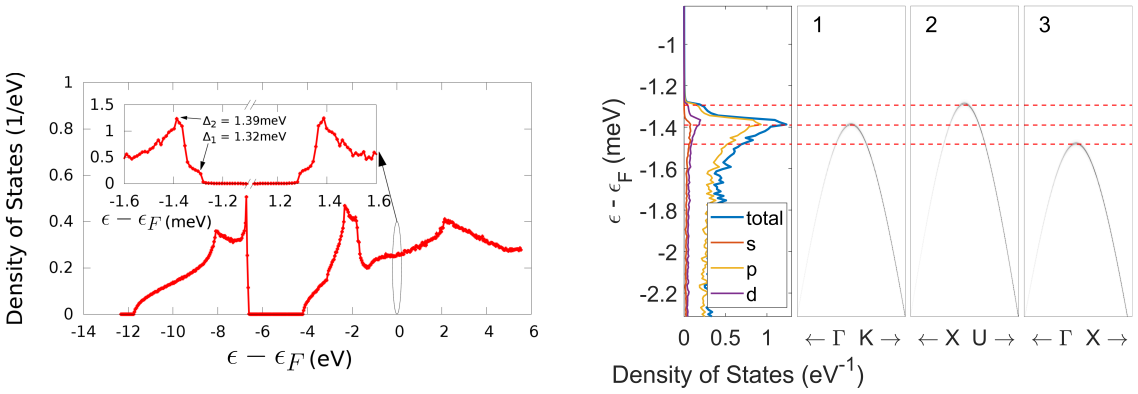

(a) (b)

Figure 4.7: (a) A scalar relativistic calculation of the electronic DOS of Pb in the superconducting state with an inset figure showing the peaks of the superconducting gap. (b) Left Panel: The total and orbital resolved DOS of Pb near the Fermi level. Panels 1-3: Band gaps in the Γ to K, X to U and Γ to X directions. Panel 1 is associated with the central coherence peak, panel 2 is associated with the small shoulder in the DOS and panel 3 is associated with the largest shoulder. The units of the spectral function are arbitrary.

For an interaction parameter of $\Lambda = 0.351$Ry the over all gap size is found to be comparable to Ruby *et al*. [2]. The inset of Fig. 4.7(a) displays the gap structure at this interaction parameter where the separation between the distinct gaps is 140μeV. This energy separation is comparable to the 150μeV identified by Ruby *et al*. [50]. In order to resolve such small separation a fine mesh of 1×10^7 k-points in the irreducible part of the Brillouin zone was required.

Following the same process as for Nb the distinct gap sizes can be traced to different points in k-space as shown in Fig. 4.7(b). However, to get the full picture of the anisotropy Fig. 4.8(b) shows the size of the gap on both Fermi surface sheets, with the relevant directions and band crossings from Fig. 4.7(b) highlighted. It is clear that the Fermi sheet in the left panel is mainly associated with the larger of the two gaps, and the sheet in the right panel contributes to the smaller shoulder. However, both sheets do contribute to a lesser extent to the other gaps as well. This is in contrast to the argument put forward by Ruby *et al*. [2] who argued that the closed Fermi sheet (left panel of Fig. 4.8(b)) contributes to the smaller gap and the open sheet (right panel of Fig. 4.8(b)) relates to the outer peak. There are many factors which could be responsible for this discrepancy. Perhaps the most obvious is the fact that we performed a bulk calculation, whereas their experiment probes the surface. An accurate calculation of the surface is therefore crucial to shed light on this aspect.

Interestingly, the Fermi velocities as shown in Fig. 4.8(a) together with the simple argument developed for Nb would suggest the open band to show the larger gap in agreement with the experimental observation. While for the closed Fermi surface sheet the simple argument connecting the Fermi velocity to the size of the gap largely holds the relationship is less convincing

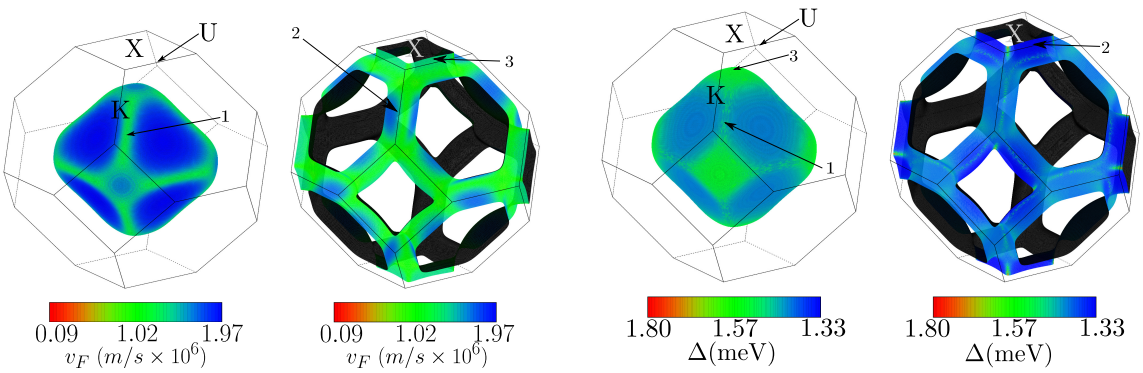

Figure 4.8: (a) The Fermi surfaces with the colour scale showing the Fermi velocity of Pb. The labels refer to the gaps identified in Fig. 4.7(b). (b) The Fermi surface sheets of Pb in the normal state with the gap size of Pb in the superconducting state superimposed as a colour scale on top. The labels refer to the panels in Fig. 4.7(b) and identify the points on the Fermi surface where the gaps in Fig. 4.7(b) appear.

for the open sheet. It is interesting to note the large value of the interaction parameter of Pb compared to Nb despite the fact that the superconducting gap of Pb is smaller than the gap of Nb (see Table 4.3.). This underlines the importance of dealing with the realistic band structure and also suggests that the superconducting state of Pb falls far from the weak coupling limit. Since BCS theory is valid in the weak coupling limit, therefore the relation between the Fermi velocity and the superconducting gap is expected to be less robust. This aspect deserves further investigation and in particular the influence of surfaces and spin-orbit coupling.

Other theoretical work on Pb by A. Floris *et al.* [6] established the anisotropic electron phonon coupling from fully first principles calculations for a bcc crystal structure. Since this is a different crystal structure, it complicates the comparison. The degree of anisotropy from Ref. [6], measuring the relative difference between the gaps on the two Fermi surface sheets, was $|\Delta_2 - \Delta_1|/\Delta_{iso} \approx 20\%$. Here Δ_1 and Δ_2 refer to $\bar{\Delta}_{\mathbf{k}}$ for bands 1 and 2, and Δ_{iso} refers to the $\bar{\Delta}_{\mathbf{k}}$ resulting from a calculation where an isotropic interaction is chosen.

For the fcc crystal considered here, the anisotropy measure is calculated by integrating $\Delta(\mathbf{k})$ from the individual Fermi surface sheets in Fig. 4.8b to obtain $\bar{\Delta}_{\mathbf{k},1}$ and $\bar{\Delta}_{\mathbf{k},2}$, whereas $\bar{\Delta}_{\mathbf{k}}$ is the integral of both Fermi surface sheets combined. The resulting anisotropy $|\bar{\Delta}_{\mathbf{k},2} - \bar{\Delta}_{\mathbf{k},1}|/\bar{\Delta}_{\mathbf{k}} \approx 4\%$. The quantities used to compute the numerator in both methods are the same, however the quantity on the denominator is not the same. In order to fully test our method to theirs, the exact numerical parameters they use to define the crystal should be chosen and the whole problem should be recalculated. In order to perform an even better comparison it would be beneficial to include temperature dependent calculations to obtain an approximate T_c. This would enable a more robust technique to compare methods as this is an easy quantity to compare.

4.2.2.2 Pb Surface

Work for this section has been done in conjunction with Ming-Hung Wu who constructed the Pb surface structure and performed the superconducting self-consistent calculations to obtain the normal state. Here, using Ming-Hung Wu's calculation, I tuned the numerical parameters for the DOS calculation and assessed the resulting anisotropy of the surface.

Within the bulk we identified three superconducting peaks for Pb. Comparing the difference in energy between the outer and inner peak gives $\Delta_3 - \Delta_1 = 140$ μeV which is comparable to the experiments performed by Ruby *et al* [2] who determined a peak separation of 150 μeV. The next obvious step is to test what happens when we perform calculations for the surface. This section will highlight the anisotropy present within (100) surfaces of Pb. Investigating the DOS of the bulk we would expect that the components of the Fermi surface which are associated with the (100) surface will be heightened. This is the orthogonal plane to the X high symmetry direction, as labelled in Fig. 4.9. Hence, by comparing this figure to the gaps highlighted in Fig. 4.8(b), we can determine that the gaps which are present in the (100) plane are Δ_1 and Δ_3. Hence the prediction is that the coherence peaks associated with these gaps will be enhanced. For the remainder of this section we define the i^{th} bulk gap as Δ_i^b, the i^{th} gap associated with the central atom as Δ_i^m, and the i^{th} gap associated with the surface as Δ_i^s.

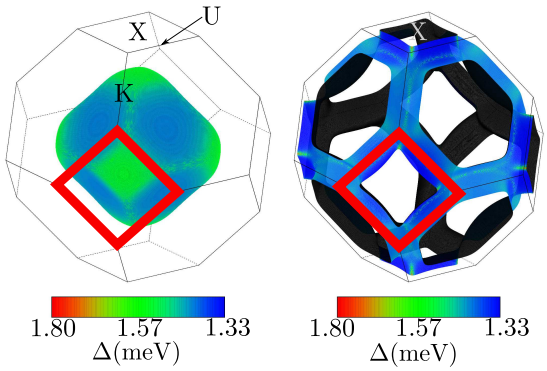

Figure 4.9: A figure with the Fermi surface of bulk fcc Pb with the gap calculated using the parameters from section 4.2.2.1 and superimposed as a colour scale on top. The red square refers to the slice of the Fermi surface which will be exemplified on the real-space (100) surface.

The calculations were constructed using supercells of nine atomic layers, with vacuum either side. Nine layers were chosen because the central atom should in principle be equivalent to the bulk. Fig. 4.10(a) shows the comparison between the DOS of the bulk vs the DOS of the central atom of the thin film. It is clear that the gap size is significantly different. This discrepancy simply arises from the comparison between nine atomic layers and pure bulk. This can be improved by employing the decimation technique [251, 252] as this will enable a proper surface between semi-infinite Pb and semi-infinite vacuum, describing the bulk and its interaction with the surface more appropriately.

Despite this, inspecting the individual coherence peaks associated with the central atom vs the bulk atom it appears that the coherence peak associated with Δ_3^m is much larger than the coherence peak associated with Δ_3^b. This is the expected result for the surface, regardless of the discrepancy of the gap size. From here, we compare the DOS of the central atom and the DOS of the atom on the surface in Fig. 4.10(b). Looking at the coherence peaks from the three gaps, all are more enhanced compared to the central atom. However the coherence peak from Δ_1^s has the largest enhancement. This is the expected result as this gap is prominent on the (001) plane as discussed earlier. The fact that the coherence peak associated with Δ_3^s is not enhanced as strongly as Δ_1^s's could be because Δ_3^s occupies less of the Fermi surface than Δ_1^s.

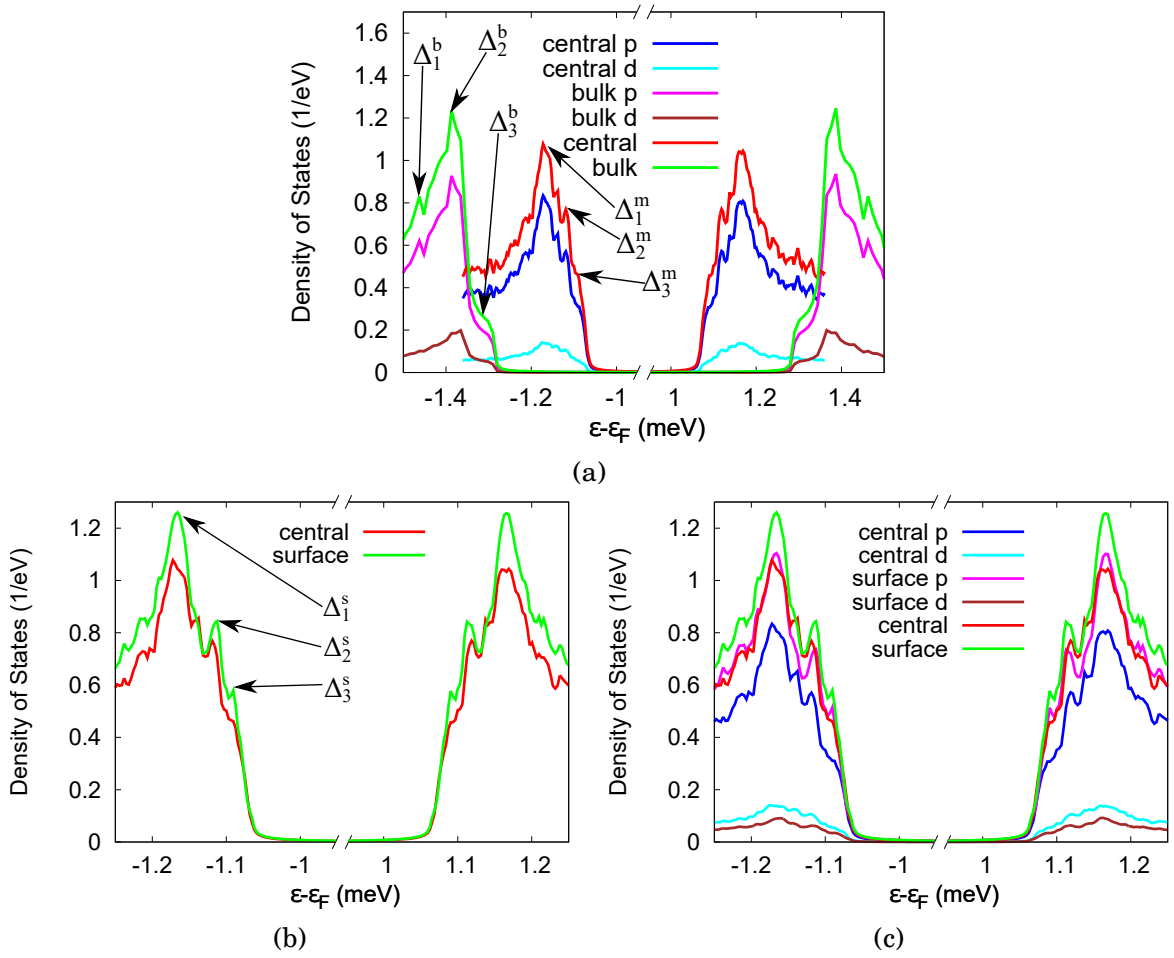

Figure 4.10: (a) The DOS of the superconducting bulk Pb calculations from section 4.2.2.1 compared to the middle atom of the nine layer superconducting Pb calculation. (b) The DOS of the central atom and the surface atom of superconducting Pb in the nine layer superconducting thin-film calculation. (c) The individual 'p' and 'd' components to the DOS of the central atom and the surface atom of superconducting Pb in the nine layer superconducting thin-film calculation.

From this analysis it is clear that further work needs to be done on the understanding of the model for the surface. As mentioned earlier the extension of the superconducting KKR formalism

to incorporate the decimation technique is naturally the next step. For now, however, we have shown that although the size of the gap is different compared to the bulk, the expected changes to the anisotropy is present. We will pick up the surface calculations again in section 5.4 where magnetic impurity calculations are performed with superconducting Pb surfaces.

4.2.3 MgB_2

The third example is MgB_2, whos superconductivity was discovered in 2001, which was of great interest as it had the highest T_c for a non-copper-oxide bulk superconductor [90]. It had other benefits, such as Mg and B being very abundant and inexpensive materials giving it great potential for use in industry. Interest in MgB_2 peaked when it was discovered that the superconducting gap was strongly anisotropic [3, 91, 94], and what was equally fascinating was that it was a conventional superconductor, as evidenced by observation of the isotope effect for the B atoms [92]. As this material is well established as an anisotropic, phonon-mediated, s-wave superconductor, we can use it as a benchmark to test how much of that anisotropy originates from the underlying complexities of the normal state electronic structure. We will now describe how we modelled MgB_2 within the scalar relativistic BdG KKR method.

One issue with modelling MgB_2 is the choice of Λ_{Mg} and Λ_B. It has been shown through the analysis of the phonon spectrum that the superconductivity is mainly driven via a large E_{2g} mode derived from the B atom [253, 254]. For this reason, we model the superconducting state with no interaction on the Mg atoms ($\Lambda_{Mg} = 0$) and the interaction parameter for the B atoms Λ_B was varied to match the zero temperature gap size from experiments [3, 91, 94]. Within these experiments the smaller gap ranges from 1.8meV [94] to approximately 3meV [3, 91], whereas the larger gap is around 7meV. It was therefore decided that Λ_B would be tuned so that the outer coherence peak in the DOS matches the outer, 7meV, coherence peak from the experiments resulting in $\Lambda_B = 0.288$Ry. In Fig. 4.11(a) we present the DOS within the superconducting state with the lattice constants $a = 3.09$Å and $c = 3.52$Å in a hexagonal lattice.

There is very good agreement between the experimental gap sizes and the smallest gap at $\Delta_1 = 3.27$meV and the largest at $\Delta_3 = 7.00$meV, which can be clearly identified in Fig. 4.11(a). In addition, there is a third peak associated with a third superconducting gap. This is obviously a surprise which conflicts with experimental data. However, it is possible to pick out the individual band gaps corresponding to this effect, as specified in Fig. 4.11(b) which shows three band gaps in high symmetry directions associated with each of the three peaks. This is interesting in a different perspective, because from our previous two materials our method predicts at least as many gaps as there are Fermi surface sheets. In this instance, MgB_2 has four Fermi surface sheets, as signified in Fig. 4.12(a), where the long, cylindrical sheets refer to the two σ bands and the other two wider sheets are the π bands. The top right contains two individual sheets from separate bands. In order to understand what is happening, Fig. 4.12(b) extends the analysis of Fig. 4.11(b) to the full Fermi surface. Each sheet can be associated with one of the three distinct

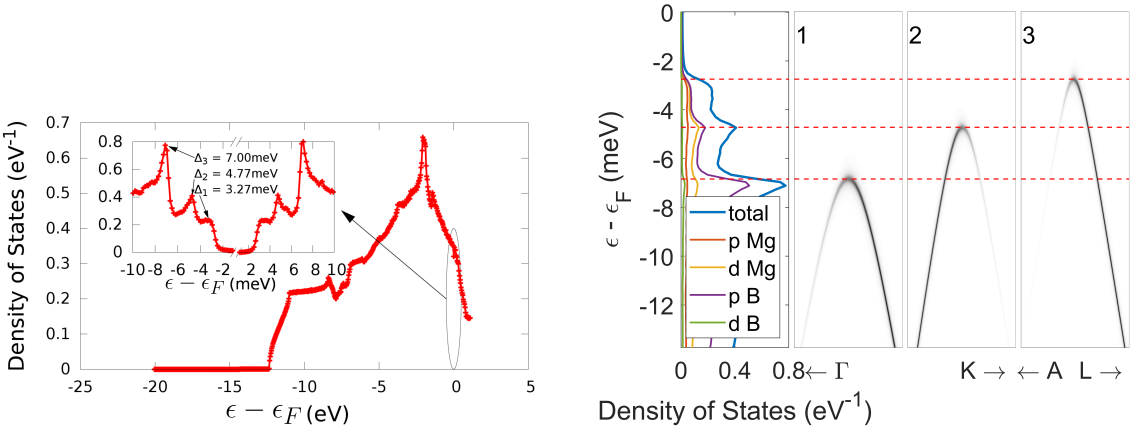

(a) (b)

Figure 4.11: (a) The electronic DOS of MgB_2 in the superconducting state. Inset shows the DOS around the superconducting gap. (b) Left Panel: The total and atom orbital resolved DOS of MgB_2 near the Fermi level. Panels 1-3: Band gaps in the Γ to K and A to L directions. Panel 1 contributes to the largest gap in the DOS, panel 2 contributes to the middle gap and panel 3 is associated with the smallest gap. The units of the spectral function are arbitrary.

gaps which are $\Delta_1 = 3.27$meV (blue), $\Delta_2 = 4.77$meV (green) and $\Delta_3 = 7.00$meV (red). This implies that the two σ bands are the contributing factors to Δ_3, whereas the π bands are associated with the other two gaps. The fact that two of the bands contribute to one of the gaps leads to three separate observable gaps as opposed to four. One possible explanation for this is that as the electronic states associated with both σ bands are mainly from the B atoms, and the interaction parameter Λ for both atoms is the same, both bands will behave similarly.

Comparing this result to the Fermi velocities (Fig. 4.12)(a) the simple relation, as established for Nb, holds to a certain extent. However for the top right panel the Fermi velocities vary quite remarkably across the Fermi surface sheets whereas the gap is relatively constant across each of the individual sheets (see Fig. 4.12(b)).

As discussed earlier, experimental evidence predicted that there were two superconducting gaps. A parameter-free calculation from A. Floris *et al*. [5] accurately predicts both gaps from experiment at T = 0K and derives the correct transition temperature T_c of MgB_2. This theoretical study, among others [94, 230, 253, 255], predicts two distinct gaps in the superconducting state. However, three gaps were identified by J. Bekaert *et al*. [256] in an *ab initio* calculation of thin films of MgB_2. This third peak vanishes going beyond a thickness of 3 MLs highlighting the importance of out of plane hybridisation. This suggests that any result will subtly depend on the out of plane lattice constant which we fixed to the experimental value rather using structural relaxation. Relaxed structures would show a smaller lattice constant possibly increasing out of plane hybridisation and suppressing the third gap. On the other hand, in experiments impurity scattering will broaden any gap structures making it difficult to resolve a possible third peak. This

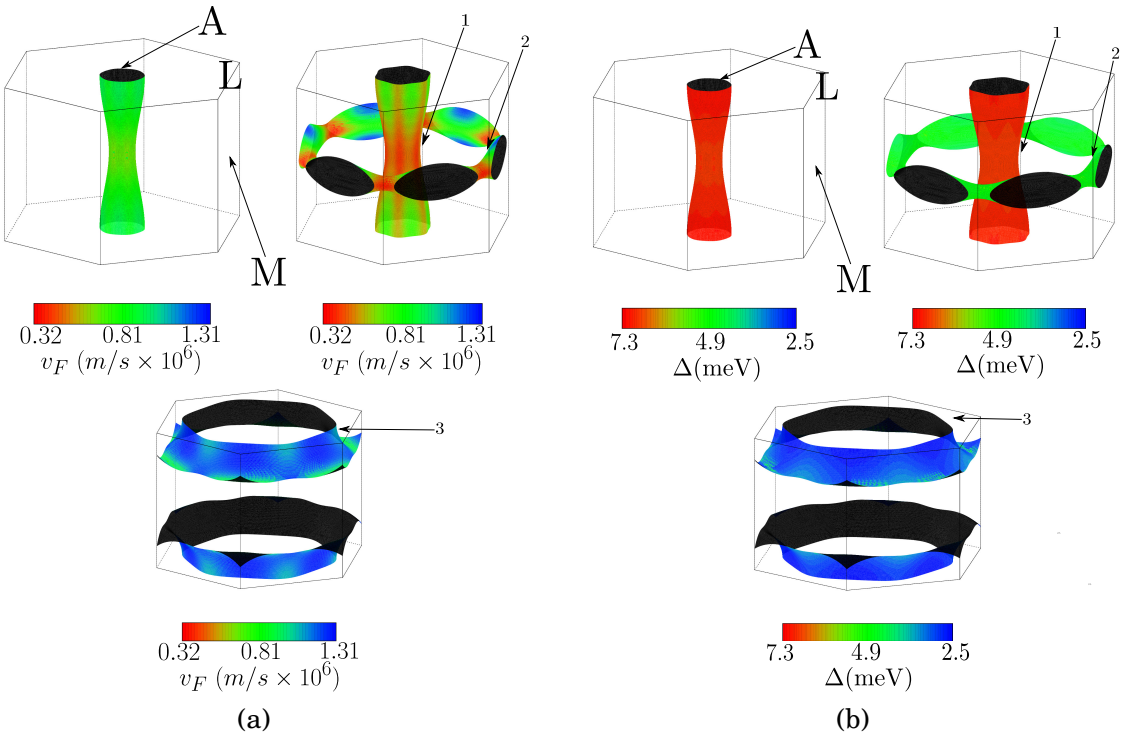

Figure 4.12: (a) The Fermi surfaces with the colour scale showing the Fermi velocity of MgB_2. The labels refer to the gaps identified in Fig. 4.11(b). (b) The Fermi surfaces of MgB_2 in the normal state with the gap size in the superconducting state superimposed as a colour scale on top. The labels refer to the panels in Fig. 4.11(b) and identify the points on the Fermi surface where the gaps in Fig. 4.11)(b) appear. The gap values Δ_i^b are associated with the gaps from the bulk, Δ_a^m from the central atom of the thin film and Δ_a^s is from the surface of the thin film.

implies that it is not necessarily an anomaly of the simplified exchange-correlation functional present in this method.

4.3 Fully Relativistic Pb

With the atomic number of Pb being 82, the effects of spin-orbit coupling in Pb will become relevant. It will have significant contributions to the Fermi surface and underlying Fermi velocity. Fig. 4.13(a) is a comparison between the normal state band structure using the scalar relativistic (green) and fully relativistic (red) solvers. On the eV scale the effects of the spin-orbit interaction are noticeable due to the large number of avoided crossings. At the scale of the gap (meV) they will be much larger.

In this section we present some preliminary findings when using the implementation of the Dirac-BdG-KKR method, detailed in section 3.6. In order to compare how the gap anisotropy from superconducting Pb changes with the inclusion of spin-orbit coupling we present results using one shot calculations of our FR code using the converged $\Delta_{eff}^{SR}(\mathbf{r})$ and $V_{eff}^{SR}(\mathbf{r})$ from section 4.2.2.

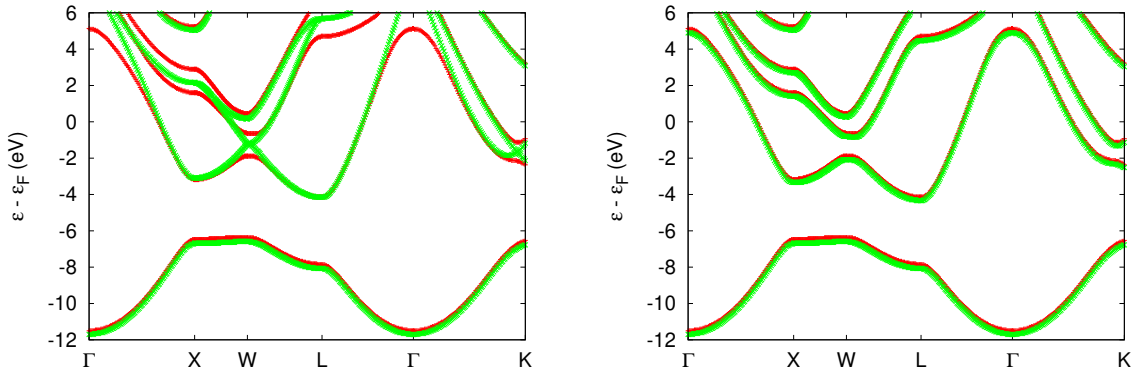

(a) (b)

Figure 4.13: (a) The normal state band structure of Pb using the SR (green) and FR (red) solvers. The potentials used to generate this figure have been converged using the SR and FR codes respectively. (b) In red, the converged FR (red) calculation from (a) has been re-plotted, in green an FR band structure has been calculated using the SR potential used in figure (a).

Not using the full self-consistency can be justified by comparing the figures 4.13(a) with 4.13(b). In Fig. 4.13(a) we see the comparison between the SR and FR results of Pb. In Fig. 4.13(b) we compare an FR band structure calculation using the SR (green) and FR (red) converged potentials respectively, implying that the one shot calculation covers the most important aspects of the bandstructure. From now we shall use the names oneshot FR and converged FR to compare the green and red bands respectively. Although there is definitely a rigid shift at the Fermi energy between the FR converged and the FR oneshot, the band crossings at the Fermi level are the same relative to each other. Conversely, looking at the converged SR and FR results from Fig. 4.13(a) the difference between the band crossings at the Fermi level is much more significant. Hence, any fundamental changes to the gap structure are going to be predominantly due to the spin-orbit coupling rather than the shift in Fermi energy. In order to test how spin-orbit coupling affects the gap anisotropy in Pb it is therefore a reasonable approximation to take the converged $\Delta_{eff}^{SR}(\mathbf{r})$ and $V_{eff}^{SR}(\mathbf{r})$ and using these to compare a SR and FR DOS. It must be stressed, however, that the future aim will be to perform the full self-consistency for the fully relativistic implementation.

To calculate the change in gap anisotropy, we present calculations of the DOS of the SR calculation from Fig. 4.7(a) against an FR one shot with the same numerical parameters in Fig. 4.14(a). From the original scalar relativistic calculation it was observed that there were three distinct superconducting gaps present $\Delta_1^{SR} = 1.32$ meV, $\Delta_2^{SR} = 1.39$ meV and $\Delta_3^{SR} = 1.46$ meV with an energy separation between Δ_1^{SR} and Δ_3^{SR} of $140\mu eV$. From the FR calculation it appears that there could, arguably, be a fourth superconducting peak within the gap. In reality an investigation into $\Delta(\mathbf{k})$ on the Fermi surface is required in order to solidify this claim as to whether the gap on the Fermi surface is legitimate and not just numerical noise. Despite this, the full level of anisotropy present within the FR calculation remains wholly unchanged from

the SR calculation as the energy seperation between Δ_1^{FR} and Δ_4^{FR} is $140\mu eV$. Investigating the individual orbital contribution to the gap in Fig. 4.14(b) we see a similar dependence as in Fig. 4.7(b) for the SR DOS.

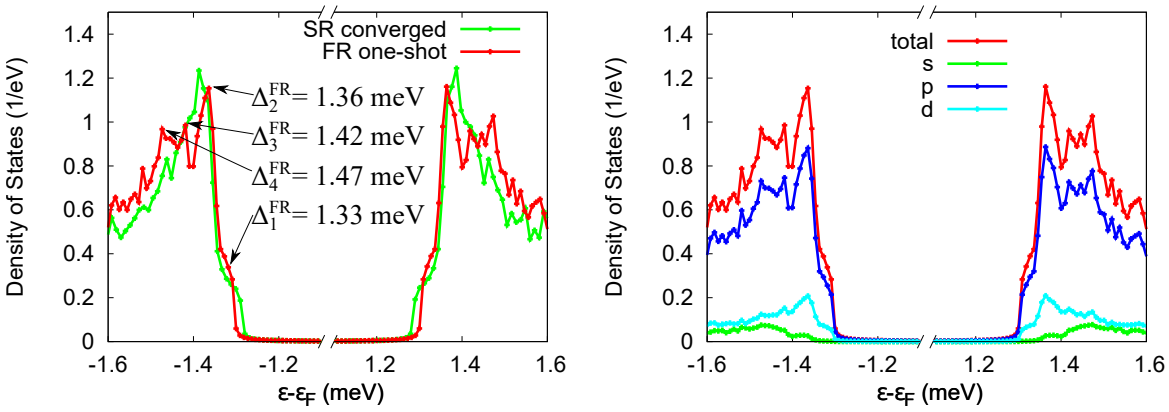

(a) (b)

Figure 4.14: (a) A fully relativistic calculation of the DOS using the converged $\Delta_{eff}^{SR}(\mathbf{r})$ and $V_{eff}^{SR}(\mathbf{r})$ potentials compared to a scalar relativistic DOS using the same potentials. The resulting gaps present in the DOS are indicated with Δ_i^{FR}, where i refers to the i^{th} coherence peak from the Fermi level. (b) The orbital decomposition of the DOS for the FR calculation.

4.4 Discussion and Conclusions

We have implemented a self-consistent solution of the BdG equations into the 3D bulk screened KKR formalism. In order to model realistic bulk systems, the BdG equation was solved self-consistently by choosing a simple exchange correlation functional (3.29) to model both the normal and superconducting order parameters $\rho(\mathbf{r})$ and $\chi(\mathbf{r})$ respectively. The key parameter is the interaction Λ. This quantity, combined with $D(\epsilon_F)$ generates λ_{BdG}, a quantity comparable to the electron-phonon coupling parameter λ from equation (3.18). We tried to calculate λ from first principles using Gaspari-Győrffy theory. Using the first principles λ in the BdG KKR formalism we were able to reproduce some predictable quantities like superconductivity in Nb and no superconductivity in Cu. However, it inconsistently described the superconducting properties of many other simple materials showing that this method is not good enough to work as an *ab initio* theory for the superconducting state. As a parameterised model, however, it is a practical accompaniment to experiment. Therefore for the remainder of the report we tuned Λ such that the zero temperature gap size matched the largest measured experimental gap. In this instance, Nb, Pb and MgB_2 were the materials chosen in this investigation. For Nb, the gap was tuned so that the outer coherence peak, Δ_3 from Fig. 4.5 matched the gap for the (111) surface, Δ_{111} of Nb from the experiment in Ref. [4]. For Pb, the highest coherence peak Δ_2 from Fig. 4.7(a) was matched to the outermost coherence peak from Ruby *et al*. [2]. Finally the outer coherence

peak from MgB_2 has been measured as ~ 7meV, from many sources [3, 91, 94], whereas the inner coherence peak is much less well defined, hence the outer coherence peak was chosen for the fitting in this case to match Δ_3 from Fig. 4.11(a).

Calculating the gap self-consistently for Nb we found two superconducting gaps from distinct Fermi surface sheets. We argued that the Fermi velocity of these bands at the Fermi level plays a key role in driving the gap anisotropy. The fully anisotropic gap on the Fermi surface supported the simple picture connecting the gap size to the inverse of the Fermi velocity. The difference between the Δ_3 and Δ_1 is 0.36meV, and is comparable to experimental results [85, 86, 227, 228]. The most recent tunnelling experiment gives roughly the same gap sizes [4] which are Δ_{001} = 1.20meV, Δ_{110} = 1.64meV and Δ_{111} = 1.79meV for the different planes. Similarly our calculations gave 3 distinct gaps of Δ_1 = 1.43meV, Δ_2 = 1.69meV and Δ_3 = 1.79meV as displayed in Fig. 4.4. These gaps are very comparable to the tunnelling experiment [4].

For fcc Pb we identified three main gaps with a total separation of 140μeV. This is comparable to tunnelling experiments performed by Ruby *et al*. [2] on single crystalline Pb surfaces where they found a difference of 150μeV. However, our calculations do not support their Fermi-surface analysis.

This leads to the investigation of Pb surfaces as it isolates specific parts of the Fermi surface. Simple investigation of just the (100) surface shows that the change in height going from the bulk to the surface of the coherence peak of Δ_2^s is reduced compared to the change in the coherence peaks of Δ_1^s and Δ_3^s. This is expected as these are the main contributing gaps associated with the (100) surface. One issue with the calculations, however, was comparing the size of the gaps in the bulk to the gaps in the thin film calculation as the gap size is noticeably different, whereas it should be the same. This calls for a more sophisticated approach to describing the surface of Pb, as this investigation used a 9 atomic layer thin film which is only an approximation of the true bulk superconductivity. In order to improve the method used here, the decimation technique [251, 252] can be employed, essentially enabling the calculation of a semi-infinite crystal of Pb.

For MgB_2 we established gap sizes of similar order as found in the literature [3, 91, 94]. Within this framework we identified three superconducting gaps which is expected in a system with three bands crossing the Fermi level and rather varied Fermi velocities. Three gaps have been predicted theoretically before in thin films only [256]. The middle gap from Ref. [256] is about 80% of the size of the outermost gap, and the inner gap about 40%. Whereas the middle gap, δ_2, in our work is about 68% of the size of the outermost gap, δ_3, and the innermost gap δ_1 about 47%. Therefore, the level of anisotropy present in Ref. [256] and our work is similar. The middle peak from Ref. [256] vanishes going beyond a thickness of 3 MLs showing that out of plane hybridisation plays a key role, and hence within our formalism the middle peak will subtly depend on the c-axis in our calculation. We used MgB_2 as a benchmark to assess how much of the anisotropy from the superconductor originates from the underlying electronic structure. We therefore have shown that this method certainly does exhibit significant anisotropy from the

underlying electronic structure, however in order to fully assess the anisotropy of MgB_2, a proper analysis of the influence of the c/a ratio must also be performed.

In summary, we showed that using a fully *ab initio* model to describe the normal state and a simple approximation for the superconducting exchange correlation functional produces gap anisotropy in Nb, Pb and MgB_2. This gap anisotropy comprises of both interband scattering from the multiband nature of the superconductors calculated, along with anisotropy present in each Fermi surface sheet as well and is of the same order as experimental data for each of these systems. One of the key features of the formation of the gap anisotropy is the inverse proportionality between the Fermi velocity and the magnitude of the gap. With just one free parameter, Λ, we have shown that it is possible to model anisotropy in superconductors to a high level of accuracy. This also shows that we are capable of modelling clean s-wave superconductors. To that end we can then use these results as the starting point for impurity calculations.

CHAPTER 5

IMPURITY RESULTS

In this chapter we investigate the effects that impurities have on the superconducting state. Firstly, as a continuation of section 4.2 we investigate the effects that impurities have on the gap anisotropy of a superconductor in section 5.1. We do this by embedding different impurities into superconducting Nb and observing how the orbital character of the impurity interacts with the multiband superconductor. Secondly, we invert the problem by considering what happens to a superconductor which has a finite size and is surrounded by a non-superconducting metallic system in 5.2. This enables us to ask how large a superconductor needs to be before it is possible to observe a gap in the excitation spectrum, and how it relates to the coherence length. Finally we investigate what happens to a superconductor in the presence of magnetic impurities by embedding 3d elements into the bulk and the surface of superconducting Pb in sections 5.3 and 5.4 respectively. The magnetic moment breaks the symmetry of the Cooper pairs, creating in-gap bound states as predicted by Yu [16], Shiba [17] and Rusinov [18]. We then decompose the resulting bound state LDOS into individual contributions of the lm decomposed orbital character. These calculations are performed in the scalar relativistic approximation.

5.1 The Effect on Gap Anisotropy

This section is a continuation of section 4.2, where we investigated the anisotropy of the superconductors Nb, Pb and MgB_2 and found that within our method these materials reproduce anisotropies comparable to experimental data [2–4]. From the analysis of section 4.2 it was clear that multiple Fermi surface sheets could give rise to multiple gaps, but not only that, also highly anisotropic Fermi surface sheets could give rise to multiple gaps in the DOS, for example the Fermi surface sheet on the left in Fig. 4.6(b) where in some places in k-space the d-band

experiences strong hybridisation from a p-type band. What is interesting is that these are the main s-wave superconductors with known anisotropy, despite the fact that many elemental superconductors have complex Fermi surfaces. There are two main reasons for this. The first is that at the time other elemental superconductors were being discovered and analysed experimental resolution was low so only the simple features of the gap could be resolved, the finer structure was missed. Secondly, due to impurity and grain boundary scattering, the coherence peaks would have been broadened making anisotropy harder to detect. These effects, coupled with the fact that anisotropy was not necessarily being sought for at the time due to the simplicity of the microscopic theories present, made it unlikely for such anisotropy be to detected. This section aims to elaborate on the second of these two points. On one hand we aim to analyse the effect of the impurity on the superconducting state in the surrounding material. On the other hand we will explore the interplay between the gap anisotropy and electron scattering off the substitutional impurity.

As a first test case we consider N impurities in Nb, a conventional impurity in this elemental superconductor. The self-consistent impurity cluster contains 89 atoms where the boundary condition is the perfect superconducting periodic crystal. The central atom of this cluster is replaced by a substitutional N impurity, the interaction parameter at the impurity site is $\Lambda_{imp} = 0$ and we relax the normal charge $\rho(\mathbf{r})$ as well as anomalous $\chi(\mathbf{r})$ density within the impurity cluster. The local density of states (LDOS) at the central N impurity is shown in Fig. 5.1(a) and compared to the Nb DOS of the periodic superconductor. As such it has the same principle size as Nb with notable absence of the outer coherence peak. This follows from the lack of d-states in N and the fact that only the inner coherence peak of Nb has a significant p-character. The larger gap, outer coherence peak, in Nb is almost entirely of d-character hence is strongly suppressed.

Reversing this argument the N impurity should induce scattering for the d-electrons of the surrounding Nb. This effect is highlighted in Fig. 5.1(b) where the LDOS of the nearest neighbour Nb atom adjacent to the N impurity is displayed. A clear broadening between the inner and outer coherence peak is visible due to the hybridisation between the p-electrons from N and d-electrons from Nb, indicating the challenge to resolve the gap anisotropy in this elemental superconductor when structural or chemical perturbations are present. In real materials such perturbations will be inevitable. Clearly, resolving gap anisotropy on the relevant energy scales will be highly demanding experimentally.

In order to support our argument that the lack of d orbital character at the N impurity site is responsible for the effective broadening of the peaks we compare the previous result to a situation where the substitutional impurity is Au, contributing significant d-character. This is evident in Figure 5.2(a) where the gap anisotropy is present on the impurity site (as shown from the green line). In addition, the main contributing factor to the outer coherence peak in Au is majority ‘d’ character, whereas the inner coherence peak is 50% ‘p’ and 50% ‘d’. This is in contrast to the Nitrogen case where on the Nitrogen site there is not enough ‘d’ character to

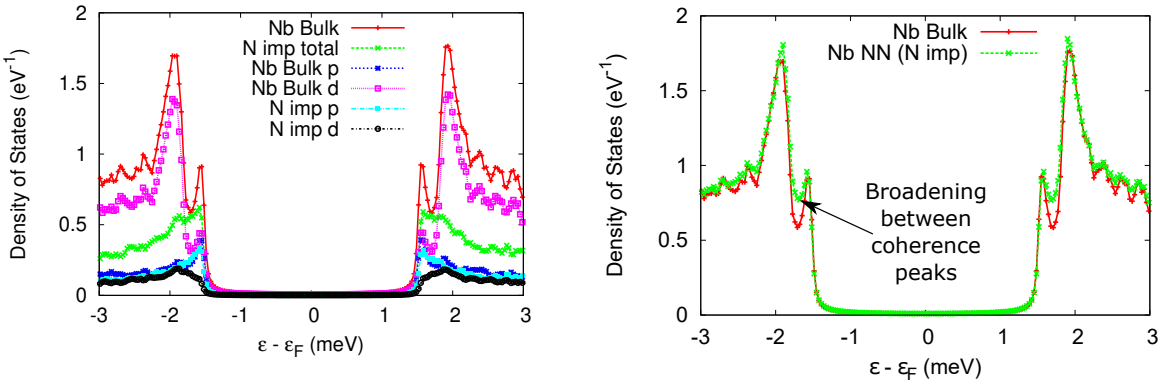

(a) (b)

Figure 5.1: (a) LDOS of an N impurity in comparison to the DOS of unperturbed periodic Nb. The LDOS of N within the impurity cluster is resolved into the separate orbital (s,p,d) contributions. (b) The DOS of unperturbed periodic Nb in comparison to the LDOS of the nearest neighbour Nb atom in the impurity cluster next to N.

contribute significantly to the gap. Figure 5.2(b) clearly shows the lack of broadening between the inner and outer coherence peak as the DOS of the unperturbed periodic Nb is compared to the LDOS of the nearest neighbour Nb in the impurity cluster containing Au at its centre. This is an interesting find, not only because we have shown that impurities can mask the anisotropy of a superconductor, but also we have shown that there are cases where some impurities cannot mask the anisotropy. It is highly unlikely for Au specifically to be an impurity in Nb, however due to this analysis we now understand that impurities cause scattering if they inhibit a particular orbital channel from hybridising effectively with the impurity. Furthermore, this technique has great potential in the investigations of quasiparticle scattering of unconventional superconducting order parameters. Theoretical modelling of these systems so far has relied on δ-like scatterers [37, 38, 46, 257] which allows for the general structure of the experimental data to be explained, however the fine structure will be essential if we are to obtain accurate determination of the superconducting order parameter and how it interacts with different impurities.

5.2 Superconducting Impurity Clusters in the Normal State

So far we have analysed the induced superconductivity at the impurity site as well as the impact of the electron scattering induced by the impurity atom on the surrounding superconductor. The fact that the superconductor induces a superconducting gap at the impurity site without an effective interaction parameter is not new in principle, and has been investigated before [30, 31]. In the following we will investigate the inverse problem, where a superconducting impurity cluster is embedded in a non-superconducting material. The relevance of this granular superconductivity is its connection to the pseudogap phase of underdoped high-Tc cuprate superconductors [9]. In

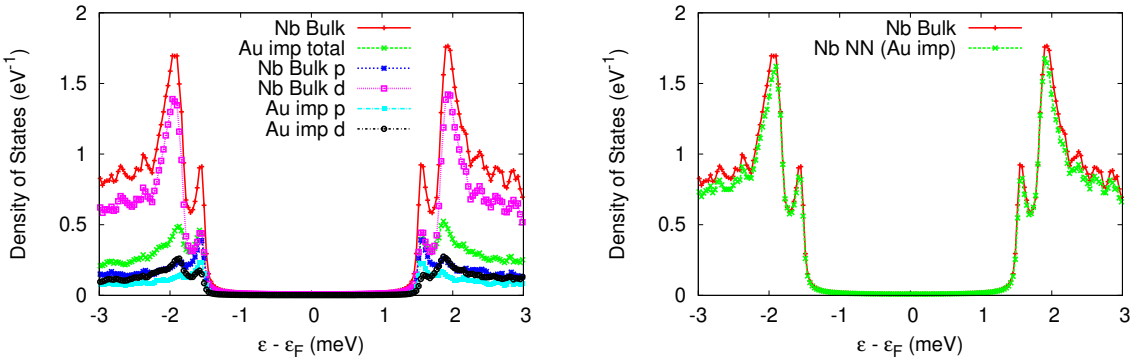

(a) (b)

Figure 5.2: (a) LDOS of an N impurity in comparison to the DOS of unperturbed periodic Nb. The LDOS of N within the impurity cluster is resolved into the separate orbital (s,p,d) contributions. (b) DOS of unperturbed periodic Nb in comparison to the LDOS of a nearest neighbour Nb atom in the impurity cluster next to the Au impurity.

general, superconductivity emerges from two distinct quantum phenomena: pairing between electrons and long range phase coherence. In conventional BCS theory, the condensation of Cooper pairs into a phase-coherent, quantum state takes place simultaneously at the transition temperature. However, in the underdoped high-Tc cuprate superconductors the electron pairing is thought to occur at higher temperatures than the long-range phase coherence [258]. In addition, this as been observed in some disordered, amorphous, superconductors [259]. In this model of granular superconductivity the existence of preformed Cooper pairs, pairing without long range phase coherence, shows similarities with the pseudogap regime of underdoped high-Tc cuprate superconductors.

For a relatively small cluster of material with non-zero interaction parameter embedded in a normal metal the superconductivity will be suppressed and the quasiparticle gap will be forced to close. However, if such a cluster reaches the size of the corresponding superconducting coherence length, ξ_0, the expectation is that superconductivity can be sustained within the cluster. Within BCS theory [23] the coherence length is given by

$$\xi_0 = \frac{\hbar v_F}{\pi \Delta}, \tag{5.1}$$

where v_F is the Fermi velocity, linking the coherence length to the inverse size of the superconducting gap Δ. The coherence length of bulk Nb is approximately 38nm [260]. A cluster of that size would roughly contain 10^6 atoms and is beyond any capability of this method. Within our standard calculation's cluster only a few hundred atoms could be considered limiting the cluster size to < 2 nm. However, it is still possible to test the relation $\xi_0 \sim \Delta^{-1}$ for artificially enlarged superconducting gaps.

The cluster was constructed from Niobium atoms with a non-zero interaction parameter Λ_i,

embedded in an infinite normal state Nb crystal. In a first step we omit self-consistency and explore the resulting superconducting gap in LDOS calculations when a constant pairing potential $\Delta_{eff}(\mathbf{r}) = \Delta_{eff}$ is applied. Figure 5.3(a) shows the LDOS of the central atom as we change the constant Δ_{eff}. For a pairing potential of $\Delta_{eff} = 0.11$Ry a gap in the quasiparticle spectrum of approximately $\Delta = 1.5$eV is induced, decreasing in size quickly with the size of the pairing potential. At $\Delta_{eff} = 5 \times 10^{-2}$Ry a suppression of the LDOS is still visible without a full opening of a gap and at $\Delta_{eff} = 2 \times 10^{-2}$Ry only a small deviation from the non-superconducting Nb remains. This implies that the surrounding metallic Nb enforces a suppression of the superconducting state as soon as the pairing potential is smaller than 5×10^{-2}Ry.

Next, we fix the pairing potential at $\Delta_{eff} = 0.11$Ry and explore how the gap in the LDOS develops as we approach the metallic Nb boundary. In Fig. 5.3(b) the corresponding results are summarised, comparing the central atom to the 5th nearest (0.57nm) and the 7th nearest (0.72nm) shell. Even at a distance of 0.57nm the coherence peak is still visible but the original gap is fully filled, it has a slightly suppressed LDOS and the local gap is gradually disappearing. There is no sudden transition from a gapped to a normal state implying the coexistence of anomalous (pairing) as well normal (electron) density.

This finding is very similar to the situation where we change the size of the region within the cluster for which we consider a non-zero and constant pairing potential. The resulting LDOS for the central atom is shown in Fig. 5.3(c). Again the coherence peak is more or less visible down to a region of nearest neighbours only but the LDOS at the Fermi energy increases as the cluster decreases.

To summarise these findings we define the anomalous charge $\bar{\chi}_i$

$$\bar{\chi}_i = \frac{1}{V_{WS}} \int_0^{r_{ASA}} d^3 r \chi_i(\mathbf{r}), \tag{5.2}$$

which is a constant for each shell at a given distance from the central atom within the cluster. In addition we define the average gap $\bar{\Delta}_i$,

$$\bar{\Delta}_i = \frac{1}{V_{WS}} \int_0^{r_{ASA}} d^3 r \Delta_i(\mathbf{r}), \tag{5.3}$$

which in the self-consistent calculations is related to $\bar{\chi}_i$ by the proportionality Λ_i. However in the non-self consistent one shot calculations the relation is more complex as discussed below. In Fig. 5.3(d) we summarise the results of the anomalous charge $\bar{\chi}_i$ as we change the region of non-zero $\bar{\Delta}_i$, the y-axis in Fig. 5.3(d). This corresponds to Fig. 5.3(c) as here we are investigating the LDOS of the central atom as we change region size. At the same time the full cluster is analysed, which is described by the x axis of Fig. 5.3(d). In all cases the anomalous charge is quickly reduced if we consider atoms outside the region with an applied non-zero $\bar{\Delta}_i$. Nevertheless, it is clearly visible how the anomalous charge is enhanced at the central atom as the region of non-zero $\bar{\Delta}_i$ is increased, while at the same time a small anomalous charge is induced beyond the region of non-zero pairing potential.

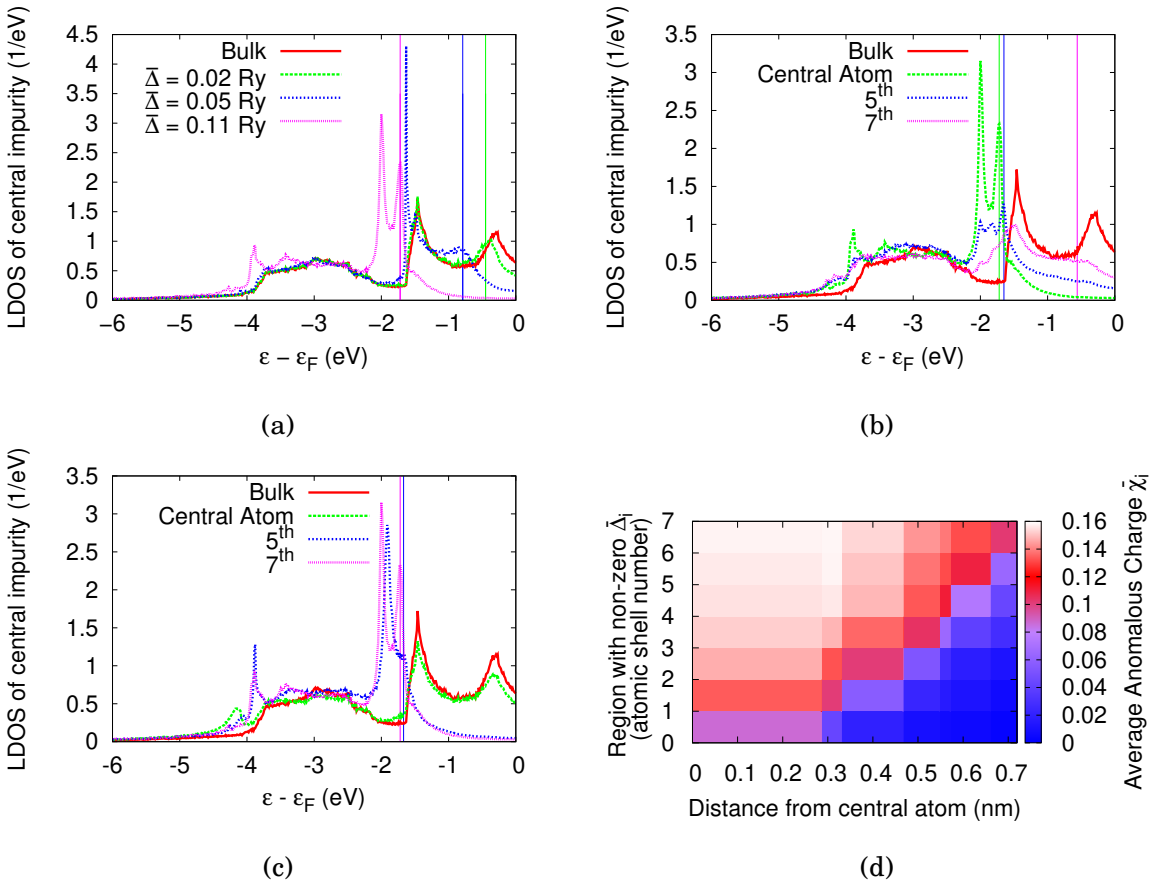

Figure 5.3: (a) The LDOS of the central atom in the cluster of 89 atoms with a constant Δ_{eff} for every atom in the cluster embedded in metallic Nb with $\bar{\Delta}_0$ defined in equation (5.3). Vertical solid lines indicate the first instance of a gap for each calculation at 0.45 eV (green), 0.79 eV (blue) and 1.72 eV (magenta). (b) The LDOS of atoms in the nth shell in a cluster of 89 atoms with a constant effective pairing potential Δ_{eff} = 0.11Ry, for every atom in the cluster. Vertical solid lines indicate the first instance of a gap for each calculation at 1.72 eV (green), 1.65 eV (blue) and 0.56 eV (magenta). (c) The LDOS of the central atom in the cluster of 89 atoms with a constant pairing potential Δ_{eff} = 0.11Ry for every atom up to and including the atoms in the nth shell. Vertical solid lines indicate the first instance of a gap for each calculation at 1.67 eV (blue) and 1.72 eV (magenta). (d) The average anomalous charge $\bar{\chi}_i$ per atom plotted as a function of distance in the cluster for the one-shot gap calculations corresponding to Fig. 5.3(c). The y axis represents the region with non-zero constant pairing potential Δ_{eff} = 0.11 Ry up to and including the nth shell. The relations between the shell indexes and distances are the following: first: 0.29 nm; second: 0.33 nm; third: 0.47 nm; fourth: 0.55 nm; fifth: 0.57 nm; sixth: 0.66 nm; and seventh: 0.72 nm.

In order to make a direct connection to the coherence length and its relation to the superconducting gap it is important to perform all calculations self-consistently. According to the BCS result the cluster needs to be larger than the coherence length to support superconductivity. The complication arises from the fact that we clearly observe pairing (anomalous charge in Fig. 5.3(d))

while there appears no gap in the quasiparticle spectrum (LDOS, see Fig. 5.3(c)). In Fig. 5.4(a) we summarise the fully self-consistent calculations changing the constant interaction Λ_i for the full cluster of 89 atoms. Shown is the LDOS of the central atom. Similarly to our discussion before, the gap in the LDOS vanishes as we reduce the interaction parameter to $\Lambda = 0.3Ry$ while the corresponding average gap stays non-zero as highlighted in the legend.

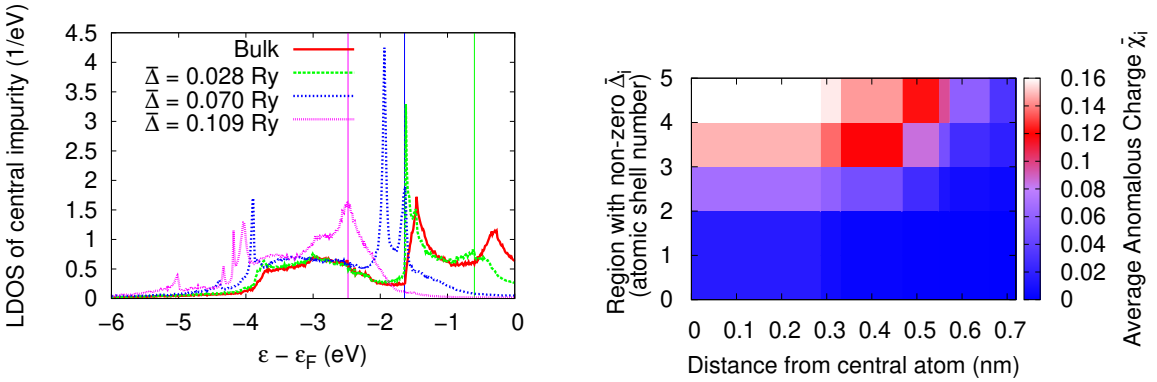

(a) (b)

Figure 5.4: (a) The LDOS of the central atom in the cluster of 89 atoms with a constant Λ_i applied to every atom in the cluster. The legend specifies the size of $\bar{\Delta}$ of the central atom. For the green line = 0.3Ry, blue $\Lambda = 0.4$Ry, pink $\Lambda = 0.5$Ry. Vertical solid lines indicate the first instance of a gap for each calculation at 0.60 eV (green), 1.64 eV (blue) and 2.48 eV (magenta). (b) The average anomalous charge $\bar{\chi}_i$ per atom as a function of distance in the cluster. This is the corresponding figure to Fig. 5.3(d) but for a fully self-consistent calculation. The y axis represents the region with non-zero coupling parameter $\Delta_i = 0.4$ Ry up to and including the nth shell. The relations between the shell indexes and distances are the following: first: 0.29 nm; second: 0.33 nm; third: 0.47 nm; fourth: 0.55 nm; fifth: 0.57 nm; sixth: 0.66 nm; and seventh: 0.72 nm.

The equivalent summary for the self-consistent calculations to Fig. 5.3(d) in case of the one-shot is shown in Fig. 5.4(b). A much sharper transition between a vanishing gap is visible in case of a cluster with an applied interaction up to the second shell only.

In order to better understand the relationship between self-consistency and one-shot LDOS calculations, we have to analyse the relationships between the anomalous charge, $\bar{\chi}$, the average gap, $\bar{\Delta}$ and the LDOS at ϵ_F, $D(\epsilon_F)$. In Fig 5.5(a) $D_i(\epsilon_F)$ as a function of $\bar{\Delta}_0$ for the central atom in a cluster of 89 atoms is shown. For the self consistent calculation, a non-zero and constant Λ_i is applied to all of the atoms up to the 7th nearest neighbour shell. For the one-shot calculations an average gap of constant pairing potential with the corresponding average gap is applied to all atoms. In this representation both approaches give very similar results. In all cases we observe a smooth transition between the opening of a gap in the quasiparticle spectrum gradually closing in as we change the superconducting strength, either via the interaction parameter or the average gap of constant pairing potential.

However, according to BCS theory, there should be a sharp transition where a gap is induced

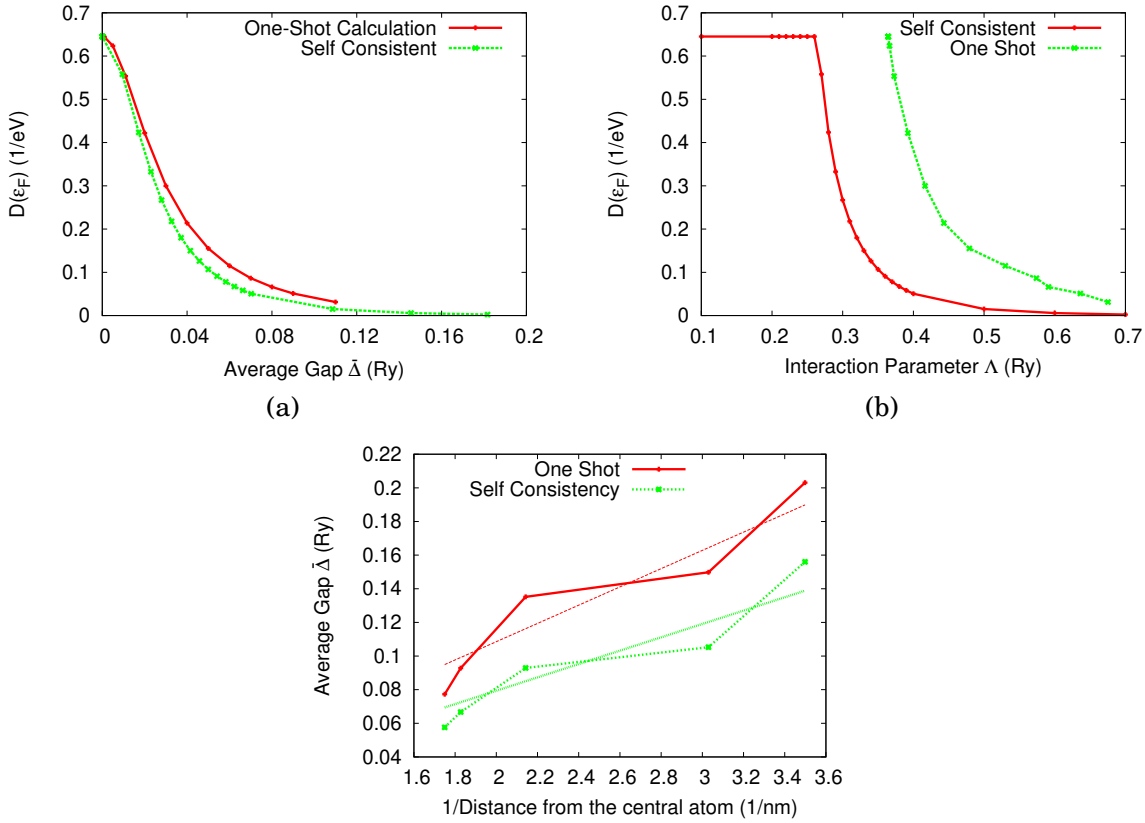

Figure 5.5: (a) The LDOS at the Fermi level as a function of the average gap $\bar{\Delta}_0$ for the central atom. (b) The LDOS for the central atom at the Fermi level as a function of the interaction parameter. In case of the on-shot calculations, the ratio between the applied average pairing potential and the anomalous charge is used to define an effective interaction parameter. (c) The average gap $\bar{\Delta}$ as a function of the inverse radius of the region of superconducting atoms.

once the coherence length is reached. This sharp transition becomes visible as we show $D_0(\epsilon_F)$ as a function of Λ_i applied to a cluster of 89 atoms in Fig. 5.5(b). This representation highlights the differences between the one shot and the fully self-consistent calculations. Only for the self-consistent calculations are we able to observe the sharp transition at which the system becomes superconducting at a non-zero interaction parameter. For the one-shot calculations as we reduce the applied average gap we will in all cases observe a non-zero induced anomalous density and as such an effective interaction parameter. In contrast, for the self-consistent calculation, as we reduce the interaction parameter we eventually reach the point where all superconductivity is suppressed, the anomalous density goes to zero, the gap in the quasiparticle spectrum vanishes and we observe a phase transition. This highlights the differences between both methods.

To finally investigate the coherence length within our method we show in Fig. 5.5(c) the average gap as a function of the size of the region with a non-zero interaction parameter. In order

to generate this figure we consider both cases the one shot and the the self consistent calculations. In the case of the one shot calculations at a given cluster size we increase the average gap, $\bar{\Delta}_i$, until the DOS as the Fermi energy is suppressed below $0.1(eV)^{-1}$. For the self-consistent calculations we do the same but varying the interaction parameter (Λ_i) until we reach the same threshold. The chosen threshold is a trade off between numerical accuracy and reaching a fully gapped situation. According to the BCS relation, equation (5.1), we should find $\bar{\Delta} \propto 1/\xi_0$ with the slope given by $\hbar v_F/\pi$. We find a roughly linear dependence with the linear fit giving the slope and as such the Fermi velocity to be $3.52 \times 10^6 \mathrm{ms}^{-1}$ and $2.58 \times 10^6 \mathrm{ms}^{-1}$ for the one shot and self-consistent calculations, respectively. This is in reasonable agreement to the average Fermi velocity, $0.62 \times 10^6 \mathrm{ms}^{-1}$, obtained from the integral of $v_F(\mathbf{k})$ in Fig. 4.6.

The deviations from the straight line is replicated in both datasets consistently. This implies that the positioning of the surrounding atoms coupled with the complex electronic structure are the key contributing factors to the error. In principle, creating a linear fit again but for a realistic sized cluster with a realistic superconducting gap would mitigate these issues. This is because the vast number of atoms will make their positioning arbitrary, and on the scale of the gap the normal state density for a conventional superconductor will change very little. Unfortunately, as mentioned earlier, it is currently impossible without further approximation. Despite this, the value of the Fermi velocity obtained from the fit with artificial gap sizes is within the order expected from Nb. From this, we therefore can say that our findings are realistic.

To summarise this section, we refer back to section 5.1. Here, we embedded a non-superconducting impurity into a superconductor. Despite there being no interaction on the impurity site, the superconductor induced a gap in its LDOS. Essentially the same is happening in section 5.2 where we have a superconducting impurity embedded within a normal state metal, resulting in normal electron density being induced in the superconducting impurity. It is correct to assume here that the coherence length of the superconductor defines the size of the region that must be superconducting for a gap to appear in the LDOS.

Interestingly, on first inspection the BCS expression (5.1) implies that there is a hard transition between having or not having a gap. This, however, turns out not to be the case when investigating this in practice as instead there is a smooth transition in the resulting LDOS between fully gapped and fully metallic implying the coexistence of anomalous (pairing) and electronic (normal) density. It is only when a self-consistency is performed, where we introduce a pairing interaction Λ_i, do we see that there is a transition for a particular superconducting region to have anomalous density. When Λ_i is large enough $D(\epsilon_F)$ will go to zero and we can argue at this point we have a fully superconducting state, whose gap size will be governed by (5.1).

However, for the creation of Fig. 5.5(c) a fixed value of $D(\epsilon_F) = 0.1\mathrm{meV}$ is used. Using this means there is clearly still a significant portion of electronic density at $D(\epsilon_F)$, implying that the condition $\bar{\Delta} \propto 1/\xi_0$ can be used for any value of $D(\epsilon_F)$ below the value at the normal state. This brings the discussion to the key finding from this section, which is that there are converged

solutions to this impurity setup where there is a non-zero, s-wave pairing potential yet $D(\epsilon_F) > 0$.

This bears a striking resemblance to the pseudogap regime in underdoped cuprates. In chapter 2 this was addressed in figure 2.2. Here, as a function of temperature, the gap appears not to close at T_c instead it remains open afterwards. In the case of our granular superconducting state, we cannot vary temperature in the present implementation of the code. Despite this, we can vary Λ which we can consider as varying the T_c. By looking at how the zero temperature gap behaves between $\lambda = 0.1$ and 0.7 Ry we see that the cluster is only completely able to expel normal state density at values of $\lambda = 0.7$. One could consider this as the point where the cluster is fully superconducting with a phase coherent state within the cluster. Before this we have a mixed state between normal and superconducting density.

In the case of the strongly correlated cuprate superconductor, the pseudogap phase could be considered as a state where there is anomalous density but no phase coherence. The question that still remains unanswered in cuprate superconductors is: where is this phase incoherence coming from? Theoretical modelling of the pseudogap phase has been going one for years [69]. They usually involve numerical modelling of Hubbard style Hamiltonians such as Ref. [139]. Recently P. Phillips [141] provided the first 'exactly solved' model including both Mottness and superconductivity. The strongly correlated superconducting ground state in this model is constructed from spinons and holons and perhaps the two particles may not form the coherent ground state simultaneously.

A potential future application using the KKR impurity method is to try to model this pseduogap regime using a cluster impurity method. The coherence length of $YBa_2Cu_3O_{6.9}$ films is $1.14 \pm 0.04nm$ [261], which is roughly the correct order for the clusters discussed in this report, so in principle this is computationally manageable to model small clusters of $YBa_2Cu_3O_{6.9}$. In order to solve this the d-wave order parameter would have to be derived within the KKR method.

5.3 Magnetic Impurities in the Bulk

Our investigations into impurities have so far looked at impurities that do not break time reversal symmetry. Now, however, we use the spin polarised implementation of the SR BdG equations in section 3.5.10 to investigate magnetic impurities in superconducting Pb. In s-wave phonon mediated superconductors, the most distinct effect from impurities comes from the introduction of magnetic impurities. This is evident from the first experiments including impurities. With amorphous Beryllium [26] it was shown that very little difference occurred, however with the introduction of magnetic impurities [27] we see that a reduction in T_c is evident.

Theoretically, the first attempts to model the effects of impurities on superconductors was performed by Abrikosov and Gor'kov [29] who showed that with the introduction of $\sim 1\%$ of paramagnetic impurities in a superconductor the energy gap in the spectrum would no longer correspond to the order parameter Δ. Beyond 1% it was theoretically predicted that superconduc-

tivity could exist without a gap [262] in so called 'gapless superconductivity'. The mechanism that drives this phenomena is that as the s-wave superconducting state is a spin-singlet state it is expected for a magnetic impurity to break up the Cooper pairs. In order to realise this effect theoretically, real space models were subsequently constructed by Yu [16], Shiba [17] and Rusinov [18] (YSR) using a local, one band model around a classical impurity spin. These papers predict the existence of a pair of localised, in-gap YSR states either side of the Fermi energy associated with the exchange splitting J of the spin. Recently S. Nadj-Perge *et al*. [186] suggested placing more than one impurity in a chain on the surface of a superconducting material. In this work they claimed that the peaks will hybridise and, assuming the superconducting substrate exhibits strong spin-orbit coupling, it would be possible to observe Majorana zero modes at the edges of the chain.

Experiments investigating YSR states have observed multiple pairs of in-gap states [7, 57, 249, 263, 264]. After the initial success of finding the YSR states, the magnetocrystalline impurity chains were constructed with Pb [50, 187] and Re [51] as the substrate, and both successfully observed Majorana zero modes. Despite this, a follow up experiment [188] discovered that they were able to produce zero modes, however after close inspection they found that these modes came from the YSR states and were not topological. It was therefore clear that the YSR states themselves must be investigated more carefully.

Looking at the recent experiments, it was argued that the origin of multiple YSR peaks can come from magnetic anisotropy [249], orbital character [7, 57] or modulations in the charge density [264, 265]. Ruby *et al*. [7] investigated a Mn impurity adsorbed onto the (001) surface of Pb. They argue that the multiple YSR resonances originate from the crystal field splitting of the Mn d-orbitals, and using energy considerations with real space dI/dV maps they were able to assign the relevant orbitals to the YSR resonances.

When investigating advanced systems like $NbSe_2$ [264, 265] or $\beta-Bi_2Pd$ [266] it becomes immediately obvious that disentangling hybridised YSR peaks, or YSR peaks entangled with coherence peaks will be very challenging. Symmetry arguments and energy consideration will not be enough, and another approach is desired. In this section we aim to showcase the superconducting KKR method as an alternative approach to solve this problem.

In the first part 5.3, we embed the 3d elements as an impurity in bulk fcc Pb and show that not only are there two distinct YSR resonance pairs coming from the t_{2g} and e_g orbitals, there is a significant but smaller diamagnetic response from the 's' component of the impurity contributing to a third pair of YSR resonances. These findings imply that the l-dependence of the moment is crucial, that multiple YSR states in the presence of 3d magnetic impurities cannot be attributed to the d-moment alone, and that even conventional s-wave superconductors exhibit YSR states that are not protected within the confines of the gap.

The second part 5.4 aims to build on this with the first preliminary results of investigating the surface of superconducting Pb, with the eventual goal of trying to theoretically describe the

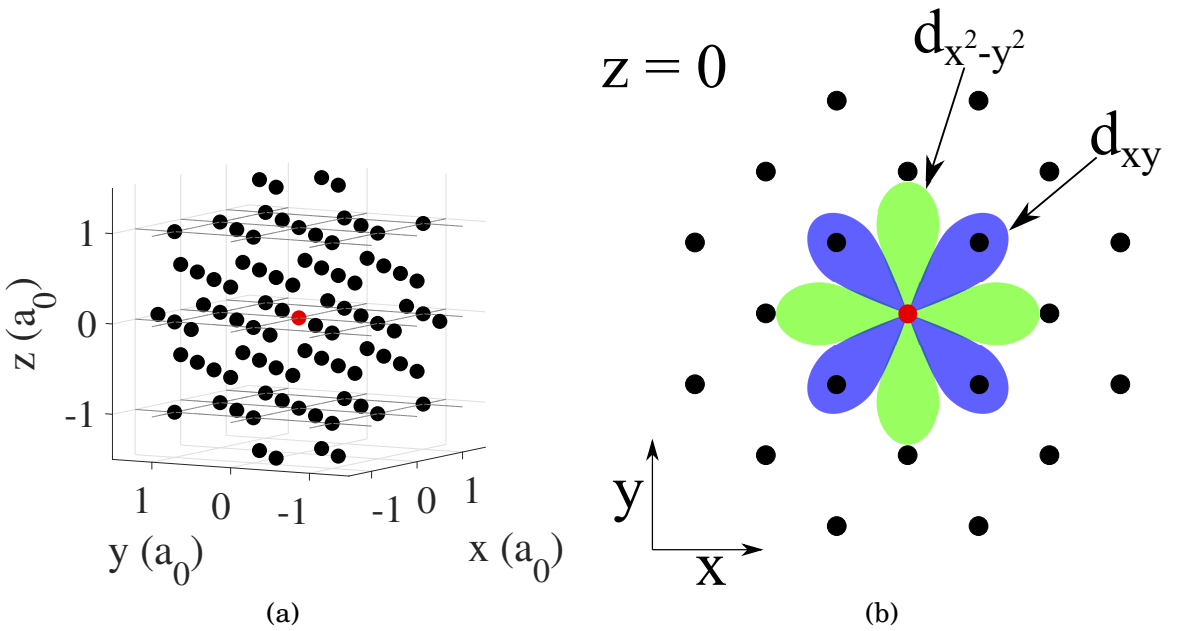

Figure 5.6: Panel (a) shows the atomic sites around the impurity atom in units of the atomic spacing, $a_0 = 4.95$Å. Black dots represent atomic sites within the cluster, the red dot represents the impurity site. Panel (b) shows the $z = 0$ crystal plane and the orientation of the $d_{x^2-y^2}$ (green) and d_{xy} (blue) orbitals.

work performed by Ruby *et al*. [7]. Calculations of (001) Pb are presented here, and it is clear from the results that the d-orbitals are split into the expected associated symmetries, however it is not always trivial to expect only d-orbitals to be present within the gap. In fact, there is even an example of a magnetic impurity that has the moment primarily coming from the d-orbitals which has no YSR peaks associated with d-orbitals. This will be explained using the electronic structure of the impurity system in the normal state.

5.3.1 Bulk

5.3.2 Normal State Analysis

To perform the superconducting magnetic impurity calculation, a cluster of atoms containing 87 atoms was constructed, as displayed in Fig. 5.6(a). Just like in section 5.1, the boundary condition is the perfect superconducting periodic crystal. In Fig. 5.6(b) the symmetry of the associated crystal structure around the impurity site is shown. The associated d-orbitals are oriented in this configuration, hence d_{xy}, d_{xz} and d_{yz} form a set of degenerate states known as the t_{2g} orbital as their wavefunctions overlap with the same number of atomic sites. Then d_{z^2} and $d_{x^2-y^2}$ form the second of the two degenerate states in this crystal system known as the e_g state.

The self consistency for the normal state was performed and Fig. 5.7(a) shows the resulting local magnetic moment from the converged solutions with each of the 3d elements embedded.

Out of the impurities, V, Cr, Mn and Fe were found to be magnetic. In an fcc structure the crystal field splits the degeneracy of the d-orbitals into the e_g and t_{2g} states. The resulting e_g and t_{2g} densities of the central impurity are extracted and shown alongside the total in Fig. 5.7(b).

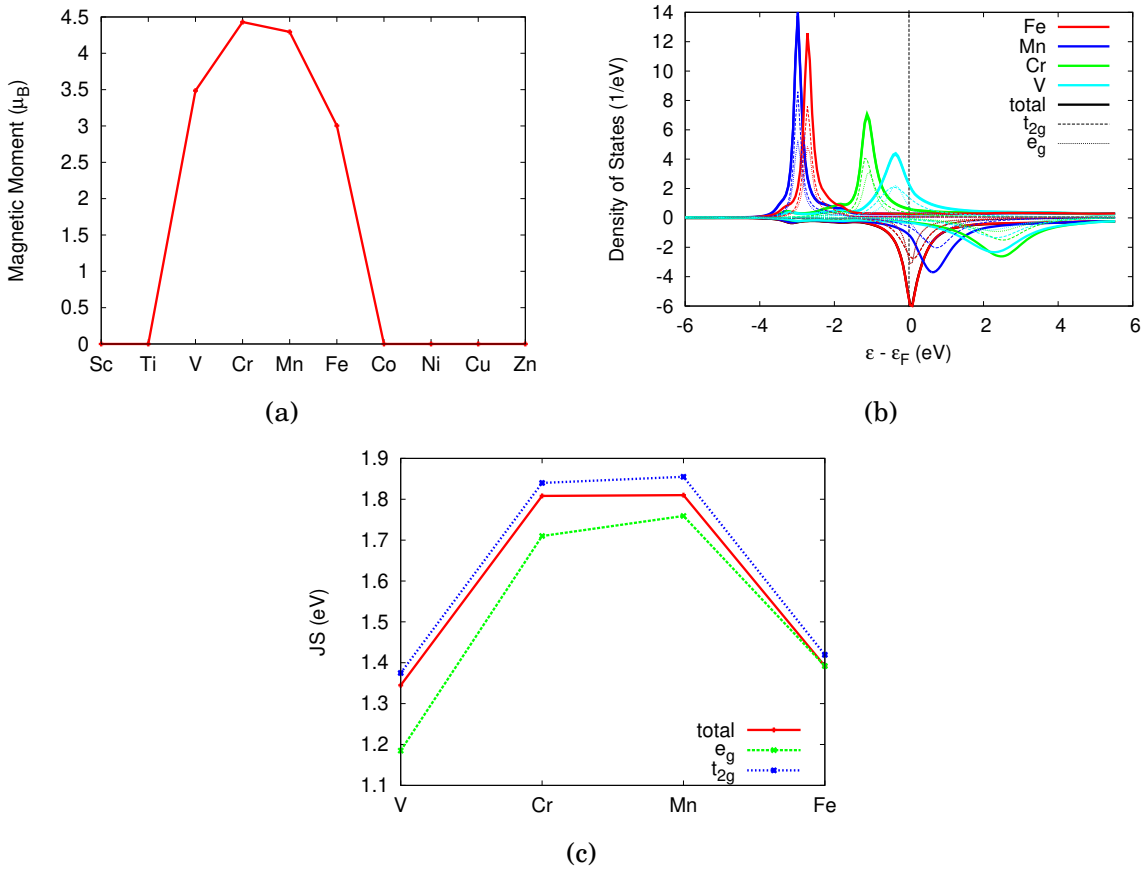

Figure 5.7: (a) The resulting local magnetic moment induced on an elemental 3d impurity when it has been embedded in a cluster of 87 Pb atoms. (b) The local, spin resolved, DOS of all magnetic impurities in the 87 atom Pb cluster in the normal state. Dashed lines represent the densities associated with the e_g and t_{2g} orbitals. (c) The value of JS for each of the impurities. Red represents the total, green represents the e_g state and blue represents the t_{2g} state.

It is clear that the e_g and t_{2g} densities are distinct from Fig. 5.7(b), however it is unclear how much the exchange splitting J differs. Therefore, it is convenient to define the spin density S and the exchange energy JS. The exchange energy can be associated with the energy splitting between spin up and spin down states. For an impurity in a vacuum JS is easy to define because the width in energy for a state is very narrow. For the definition here we use the spin up peak position, $p^{\uparrow}$, and the spin down peak position $p^{\downarrow}$ to define JS

$$JS = \frac{p^{\uparrow} - p^{\downarrow}}{2}. \tag{5.4}$$

Using this quantity it is much easier to discern the magnetic splitting of the individual crystal

Impurity atom	Cr	V	Mn	Fe
t_{2g} state (meV)	±1.13	±0.36	±1.12	±0.40
e_g state (meV)	±1.26	±0.95	±1.24	±0.48

Table 5.1: A table with the calculated energies of the in-gap bound states of the superconductor.

field split states. Fig. 5.7(c) shows this comparison between JS for each orbital and the total. There is a noticeable change, within a 100 meV, between the e_g and t_{2g} JS values, which is significantly larger than the superconducting gap Δ. This implies that the individual orbital contributions will each have separate effects on the superconducting state.

5.3.3 Superconducting state analysis

We then performed the self consistency with the embedded magnetic impurities in superconducting Pb. The LDOS around the superconducting gap for each system was calculated and the results for every magnetic impurity are displayed in Fig. 5.8. In every case, two pairs of bound states are produced, one pair from the e_g state and another from the t_{2g} states. Table 5.1 shows the associated energies of the bound states produced by embedding the impurity into the cluster. By comparing the JS values from Fig. 5.7(c) and the YSR peak separations in Table. 5.1 there is clearly a relationship between these two quantities. The first observation is that the e_g state is always closest to the edge of the gap. This is because it consistently has the smallest JS. The second observation is that as the separation of the JS values gets closer, the YSR peaks get closer together, however the relationship is non-linear.

Previous efforts to understand the relationship between JS and ϵ, the position of the YSR peak in the gap, [16–19], resulted in the derivation of an expression describing isotropic ($l = 0$) scattering,

$$\epsilon = \pm\Delta_0 \frac{1-\alpha^2+\beta^2}{\sqrt{(1-\alpha^2+\beta^2)^2+4\alpha^2}} \tag{5.5}$$

where

$$\alpha = \pi N_0 JS, \tag{5.6}$$

$$\beta = \pi N_0 V, \tag{5.7}$$

N_0 is the DOS at the Fermi level of the substrate in the normal state, and V is the non-magnetic scattering potential. By considering $\beta = 0$, the equation becomes

$$\epsilon_a^b = \pm\Delta_0 \frac{1-\left(\alpha_a^b\right)^2}{1+\left(\alpha_a^b\right)^2} \tag{5.8}$$

where a labels the orbitals e_g and t_{2g}, and b is the impurity index V, Cr, Mn, Fe and α_a^b is

$$\alpha_a^b = \pi N_0 (JS)_a^b. \tag{5.9}$$

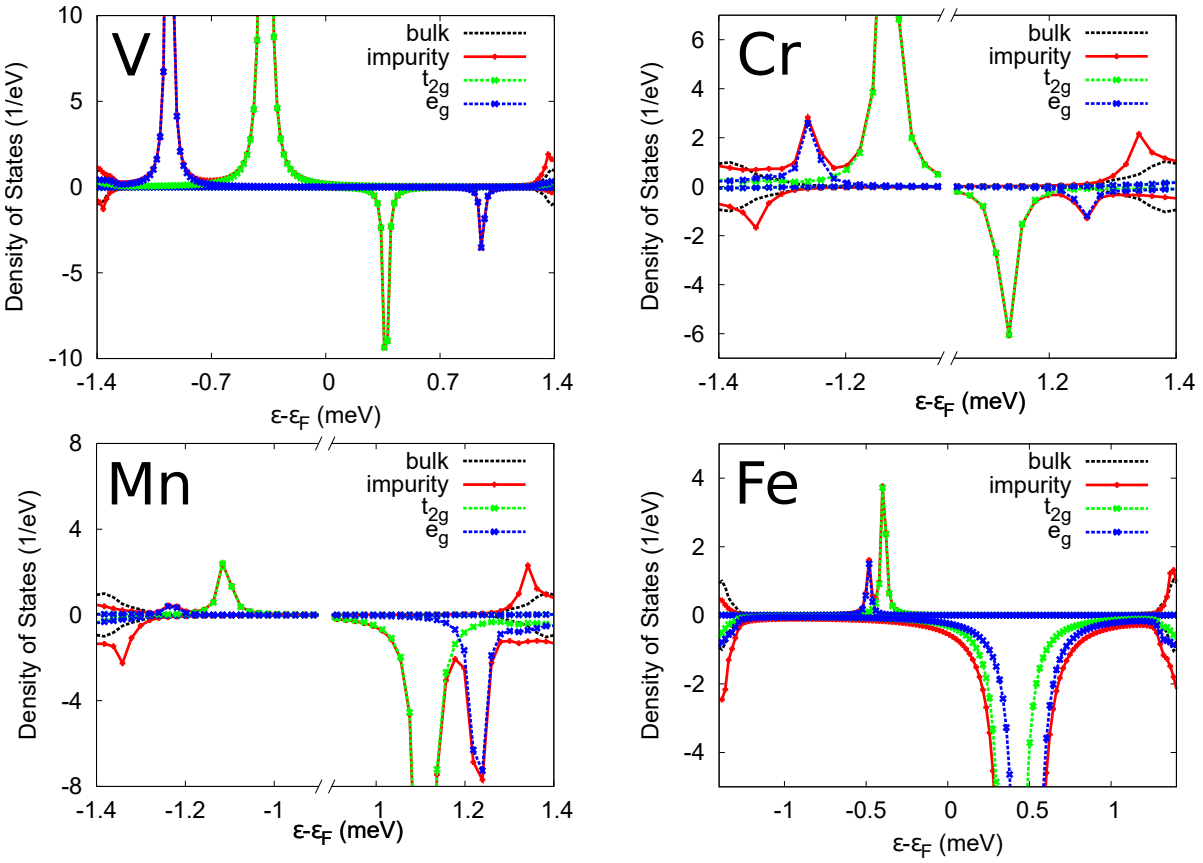

Figure 5.8: A figure of the LDOS (red) of 4 different magnetic impurities (V, Fe, Mn, Cr) plotted with the t_{2g} (green dashed) and e_g (blue dashed) densities from the impurity site, and the bulk Pb DOS (black dashed) within the energy resolution of the superconducting gap.

By taking the JS values from Fig. 5.7(c) one can obtain predictions for the energies of the YSR states. An alternative method to calculate the energies of the YSR states is also used in this report. The alternative method tries to avoid dealing with normalisation issues by calculating the YSR states with respect to a reference impurity. In this instance, Mn was chosen as the reference impurity. The method is as follows, firstly define a impurity independent constant c_a as,

$$\alpha_a^b = (JS)_a^b c_a, \tag{5.10}$$

then use Fig. 5.8 to obtain ϵ_a^{Mn} and calculate α_a^{Mn} by rearranging equation (5.8). From here, c_a is found using equation (5.10). The subsequent α_a^b's for each impurity can be found, and therefore their corresponding ϵ_a^b values. Both methods, along with the values from Fig. 5.8 are shown in Fig. 5.9. Although both methods are particularly good at describing Cr and Mn, they fall short when attempting to calculate Fe and V. In addition the 'theoretical' calculations obtain the incorrect energy ordering of the individual crystal-field split states relative to the KKR calculation. This implies that due to the complexity of the underlying electronic structure it is not possible to use such a simple model for the scattering to predict the bound states.

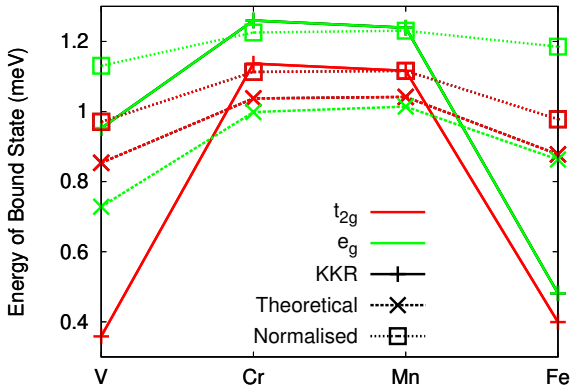

Figure 5.9: A figure comparing the positions of the peaks from Fig. 5.8 to the model Hamiltonian version from equation (5.5), which is provided by references [16–19].

The other approximation used in many experimental investigations is that only the $l = 2$ conduction electrons are considered [7]. The general consideration comes from Schrieffer [267] and is a reasonable approximation when considering the fact that the other components of the orbital will not have a strong effect on the impurity. Such constraints are not employed here, and the result is a third pair of resonances present within the superconducting gap originating from the $l = 0$ component of the density. This pair is most easily visible in the Cr and Mn panels of Fig. 5.8 and is strongly hybridised with the coherence peak. Despite this, it is still a reasonable approximation to consider just the $l = 2$ conduction electrons to get simplified picture of the underlying mechanism that drives YSR resonances. However, if the investigation of in-gap states requires analysis of the resonances close to the coherence peak or the system gets more complex, such as chains of magnetic impurities or unconventional superconductors simple models will fail profoundly.

We also investigated the angular dependence of the individual m contributions to the e_g and the t_{2g} orbitals to assess the real-space modulation of the wavefunction within the KKR method. The e_g consists of d_{z^2} and $d_{x^2-y^2}$ orbitals, and the t_{2g} orbital consists of the d_{yz}, d_{xz} and d_{xy} orbitals. Even though the total wavefunction has no angular dependence, the individual components should. Fig. 5.10 shows the results of investigating the angular dependence of the wavefunction with the Vanadium impurity. For d_{z^2} and $d_{x^2-y^2}$ orbitals, the energy chosen is $\epsilon = 0.95$meV and for d_{yz}, d_{xz} and d_{xy} the energy is $\epsilon = 0.35$meV. Although within the KKR method it is not currently possible to resolve sub-atomic distances, unlike STM experiments, the resolution is enough to visualise the angular dependence of the individual d-orbitals. For the d_{yz}, d_{xz} and d_{xy} orbitals the extremal parts of the lobes, identifiable as the red components, point clearly in the direction of the symmetry of the orbital. For example the red parts of d_{yz} and d_{xz} point along the y and x planes respectively. The same is true for d_{xy} which is oriented on the xy plane, however for $d_{x^2-y^2}$ it is less clear as it is in the same plane as d_{xy} but is rotated by 45

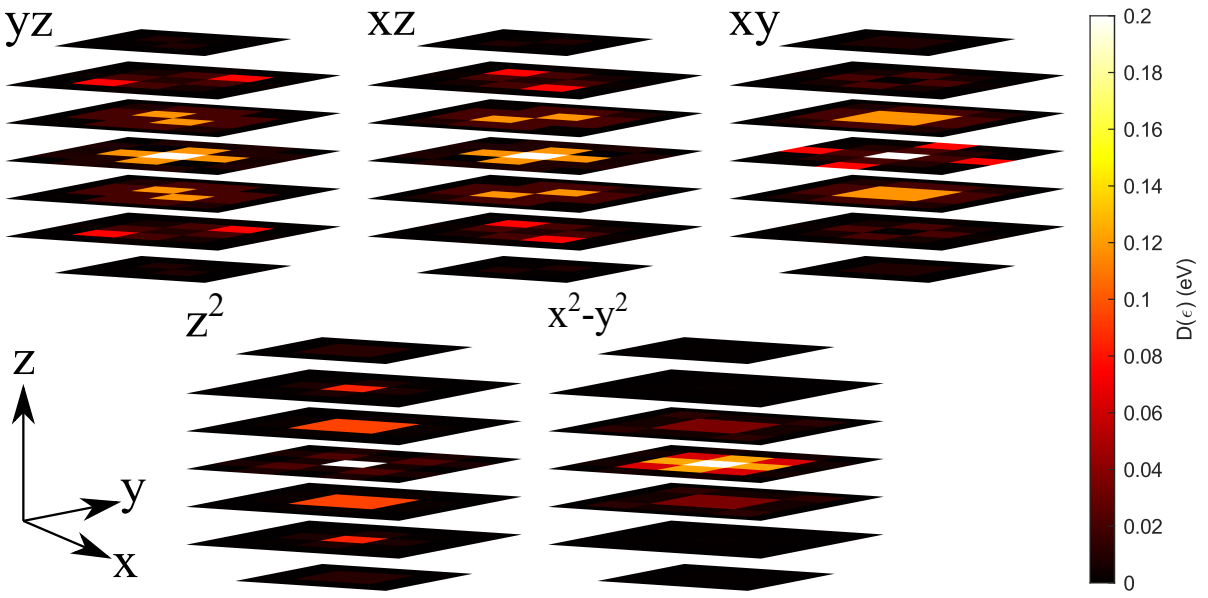

Figure 5.10: Figure of the densities of each atom centred on the spin down peak in the z={-1.50,-1.0,-0.5,0.0,0.5,1.0,1.5}a_0 planes around the impurity for Vanadium. For d_{yz}, d_{xz} and d_{xy} the energy chosen is $\epsilon = 0.36$meV and for d_{z^2} and $d_{x^2-y^2}$ $\epsilon = 0.95$meV. The colour scale is cut so that the low values are amplified and the higher peak values are saturated. These figures go to a maximum radius of 0.78nm.

degrees. Looking at Fig.5.6(b) it is evident that fewer atoms in the cluster are oriented in the direction the $d_{x^2-y^2}$ orbital meaning that it is less likely for the correct symmetry to be picked up, thus making it difficult to determine on its own. Within the KKR method an r dependent LDOS would solve this issue. This could be done by implementing the full potential KKR [213] formalism or projecting the Green's function into a maximally localised Wannier orbital basis set [268].

The height of the YSR resonance peaks in Fig. 5.8 are governed by the DOS in the normal state in Fig. 5.7(b). For example, Fe has the largest minority peak, therefore the largest spin down YSR resonance, however the majority DOS is completely below the Fermi level, meaning that the spin up YSR peaks are much smaller. This is just another example of how the underlying first principles electronic structure plays a key role in determining the behaviour in the superconducting state.

Experimentally, this setup will be challenging to investigate as probing the local electronic structure of an impurity in the bulk is complicated, and usually experiments in the bulk will either probe the thermodynamic properties such as specific heat, or they will try to probe using diffraction with x-rays or neutrons [269]. To probe local electronic structure easily, one can turn to STM. This, however, only accesses the surface states. Hence the next section will be investigating how magnetic impurities affect the surface superconducting states of Pb.

5.4 Magnetic Impurities on the Surface

This work has been performed in conjunction with Ming-Hung Wu, Emma Thill and Jacob Crosbie. Ming-Hung Wu performed the self-consistencies and calculations of the reference Green's function, which has been highlighted in section 4.2.2.2. Jacob and Emma performed the impurity self-consistencies and LDOS calculations under our supervision. This section will highlight the work they have performed and compare the resulting bound states produced from the surface to the results from Ruby *et al*. [7].

Firstly, two different impurity systems were setup in this work. The first system was an adatom on the (001) surface of superconducting Pb, which is shown in Fig. 5.11(a). The distance from the surface is $0.5a_0 \approx 2.48$Å, whereas in the real experiment the distance is 0.15Å. Due to the discrepancy between the heights of the impurity, we choose a second impurity system where the impurity is embedded in the surface as a subtitutional impurity described by Fig. 5.11(b). These two calculations clearly have their limitations with respect to the real system, however should give us a good idea of what to expect when a calculation with a proper adatom impurity site at 0.15Å is performed. These two systems have different symmetry configurations as in the adatom case the $d_{x^2-y^2}$ orbital will need to be compared to the d_{xy} orbital in the embedded case, as exemplified in Figs. 5.11(c) and (d).

Of the ten 3d elemental impurities, eight were magnetic in the adatom case, whereas in the surface six atoms were magnetic. Fig. 5.12 shows the resulting moments from the normal state. This in an interesting result compared to the moments produced in bulk Pb, in Fig. 5.7(a), where only four impurities were magnetic. The resulting overall increase in moment arises from the extra constraints the impurity has when on a surface as opposed to the bulk. On the surface, the electrons cannot flow in the positive z direction due to the presence of a vacuum, giving them a tendency to magnetise more readily than in the bulk. For the remainder of this section the key features of these results will be covered by investigating the resulting bound states produced in Mn, Co and Cr.

Investigating the effects of the Co impurity we see that for the case of the adatom in Fig. 5.13(a) there is a clear splitting of the d-orbitals into d_{xy}, $d_{yz}+d_{xz}$ (degenerate), d_{z^2} and $d_{x^2-y^2}$. This splitting of the orbitals is the same as theorised by Ruby *et al*. [7] for Mn using group theory considerations. As an embedded impurity the resulting symmetry appears to be in two groups as opposed to four, being the d_{yz}, d_{xz} and d_{z^2} orbitals as one group and the d_{xy} and $d_{x^2-y^2}$ orbitals as the other. There is a slight splitting of the d_{xy} and $d_{x^2-y^2}$ orbitals which are not identically degenerate, which could be coming from the thin film geometry.

Mn was then investigated in Fig. 5.14. The orbital ordering of the embedded and adatom impurities is compared to Ruby et al [7] in table 5.2 along with the associated energies. The energies for the embedded and adatom case do not match to experiment. This is hardly surprising because the orbital orderings for both the embedded and adatom also do not match. For both systems there are different reasons for this. In the adatom case the height of the impurity is 2.48Å,

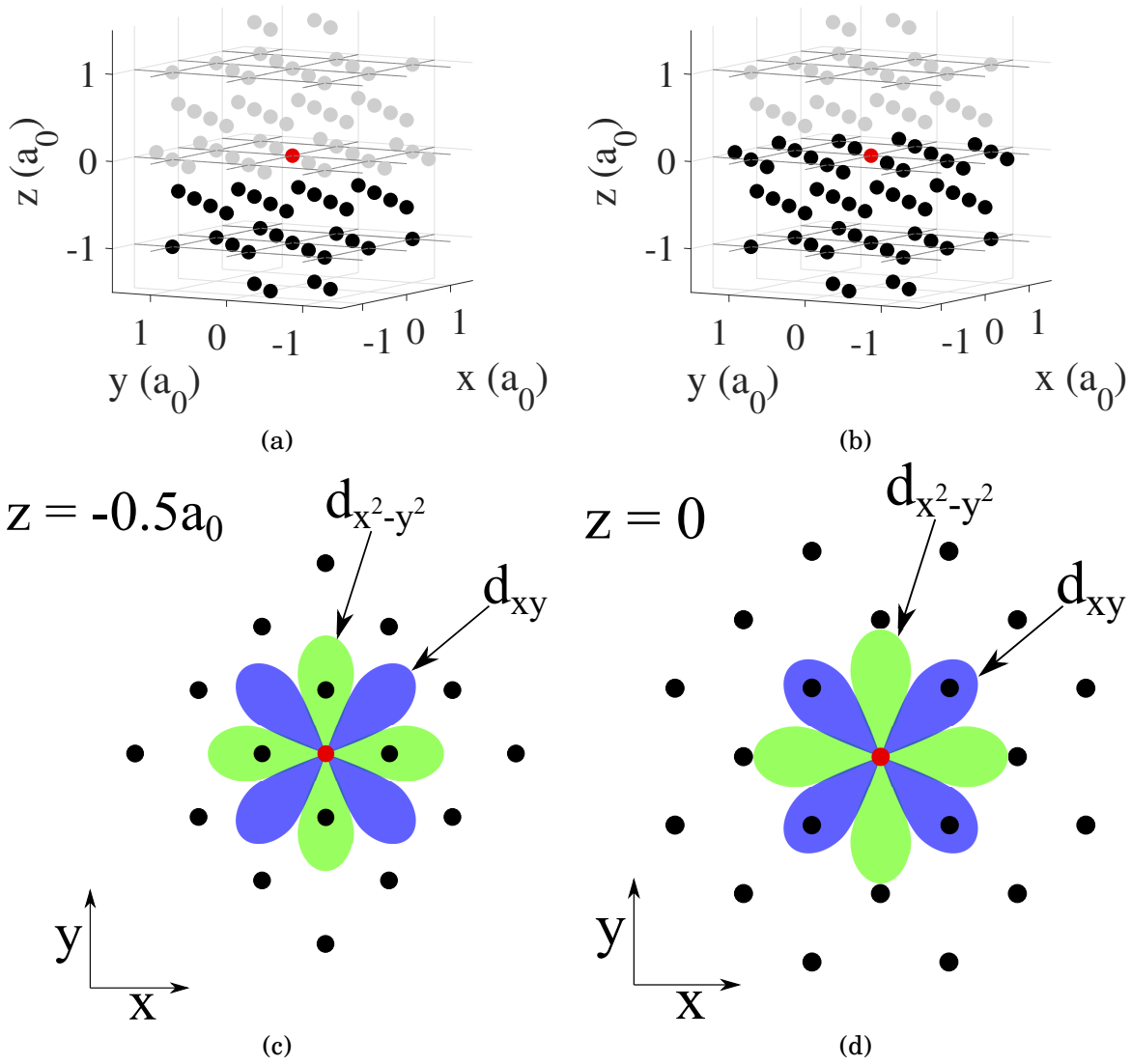

Figure 5.11: (a) Schematic diagram showing the atomic sites around the impurity adatom in units of the atomic spacing, a_0 = 4.95Å. Black dots represent a Pb atomic position, grey dots represent the positions of empty sites above the impurity, the red dot represents the impurity site (b) Similar diagram to (a), but for the embedded impurity calculation. (c) A diagram of the $z = -0.5a_0$ crystal plane and the orientation of the $d_{x^2-y^2}$ (green) and d_{xy} (blue) orbitals for the adatom impurity system. Orbitals are not to scale. (d) The same diagram as panel (c), but describing the atomic sites on the z=0 plane for the case of the embedded impurity.

whereas in Ruby *et al*. the height is 0.15Å. In the embedded impurity case the impurity is close to the experimental value however the symmetry is different. To fully realise the experimental findings from Ref. [7], an impurity embedded at 0.15Å is essential. Computationally, the most numerically stable method will be to embed the impurity at 0Å like in Fig. 5.11(b), however the difference will be that the impurity will be in between the Pb atoms as opposed to substituting a Pb atom, like in Fig. 5.11(a). The symmetry will then be in agreement with experiment, and the

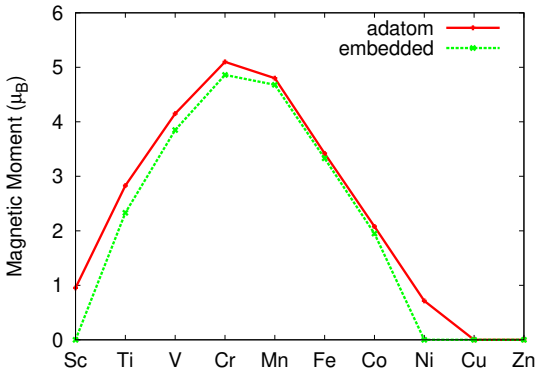

Figure 5.12: The resulting local magnetic moment induced on an elemental 3d impurity when either embedded on the surface of Pb or as an adatom, as described in panels (a) and (b) of Fig. 5.11.

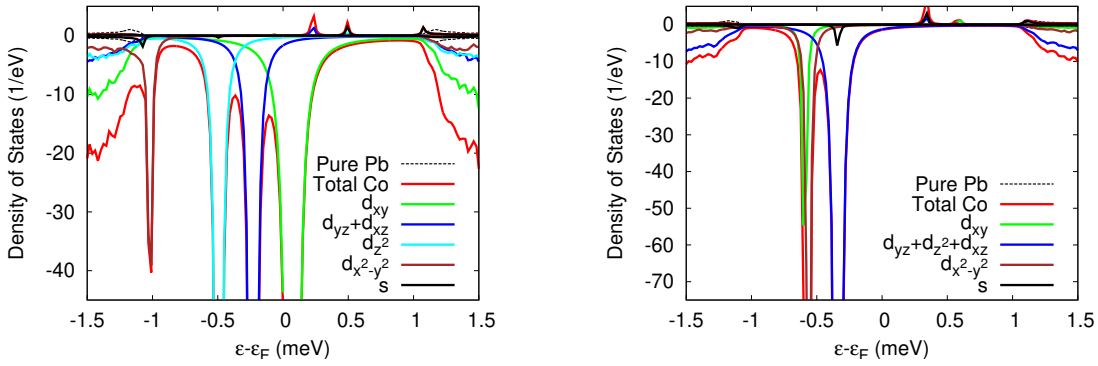

Figure 5.13: (a) The total LDOS of the adatom Co (red) on superconducting Pb compared to the pure surface Pb (black dashed). The other coloured lines are the densities of the associated orbital character. Orbitals d_{yz} and d_{xz} are combined because they are degenerate. (b) The total LDOS of the embedded Co impurity (red) on superconducting Pb compared to the pure surface Pb (black dashed). The other coloured lines are the densities of the associated orbital character. Orbitals d_{yz}, d_{z^2} and d_{xz} are combined as they are degenerate.

distance will be much more comparable.

Another feature present in Figs. 5.14(a) and (b) are the YSR peaks with density coming from s orbitals. This is unsurprising as the same was observed in bulk fcc Pb in Fig. 5.8. The spin up YSR peak for the s-orbital is below the Fermi energy and the spin down YSR peak for the s-orbital is above. This is in contrast with the YSR peaks associated with the d orbitals as their spin up peaks are above the Fermi energy, and their spin down YSR peaks lie below. Looking back at Fig. 5.8 the same feature is present, however here it is more pronounced as the s-orbital YSR peaks are closer to the centre of the gap.

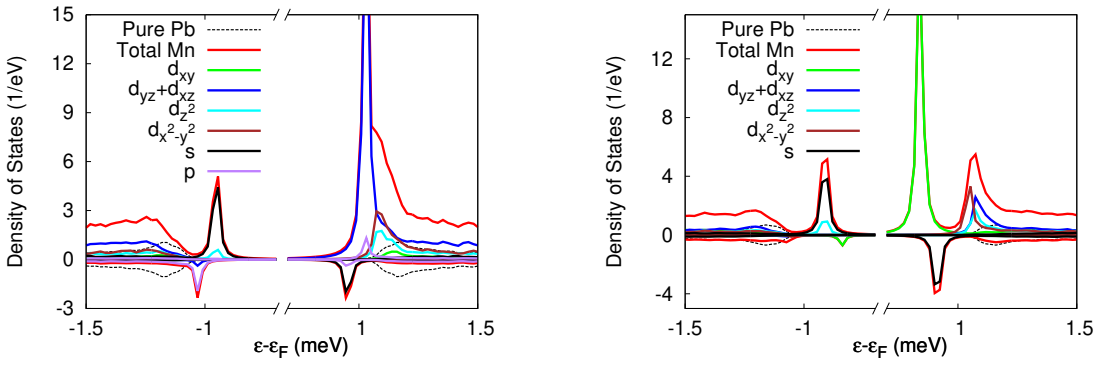

(a) (b)

Figure 5.14: (a) The total LDOS of the adatom Mn (red) on superconducting Pb compared to the pure surface Pb (black dashed). The other coloured lines are the densities of the associated orbital character. (b) The total LDOS of the embedded Mn impurity (red) on superconducting Pb compared to the pure surface Pb (black dashed). The other coloured lines are the densities of the associated orbital character.

Adatom	**Energy** (meV)	**Embedded**	**Energy** (meV)	**Experiment**	$d_a - d_{xy}$ (mV)
d_{yz}, d_{xz}	1.03	d_{xy}	0.84	d_{xy}	0
$d_{x^2-y^2}$, d_{z^2}	1.08	$d_{x^2-y^2}$	1.05	d_{yz}, d_{xz}	0
d_{xy}	1.15	d_{yz}, d_{xz}, d_{z^2}	1.07	d_{z^2}	0.51
				$d_{x^2-y^2}$	0.90

Table 5.2: The energetic ordering of the d-orbitals of a Mn impurity in the adatom position, surface position and from Ruby *et al*. [7]. The associated energies of the peaks are also written down. For the experiment, the peak energies are written down as a difference between the bias voltage of that peak (d_a, where $a = \{xz, yz, xy, x^2-y^2, z^2\}$) and the bias voltage of the d_{xy} peak. The reason for this is because the STM tip used is superconducting W, so the bias voltage for each peak is shifted by the gap from the tip.

The final result worthy of note is the results from adatom Chromium in Fig. 5.15. Here only one pair of resonances inside the superconducting gap is visible and, despite the fact that the moment is of majority d-character, the resonance is pure 's'. This arises from the fact that there is simply no density associated with a d-moment at the Fermi level in the normal state and so those resonances cannot form. Although these pure 's' states are equally present in Mn and Co they are harder to observe due to the strength of the d-orbital resonances. These findings highlight the importance of using an all-electron formalism with real impurities.

5.5 Discussions and conclusions

From section 4.2 we showed that the gap anisotropy was successfully reproduced. Here we show that in the presence of impurities, gap anisotropy gets broadened by impurity scatterers which

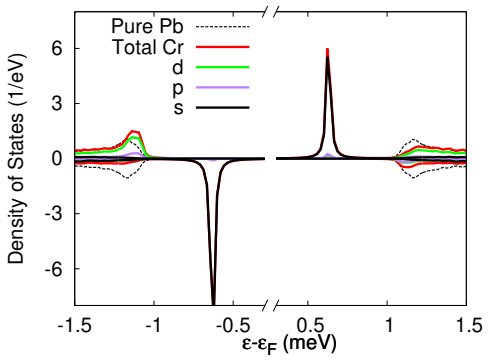

Figure 5.15: The total LDOS of the adatom Cr (red) on superconducting Pb compared to the pure surface Pb (black dashed). The other coloured lines are the densities of the associated orbital character.

contain no 'd' states as that is the main contributor to density of states around the gap. It was not possible to find an impurity which only contained 's' orbitals at this energy level, potentially obscuring the peaks entirely. However when introducing impurity scattering from Au, an element with 'p' and 'd' character close to the Fermi level, no broadening of the peaks was observed at all. This confirmed our argument and underlined the importance of the detailed knowledge of the orbital character of the impurity electrons.

After this we inverted the problem, considering the effect of a non-superconducting bulk on a cluster of superconducting impurity atoms. We found that the bulk strongly influences the impurity atoms, similar to section 5.1. The gap and the corresponding interaction parameter had to be artificially increased by approximately 1000 times in order to induce a gap within an 89 atom cluster. This is directly related to the superconducting coherence length of the superconducting material. We showed that we were able to reproduce the BCS expression of the coherence length as a function of the superconducting gap. However, we would like to highlight that we clearly observe distinct states of our system. Below a certain threshold the interaction is too weak and superconductivity is suppressed throughout the entire system. Passing a critical value we observe the formation of Cooper pairs without full phase coherence leading to a suppression of the LDOS at the Fermi energy without the formation of a full energy gap. Only upon increasing the interaction parameter further phase coherence across the system is achieved and a full gap opens. This bears a striking resemblance to the pseudogap in underoped cuprates, as displayed in Fig. 2.2 where coherence peaks persist when above superconducting transition temperature, however the gap is filled in, implying no phase coherence.

After testing superconducting clusters within a normal metal, we turned to investigating the effects of magnetic impurities. Using the numerical parameters from section 4.2.2, we then created a 87 Pb atom cluster with the boundary being pure fcc metallic crystal. From here, all of the 3d-shell elements were investigated by embedding each of them in turn into the cluster. Out

of the ten impurities, four (V, Cr, Mn, Fe) became magnetic in the normal state. Their magnetic moments are mainly due to the d-shell, however small components from s were also present. Due to crystal field splitting, the degeneracy of the d-orbitals is broken into the e_g and t_{2g} states. The exchange splitting energy JS therefore is distinct for both states, as shown in Fig. 5.7(c). This implies, from equation (5.5), that the energies for both states should be distinct, implying that in the superconducting state, two pairs of bound states should be found in the gap.

The impurities were then embedded into the superconducting Pb cluster. The potentials were calculated self-consistently, allowing both $\chi(\mathbf{r})$ and $\rho(\mathbf{r})$ to relax. The resulting LDOS for the impurity sites are plotted in Fig. 5.8, clearly showing the predicted two pairs of YSR resonances present in the impurity site. Additionally, the peaks are purely of e_g and t_{2g} character respectively. On closer inspection, however, it is also clear that a third pair of YSR resonances are found. The third resonance is clearest in Mn and Cr of Fig. 5.8, however it is present in Fe and V as well. This peak comes from the small magnetic moment present in the s-component of the DOS. The peak is strongly hybridised with the coherence peak, meaning that it would be hard to detect experimentally, however it shows that considering YSR resonances from the d-component of the density alone will ultimately not be enough. This is especially relevant considering that not only have YSR resonances like this already been investigated [265], but systems get very quickly more complex with the addition of multiple magnetic impurities.

By investigating the underlying orbital character of the e_g and t_{2g} states it is also possible to observe clearly the individual components. The orbitals d_{yz}, d_{xz}, d_{xy}, d_{z^2} and $d_{x^2-y^2}$ orbitals are plotted in Fig. 5.10 and their characteristic angular dependence is shown. This acts as a secondary confirmation of the orbital composition of both YSR peaks.

Using equation (5.8) the energies of the YSR states are predicted and compared against the results from Fig. 5.8. Two separate attempts were made using equation (5.8). The first took the normal state parameters from Fig. 5.7(b), the second fixed the Mn impurity as a reference and calculated the states associated with the other impurities using equation (5.10). Both methods were able to predict Cr to a reasonable level of accuracy, however they fall short when predicting V and Fe. It shows that the underlying complexities of describing the normal state from first principles, and the elemental impurities embedded have a strong effect on the position of the bound states. Clearly the model gives a flavour of the ensuing bound states, however they would not be able to directly predict their energies.

Finally we investigated how the magnetic impurities affect the surface of superconducting Pb. In the adatom case it was found that eight impurities were magnetic, and in the embedded case six became magnetic as shown in figure 5.13. Due to the number of results it is more important here to focus on the key findings relative to impurities in bulk Pb. For adatom Co, the energy ordering of the YSR orbitals is the same as for experimental evidence of Mn in Ruby *et al*. [7], however for our calculations with Mn the ordering does not coincide. This ultimately shows that each impurity has significantly different behaviour, and that Co matches with experimental data

for Mn may just be a coincidence. What is interesting is that on the surface the YSR resonances for both s and p orbitals are more central within the gap compared to the bulk, however their strength is still small compared to the resonances of the d-moments. There are some cases, for example adatom Cr, where only YSR resonances from the 's' component of the density are present. This is because in the normal state density the majority 'd' density was completely below the Fermi level and the minority 'd' density was completely above. The next step in performing these calculations is the need to have a more accurate impurity position that reflects the experiment. At present, the adatom case the height of the impurity is 2.48Å whereas in Ruby et al the height was 0.15Å, and in the embedded case, although the height was 0Å so arguably closer to the experiment, the symmetry is wrong and the distances from the nearest neighbour is smaller.

In summary we have shown that using a fully ab initio method to describe the normal state and a simple phenomenological parametrisation to describe the superconducting exchange correlation functional we can describe the effect of impurities on the superconducting state. Even in the presence of impurities it is still possible to observe the gap anisotropy in Nb while depending on the orbital character of the impurity atom a significant broadening of the coherence peaks can be observed. In addition, we have applied a direct method to test the coherence length of superconducting materials which is concurrent with BCS theory. Investigating the effect of superconducting impurity clusters, the dependence of the LDOS at the Fermi level behaves in the same way as the pseudogap phase in underdoped cuprate superconductors, implying the existence of Cooper pairs but no phase coherence. In addition to this, we have observed a coexistence of anomalous (pairing) as well normal (electron) density in superconducting clusters who's size are of the order of the coherence length. Finally we investigated the effects of magnetic impurities in superconducting bulk and surface Pb. In the bulk we found two YSR resonances associated with the magnetic moment from the e_g and t_{2g} orbitals were produced as predicted, along with a third YSR resonance coming from the small magnetic moment in the $l = 0$ component of the density. This highlights the need for a more sophisticated theory to describe these systems. This claim is further reinforced when the associated energies for the e_g and t_2g orbitals could not be consistently predicted using pre-existing theories. On the surface the symmetry of the d-orbitals were split not quite in the way predicted by Ruby *et al*. [7], however in the adatom case the height the impurity atom from the surface is ~ 17 times that of the experiment, and in the embedded case the symmetry is wrong, so therefore we cannot make an accurate comparison. When investigating embedded Cr impurities it was found that no YSR resonances came from d-orbitals, they were purely coming from s-orbitals. This shows that equation (5.8) gives a flavour of the associated resonances from a magnetic impurity, however to more accurately predict their formation a more sophisticated method must be employed. The BdG KKR method is presented as the solution to this, however more work needs to be done, such as accurately predicting the height of the impurity site on the surface, and investigating the effects of spin-orbit coupling on impurities in Pb.

CHAPTER 6

SUMMARY AND OUTLOOK

In chapter 2 the field of superconductivity in its present state is addressed. It investigates the various families of superconductors that have been discovered, and assesses which aspects are of current interest. For conventional superconducting materials, modelling the gap anisotropy is a key factor, specifically for materials such as MgB_2 and Pb. This is because anisotropy can enhance the T_c [6], but also creating wires with anisotropic superconductors becomes more complex [97]. In addition, the high pressure conventional systems are playing a large role in the literature today, including recent milestones such as a possible metalisation of hydrogen [125] and room temperature superconductivity in a carbonaceous sulphur hydride [131]. Strongly correlated superconducting families such as the cuprates [33, 132, 270], iron pnictides [143] and heavy Fermion systems [163] all have a key role to play in high temperature superconductivity, however theoretical methods to describe these systems are ongoing [141]. One of the most elusive quantities is the pseudogap which, described in Fig. 2.2, is a phase that occurs above the T_c where a gap appears in the excitation spectrum which has non-zero density at the Fermi level. This suggests that within this phase there are pre-formed incoherent cooper pairs, a phenomena also observed in amorphous systems [259]. Finally, engineering topological superconducting states has been of intense interest within the community due to the possible realisation of Majorana fermions [66], which could have a great application within the field of quantum computation [52]. Experimentally these exotic states have been discovered at the interface between topological insulators and s-wave superconductors [179, 180], Rashba-split semiconductors [185] and chains of magnetic impurities on superconductors [50, 51].

In chapter 3 the theoretical method for describing how impurities effect the superconducting state is addressed. To start, the BCS equations are introduced, along with their limitations and how they are rectified by later works. From here the Bogoliubov de-Gennes equations are

introduced, along with investigating the properties of $u_{\mathbf{k}}$ and $v_{\mathbf{k}}$. The Bogoliubov formalism is then incorporated into density functional theory, and from here the Green's function method is introduced. The Green's function is then written in the multiple scattering formalism, and the various technical details of how to extend the KKR formalism to incorporate superconductivity is addressed. It is then shown how to spin polarise the KKR equations, leading to spin polarised superconducting KKR. Next, the method of incorporating impurities via substitution is extended to the superconducting formalism. Finally the Dirac-Bogoliubov-de Gennes equations along with its implementation is discussed in order to introduce spin-orbit coupling.

In chapter 4 the numerical robustness of this method is addressed. In order to have a state which is converged in a computationally efficient manner, a k-mesh of at least 2×10^5 k-points in the irreducible Brillouin zone is required, and an energy mesh of 50 energy points is also desired. The comparison between a scalar relativistic superconducting calculation compared to a non relativistic superconducting calculation as a function of atomic number is addressed. The choice of Λ is then elaborated on. Initially we used Gaspari-Győrffy theory [219] to try and calculate Λ from first principles, however some of the materials were an order of magnitude incorrect compared to experimental values showing that this method cannot be used for material prediction. To avoid this issue, Λ was then treated as a tunable parameter which was matched to the zero temperature gap size from experiments. Finally we discuss the relationship between $\Delta_{eff}(\mathbf{r})$ and $\Delta(\mathbf{k})$. In a simplified one band picture the relationship is direct, however within this formalism due to the complex underlying electronic structure the relationship becomes more complex.

In the second part of chapter 4 the gap anisotropy of the conventional superconductors Nb, Pb and MgB_2 is discussed. For Nb three different coherence peaks are observed, all with comparable energy separation to experiment. Attempting to relate this to the Fermi velocity in Fig. 4.6(a), in order to match the BCS description in equation (4.4), it is obvious that the more decoupled Fermi surface sheet behaves like a BCS superconductor, however the sheet with the more complex Fermi surface gap structure and orbital character diverges from that description. The materials Pb and MgB_2 follow essentially the same story where the only major different property is that MgB_2, although with the same level of anisotropy, has three coherence peaks as opposed to two as experiments suggest. This could be explained by the presence of three coherence peaks in thin films of MgB_2 [256], which disappear when adding extra monolayers.

Chapter 5 is divided into four sections. Section 5.1 of chapter 5 investigates the effect of non-magnetic impurities on superconductors. Nb is used as the bulk superconductor, and when the impurity nitrogen is added, it is observed that the local density of states of the nitrogen atom observes the induction of a gap of the same magnitude as Nb, however the outer coherence peak is suppressed relative to the bulk. Observing the nearest neighbour Nb atoms to the impurity it is clear that scattering is causing broadening of the coherence peaks, making them more difficult to measure. Alternatively, replacing nitrogen with a gold atom produces no scattering as there

are sufficient p and d states in this impurity.

Section 5.2 is focused primarily on investigating how a superconducting impurity interacts with non superconducting bulk. The aim of this section is to investigate what happens to the superconducting gap when we are at the limit of the coherence length. This section is purely theoretical as the cluster size of the system is 89 atoms which corresponds to a diameter of 1.4nm, much too small for a conventional superconductor such as Nb which has a coherence length of 38 nm, so the gap size had to be amplified by 1000 times. It was shown that the induction of the gap in the density of states was gradual, like in Fig. 5.3(a), and there was no sudden zero density at ϵ_F. This was a surprising result as it was expected that the gap would be either completely induced, or not there at all. It was then found that the interaction parameter Λ in Fig. 5.5(b) experienced a converged superconducting solution only once over the threshold. This relationship, as a function of cluster radius, fulfils the BCS coherence length equation (5.1). This solution is very similar to the pseudogap phase in underdoped cuprates [11].

Section 5.3 of chapter 5 investigates how magnetic impurities affect the superconducting state. Pb was the chosen superconductor, and all d-shell impurities were tested in the material, whereupon it was found that V, Cr, Mn and Fe were magnetic. Fig. 5.8 shows the in-gap states produced on the local impurity site by the magnetic impurities. It has shown that two YSR resonances associated with the magnetic moment from the e_g and t_{2g} orbitals were produced as predicted, along with a third YSR resonance coming from the small magnetic moment in the $l = 0$ component of the density, highlighting the need for a more sophisticated theory to describe these systems. This claim is further reinforced when the associated energies for the e_g and t_{2g} orbitals could not be consistently predicted using pre-existing theories in Fig. 5.7(c). In each case, two pairs of YSR resonances were produced, with one pair associated with the e_g orbital and the other associated with the t_{2g} as predicted from pre existing theories. A third pair of resonances is also discovered quite close to the coherence peaks coming purely from s orbitals, highlighting that a more sophisticated theory must be established to predict these states consistently. This is further reinforced when trying to predict associated energies for the e_g and t_{2g} orbitals could not be consistently predicted using pre-existing theories.

Finally, the effect of magnetic impurities on the surface of superconducting (001) Pb was investigated in 5.4. Two systems were constructed, an adatom case and an embedded case, displayed in Fig. 5.11, with the aim to describe the experiments by Ruby *et al*. [7]. Although both the adatom and embedded impurity setups did not match to their work, there was clear reasoning as to why this occurred. Firstly for the adatom case the impurity height was 17 times the height of the impurity in Ref. [7], and for the embedded case the symmetry was different. These changes, however, only further reinforce the findings from section 5.3 that a more sophisticated model is required, it also highlights the fact that every experiment must be coupled with material specific calculations. Furthermore, the future aim will be to focus on creating an impurity environment that more closely models the work performed in the experiment.

Future challenges

Experiments by Ruby *et al*. probe the influence of magnetic impurities placed on the surface of superconducting Pb [7, 189]. The presented formalism solves for such impurity systems, enabling the study of localised Yu-Shiba-Rusinov states [7, 49, 50]. The ultimate direction of this will be to generate chains of magnetic impurities as this has been shown to generate Majorana zero modes at the edges of the chain [50, 53, 187]. In order to fully describe how a chain of magnetic impurities affect a superconductor, implementation of the fully relativistic, non-colinear BdG solver must be performed. The formalism for this is present in the paper by G. Csire *et al*. [62], and so all that is left is for the extension to impurities. Spin dependent transport in superconductors is already of strong interest [271, 272] and has been formulated using the Bogoliubov de Gennes equation in a tight-binding formalism [273]. Spin dependent transport for conventional conductors using the Boltzmann method [274] including extrinsic effects due to impurities [275] has already been done for conventional conducting materials with the KKR method, so the extension to superconductivity is within reach. The alternative method for modelling spin dependent transport is with the Kubo formula [276–278], which can be done combined with the coherent potential approximation (CPA) [279–281] which is a powerful tool to describe the macroscopic effects of high concentrations of impurities. These extensions would enable a theoretical description to describe the spin hall effect in superconductors which has already been observed in Ref.[272]. This effect is exciting because in that work the signal was enhanced dramatically compared to the normal state. To more accurately model these materials it would be beneficial to extend the superconducting KKR method to full potential [214] as access to the interstitial region is still a large challenge. Such methods would be beneficial to describe the Van de Waals materials such as twisted bilayer graphene [14]. Pushing this aspect will, in addition, require the modelling of unconventional superconductivity. The p-wave order parameter has already been implemented into the KKR formalism to describe the superconductor $LaNiC_2$ [63]. Strongly correlated superconductivity has recently been solved exactly using a simplified model [141], and could be extended the KKR formalism. Another route to realise strong correlations is by using implementations of DMFT [282, 283] or the GW [118, 284] approximations. A combined approach for solving DMFT and the GW approximation has been implemented into the LMTO code Questaal [140]. In addition using the KKR method to model the underlying electronic structure of Sr_2RuO_4 [246] would be very powerful. The main problem with modelling this material is that the KKR formalism must be extended to describe non-local pairing. This is a major challenge as the t-matrix method relies on localised potentials.

APPENDIX A

SCALAR RELATIVISTIC SOLVER

This appendix details the information on how to calculate the regular $\mathbf{R}_{lm}(\epsilon, \mathbf{r})$ and irregular $\mathbf{H}_{lm}(\epsilon, \mathbf{r})$ solutions to the wavefunctions. The scalar relativistic BdG equations can be derived by starting at the relativistic Dirac BdG equations and neglecting the spin-orbit coupling term. More detail is described in G. Csire's thesis [64], in addition the full explicit derivation for the non-superconducting case can be found in Zabloudil [213]. One fundamental difference between the derivation used in this method and G. Csire's is that the relativistic corrections to the pairing potential are omitted in his work, whereas here I chose to keep them as one could argue that this is the more formally exact description of the scalar relativistic BdG equations. This is because with the extra term included the t-matrix obtains an extra symmetry, namely,

$$t_l^{eh}(\epsilon + i0) = t_l^{eh}(-\epsilon + i0) \tag{A.1}$$

$$t_l^{he}(\epsilon + i0) = t_l^{he}(-\epsilon + i0) \tag{A.2}$$

which is a symmetry present in the fully relativistic implementation with spin-orbit coupling scaled to zero. As the 'scalar relativistic' equations are historically supposed to contain all of the relativistic corrections to the Schrödinger equation except for spin orbit coupling, this seems to be the more natural choice. The resulting solution to, for example, the density with or without these terms is negligible, however for the purposes of testing both solvers this change is invaluable.

In order to solve the radial equations effectively a logarithmic mesh is chosen such that $r = e^x$ so that more points are chosen for the low r values. In addition the wavefunctions are solved using,

$$P_l^{ab}(\epsilon, x) = e^x R_l^{ab}(\epsilon, x) \tag{A.3}$$

such that the functions are more numerically stable. It is possible to split the Bogoliubov-de Gennes equations from two 2nd order differential equations into four 1st order differential equations, giving,

$$\frac{d}{dx}Q_l^{ea}(\epsilon,x) = -Q_l^{ea}(\epsilon,x) + U_l^e(\epsilon,x)P_l^{ea}(\epsilon,x) + e^x\Delta(x)P_l^{ha}(\epsilon,x), \tag{A.4}$$

$$\frac{d}{dx}Q_l^{ha}(\epsilon,x) = -Q_l^{ha}(\epsilon,x) + U_l^h(\epsilon,x)P_l^{ha}(\epsilon,x) + e^x\Delta^*(x)P_l^{ea}(\epsilon,x), \tag{A.5}$$

$$\frac{d}{dx}P_l^{ea}(\epsilon,x) = P_l^{ea}(\epsilon,x) + e^x B_l^e(\epsilon,x)Q_l^{ea}(\epsilon,x) - \frac{e^x\Delta(x)}{c^2}Q_l^{ha}(\epsilon,x), \tag{A.6}$$

$$\frac{d}{dx}P_l^{ha}(\epsilon,x) = P_l^{ha}(\epsilon,x) + e^x B_l^h(\epsilon,x)Q_l^{ha}(\epsilon,x) - \frac{e^x\Delta^*(x)}{c^2}Q_l^{ea}(\epsilon,x), \tag{A.7}$$

where,

$$U^e(\epsilon,x) = \frac{l(l+1)}{e^x B^e(\epsilon,x)} + e^x(V(x)-\epsilon), \tag{A.8}$$

$$U^h(\epsilon,x) = \frac{l(l+1)}{e^x B^h(\epsilon,x)} + e^x(V(x)+\epsilon), \tag{A.9}$$

$$B_l^e(\epsilon,x) = 1 + \frac{\epsilon - V(r)}{c^2}, \tag{A.10}$$

$$B_l^h(\epsilon,x) = 1 - \frac{\epsilon + V(r)}{c^2}. \tag{A.11}$$

The conventional way to solve this is with a Runge-Kutte solver for 4 points, and then a predictor-corrector algorithm for the remaining points. The starting values for the wavefunctions can be found by, $x \to \infty$ giving,

$$P_l^{ee}(\epsilon,x_1) = 10^{-20}, \tag{A.12}$$

$$Q_l^{ee}(\epsilon,x_1) = \frac{c^2}{2Z}\left(\frac{-1+\sqrt{l(l+1)+1-b^2}}{b/c}\right)P_l^{ee}(\epsilon,x_1), \tag{A.13}$$

$$P_l^{he}(\epsilon,x_1) = 0, \tag{A.14}$$

$$Q_l^{he}(\epsilon,x_1) = 0, \tag{A.15}$$

where $b = 2Z/c$, and,

$$P_l^{eh}(\epsilon,x_1) = 0, \tag{A.16}$$

$$Q_l^{eh}(\epsilon,x_1) = 0, \tag{A.17}$$

$$P_l^{hh}(\epsilon,x_1) = 10^{-20}, \tag{A.18}$$

$$Q_l^{hh}(\epsilon,x_1) = \frac{c^2}{2Z}\left(\frac{-1+\sqrt{l(l+1)+1-b^2}}{b/c}\right)P_l^{hh}(\epsilon,x_1), \tag{A.19}$$

In order to solve the irregular solutions the same equations are used, however it starts at muffin tin radius and is solved backwards. For further reading I refer to Csire [64] for the starting solution derivation and to Zabloudil [213] for the numerical algorithms for solving the equations.

APPENDIX B

FULLY RELATIVISTIC SOLVER

This appendix details the information on how to calculate the regular $\mathbf{R}_{lm}(\epsilon,\mathbf{r})$ and irregular $\mathbf{H}_{lm}(\epsilon,\mathbf{r})$ solutions to the wavefunctions. In order to do this, the Dirac-Bogoliubov-de Gennes equation must be expanded into scattering solutions. Assuming s-wave pairing, the equations become,

$$\begin{aligned}
\frac{d}{dr}Q^{ea}_{\kappa\mu\kappa\mu}(z,r) &= \frac{\kappa}{r}Q^{ea}_{\kappa\mu\kappa\mu}(z,r) - (E_F+z)P^{ea}_{\kappa\mu\kappa\mu}(z,r) + (-1)^{-\mu-1/2}S_\kappa D(r)P^{ha}_{\kappa-\mu\kappa\mu}(z,r) \\
&\quad + \sum_{\kappa\mu\kappa'\mu'} u^{++}_{\kappa\mu\kappa'\mu'}P^{ea}_{\kappa'\mu'\kappa\mu}(z,r) \\
\frac{d}{dr}Q^{ha}_{\kappa-\mu\kappa\mu}(z,r) &= \frac{\kappa}{r}Q^{ha}_{\kappa-\mu\kappa\mu}(z,r) - (E_F-z)P^{ha}_{\kappa-\mu\kappa\mu}(z,r) + (-1)^{\mu-1/2}S_\kappa D(r)P^{ea}_{\kappa\mu\kappa\mu}(z,r) \\
&\quad + \sum_{\kappa-\mu\kappa'\mu'} (u^{++}_{\kappa\mu\kappa'\mu'})^* P^{ha}_{\kappa'\mu'\kappa\mu}(z,r) \\
\frac{d}{dr}P^{ea}_{\kappa\mu\kappa\mu}(z,r) &= -\frac{\kappa}{r}P^{ea}_{\kappa\mu\kappa\mu}(z,r) + (\frac{E_F+z}{c^2}+1)Q^{ea}_{\kappa\mu\kappa\mu}(z,r) - \frac{1}{c^2}(-1)^{-\mu-1/2}S_\kappa D(r)Q^{ha}_{\kappa-\mu\kappa\mu}(z,r) \\
&\quad - \sum_{\kappa\mu\kappa'\mu'} \frac{1}{c^2}u^{--}_{\kappa\mu\kappa'\mu'}Q^{ea}_{\kappa'\mu'\kappa\mu}(z,r) \\
\frac{d}{dr}P^{ha}_{\kappa-\mu\kappa\mu}(z,r) &= -\frac{\kappa}{r}P^{ha}_{\kappa-\mu\kappa\mu}(z,r) + (\frac{E_F-z}{c^2}+1)Q^{ha}_{\kappa-\mu\kappa\mu}(z,r) - \frac{1}{c^2}(-1)^{\mu-1/2}S_\kappa D(r)Q^{ea}_{\kappa\mu\kappa\mu}(z,r) \\
&\quad - \sum_{\kappa-\mu\kappa'\mu'} \frac{1}{c^2}(u^{--}_{\kappa\mu\kappa'\mu'})^* Q^{ea}_{\kappa'\mu'\kappa\mu}(z,r)
\end{aligned}$$

where,

$$u^{++}_{\mu\kappa\mu'\kappa'}(\epsilon,r) = V(r) + \langle\chi_{\kappa\mu}|\sigma_z B(r)|\chi_{\kappa'\mu'}\rangle, \qquad u^{--}_{\mu\kappa\mu'\kappa'}(\epsilon,r) = V(r) - \langle\chi_{\kappa\mu}|\sigma_z B(r)|\chi_{\kappa'\mu'}\rangle, \tag{B.1}$$

and the wavefunctions

$$Q^{ab}_{\kappa\mu\kappa'\mu'}(z,r) = \hbar c r f^{ab}_{\kappa\mu\kappa'\mu'}(z,r), \qquad P^{ab}_{\kappa\mu\kappa'\mu'}(z,r) = r g^{ab}_{\kappa\mu\kappa'\mu'}(z,r). \tag{B.2}$$

Expanding the matrix elements

$$\langle\chi_{\kappa\mu}|\sigma_z B(r)|\chi_{\kappa'\mu'}\rangle = \delta_{ll'}\delta_{\mu\mu'}B_{\kappa\kappa'\mu}(r), \qquad \langle\chi_{\bar{\kappa}\mu}|\sigma_z B(r)|\chi_{\bar{\kappa}'\mu'}\rangle = \delta_{\bar{l}\bar{l}'}\delta_{\mu\mu'}\bar{B}_{\kappa\kappa'\mu}(r), \tag{B.3}$$

one obtains,

$$\begin{aligned}
\frac{d}{dx}Q^{ea}_{\kappa\mu\kappa\mu}(z,x) =& \kappa Q^{ea}_{\kappa\mu\kappa\mu}(z,x) - e^x(E_F + z - V(x))P^{ea}_{\kappa\mu\kappa\mu}(z,x) + e^x(-1)^{-\mu-1/2}S_\kappa D(x)P^{ha}_{\kappa-\mu\kappa\mu}(z,x) \\
&+ e^x\sum_{\kappa\kappa'}B_{\kappa\kappa'\mu}(x)P^{ea}_{\kappa'\mu\kappa\mu}(z,x), \\
\frac{d}{dx}Q^{ha}_{\kappa-\mu\kappa\mu}(z,x) =& \kappa Q^{ha}_{\kappa-\mu\kappa\mu}(z,x) - e^x(E_F - z - V(x))P^{ha}_{\kappa-\mu\kappa\mu}(z,x) + e^x(-1)^{\mu-1/2}S_\kappa D(x)P^{ea}_{\kappa\mu\kappa\mu}(z,x) \\
&+ e^x\sum_{\kappa\kappa'}B^*_{\kappa\kappa'\mu}(x)P^{ha}_{\kappa'\mu\kappa\mu}(z,x), \\
\frac{d}{dx}P^{ea}_{\kappa\mu\kappa\mu}(z,x) =& -\kappa P^{ea}_{\kappa\mu\kappa\mu}(z,x) + e^x(\frac{E_F + z - V(x)}{c^2} + 1)Q^{ea}_{\kappa\mu\kappa\mu}(z,x) - e^x\frac{1}{c^2}(-1)^{-\mu-1/2}S_\kappa D(x)Q^{ha}_{\kappa-\mu\kappa\mu}(z,x) \\
&- e^x\sum_{\kappa\kappa'}\frac{1}{c^2}\bar{B}_{\kappa\kappa'\mu}(x)Q^{ea}_{\kappa'\mu\kappa\mu}(z,x), \\
\frac{d}{dx}P^{ha}_{\kappa-\mu\kappa\mu}(z,x) =& -\kappa P^{ha}_{\kappa-\mu\kappa\mu}(z,x) + e^x(\frac{E_F - z - V(x)}{c^2} + 1)Q^{ha}_{\kappa-\mu\kappa\mu}(z,x) - e^x\frac{1}{c^2}(-1)^{\mu-1/2}S_\kappa D(x)Q^{ea}_{\kappa\mu\kappa\mu}(z,x) \\
&- e^x\sum_{\kappa\kappa'}\frac{1}{c^2}\bar{B}^*_{\kappa\kappa'\mu}(x)Q^{ha}_{\kappa'\mu\kappa\mu}(z,x),
\end{aligned}$$

where the non-zero quantities are,

$$\begin{aligned}
B_{\kappa,\kappa,\mu}(r) &= -\frac{\mu B(r)}{\kappa + 1/2}, \\
\bar{B}_{\kappa,\kappa,\mu}(r) &= \frac{\mu B(r)}{\kappa - 1/2}, \\
B_{\kappa,-\kappa-1,\mu}(r) &= B_{-\kappa-1,\kappa,\mu}(r) = -\sqrt{1-\left(\frac{\mu}{\kappa+1/2}\right)^2}B(r), \\
B_{-\kappa-1,-\kappa-1,\mu}(r) &= \frac{\mu B(r)}{\kappa + 1/2}, \\
\bar{B}_{-\kappa-1,-\kappa-1,\mu}(r) &= -\frac{\mu B(r)}{\kappa + 3/2},
\end{aligned}$$

and thus there is a total of eight coupled differential equations. The starting values can be obtained by the same method as before and they follow a similar format. The difference is that the equations can be separated into two cases,

B.0.0.1 Case 1: $\kappa = -l-1,\ \mu = \pm(l+1/2)$

In this case the expression,

$$\sqrt{1-\left(\frac{\mu}{\kappa+1/2}\right)^2} = \sqrt{1-\left(\frac{l+1/2}{l+1/2}\right)^2} = 0, \tag{B.4}$$

$$B_{\kappa,-\kappa-1,\mu}(r) = B_{-\kappa-1,\kappa,\mu}(r) = 0 \tag{B.5}$$

Which means the coupled differential equations reduce from eight to four, and the starting values for this special case are,

$$
\begin{aligned}
P^{ee}_{-l-1,\mu,-l-1,\mu}(x_1) &= 10^{-20}, \\
Q^{ee}_{-l-1,\mu,-l-1,\mu}(x_1) &= \left(\frac{-l-1+\sqrt{(l+1)^2-b^2}}{b/c}\right) P^{ee}_{-l-1,\mu,-l-1,\mu}(x_1) \\
P^{he}_{-l-1,-\mu,-l-1,\mu}(x_1) &= 0, \\
Q^{he}_{-l-1,-\mu,,-l-1,\mu}(x_1) &= 0
\end{aligned}
$$

and

$$
\begin{aligned}
P^{eh}_{-l-1,\mu,-l-1,-\mu}(x_1) &= 0, \\
Q^{eh}_{-l-1,\mu,-l-1,-\mu}(x_1) &= 0, \\
P^{hh}_{-l-1,-\mu,-l-1,-\mu}(x_1) &= 10^{-20}, \\
Q^{hh}_{-l-1,-\mu,-l-1,-\mu}(x_1) &= \left(\frac{-l-1+\sqrt{(l+1)^2-b^2}}{b/c}\right) P^{hh}_{-l-1,-\mu,-l-1,-\mu}(x_1)
\end{aligned}
$$

B.0.0.2 Case 2: $\kappa = l,\ \kappa = -l-1,\ |\mu| < l + 1/2$

For the second case the starting values are muich the same as before, however there are 8 terms considered for the differential equation. This means that there are 4 sets of starting values. These are listed below:
Starting values 1,

$$
\begin{aligned}
P^{ee}_{l,\mu,l,\mu}(x_1) &= 10^{-20}, \\
Q^{ee}_{l,\mu,l,\mu}(x_1) &= \left(\frac{l+\sqrt{l^2-b^2}}{b/c}\right) P^{ee}_{l,\mu,l,\mu}(x_1), \\
P^{ee}_{-l-1,-\mu,l,\mu}(x_1) &= Q^{ee}_{-l-1,-\mu,l,\mu}(x_1) = 0, \\
P^{he}_{l,-\mu,l,\mu}(x_1) &= Q^{he}_{l,-\mu,l,\mu}(x_1) = 0, \\
P^{he}_{-l-1,-\mu,l,\mu}(x_1) &= Q^{he}_{-l-1,-\mu,l,\mu}(x_1) = 0.
\end{aligned}
$$

Starting values 2,

$$\begin{aligned}
P^{ee}_{l,\mu,-l-1,\mu}(x_1) &= Q^{ee}_{l,\mu,-l-1,\mu}(x_1) = 0,\\
P^{ee}_{-l-1,\mu,-l-1,\mu}(x_1) &= 10^{-20},\\
Q^{ee}_{-l-1,\mu,-l-1,\mu}(x_1) &= \left(\frac{-l-1+\sqrt{(l+1)^2-b^2}}{b/c}\right) P^{ee}_{-l-1,\mu,-l-1,\mu}(x_1),\\
P^{he}_{l,-\mu,-l-1,\mu}(x_1) &= Q^{he}_{l,-\mu,-l-1,\mu}(x_1) = 0,\\
P^{he}_{-l-1,-\mu,-l-1,\mu}(x_1) &= Q^{he}_{-l-1,-\mu,-l-1,\mu}(x_1) = 0.
\end{aligned}$$

Starting values 3,

$$\begin{aligned}
P^{eh}_{l,\mu,l,-\mu}(x_1) &= Q^{eh}_{l,\mu,l,-\mu}(x_1) = 0,\\
P^{eh}_{-l-1,-\mu,l,-\mu}(x_1) &= Q^{eh}_{-l-1,-\mu,l,-\mu}(x_1) = 0,\\
P^{hh}_{l,-\mu,l,-\mu}(x_1) &= 10^{-20},\\
Q^{hh}_{l,-\mu,l,-\mu}(x_1) &= \left(\frac{l+\sqrt{l^2-b^2}}{b/c}\right) P^{hh}_{l,-\mu,l,-\mu}(x_1),\\
P^{hh}_{-l-1,-\mu,l,-\mu}(x_1) &= Q^{hh}_{-l-1,-\mu,l,-\mu}(x_1) = 0.
\end{aligned}$$

Starting values 4,

$$\begin{aligned}
P^{eh}_{l,\mu,-l-1,-\mu}(x_1) &= Q^{eh}_{l,\mu,-l-1,-\mu}(x_1) = 0,\\
P^{eh}_{-l-1,-\mu,-l-1,-\mu}(x_1) &= Q^{eh}_{-l-1,\mu,-l-1,-\mu}(x_1) = 0,\\
P^{hh}_{l,-\mu,-l-1,-\mu}(x_1) &= Q^{hh}_{l,-\mu,-l-1,-\mu}(x_1) = 0,\\
P^{hh}_{-l-1,-\mu,-l-1,-\mu}(x_1) &= 10^{-20},\\
Q^{hh}_{-l-1,-\mu,-l-1,-\mu}(x_1) &= \left(\frac{-l-1+\sqrt{(l+1)^2-b^2}}{b/c}\right) P^{hh}_{-l-1,-\mu,-l-1,-\mu}(x_1).
\end{aligned}$$

BIBLIOGRAPHY

[1] S. Savrasov and D. Savrasov.
Electron-phonon interactions and related physical properties of metals from linear-response theory.
Phys. Rev. B, 54(23):16487–16501, 1996.

[2] M. Ruby, B. W. Heinrich, J. I. Pascual, and K. J. Franke.
Experimental demonstration of a two-band superconducting state for lead using scanning tunneling spectroscopy.
Phys. Rev. Lett., 114(15):157001, 2015.

[3] D. Mou, R. Jiang, V. Taufour, S. L. Bud'ko, P. C. Canfield, and A. Kaminski.
Momentum dependence of the superconducting gap and in-gap states in MgB_2 multiband superconductor.
Phys. Rev. B, 91(21):214519, 2015.

[4] A. Hahn, S. Hofmann, A. Krause, and P. Seidel.
Tunneling results on gap anisotropy in niobium.
Phys. C, 296(1-2):103–118, 1998.

[5] A. Floris, G. Profeta, N. N. Lathiotakis, M. Lüders, M. A. L. Marques, C. Franchini, E. K. U. Gross, A. Continenza, and S. Massidda.
Superconducting Properties of MgB_2 from First Principles.
Phys. Rev. Lett., 94(3):037004, 2005.

[6] A. Floris, A. Sanna, S. Massidda, and E. K. U. Gross.
Two-band superconductivity in Pb from ab initio calculations.
Phys. Rev. B, 75(5):054508, 2007.

[7] M. Ruby, Y. Peng, F. Von Oppen, B. W. Heinrich, and K. J. Franke.
Orbital Picture of Yu-Shiba-Rusinov Multiplets.
Phys. Rev. Lett., 117(18):186801, 2016.

[8] P. J. Ray.

Master's thesis: Structural investigation of $La_{2-x}Sr_xCuO_{4+y}$ - Following staging as a function of temperature.
PhD thesis, University of Copenhagen, 2016.

[9] Ø. Fischer, M. Kugler, I. Maggio-Aprile, C. Berthod, and C. Renner.
Scanning tunneling spectroscopy of high-temperature superconductors.
Rev. Mod. Phys., 79(1):353–419, 2007.

[10] S. H. Pan, E. W. Hudson, and J. C. S. Davis.
Vacuum tunneling of superconducting quasiparticles from atomically sharp scanning tunneling microscope tips.
Appl. Phys. Lett., 73(20):2992–2994, 1998.

[11] C. Renner, B. Revaz, J. Y. Genoud, K. Kadowaki, and Fischer.
Pseudogap Precursor of the Superconducting Gap in Under- and Overdoped $Bi_2Sr_2CaCu_2O_{8+\delta}$.
Phys. Rev. Lett., 80(1):149–152, 1998.

[12] J. Chang, E. Blackburn, A. T. Holmes, N. B. Christensen, J. Larsen, J. Mesot, R. Liang, D. A. Bonn, W. N. Hardy, A. Watenphul, M. v. Zimmermann, E. M. Forgan, and S. M. Hayden.
Direct observation of competition between superconductivity and charge density wave order in $YBa_2Cu_3O_{6.67}$.
Nat. Phys., 8(12):871–876, 2012.

[13] A. A. Kordyuk.
Iron-based superconductors: Magnetism, superconductivity, and electronic structure.
Low Temp. Phys., 38(9):888–899, 2012.

[14] Y. Cao, V. Fatemi, S. Fang, K. Watanabe, T. Taniguchi, E. Kaxiras, and P. Jarillo-Herrero.
Unconventional superconductivity in magic-angle graphene superlattices.
Nature, 556(7699):43–50, 2018.

[15] C. Kittel.
Elementary Solid State Physics.
Wiley, New York, 2005.

[16] L. Yu.
Bound State in Superconductors With Paramagnetic Impurities.
Acta Phys. Sin., 21(1):75–91, 1965.

[17] H. Shiba.
Classical Spins in Superconductors.
Prog. Theor. Phys., 40(3):435–451, 1968.

[18] A. I. Rusinov.
Superconductivity Near a Paramagnetic Impurity.
JETP Lett., 9(2):85–87, 1969.

[19] A. V. Balatsky, I. Vekhter, and J. X. Zhu.
Impurity-induced states in conventional and unconventional superconductors.
Rev. Mod. Phys., 78(2):373–433, 2006.

[20] H. K. Onnes.
Investigations into the properties of substances at low temperatures, which have led, amongst other things, to the preparation of liquid helium.
Nobel Lect., pages 306–336, 1913.

[21] H. K. Onnes.
Through Measurement to Knowledge: The Selected Papers of Heike Kamerlingh Onnes 1853–1926, pages 261–272.
Springer Netherlands, Dordrecht, 1991.

[22] H. K. Onnes and K. Hof.
Further Experiments with Liquid Helium N. Hall-Effect and the Change of Resistance in a Magnetic Field. X. Measurements on Cadmium, Graphite, Gold, Silver, Bismuth, Lead, Tin and Nickel, at Hydrogen- and Helium-Temperatures.
Proc. R. Acad. Sci. Amsterdam, 17:520–527, 1914.

[23] J. B. Ketterson and S. N. Song.
Superconductivity.
Cambridge University Press, 1999.

[24] J. Bardeen, L. N. Cooper, and J. R. Schrieffer.
Theory of superconductivity.
Phys. Rev., 108(5):1175–1204, 1957.

[25] B. T. Matthias, E. A. Wood, E. Corenzwit, and V. B. Bala.
Superconductivity and electron concentration.
J. Phys. Chem. Solids, 1(3):188–190, 1956.

[26] B. G. Lazarev, A. I. Sudovtsev, and A. P. Smirnov.
Superconductivity of Beryllium Films Condensed on a Cold Backing.
Sov. Phys. JETP, Vol: 6:816–817, 1958.

[27] B. T. Matthias, H. Suhl, and E. Corenzwit.
Spin exchange in superconductors.
Phys. Rev. Lett., 1(3):92–94, 1958.

[28] P. W. Anderson.
Theory of dirty superconductors.
J. Phys. Chem. Solids, 11(1-2):26–30, 1959.

[29] A. A. Abrikosov and L. P. Gor' Kov.
Superconducting alloys at finite temperatures.
Sov. Phys. JETP, 8:220–221, 1959.

[30] A. L. Fetter.
Spherical impurity in an infinite superconductor.
Phys. Rev., 140(6A):1921, 1965.

[31] M. E. Flatté and J. M. Byers.
Local electronic structure of defects in superconductors.
Phys. Rev. B, 56(17):11213–11231, 1997.

[32] A. M. Stacy, J. V. Badding, M. J. Geselbracht, W. K. Ham, G. F. Holland, R. L. Hoskins, S. W. Keller, C. F. Millikan, and H. C. Zur Loye.
High-temperature superconductivity in yttrium-barium-copper oxide: identification of a copper-rich superconducting phase.
J. Am. Chem. Soc., 109(8):2528–2530, 1987.

[33] M. K. Wu, J. R. Ashburn, C. J. Torng, P. H. Hor, R. L. Meng, L. Gao, Z. J. Huang, Y. Q. Wang, and C. W. Chu.
Superconductivity at 93 K in a new mixed-phase Y-Ba-Cu-O compound system at ambient pressure.
Phys. Rev. Lett., 58(9):908–910, 1987.

[34] Y. Enomoto, T. Murakami, M. Suzuki, and K. Moriwaki.
Related content Largely Anisotropic Superconducting Critical Current in Epitaxially Grown $Ba_2YCu_3O_{7-y}$ Thin Film.
Jpn. J. Appl. Phys., 26(7):1248–1250, 1987.

[35] Y. Kamihara, T. Watanabe, M. Hirano, and H. Hosono.
Iron-Based Layered Superconductor $La[O_{1-x}F_x]$ FeAs (x = 0.05 - 0.12) with T_c 26 K.
J. Am. Chem. Soc., 130:3296–3297, 2008.

[36] T. M. Rice.
Twenty years of RVB theory.
J. Magn. Magn. Mater., 310(2, Part 1):454–459, 2007.

[37] P. O. Sprau, A. Kostin, A. Kreisel, A. E. Böhmer, V. Taufour, P. C. Canfield, S. Mukherjee, P. J. Hirschfeld, B. M. Andersen, and J. C. S. Davis.

Discovery of orbital-selective Cooper pairing in FeSe.
Science, 357(6346):75–80, 2017.

[38] M. P. Allen, A. W. Rost, A. P. Mackenzie, Y. Xie, J. C. S. Davis, K. Kihou, C. H. Lee, A. Iyo, H. Eisaki, and T.-M. Chuang.
Anisotropic Energy Gaps of Iron-Based Superconductivity from Intraband Quasiparticle Interference in LiFeAs.
Science, 336(6081):563–567, 2012.

[39] B. B. Zhou, S. Misra, E. H. Da Silva Neto, P. Aynajian, R. E. Baumbach, J. D. Thompson, E. D. Bauer, and A. Yazdani.
Visualizing nodal heavy fermion superconductivity in $CeCoIn_5$.
Nat. Phys., 9(8):474–479, 2013.

[40] I. M. Vishik, E. A. Nowadnick, W. S. Lee, Z. X. Shen, B. Moritz, T. P. Devereaux, K. Tanaka, T. Sasagawa, and T. Fujii.
A momentum-dependent perspective on quasiparticle interference in $Bi_2Sr_2CaCu_2O_{8+\delta}$.
Nat. Phys., 5(10):718–721, 2009.

[41] Y. Y. Zhang, C. Fang, X. Zhou, K. Seo, W. F. Tsai, B. A. Bernevig, and J. Hu.
Quasiparticle scattering interference in superconducting iron pnictides.
Phys. Rev. B, 80(9):094528, 2009.

[42] P. J. Hirschfeld, M. M. Korshunov, and I. I. Mazin.
Gap symmetry and structure of Fe-based superconductors.
Reports Prog. Phys., 74(12):124508, 2011.

[43] P. J. Hirschfeld, D. Altenfeld, I. Eremin, and I. I. Mazin.
Robust determination of the superconducting gap sign structure via quasiparticle interference.
Phys. Rev. B, 92(18):184513, 2015.

[44] A. Kreisel, B. M. Andersen, P. O. Sprau, A. Kostin, J. C. S. Davis, and P. J. Hirschfeld.
Orbital selective pairing and gap structures of iron-based superconductors.
Phys. Rev. B, 95(17):174504, 2017.

[45] T. Pereg-Barnea and M. Franz.
Magnetic-field dependence of quasiparticle interference peaks in a d-wave superconductor with weak disorder.
Phys. Rev. B, 78(2):020509, 2008.

[46] Q.-H. Wang and D.-H. Lee.
Quasiparticle scattering interference in high-temperature superconductors.

Phys. Rev. B, 67(2):020511, 2003.

[47] M. A. Sulangi, M. P. Allan, and J. Zaanen.
Revisiting quasiparticle scattering interference in high-temperature superconductors: The problem of narrow peaks.
Phys. Rev. B, 96(13):134507, 2017.

[48] J. S. Van Dyke, J. C. S. Davis, and D. K. Morr.
Differential conductance and defect states in the heavy-fermion superconductor $CeCoIn_5$.
Phys. Rev. B, 93(4):041107, 2016.

[49] B. W. Heinrich, J. I. Pascual, and K. J. Franke.
Single magnetic adsorbates on s-wave superconductors.
Prog. Surf. Sci., 93(1):1–19, 2018.

[50] M. Ruby, F. Pientka, Y. Peng, F. Von Oppen, B. W. Heinrich, and K. J. Franke.
End States and Subgap Structure in Proximity-Coupled Chains of Magnetic Adatoms.
Phys. Rev. Lett., 115(19):197204, 2015.

[51] H. Kim, A. Palacio-Morales, T. Posske, L. Rózsa, K. Palotás, L. Szunyogh, M. Thorwart, and R. Wiesendanger.
Toward tailoring Majorana bound states in artificially constructed magnetic atom chains on elemental superconductors.
Sci. Adv., 4(5):eaar5251, 2018.

[52] C. Nayak, S. H. Simon, A. Stern, M. Freedman, and S. Das Sarma.
Non-Abelian anyons and topological quantum computation.
Rev. Mod. Phys., 80(3):1083–1159, 2008.

[53] J. Li, H. Chen, I. K. Drozdov, A. Yazdani, B. A. Bernevig, and A. H. Macdonald.
Topological superconductivity induced by ferromagnetic metal chains.
Phys. Rev. B, 90(23):235433, 2014.

[54] J.-X. Zhu.
Bogoliubov-de Gennes Method and Its Applications.
Springer, Heidelberg, 2016.

[55] L. Schneider, S. Brinker, M. Steinbrecher, J. Hermenau, T. Posske, M. dos Santos Dias, S. Lounis, R. Wiesendanger, and J. Wiebe.
Controlling in-gap end states by linking nonmagnetic atoms and artificially-constructed spin chains on superconductors.
Nat. Commun., 11(1):1–6, 2020.

[56] F. Giustino.
Electron-phonon interactions from first principles.
Rev. Mod. Phys., 89(1):015003, 2017.

[57] D. J. Choi, C. Rubio-Verdú, J. De Bruijckere, M. M. Ugeda, N. Lorente, and J. I. Pascual.
Mapping the orbital structure of impurity bound states in a superconductor.
Nat. Commun., 8:15175, 2017.

[58] H. Ebert, D. Ködderitzsch, and J. Minár.
Calculating condensed matter properties using the KKR-Green's function method - Recent developments and applications.
Reports Prog. Phys., 74(9):096501, 2011.

[59] G. Csire, B. Újfalussy, J. Cserti, and B. Győrffy.
Multiple scattering theory for superconducting heterostructures.
Phys. Rev. B, 91(16):165142, 2015.

[60] G. Csire, J. Cserti, and B. Újfalussy.
First principles based proximity effect of superconductor-normal metal heterostructures.
J. Phys. Condens. Matter, 28(49):495701, 2016.

[61] G. Csire, J. Cserti, I. Tütto, and B. Újfalussy.
Prediction of superconducting transition temperatures of heterostructures based on the quasiparticle spectrum.
Phys. Rev. B, 94(10):104511, 2016.

[62] G. Csire, A. Deák, B. Nyári, H. Ebert, J. F. Annett, and B. Újfalussy.
Relativistic spin-polarized KKR theory for superconducting heterostructures: Oscillating order parameter in the Au layer of Nb/Au/Fe trilayers.
Phys. Rev. B, 97(2):024514, 2018.

[63] G. Csire, B. Újfalussy, and J. F Annett.
Nonunitary triplet pairing in the noncentrosymmetric superconductor $LaNiC_2$.
Eur. Phys. J. B, 91:217, 2018.

[64] G. Csire.
Quasiparticle spectrum of superconducting heterostructures.
PhD thesis, Eötvös Loránd University, 2017.

[65] E. Abrahams and Q. Si.
Quantum criticality in the iron pnictides and chalcogenides.
J. Phys. Condens. Matter, 23(22):223201, 2011.

[66] M. Sato and Y. Ando.
Topological superconductors: A review.
Reports Prog. Phys., 80(7):076501, 2017.

[67] R. Shimano and N. Tsuji.
Higgs Mode in Superconductors.
Annu. Rev. Condens. Matter Phys., 11:103–124, 2020.

[68] E. J. Mueller.
Review of pseudogaps in strongly interacting Fermi gases.
Reports Prog. Phys., 80(10):104401, 2017.

[69] P. A. Lee.
From high temperature superconductivity to quantum spin liquid: Progress in strong correlation physics.
Reports Prog. Phys., 71(1):012501, 2008.

[70] J. K. Hulm, J. E. Kunzler, and B. T. Matthias.
The road to superconducting materials.
Phys. Today, 34(1):34–43, 1981.

[71] J. K. Hulm and B. T. Matthias.
New superconducting borides and nitrides.
Phys. Rev., 82(2):273–274, 1951.

[72] B. T. Matthias, T. H. Geballe, L. D. Longinotti, E. Corenzwit, G. W. Hull, R. H. Willens, and J. P. Maita.
Superconductivity at 20 Degrees Kelvin.
Science, 156(3775):645–646, 1967.

[73] B. T. Matthias, M. Marezio, E. Corenzwit, A. S. Cooper, and H. E. Barz.
High-Temperature Superconductors, the First Ternary System.
Science, 175(4029):1465–1466, 1972.

[74] B. T. Matthias and J. K. Hulm.
A search for new superconducting compounds.
Phys. Rev., 87(5):799–806, 1952.

[75] J. R. Clement and E. H. Quinnel.
The Atomic Head of Lead in the Region of its Transition to Superconductivity.
Phys. Rev., 85(3):502–503, 1952.

[76] M. Horowitz, A. A. Silvidi, S. F. Malaker, and J. G. Daunt.

The specific heat of lead in the temperature range 1K to 75K.
Phys. Rev., 88(5):1182–1186, 1952.

[77] C. A. Shiffman, J. F. Cochran, and M. Garber.
The specific heat jump in superconducting lead.
J. Phys. Chem. Solids, 24(11):1369–1373, 1963.

[78] G. M. Eliashberg.
Interactions between electrons and lattice vibrations in a superconductor.
Sov. Phys. JETP, 11(3):696–702, 1960.

[79] P. Townsend and J. Sutton.
Investigation by electron tunneling of the superconducting energy gaps in Nb, Ta, Sn, and Pb.
Phys. Rev., 128(2):591–595, 1962.

[80] B. J. C. van der Hoeven Jr and P. H. Keesom.
Specific Heat of Lead Alloys Between 0.4 and 4.2K.
Phys. Rev., 137(1A):A103–A107, 1965.

[81] A. J. Bennett.
Theory of the anisotropic energy gap in superconducting lead.
Phys. Rev., 140(6A), 1965.

[82] G. I. Rochlin.
Determination of the anisotropy of the energy gap in superconducting Pb by superconductive tunneling.
Phys. Rev., 153(2):513–532, 1967.

[83] B. L. Blackford and R. H. March.
Tunneling investigation of energy-gap anisotropy in superconducting bulk Pb.
Phys. Rev., 186(2):397–399, 1969.

[84] R. Radebaugh and P. H. Keesom.
Low-temperature thermodynamic properties of vanadium. I. Superconducting and normal states.
Phys. Rev., 149(1):209–216, 1966.

[85] E. R. Dobbs and J. M. Perz.
Anisotropy of the Energy Gap in Niobium from Ultrasonic Measurements.
Rev. Mod. Phys., 36:257–260, 1964.

[86] M. L. A. MacVicar and R. M. Rose.

Anisotropic energy-gap measurements on superconducting niobium single crystals by tunneling.
J. Appl. Phys., 39(3):1721–1727, 1968.

[87] A. C. Anderson, C. B. Satterthwaite, and S. C. Smith.
Thermal Conductivity of Superconducting Niobium.
Phys. Rev. B., 3(11):3762–3764, 1971.

[88] V. Novotny and P. P. M. Meincke.
Single superconducting energy gap in pure niobium.
J. Low Temp. Phys., 18(1-2):147–157, 1975.

[89] J. G. Bednorz, M. Takashige, and K. A. Müller.
Possible High-Tc Superconductivity in the Ba-La-Cu-O System.
Zeitschrift für Phys. B, 64:189, 1986.

[90] N. Jun, N. Norimasa, M. Takahiro, Z. Yuji, and A. Jun.
Superconductivity at 39 K in magnesium diboride.
Nature, 410(1):63–64, 2001.

[91] P. Szabó, P. Samuely, J. Kačmarčík, T. Klein, J. Marcus, D. Fruchart, S. Miraglia, C. Marcenat, and A. G. M. Jansen.
Evidence for Two Superconducting Energy Gaps in MgB_2 by Point-Contact Spectroscopy.
Phys. Rev. Lett., 87(13):137005, 2001.

[92] S. L. Bud'ko, G. Lapertot, C. Petrovic, C. E. Cunningham, N. Anderson, and P. C. Canfield.
Boron isotope effect in superconducting MgB_2.
Phys. Rev. Lett., 86(9):1877–1880, 2001.

[93] H. J. Choi, D. Roundy, H. Sun, M. L. Cohen, and S. G. Louie.
First-principles calculation of the superconducting transition in MgB_2 within the anisotropic Eliashberg formalism.
Phys. Rev. B, 66(2):020513, 2002.

[94] H. J. Choi, D. Roundy, H. Sun, M. L. Cohen, and S. G. Louie.
The origin of the anomalous superconducting properties of MgB_2.
Nature, 418(6899):758–760, 2002.

[95] B. B. Goodman.
The thermal conductivity of superconducting tin below 1°K.
Proc. Phys. Soc. Sect. A, 66(3):217–227, 1953.

[96] A. Brown, M. W. Zemansky, and H. A. Boorse.

The superconducting and normal heat capacities of niobium.
Phys. Rev., 92(1):52–58, 1953.

[97] A. Ballarino and R. Flukiger.
Status of MgB_2 wire and cable applications in Europe Related content.
J. Phys. Conf. Ser, 871(012098), 2017.

[98] Z. K. Tang, L. Zhang, N. Wang, X. X. Zhang, G. H. Wen, G. D. Li, J. N. Wang, C. T. Chan, and P. Sheng.
Superconductivity in 4 Angstrom Single-Walled Carbon Nanotubes.
Science, 292(5526):2462–2465, jun 2001.

[99] E. A. Ekimov, V. A. Sidorov, E. D. Bauer, N. N. Mel'nik, N. J. Curro, J. D. Thompson, and S. M. Stishov.
Superconductivity in diamond.
Nature, 428(6982):542–545, 2004.

[100] O. Gunnarsson.
Superconductivity in fullerides.
Rev. Mod. Phys., 69(2):575–606, 1997.

[101] A. F. Hebard, M. J. Rosseinsky, R. C. Haddon, D. W. Murphy, S. H. Glarum, T. T. M. Palstra, A. P. Ramirez, and A. R. Kortan.
Superconductivity at 18 K in potassium-doped C_{60}.
Nature, 350(6319):600–601, 1991.

[102] C. C. Chen and C. M. Lieber.
Isotope Effect and Superconductivity in Metal-Doped C_{60}.
Science, 259(5095):655 LP – 658, 1993.

[103] M. Mitrano, A. Cantaluppi, D. Nicoletti, S. Kaiser, A. Perucchi, S. Lupi, P. Di Pietro, D. Pontiroli, M. Riccò, S. R. Clark, D. Jaksch, and A. Cavalleri.
Possible light-induced superconductivity in K_3C_{60} at high temperature.
Nature, 530(7591):461–464, 2016.

[104] A. Cantaluppi, M. Buzzi, G. Jotzu, D. Nicoletti, M. Mitrano, D. Pontiroli, M. Riccò, A. Perucchi, P. Di Pietro, and A. Cavalleri.
Pressure tuning of light-induced superconductivity in K_3C_{60}.
Nat. Phys., 14(8):837–841, 2018.

[105] H. Luo, S. Desgreniers, Y. K. Vohra, and A. L. Ruoff.
High-pressure optical studies on sulfur to 121 GPa: Optical evidence for metallization.
Phys. Rev. Lett., 67(21):2998–3001, 1991.

[106] S. Desgreniers, Y. K. Vohra, and A. L. Ruoff.
Optical response of very high density solid oxygen to 132 GPa.
J. Phys. Chem., 94(3):1117–1122, 1990.

[107] K. Shimizu, K. Suhara, M. Ikumo, M. I. Eremets, and K. Amaya.
Superconductivity in oxygen.
Nature, 393(6687):767–769, 1998.

[108] E. Gregoryanz, V. V. Struzhkin, R. J. Hemley, M. I. Eremets, H.-K. Mao, and Y. A. Timofeev.
Superconductivity in the chalcogens up to multimegabar pressures.
Phys. Rev. B, 65(6):064504, 2002.

[109] J. M. Dewar.
Sur La Solidification De L'Hydrogene.
Ann. Chim. Phys., 18(7):145–149, 1899.

[110] E. Wigner and H. B. Huntington.
On the possibility of a metallic modification of hydrogen.
J. Chem. Phys., 3(12):764–770, 1935.

[111] N. Ashcroft and N. Mermin.
Solid State Physics.
Harcourt College Publishers, Fort Worth, 1976.

[112] J. M. McMahon, M. A. Morales, C. Pierleoni, and D. M. Ceperley.
The properties of hydrogen and helium under extreme conditions.
Rev. Mod. Phys., 84(4), 2012.

[113] B. Rousseau, Y. Xie, Y. Ma, and A. Bergara.
Exotic high pressure behavior of light alkali metals, lithium and sodium.
Eur. Phys. J. B, 81(1):1–14, 2011.

[114] M. Städele and R. M. Martin.
Metallization of molecular hydrogen: Predictions from exact-exchange calculations.
Phys. Rev. Lett., 84(26):6070–6073, 2000.

[115] A. Zunger and J. P. Perdew.
Self-interaction correction to density functional approximations for many-electron systems.
Phys. Rev. B, 23(10):5048, 1981.

[116] J. P. Perdew and M. Levy.
Physical content of the exact Kohn-Sham orbital energies: band gaps and derivative discontinuities.
Phys. Rev. Lett., 51(20):1884–1887, 1983.

[117] L. J. Sham and M. Schlter.
Density-functional theory of the energy gap.
Phys. Rev. Lett., 51(20):1888–1891, 1983.

[118] F. Aryasetiawan and O. Gunnarsson.
The GW method.
Reports Prog. Phys., 61(3):237–312, mar 1998.

[119] K. A. Johnson and N. W. Ashcroft.
Structure and bandgap closure in dense hydrogen.
Nature, 403(6770):632–635, 2000.

[120] J. McMinis, R. C. Clay, D. Lee, and M. A. Morales.
Molecular to Atomic Phase Transition in Hydrogen under High Pressure.
Phys. Rev. Lett., 114(10):105305, 2015.

[121] P. Loubeyre, F. Occelli, and R. LeToullec.
Optical studies of solid hydrogen to 320 GPa and evidence for black hydrogen.
Nature, 416(6881):613–617, 2002.

[122] R. P. Dias and I. F. Silvera.
Observation of the Wigner-Huntington transition to metallic hydrogen.
Science, 357(6353):715–718, 2017.

[123] I. Johnston.
World's only piece of a metal that could revolutionise technology has disappeared, scientists reveal.
Independent, UK, 2017.

[124] D. Castelvecchi.
Hydrogen yet to prove it's metal.
Nature, 542(7639):17, 2017.

[125] P. Loubeyre, F. Occelli, and P. Dumas.
Synchrotron infrared spectroscopic evidence of the probable transition to metal hydrogen.
Nature, 577(7792):631–635, 2020.

[126] J. P. Carbotte, E. J. Nicol, and T. Timusk.
Detecting Superconductivity in the High Pressure Hydrides and Metallic Hydrogen from Optical Properties.
Phys. Rev. Lett., 121(4):47002, 2018.

[127] E. Liberatore, C. Pierleoni, and D. M. Ceperley.

Liquid-solid transition in fully ionized hydrogen at ultra-high pressures.
J. Chem. Phys., 134(18), 2011.

[128] A. P. Drozdov, M. I. Eremets, I. A. Troyan, V. Ksenofontov, and S. I. Shylin.
Conventional superconductivity at 203 kelvin at high pressures in the sulfur hydride system.
Nature, 525(7567):73–76, 2015.

[129] I. Errea, F. Belli, L. Monacelli, A. Sanna, T. Koretsune, T. Tadano, R. Bianco, M. Calandra, R. Arita, F. Mauri, and J. A. Flores-Livas.
Quantum crystal structure in the 250-kelvin superconducting lanthanum hydride.
Nature, 578(7793):66–69, 2020.

[130] Y. Sun, J. Lv, Y. Xie, H. Liu, and Y. Ma.
Route to a Superconducting Phase above Room Temperature in Electron-Doped Hydride Compounds under High Pressure.
Phys. Rev. Lett., 123(9):97001, 2019.

[131] E. Snider, N. Dasenbrock-Gammon, R. McBride, M. Debessai, H. Vindana, K. Vencatasamy, K. V. Lawler, A. Salamat, and R. P. Dias.
Room-temperature superconductivity in a carbonaceous sulfur hydride.
Nature, 586(7829):373–377, 2020.

[132] H. Maeda, Y. Tanaka, M. Fukutomi, and T. Asano.
A New High-Tc Oxide Superconductor without a Rare Earth Element.
Jpn. J. Appl. Phys., 27(2):209–210, 1988.

[133] A. Schilling, M. Cantoni, J. D. Guo, and H. K. Ott.
Superconductivity above 130K in the Hg-Ba-Ca-Cu-O system.
Nature, 363:56–58, 1993.

[134] T. Nakano, N. Momono, M. Oda, and M. Ido.
Correlation between the Doping Dependences of Superconducting Gap Magnitude $2\Delta_0$ and Pseudogap Temperature T^* in High-T_c Cuprates.
J. Phys. Soc. Japan, 67(8):2622–2625, 1998.

[135] B. W. Hoogenboom, K. Kadowaki, B. Revaz, M. Li, C. H. Renner, and Ø. Fischer.
Linear and field-independent relation between vortex core state energy and gap in $Bi_2Sr_2CaCu_2O_{8+\delta}$.
Phys. Rev. Lett., 87(26):267001, 2001.

[136] J. E. Hoffman, K. McElroy, D.-H. Lee, K. M. Lang, H. Eisaki, S. Uchida, and J. C. S. Davis.
Imaging Quasiparticle Interference in $Bi_2Sr_2CaCu_2O_{8+\delta}$.

Sci. Rep., 297:1148–1151, 2002.

[137] S. Misra, S. Oh, D. J. Hornbaker, T. DiLuccio, J. N. Eckstein, and A. Yazdani.
Atomic Scale Imaging and Spectroscopy of a CuO_2 Plane at the Surface of $Bi_2Sr_2CaCu_2O_{8+\delta}$.
Phys. Rev. Lett., 89(8):087002, 2002.

[138] P. W. Anderson.
The Resonating Valence Bond State in La_2CuO_4 and Superconductivity.
Science, 235(4793):1196–1198, 1986.

[139] C. J. Halboth and W. Metzner.
D-wave superconductivity and Pomeranchuk instability in the two-dimensional Hubbard model.
Phys. Rev. Lett., 85(24):5162–5165, 2000.

[140] D. Pashov, S. Acharya, W. R. L. Lambrecht, J. Jackson, K. D. Belashchenko, A. Chantis, F. Jamet, and M. van Schilfgaarde.
Questaal: A package of electronic structure methods based on the linear muffin-tin orbital technique.
Comput. Phys. Commun., 249:107065, 2020.

[141] P. W. Phillips, L. Yeo, and E. W. Huang.
Exact theory for superconductivity in a doped Mott insulator.
Nat. Phys., 16:1175–1180, 2020.

[142] H. J. A. Molegraaf, C. Presura, D. van der Marel, P. H. Kes, and M. Li.
Superconductivity-Induced Transfer of In-Plane Spectral Weight in $Bi_2Sr_2CaCu_2O_{8+\delta}$.
Science, 295(5563):2239–2242, 2002.

[143] Q. Si, R. Yu, and E. Abrahams.
High-temperature superconductivity in iron pnictides and chalcogenides.
Nat. Rev. Mater., 1(4):16017, 2016.

[144] W. Meissner and R. Ochsenfeld.
Ein neuer Effekt bei Eintritt der Supraleitfähigkeit.
Naturwissenschaften, 21(44):787–788, 1933.

[145] T. Shimojima, T. Sonobe, W. Malaeb, K. Shinada, A. Chainani, S. Shin, T. Yoshida, S. Ideta, A. Fujimori, H. Kumigashira, K. Ono, Y. Nakashima, H. Anzai, M. Arita, A. Ino, H. Namatame, M. Taniguchi, M. Nakajima, S. Uchida, Y. Tomioka, T. Ito, K. Kihou, C. H. Lee, A. Iyo, H. Eisaki, K. Ohgushi, S. Kasahara, T. Terashima, H. Ikeda, T. Shibauchi, Y. Matsuda, and K. Ishizaka.

Pseudogap formation above the superconducting dome in iron pnictides.
Phys. Rev. B, 89(4):45101, 2014.

[146] S. Takafumi, S. Seigo, N. Kosuke, T. Kensei, S. Katsuaki, T. Takashi, K. Yoichi, H. Masahiro, and H. Hideo.
Superconducting Gap and Pseudogap in Iron-Based Layered Superconductor $La(O_{1-x}F_x)FeAs$.
J. Phys. Soc. Japan, 77(6):63708, 2008.

[147] J. F. Ge, Z. L. Liu, C. Liu, C. L. Gao, D. Qian, Q. K. Xue, Y. Liu, and J. F. Jia.
Superconductivity above 100 K in single-layer FeSe films on doped $SrTiO_3$.
Nat. Mater., 14(3):285–289, 2015.

[148] A. Gozar, G. Logvenov, L. Fitting Kourkoutis, A. T. Bollinger, L. A. Giannuzzi, D. A. Muller, and I. Bozovic.
High-temperature interface superconductivity between metallic and insulating copper oxides.
Nature, 455(7214):782–785, 2008.

[149] C. Richter, H. Boschker, W. Dietsche, E. Fillis-Tsirakis, R. Jany, F. Loder, L. F. Kourkoutis, D. A. Muller, J. R. Kirtley, C. W. Schneider, and J. Mannhart.
Interface superconductor with gap behaviour like a high-temperature superconductor.
Nature, 502(7472):528–531, 2013.

[150] Y. Maeno, H. Hashimoto, K. Yoshida, S. Nishizaki, T. Fujita, J. G. Bednorz, and F. Lichtenberg.
Superconductivity in a layered perovskite without copper.
Nature, 372(6506):532–534, 1994.

[151] T. M. Rice and M. Sigrist.
Sr_2RuO_4: an electronic analogue of ^{3}He?
J. Phys. Condens. Matter, 7(47):L643, 1995.

[152] J. Robbins, J. F. Annett, and M. Gradhand.
Theory of the orbital moment in a superconductor.
Phys. Rev. B, 101(13):134505, 2020.

[153] K. Ishida, H. Mukuda, Y. Kitaoka, K. Asayama, Z. Q. Mao, Y. Mori, and Y. Maeno.
Spin-triplet superconductivity in Sr_2RuO_4 identified by ^{1}7O Knight Shift.
Nature, 396(6712):658–660, 1998.

[154] A. Pustogow, Y. Luo, A. Chronister, Y. S. Su, D. A. Sokolov, F. Jerzembeck, A. P. Mackenzie, C. W. Hicks, N. Kikugawa, S. Raghu, E. D. Bauer, and S. E. Brown.

Constraints on the superconducting order parameter in Sr_2RuO_4 from oxygen-17 nuclear magnetic resonance.
Nature, 574(7776):72–75, 2019.

[155] R. Sharma, S. D. Edkins, Z. Wang, A. Kostin, C. Sow, Y. Maeno, A. P. Mackenzie, J. C. S. Davis, and V. Madhavan.
Momentum-resolved superconducting energy gaps of Sr_2RuO_4 from quasiparticle interference imaging.
Proc. Natl. Acad. Sci. U. S. A., 117(10):5222–5227, 2020.

[156] S. Ghosh, A. Shekhter, F. Jerzembeck, N. Kikugawa, D. A. Sokolov, M. Brando, A. P. Mackenzie, C. W. Hicks, and B. J. Ramshaw.
Thermodynamic evidence for a two-component superconducting order parameter in Sr_2RuO_4.
Nat. Phys., Accepted, 2020.

[157] S. Benhabib, C. Lupien, I. Paul, L. Berges, M. Dion, M. Nardone, A. Zitouni, Z. Q. Mao, Y. Maeno, A. Georges, L. Taillefer, and C. Proust.
Ultrasound evidence for a two-component superconducting order parameter in Sr_2RuO_4.
Nat. Phys., Accepted, 2020.

[158] D. F. Agterberg.
The symmetry of superconducting Sr_2RuO_4.
Nat. Phys., 2020.

[159] F. Steglich, J. Aarts, C. D. Bredl, W. Lieke, D. Meschede, W. Franz, and H. Schäfer.
Superconductivity in the presence of strong pauli paramagnetism: $CeCu_2Si_2$.
Phys. Rev. Lett., 43(25):1892–1896, 1979.

[160] N. J. Curro, T. Caldwell, E. D. Bauer, L. A. Morales, M. J. Graf, Y. Bang, A. V. Balatsky, J. D. Thompson, and J. L. Sarrao.
Unconventional superconductivity in $PuCoGa_5$.
Nature, 434:622–625, 2005.

[161] C. Petrovic, P. G. Pagliuso, M. F. Hundley, R. Movshovich, J. L. Sarrao, J. D. Thompson, Z. Fisk, and P. Monthoux.
Heavy-fermion superconductivity in $CeCoIn_5$ at 2.3 K.
J. Phys. Condens. Matter, 13:L337–L342, 2001.

[162] M. P. Allan, F. Massee, D. K. Morr, J. Van Dyke, A. W. Rost, A. P. Mackenzie, C. Petrovic, and J. C. S. Davis.
Imaging Cooper pairing of heavy fermions in $CeCoIn_5$.
Nat. Phys., 9(8):468–473, 2013.

[163] O. Stockert and F. Steglich.
Unconventional Quantum Criticality in Heavy-Fermion Compounds.
Annu. Rev. Condens. Matter Phys., 2(1):79–99, 2011.

[164] B. Michon, C. Girod, S. Badoux, J. Kačmarčík, Q. Ma, M. Dragomir, H. A. Dabkowska, B. D. Gaulin, J. S. Zhou, S. Pyon, T. Takayama, H. Takagi, S. Verret, N. Doiron-Leyraud, C. Marcenat, L. Taillefer, and T. Klein.
Thermodynamic signatures of quantum criticality in cuprate superconductors.
Nature, 567(7747):218–222, 2019.

[165] Y. Jiang, X. Lai, K. Watanabe, T. Taniguchi, K. Haule, J. Mao, and E. Y. Andrei.
Charge order and broken rotational symmetry in magic-angle twisted bilayer graphene.
Nature, 573(7772):91–95, 2019.

[166] D. Fausti, R. I. Tobey, N. Dean, S. Kaiser, A. Dienst, M. C. Hoffmann, S. Pyon, T. Takayama, H. Takagi, and A. Cavalleri.
Light-Induced Superconductivity in a Stripe-ordered Cuprate.
Science, 331(6014):189–191, 2011.

[167] Y. S. Hor, A. J. Williams, J. G. Checkelsky, P. Roushan, J. Seo, Q. Xu, H. W. Zandbergen, A. Yazdani, N. P. Ong, and R. J. Cava.
Superconductivity in $Cu_xBi_2Se_3$ and its implications for pairing in the undoped topological insulator.
Phys. Rev. Lett., 104(5):057001, 2010.

[168] S. Sasaki, M. Kriener, K. Segawa, K. Yada, Y. Tanaka, M. Sato, and Y. Ando.
Topological superconductivity in $Cu_xBi_2Se_3$.
Phys. Rev. Lett., 107(21):217001, 2011.

[169] A. Yamakage, K. Yada, M. Sato, and Y. Tanaka.
Theory of tunneling conductance and surface-state transition in superconducting topological insulators.
Phys. Rev. B, 85(18):180509, 2012.

[170] T. H. Hsieh, H. Lin, J. Liu, W. Duan, A. Bansil, and L. Fu.
Topological crystalline insulators in the SnTe material class.
Nat. Commun., 3(1):982, 2012.

[171] Y. Tanaka, Z. Ren, T. Sato, K. Nakayama, S. Souma, T. Takahashi, K. Segawa, and Y. Ando.
Experimental realization of a topological crystalline insulator in SnTe.
Nat. Phys., 8(11):800–803, 2012.

[172] A. S. Erickson, J. H. Chu, M. F. Toney, T. H. Geballe, and I. R. Fisher.
Enhanced superconducting pairing interaction in indium-doped tin telluride.
Phys. Rev. B, 79(2):024520, 2009.

[173] M. Novak, S. Sasaki, M. Kriener, K. Segawa, and Y. Ando.
Unusual nature of fully gapped superconductivity in In-doped SnTe.
Phys. Rev. B, 88(14):140502, 2013.

[174] R. Joynt and L. Taillefer.
The superconducting phases of UPt_3.
Rev. Mod. Phys., 74(1):235–294, 2002.

[175] Y. Tsutsumi, M. Ishikawa, T. Kawakami, T. Mizushima, M. Sato, M. Ichioka, and K. Machida.
UPt_3 as a topological crystalline superconductor.
J. Phys. Soc. Japan, 82(11):113707, 2013.

[176] Y. Machida, A. Itoh, Y. So, K. Izawa, Y. Haga, E. Yamamoto, N. Kimura, Y. Onuki, Y. Tsutsumi, and K. MacHida.
Twofold spontaneous symmetry breaking in the heavy-fermion superconductor UPt_3.
Phys. Rev. Lett., 108(15):157002, 2012.

[177] Y. Yanase and K. Shiozaki.
Möbius topological superconductivity in UPt_3.
Phys. Rev. B, 95(22):224514, 2017.

[178] L. Fu and C. L. Kane.
Superconducting proximity effect and majorana fermions at the surface of a topological insulator.
Phys. Rev. Lett., 100(9):096407, 2008.

[179] L.-H. Hu, C.-X. Liu, and F.-C. Zhang.
Topological Larkin-Ovchinnikov phase and Majorana zero mode chain in bilayer superconducting topological insulator films.
Commun. Phys., 2(1):25, 2019.

[180] B. Jäck, Y. Xie, J. Li, S. Jeon, B. A. Bernevig, and A. Yazdani.
Observation of a Majorana zero mode in a topologically protected edge channel.
Science, 364(6447):1255–1259, 2019.

[181] M. T. Deng, C. L. Yu, G. Y. Huang, M. Larsson, P. Caroff, and H. Q. Xu.
Anomalous zero-bias conductance peak in a Nb-InSb nanowire-Nb hybrid device.
Nano Lett., 12(12):6414–6419, 2012.

[182] V. Mourik, K. Zuo, S. M. Frolov, S. R. Plissard, E. P. A. M. Bakkers, and L. P. Kouwenhoven.
Signatures of majorana fermions in hybrid superconductor-semiconductor nanowire devices.
Science, 336(6084):1003–1007, 2012.

[183] A. Das, Y. Ronen, Y. Most, Y. Oreg, M. Heiblum, and H. Shtrikman.
Zero-bias peaks and splitting in an Al-InAs nanowire topological superconductor as a signature of Majorana fermions.
Nat. Phys., 8(12):887–895, 2012.

[184] E. J. H. Lee, X. Jiang, M. Houzet, R. Aguado, C. M. Lieber, and S. De Franceschi.
Spin-resolved Andreev levels and parity crossings in hybrid superconductor-semiconductor nanostructures.
Nat. Nanotechnol., 9(1):79–84, 2014.

[185] S. M. Albrecht, A. P. Higginbotham, M. Madsen, F. Kuemmeth, T. S. Jespersen, J. Nygård, P. Krogstrup, and C. M. Marcus.
Exponential protection of zero modes in Majorana islands.
Nature, 531(7593):206–209, 2016.

[186] S. Nadj-Perge, I. K. Drozdov, B. A. Bernevig, and A. Yazdani.
Proposal for realizing Majorana fermions in chains of magnetic atoms on a superconductor.
Phys. Rev. B, 88(2):020407, 2013.

[187] S. Nadj-Perge, I. K. Drozdov, J. Li, H. Chen, S. Jeon, J. Seo, A. H. MacDonald, B. A. Bernevig, and A. Yazdani.
Observation of Majorana fermions in ferromagnetic atomic chains on a superconductor.
Science, 346(6209):1259327, 2014.

[188] M. Ruby, B. W. Heinrich, Y. Peng, F. Von Oppen, and K. J. Franke.
Exploring a Proximity-Coupled Co Chain on Pb(110) as a Possible Majorana Platform.
Nano Lett., 17(7):4473–4477, 2017.

[189] M. Ruby, B. W. Heinrich, Y. Peng, F. von Oppen, and K. J. Franke.
Wave-Function Hybridization in Yu-Shiba-Rusinov Dimers.
Phys. Rev. Lett., 120(15):156803, 2018.

[190] T. Meng, J. Klinovaja, S. Hoffman, P. Simon, and D. Loss.
Superconducting gap renormalization around two magnetic impurities: From Shiba to Andreev bound states.
Phys. Rev. B, 92(6):064503, 2015.

[191] S. Hoffman, J. Klinovaja, T. Meng, and D. Loss.
Impurity-induced quantum phase transitions and magnetic order in conventional superconductors: Competition between bound and quasiparticle states.
Phys. Rev. B, 92(12):125422, 2015.

[192] D. K. Morr and N. A. Stavropoulos.
Quantum interference between impurities: Creating novel many-body states in s-wave superconductors.
Phys. Rev. B, 67(2):020502, 2003.

[193] L. N. Cooper.
Bound Electron Pairs in a Degenerate Fermi Gas.
Phys. Rev., 104(4):1189, 1956.

[194] J. F. Annett.
Superconductivity, Superfluidity and Condensates.
Oxford University of Press, New York, 2004.

[195] G. C. Wick.
The Evaluation of the Collision Matrix.
Phys. Rev., 80(2):268–272, 1950.

[196] W. L. McMillan.
Transition Temperature of Strong-Coupled Superconductors.
Phys. Rev., 167(2):331–344, 1968.

[197] R. C. Dynes.
McMillan's equation and the Tc of superconductors.
Solid State Commun., 10(7):615–618, 1972.

[198] N. N. Bogoliubov.
A new method in the theory of superconductivity. I.
Sov. Phys. JETP, 34(7):41–46, 1958.

[199] N. N. Bogoliubov, V. V. Tolmachov, and D. V. Širkov.
A new method in the theory of superconductivity. III.
Sov. Phys. JETP, 34(7):51–55, 1958.

[200] A. J. Leggett.
Modern Trends in the Theory of Condensed Matter.
Springer-Verlag, Berlin, 1980.

[201] L. N. Oliveira, E. K. U. Gross, and W. Kohn.

Density-functional theory for superconductors.
Phys. Rev. Lett., 60(23):2430–2433, 1988.

[202] M. Lüders, M. A. L. Marques, N. N. Lathiotakis, A. Floris, G. Profeta, L. Fast, A. Continenza, S. Massidda, and E. K. U. Gross.
Ab initio theory of superconductivity. I. Density functional formalism and approximate functionals.
Phys. Rev. B, 72(2):024545, 2005.

[203] M. A. L. Marques, M. Lüders, N. N. Lathiotakis, G. Profeta, A. Floris, L. Fast, A. Continenza, E. K. U. Gross, and S. Massidda.
Ab initio theory of superconductivity. II. Application to elemental metals.
Phys. Rev. B, 72(2):024546, 2005.

[204] M. Born and R. Oppenheimer.
Zur Quantentheorie der Moleküle.
Ann. Phys., 84:457, 1927.

[205] P. Hohenberg and W. Kohn.
Inhomogeneous electron gas.
Phys. Rev., 136(3B):B864–B871, 1964.

[206] W. Kohn and L. J. Sham.
Self-Consistent Equations Including Exchange and Correlation Effects.
Phys. Rev., 140(4A):A1133–A1138, 1965.

[207] M. B. Suvasani, W. M. Temmerman, and B. Győrffy.
Computational aspects of density-functional theories of superconductors.
Phys. Rev. B, 48(2):1202–1210, 1993.

[208] O. Gunnarsson and B. I. Lundqvist.
Exchange and correlation in atoms, molecules, and solids by the spin-density-functional formalism.
Phys. Rev. B, 13(10):4274–4298, 1976.

[209] F. J. Dyson.
The S matrix in quantum electrodynamics.
Phys. Rev., 75(11):1736–1755, 1949.

[210] J. Korringa.
On the calculation of the energy of a Bloch wave in a metal.
Physica, 13(6-7):392–400, 1947.

[211] W. Kohn and N. Rostoker.
Solution of the Schrödinger equation in periodic lattices with an application to metallic lithium.
Phys. Rev., 94(5):1111–1120, 1954.

[212] Martin Gradhand.
The Extrinsic Spin Hall Effect.
PhD thesis, Martin-Luther-Universität Halle-Wittenberg, 2010.

[213] J. Zabloudil, R. Hammerling, L. Szunyogh, and P. Weinberger.
Electron Scattering in Solid Matter: a theoretical and computational treatise.
Springer Berlin Heidelberg New York, 2004.

[214] N. Papanikolaou, R. Zeller, and P. H. Dederichs.
Conceptual improvements of the KKR method.
J. Phys. Condens. Matter, 14(11):2799–2823, 2002.

[215] R. Zeller, P. H. Dederichs, B. Ujfalussy, L. Szunyogh, and P. Weinberger.
Theory and convergence properties of the screened Korringa-Kohn-Rostoker method.
Phys. Rev. B, 52(12):8807–8812, 1995.

[216] K. Capelle and E. K. U. Gross.
Relativistic framework for microscopic theories of superconductivity. II. The Pauli equation for superconductors.
Phys. Rev. B, 59(10):7155–7165, 1999.

[217] K. Capelle and E. K. U. Gross.
Relativistic framework for microscopic theories of superconductivity. I. The Dirac equation for superconductors.
Phys. Rev. B, 59(10):7140–7154, 1999.

[218] P. Weinberger, I. Turek, and L. Szunyoch.
The TB-LMTO method and its relation to the screened KKR method.
Int. J. Quantum Chem., 63(1):165–188, 1997.

[219] G. D. Gaspari and B. L. Győrffy.
Electron-phonon interactions, D resonances, and superconductivity in transition metals.
Phys. Rev. Lett., 28(13):801–805, 1972.

[220] H Rietschel.
A non-local extension of the Gaspari-Gyorffy theory for superconductors.
Zeitschrift für Phys. B Condens. Matter, 30(3):271–275, 1978.

[221] P. Mori-Sánchez, A. J. Cohen, and W. Yang.
Localization and delocalization errors in density functional theory and implications for band-gap prediction.
Phys. Rev. Lett., 100(14):146401, 2008.

[222] O. V. Gritsenko, M. Mentel, and E. J. Baerends.
On the errors of local density (LDA) and generalized gradient (GGA) approximations to the Kohn-Sham potential and orbital energies.
J. Chem. Phys., 144(20):204114, 2016.

[223] S. De Waele, K. Lejaeghere, M. Sluydts, and S. Cottenier.
Error estimates for density-functional theory predictions of surface energy and work function.
Phys. Rev. B, 94(23):235418, 2016.

[224] P. G. Tomlinson and J. P. Carbotte.
Anisotropic superconducting energy gap in Pb.
Phys. Rev. B, 13(11):4738–4744, 1976.

[225] B. L. Blackford.
Energy gap anisotropy in bulk Pb via tunneling.
Physica, 55(C):475–483, 1971.

[226] J. D. Short and J. P. Wolfe.
Evidence for large gap anisotropy in superconducting Pb from phonon imaging.
Phys. Rev. Lett., 85(24):5198–5201, 2000.

[227] H. Berndt and F. Sernetz.
Effect of Neutron Irradiation at 4.6 K on the Critical Temperature of Superconducting Niobium.
Phys. Lett. A, 33(7):427–428, 1970.

[228] S. Klaumünzer, G. Ischenko, and P. Müller.
Effects of low temperature irradiation with heavy ions on superconductor niobium.
Zeitschrift für Phys., 268(2):189–196, 1974.

[229] J. P. Carbotte.
Properties of boson-exchange superconductors.
Rev. Mod. Phys., 62(4):1027–1157, 1990.

[230] E. R. Margine and F. Giustino.
Anisotropic Migdal-Eliashberg theory using Wannier functions.
Phys. Rev. B, 87(2):024505, 2013.

[231] J. A. Flores-Livas, A. Sanna, and E. K. U. Gross.
High temperature superconductivity in sulfur and selenium hydrides at high pressure.
Eur. Phys. J. B, 89(3):63, 2016.

[232] A. Sanna, J. A. Flores-Livas, A. Davydov, G. Profeta, K. Dewhurst, S. Sharma, and E. K. U. Gross.
Ab initio eliashberg theory: Making genuine predictions of superconducting features.
J. Phys. Soc. Japan, 87(4):041012, 2018.

[233] F. Schrodi, A. Aperis, and P. M. Oppeneer.
Self-consistent temperature dependence of quasiparticle bands in monolayer FeSe on $SrTiO_3$.
Phys. Rev. B, 98(9):094509, 2018.

[234] M. N. Gastiasoro, A. V. Chubukov, and R. M. Fernandes.
Phonon-mediated superconductivity in low carrier-density systems.
Phys. Rev. B, 99(9):094524, 2019.

[235] F. Essenberger, A. Sanna, P. Buczek, A. Ernst, L. Sandratskii, and E. K. U. Gross.
Ab initio theory of iron-based superconductors.
Phys. Rev. B, 94(1):014503, 2016.

[236] F. Essenberger, A. Sanna, A. Linscheid, F. Tandetzky, G. Profeta, P. Cudazzo, and E. K. U. Gross.
Superconducting pairing mediated by spin fluctuations from first principles.
Phys. Rev. B, 90(21):214504, 2014.

[237] A. Linscheid, A. Sanna, F. Essenberger, and E. K. U. Gross.
Ab initio theory of superconductivity in a magnetic field. I. Spin density functional theory for superconductors and Eliashberg equations.
Phys. Rev. B, 92(2):024505, 2015.

[238] A. Linscheid, A. Sanna, and E. K. U. Gross.
Ab initio theory of superconductivity in a magnetic field. II. Numerical solution.
Phys. Rev. B, 92(2):024506, 2015.

[239] M. Sigrist and K. Ueda.
Phenomenological theory of unconventional superconductivity.
Rev. Mod. Phys., 63(2):239–311, 1991.

[240] A. P. Mackenzie.
The superconductivity of Sr_2RuO_4 and the physics of spin-triplet pairing.
Rev. Mod. Phys., 75(2):657–712, 2003.

[241] J. F. Annett, G. Litak, B. Győrffy, and K. I. Wysokiński.
Spin-orbit coupling and symmetry of the order parameter in strontium ruthenate.
Phys. Rev. B, 73(13):135401, 2006.

[242] A. D. Hillier, J. Quintanilla, B. Mazidian, J. F. Annett, and R. Cywinski.
Nonunitary triplet pairing in the centrosymmetric superconductor $LaNiGa_2$.
Phys. Rev. Lett., 109(9):097001, 2012.

[243] B. Mazidian, J. Quintanilla, A. D. Hillier, and J. F. Annett.
Anomalous thermodynamic power laws near topological transitions in nodal superconductors.
Phys. Rev. B, 88(22):224504, 2013.

[244] R. P. Singh, A. D. Hillier, B. Mazidian, J. Quintanilla, J. F. Annett, D. McK. Paul, G. Balakrishnan, and M. R. Lees.
Observation of Time-Reversal Symmetry Breaking in the Non-Centrosymmetric Superconductor Re_6Zr.
Phys. Rev. Lett., 112:107002, 2014.

[245] Z. F. Weng, J. L. Zhang, M. Smidman, T. Shang, J. Quintanilla, J. F. Annett, M. Nicklas, G. M. Pang, L. Jiao, W. B. Jiang, Y. Chen, F. Steglich, and H. Q. Yuan.
Two-Gap Superconductivity in $LaNiGa_2$ with Nonunitary Triplet Pairing and Even Parity Gap Symmetry.
Phys. Rev. Lett., 117(2):027001, 2016.

[246] J. Robbins, J. F. Annett, and M. Gradhand.
Effect of spin-orbit coupling on the polar Kerr effect in Sr_2RuO_4.
Phys. Rev. B, 96(14):144503, 2017.

[247] P. M. R. Brydon, D. F. Agterberg, H. Menke, and C. Timm.
Bogoliubov Fermi surfaces: General theory, magnetic order, and topology.
Phys. Rev. B, 98(22):224509, 2018.

[248] M. Ruby, F. Pientka, Y. Peng, F. Von Oppen, B. W. Heinrich, and K. J. Franke.
Tunneling Processes into Localized Subgap States in Superconductors.
Phys. Rev. Lett., 115(8):087001, 2015.

[249] N. Hatter, B. W. Heinrich, M. Ruby, J. I. Pascual, and K. J. Franke.
Magnetic anisotropy in Shiba bound states across a quantum phase transition.
Nat. Commun., 6(1):8988, 2015.

[250] L. Farinacci, G. Ahmadi, G. Reecht, M. Ruby, N. Bogdanoff, O. Peters, B. W. Heinrich, F. Von Oppen, and K. J. Franke.

Tuning the Coupling of an Individual Magnetic Impurity to a Superconductor: Quantum Phase Transition and Transport.
Phys. Rev. Lett., 121(19):196803, 2018.

[251] L. Szunyogh, B. Újfalussy, P. Weinberger, and J. Kollar.
The self-consistent fully relativistic SKKR Green function method: Applications to the (100), (110) and (111) surfaces of Au and Pt.
J. Phys. Condens. Matter, 6(18):3301–3306, 1994.

[252] K. Wildberger, R. Zeller, and P. Dederichs.
Screened KKR-Green's-function method for layered systems.
Phys. Rev. B, 55(15):10074–10080, 1997.

[253] I. I. Mazin and V. P. Antropov.
Electronic structure, electron-phonon coupling, and multiband effects in MgB_2.
Phys. C, 385(1-2):49–65, 2003.

[254] A. Shukla, M. Calandra, M. D'Astuto, M. Lazzeri, F. Mauri, C. Bellin, M. Krisch, J. Karpinski, S. M. Kazakov, J. Jun, D. Daghero, and K. Parlinski.
Phonon Dispersion and Lifetimes in MgB_2.
Phys. Rev. Lett., 90(9):095506, 2003.

[255] A. Y. Liu, I. I. Mazin, and J. Kortus.
Beyond eliashberg superconductivity in MgB_2: Anharmonicity, two-phonon scattering, and multiple gaps.
Phys. Rev. Lett., 87(8):087005, 2001.

[256] J. Bekaert, A. Aperis, B. Partoens, P. M. Oppeneer, and M. V. Milošević.
Evolution of multigap superconductivity in the atomically thin limit: Strain-enhanced three-gap superconductivity in monolayer MgB_2.
Phys. Rev. B, 96(9):094510, 2017.

[257] J. C. S. Davis.
Impurity atoms on view in cuprates.
Mater. Today, 5(4):24–33, 2002.

[258] V. J. Emery and S. A. Kivelson.
Importance of phase fluctuations in superconductors with small superfluid density.
Nature, 374(6521):434–437, 1995.

[259] T. Dubouchet, B. Sacépé, J. Seidemann, D. Shahar, M. Sanquer, and C. Chapelier.
Collective energy gap of preformed Cooper pairs in disordered superconductors.
Nat. Phys., 15(3):233–236, 2019.

[260] C. Kittel.
Elementary Solid State Physics.
Wiley, New York, 2005.

[261] A. Gauzzi, B. J. Jönsson-Åkerman, A. Clerc-Dubois, and D. Pavuna.
Scaling between superconducting critical temperature and structural coherence length in $YBa_2Cu_3O_{6.9}$ films.
Europhys. Lett., 51(6):667–673, 2000.

[262] J. C. Phillips.
Gapless superconductivity.
Phys. Rev. Lett., 10(3):96–98, 1963.

[263] S. H. Ji, T. Zhang, Y. S. Fu, X. Chen, X. C. Ma, J. Li, W. H. Duan, J. F. Jia, and Q. K. Xue.
High-resolution scanning tunneling spectroscopy of magnetic impurity induced bound states in the superconducting gap of Pb thin films.
Phys. Rev. Lett., 100(22):226801, 2008.

[264] E. Liebhaber, S. Acero González, R. Baba, G. Reecht, B. W. Heinrich, S. Rohlf, K. Rossnagel, F. Von Oppen, and K. J. Franke.
Yu-Shiba-Rusinov States in the Charge-Density Modulated Superconductor $NbSe_2$.
Nano Lett., 20(1):339–344, 2020.

[265] J. Senkpiel, C. Rubio-Verdú, M. Etzkorn, R. Drost, L. M. Schoop, S. Dambach, C. Padurariu, B. Kubala, J. Ankerhold, C. R. Ast, and K. Kern.
Robustness of Yu-Shiba-Rusinov resonances in the presence of a complex superconducting order parameter.
Phys. Rev. B, 100(1):014502, 2019.

[266] D. J. Choi, C. G. Fernández, E. Herrera, C. Rubio-Verdú, M. M. Ugeda, I. Guillamón, H. Suderow, J. I. Pascual, and N. Lorente.
Influence of Magnetic Ordering between Cr Adatoms on the Yu-Shiba-Rusinov States of the β-Bi_2Pd Superconductor.
Phys. Rev. Lett., 120(16):167001, 2018.

[267] J. R. Schrieffer.
The Kondo effect - The link between magnetic and nonmagnetic impurities in metals?
J. Appl. Phys., 38(3):1143–1150, 1967.

[268] N. Marzari, A. A. Mostofi, J. R. Yates, I. Souza, and D. Vanderbilt.
Maximally localized Wannier functions: Theory and applications.
Rev. Mod. Phys., 84(4):1419–1475, 2012.

[269] S. Mühlbauer, D. Honecker, É. A. Périgo, F. Bergner, S. Disch, A. Heinemann, S. Erokhin, D. Berkov, C. Leighton, M. R. Eskildsen, and A. Michels.
Magnetic small-angle neutron scattering.
Rev. Mod. Phys., 91(1):015004, 2019.

[270] S. N. Putilin, E. V. Antipov, O. Chmaissem, and M. Marezio.
Superconductivity at 94K in $HgBa_2CuO_{4+\delta}$.
Nature, 362(March):1990–1992, 1993.

[271] J. Linder and J. W. A. Robinson.
Superconducting spintronics.
Nat. Phys., 11(4):307–315, 2015.

[272] T. Wakamura, H. Akaike, Y. Omori, Y. Niimi, S. Takahashi, A. Fujimaki, S. Maekawa, and Y. Otani.
Quasiparticle-mediated spin Hall effect in a superconductor.
Nat. Mater., 14(7):675–678, 2015.

[273] M. Gradhand and J. F. Annett.
The Berry curvature of the Bogoliubov quasiparticle Bloch states in the unconventional superconductor Sr_2RuO_4.
J. Phys. Condens. Matter, 26(27):274205, 2014.

[274] M. Gradhand, D. V. Fedorov, F. Pientka, P. Zahn, I. Mertig, and B. Győrffy.
Calculating the Berry curvature of Bloch electrons using the KKR method.
Phys. Rev. B, 84(7):075113, 2011.

[275] M. Gradhand, D. V. Fedorov, P. Zahn, and I. Mertig.
Extrinsic spin hall effect from first principles.
Phys. Rev. Lett., 104(18):186403, 2010.

[276] I. Turek, J. Kudrnovský, V. Drchal, L. Szunyogh, and P. Weinberger.
Interatomic electron transport by semiempirical and ab initio tight-binding approaches.
Phys. Rev. B, 65(12):125101, 2002.

[277] A. Vernes, B. Győrffy, and P. Weinberger.
Spin currents, spin-transfer torque, and spin-Hall effects in relativistic quantum mechanics.
Phys. Rev. B, 76(1):012408, 2007.

[278] M. Oshita, S. Yotsuhashi, H. Adachi, and H. Akai.
Seebeck coefficient calculated by Kubo-Greenwood formula on the basis of density functional theory.

J. Phys. Soc. Japan, 78(2):024708, 2009.

[279] P. Soven.
Coherent-potential model of substitutional disordered alloys.
Phys. Rev., 156(3):809–813, 1967.

[280] H. Ebert, D. Ködderitzsch, and J. Minár.
Calculating condensed matter properties using the KKR-Green's function method - Recent developments and applications.
Reports Prog. Phys., 74(9):096501, 2011.

[281] S. N. Khan, J. B. Staunton, and G. M. Stocks.
Statistical physics of multicomponent alloys using KKR-CPA.
Phys. Rev. B, 93(5):054206, 2016.

[282] A. Georges and G. Kotliar.
Dynamical mean-field theory of strongly correlated fermion systems and the limit of infinite dimensions.
Rev. Mod. Phys., 68(1):13–125, 1996.

[283] J. Minár, L. Chioncel, A. Perlov, H. Ebert, M. I. Katsnelson, and A. I. Lichtenstein.
Multiple-scattering formalism for correlated systems: A KKR-DMFT approach.
Phys. Rev. B, 72(4):045125, 2005.

[284] T. Kotani and M. van Schilfgaarde.
All-electron GW approximation with the mixed basis expansion based on the full-potential LMTO method.
Solid State Commun., 121:461, 2002.

PUBLICATIONS

- Tom G. Saunderson, James F. Annett, Balázs Újfalussy, Gábor Csire, Martin Gradhand, *'Gap anisotropy in multiband superconductors based on multiple scattering theory'*, Phys. Rev. B **101**, 064510 (2020)
- Tom G. Saunderson, Zsolt Győrgypál, James F. Annett, Balázs Újfalussy, Gábor Csire, Martin Gradhand, *'Real-space multiple scattering theory for superconductors with impurities'*, Phys. Rev. B **102**, 245106 (2020)
- Tom G. Saunderson, James F. Annett, Martin Gradhand, *'Full orbital decomposition of Yu-Shiba-Rusinov states using multiple scattering theory'*, manuscript in preparation
- Emma Thill and Jacob Crosbie, Ming-Hung Wu, Tom G. Saunderson and Martin Gradhand *'Orbitals of YSR States for 3d Transition Elements and Magnetic Chains'*, manuscript in preparation
- Reena Gupta, Tom G. Saunderson, Sam Shallcross, Martin Gradhand, Jorge Quintanilla, James F. Annett, *'Superconducting double transition and substantial Knight shift in Sr_2RuO_4'*, Phys. Rev. B **102**, 235203 (2020)